Proceedings of the 16th CEReS International Symposium on Climate Change Studies through Activities of SKYNET and Virtual Laboratory for Climate Diagnostics

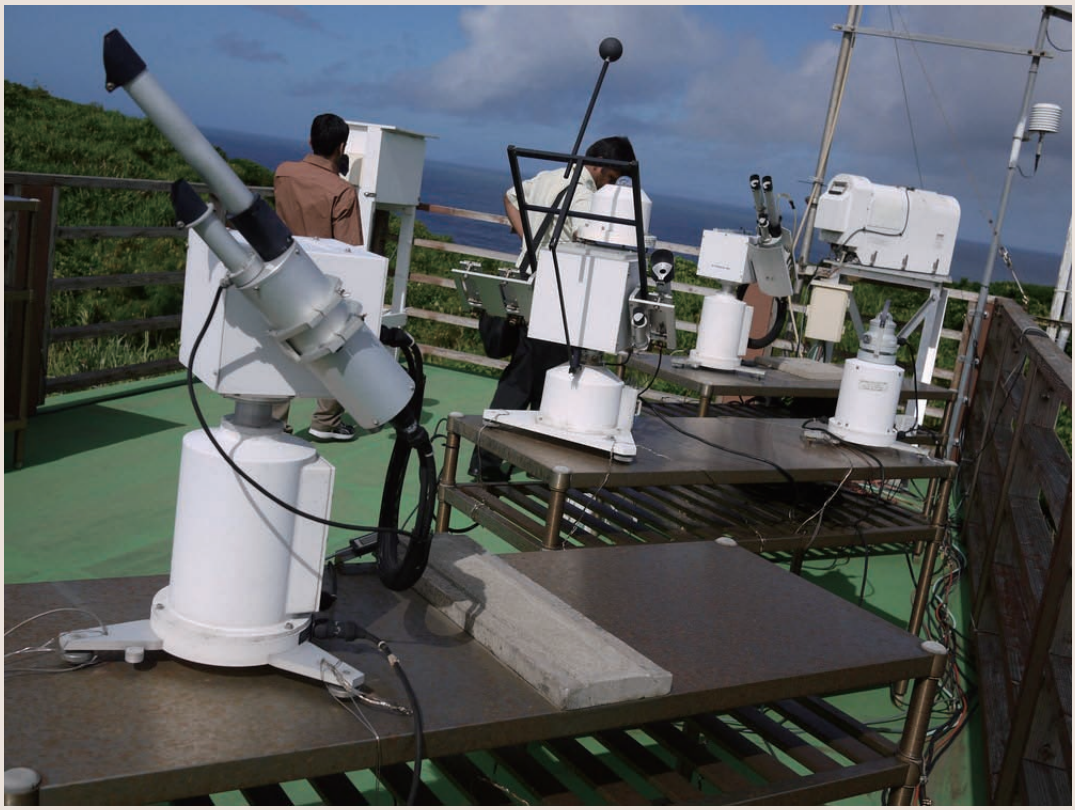

October 21-23, 2010

Nago, Okinawa, Japan

The 16th CEReS International Symposium has been supported and sponsored by the National University Corporation Chiba University and the Japan Society of the Promotion of Science (JSPS) under the CEReS research frames of the Virtual Laboratory for the climate diagnostics, SKYNET observation activity and CEReS cooperative program.

Published by
Center for Environmental Remote Sensing (CEReS),
Chiba University, Japan
1-33 Yayoi-cho, Inage, Chiba, 263-8522 Japan

Proceedings of the 16th CEReS International Symposium on Climate Change Studies through Activities of SKYNET and Virtual Laboratory for Climate Diagnostics

October 21 – 23, 2010

Nago, Okinawa, Japan

Organized by

Japan Society for the Promotion of Science

Center for Environmental Remote Sensing (CEReS), Chiba University, Japan

SKYNET

Formation of a Virtual Laboratory for Diagnosing the Earth's Climate System

(Editors)

M. K. Yamamoto, A. Higuchi, and T. Takamura

Contents

Evaluation and data assimilation of aerosol distributions and climate effects simulated by SPRINTARS using remote sensing observations in the Asian region

Toshihiko Takemura[1]
[1]*Research Institute for Applied Mechanics, Kyushu University*
6-1 Kasuga-koen, Kasuga, Fukuoka 816-8580, Japan
toshi@riam.kyushu-u.ac.jp

Abstract

A global aerosol transport-climate model, SPRINTARS, has been developed to simulate aerosol global distributions, radiative forcing, and climate effects. Remote sensing data from the surface and satellites are used to check simulated aerosol optical properties and to assimilate SPRINTARS. Quality-assured and long-term observations are essential in order to use in researches on the climate change and data assimilation.
Keywords **:** aerosol, SPRINTARS, radiative forcing, climate change, forecast, data assimilation

1. Introduction

There are still uncertainties in estimating aerosol effects on the climate system (IPCC, 2007). A global aerosol transport-climate model, SPRINTARS, has been developed to simulate aerosol global distributions and climate effects, which are the direct, semi-direct, and indirect effects and their feedback effects.

2. Model description

SPRINTARS (http://sprintars.net/) is coupled with MIROC which is a Japanese general circulation model (GCM) (K-1 Model Developers, 2004). The horizontal and vertical resolutions are T106 (approximately 1.1 by 1.1 degrees in longitude and latitude) and 56 layers, respectively. SPRINTARS includes the transport (emission, advection, diffusion, sulfur chemistry, and deposition), radiation, cloud, and precipitation processes of all main tropospheric aerosols (black carbon, organic matter, sulfate, soil dust, and sea salt) to simulate aerosol distributions and climate effects. Aerosol optical properties, i.e., optical thickness, Ångström exponent, and single scattering albedo, are also calculated at specific wavelengths to compare with remote sensing data. The model treats not only the aerosol mass mixing ratios but also the cloud droplet and ice crystal number concentrations as prognostic variables, and the nucleation processes of cloud droplets and ice crystals depend on the number concentrations of each aerosol species. Changes in the cloud droplet and ice crystal number concentrations affect the cloud radiation and precipitation processes in the model. The detailed models description in Takemura et al. (2000, 2002, 2005, 2009a).

3. Discussion

SPRINTARS has been improved referring a lot of aerosol and cloud parameters measured by remote sensing from satellites (e.g., AVHRR, MODIS, and CALIOP) and the surface (e.g., AERONET and SKYNET). Simulated aerosol optical properties capture observational characteristics, for example, high optical thickness and high Ångström exponent in urban areas and biomass burning areas/seasons, high optical thickness and low Ångström exponent in dusty areas/seasons, and low optical thickness and low Ångström exponent over remote ocean. There is, however, a systematic differences in the global mean optical thickness between simulations and satellite retrievals although anthropogenic optical thickness agrees well (Kaufman et al., 2005). This may be because satellite sensors cannot detect thin optical thickness over remote ocean. To understand and reduce uncertainties in simulated aerosol distributions and effects, the global aerosol model intercomparison project, AeroCom, is acting, comparing with various aerosol observations (http://nansen.ipsl.jussieu.fr/AEROCOM/).

SPRINTARS can calculate aerosol radiative forcing due to the direct, indirect, and semi-direct effects (Takemura et al., 2002, 2003, 2005). MIROC coupled with SPRINTARS also estimated the trend of radiative forcings from the year 1850 to present day due to various climate forcing agents, i.e., long-lived greenhouse gases, ozone, aerosol, volcanic activity, and land use change (Takemura et al., 2006). It is essential to use long-term observational data for comparing with simulations on the climate change.

As an application of using SPRINTARS, a weekly aerosol forecasting system has been developed (Takemura et al., 2009b). The forecasting system is automatically performed every day and simulated results are uploaded to the SPRINTARS homepage (http://sprintars.net/) about 06JST

(23 UTC). The other application is construction of data assimilation system. Quality-assured observational data is essential to check the forecasting system and to drive the assimilation system.

Acknowledgements

I would like to thank the contributors of development of SPRINTARS and MIROC. The simulation in this study was performed on the NIES supercomputer system (NEC SX-8R). This study is supported by the Grant-in-Aid for Young Scientists (21681001) of the Ministry of Education, Culture, Sports, Science, and Technology of Japan, Environment Research and Technology Development Fund (RF-0901) by the Ministry of the Environment, Japan, and Mitsui & Co., Ltd. Environment Fund (R08-D035).

References

1) IPCC, 2007: Climate Change 2007: The Physical Science Basis. Contributing of Working Group I to the Fourth Assessment Report of the Intergovernmental Panel on Climate Change, edited by S. Solomon, D. Qin, M. Manning, Z. Chen, M. Marquis, K. B. Averyt, M. Tignor, and H. L. Miller, 996 pp., Cambridge Univ. Press, Cambridge, United Kingdom and New York, NY, USA.
2) K-1 Model Developers, 2004: K-1 coupled GCM (MIROC) description. edited by H. Hasumi and S. Emori, K-1 Tech. Rep. 1, 34 pp., Center for Climate System Research, University of Tokyo, Tokyo, Japan.
3) Kaufman, Y. J., O. Boucher, D. Tanre, M. Chin, L. Remer, and T. Takemura, 2005: Aerosol anthropogenic component estimated from satellite data. Geophysical Research Letters, 32, L17804, doi:10.1029/2005GL023125.
4) Takemura, T., H. Okamoto, Y. Maruyama, A. Numaguti, A. Higurashi, and T. Nakajima, 2000: Global three-dimensional simulation of aerosol optical thickness distribution of various origins. Journal of Geophysical Research, 105, 17853–17873.
5) Takemura, T., T. Nakajima, O. Dubovik, B. N. Holben, and S. Kinne, 2002: Single-scattering albedo and radiative forcing of various aerosol species with a global three-dimensional model. Journal of Climate, 15, 333–352.
6) Takemura, T., T. Nakajima, A. Higurashi, S. Ohta, and N. Sugimoto, 2003: Aerosol distributions and radiative forcing over the Asian-Pacific region simulated by Spectral Radiation-Transport Model for Aerosol Species (SPRINTARS). Journal of Geophysical Research, 108(D23), 8659, doi:10.1029/2002JD003210.
7) Takemura, T., T. Nozawa, S. Emori, T. Y. Nakajima, and T. Nakajima, 2005: Simulation of climate response to aerosol direct and indirect effects with aerosol transport-radiation model. Journal of Geophysical Research, 110, D02202, doi:10.1029/2004JD005029.
8) Takemura, T., Y. Tsushima, T. Yokohata, T. Nozawa, T. Nagashima, and T. Nakajima, 2006: Time evolutions of various radiative forcings for the past 150 years estimated by a general circulation model. Geophysical Research Letters, 33, L19705, doi:10.1029/2006GL026666.
9) Takemura, T., M. Egashira, K. Matsuzawa, H. Ichijo, R. O'ishi, and A. Abe-Ouchi, 2009a: A simulation of the global distribution and radiative forcing of soil dust aerosols at the Last Glacial Maximum. Atmospheric Chemistry and Physics, 9, 3061–3073.
10) Takemura, T., 2009b: Development of Forecasting System for Atmospheric Aerosols. Tenki, 56, 455–461 (in Japanese).

The use of SKYNET observations for aerosol assimilation

Nick Schutgens[1], Takamichi Iguchi[2], Teruyuki Nakajima[1]

[1]*AORI, University of Tokyo, 5-1-5 Kashiwanoha, Kashiwa, Chiba 277-8568, Japan, schutgen@aori.u-tokyo.ac.jp*

[2]*NASA Goddard Space Flight Center, Greenbelt, MD 20771, USA, iguchi@agnes.gsfc.nasa.gov*

Abstract

Assimilation of global aerosol is a new technique to circumvent certain limitations in our knowledge of the aerosol system. By assimilating observations of aerosol in a global transport model, uncertainties in e.g. aerosol emissions may be reduced. Due to rapid economic growth, the Asian region has become an important source region for aerosols, and the interest in its effects on human health and the Earth's climate are only increasing. SKYNET provides observational coverage of this important region and we will show several examples of the use of SKYNET data in aerosol assimilation.

Keywords **:** SKYNET, aerosol, assimilation

1. Introduction

To understand the climatological impact of aerosols or to forecast air-quality, it is indisputably necessary to resort to models to obtain a spatially and temporally consistent picture of the aerosol system. Observations will always be limited in their coverage. Unfortunately, global and regional aerosol modeling is hampered by poorly known emission scenarios of both man-made and natural aerosols.. The emission of sea-salt and mineral dust is usually described through parametrisations (in mainly 10m windspeed, e.g. [1]), based on limited observational campaigns or incomplete models. More-over, there is a scale problem for in particular global models that have to assume constant emissions over several 100's of kilometers. The emission of man-made aerosol is usually based on conversions of governmental statistics of energy use by various industries, e.g. [2]. In addition to the obvious limitation of questionable representativeness, these emission scenarios are often monthly if not yearly averages only.

Assimilation [3] is a common denominator for a variety of techniques to combine aerosol simulations and observations in a more reliable and comprehensive dataset. During assimilation, a variety of observations are used to improve the model state of an aerosol transport model. A new, flexible and physically consistent assimilation scheme is the so-called ensemble Kalman filter [4] that uses an ensemble of model simulations to represent model prediction uncertainty which may then be compared to observational errors. In this paper, we apply this ensemble Kalman filter to the global aerosol transport model SPRINTARS [5,6].

SKYNET (http://atmos.cr.chiba-u.ac.jp/) is a network of photometers dedicated to aerosol observations in Asia. The network provides AOT (aerosol optical thickness), AE (Angstrom exponent) and SSA (single scattering albedo) for clear sky observations, every 15 minutes.

In this paper, we show several examples of the use of SKYNET observations for aerosol assimilation. We start by discussing the validation of assimilated AOT and AE, and continue with an example where SKYNET data themselves are assimilated. Finally, we discuss the possibility of assimilating SKYNET SSA.

2. The Local Ensemble Kalman filter

If we define the state $\mathbf{x}$ of our model as a vector with the mixing ratios of simulated aerosols all over the globe, we can define a model prediction error as

$$\mathbf{P} = \left\langle \left(\mathbf{x} - \langle \mathbf{x} \rangle\right)^T \left(\mathbf{x} - \langle \mathbf{x} \rangle\right) \right\rangle,$$

where $\langle\ \rangle$ denotes an ensemble average. The members of the ensemble use perturbed emission scenarios that represent our uncertainty in source strengths. The covariant matrix $\mathbf{P}$ then represents the uncertainty in mixing ratios at a certain moment, with of course associated uncertainties in e.g. AOT and AE. Now if we have a set of observations $\mathbf{y}$, with an error covariant $\mathbf{R}$, defined similarly to $\mathbf{P}$, and simulated observations $H(\mathbf{x})$, we may combine our model and observational information into an optimal new state that is, broadly speaking, a average between the original state and the observations, each weighted by their relative errors (covariants). The original state is usually called the background, apriori or forecast state $\mathbf{x}^f$ and the new state is usually called the analysis state $\mathbf{x}^a$, and they are

connected through the well-known Kalman filter equation

$$\mathbf{x}^a = \mathbf{x}^f + \mathbf{P}^a\mathbf{H}^T\mathbf{R}^{-1}\left(\mathbf{y} - \mathbf{H}\mathbf{x}\right)$$

$$\mathbf{P}^a = \left(\mathbf{I} + \mathbf{P}^f\mathbf{H}^T\mathbf{R}^{-1}\mathbf{H}\right)^{-1}\mathbf{P}^f$$

We use a 24-member ensemble for perturbed emissions of fine (sulfate & carbon) and coarse (seasalt and dust) aerosol. The average emission in the ensemble is different from the standard emission, so that the assimilation has a substantially different AOT and AE than the standard simulation, when cloudiness or such temporarily prevents observations.

3. Validation of assimilation products

In [7], we assimilated AERONET observations of AOT and AE for the month July 2005. Part of the validation was done by SKYNET observations at Cape-Hedo and Toyama. Since AERONET had only a few sites in Asia in 2005, we cannot expect assimilation results to be very robust. In Fig. 1, we show AOT from a standard SPRINTARS simulation, observations by SKYNET and simulated results after assimilation of AERONET.

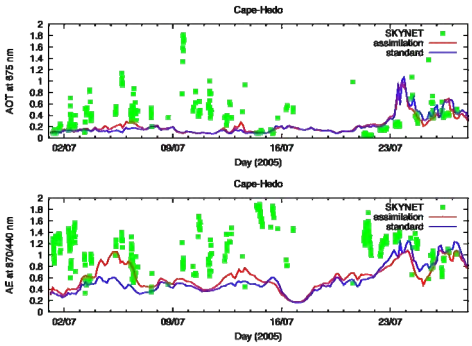

Figure 1: Aerosol as observed and simulated at Cape-Hedo.

This comprises an independent validation of the assimilation. Immediately, it is obvious that for the first two weeks both the standard simulation and the assimilation results are quite poor, but they are significantly better during the last week (remember that the assimilation uses different average emissions than the standard simulation, so the AERONET observations obviously have a positive effect). The main difference between these two periods is the dominant wind direction. During the first two weeks it is mainly South-Easterly, but later it changes to North-Westerly. That implies that during the last week, aerosols from the Asian mainland dominated while earlier marine aerosol dominated. Or did they? The SKYNET observations, combined with surface observations by EANET [8], strongly suggest that Cape-Hedo had a lot of sulfate aerosol during this period. As it turns out, the Mt. Anathahan volcano emitted large amounts of SO_2 during this period, as can be clearly seen in OMI imagery (a timeseries of observations is found at http://so2.umbc.edu/omi/movies/wpac_omso2_1jan-30sep05.mov). So we conclude that the AERONET assimilation yields good results at Cape-Hedo, except in the unusual case of the erupting volcano which is at the moment not accounted for in our perturbed emission scenarios.

4. Assimilation of SKYNET data

In another experiment, we assimilated SKYNET AOT and AE, in addition to AERONET and CHSNET AOT and AE as well as MODIS Aqua AOT over ocean for March 2005. The combination of these three surface networks provides very good coverage of the Asian region (with the exception of India), although the number of AERONET sites is rather limited and CSHNET (a network of handheld photometers in China) is less accurate than AERONET and SKYNET. In all, SKYNET is an important contribution to any experiment that focuses on the Asian region.

In Fig. 2, we show consistency of the assimilation for SKYNET. That is: after assimilation ,AOT, monthly biases should be much reduced. For AERONET, with globally 216 sites , this is clearly the case. For SKYNET, the low number of regional sites (10) muddles the picture. However, when the standard bias is large, the assimilation can strongly improve the simulation. This suggests both that transport by SPRINTARS is sufficiently appropriate and that the assimilation of SKYNET data has an impact. Systematic errors in both AOT and AE (not shown) are reduced.

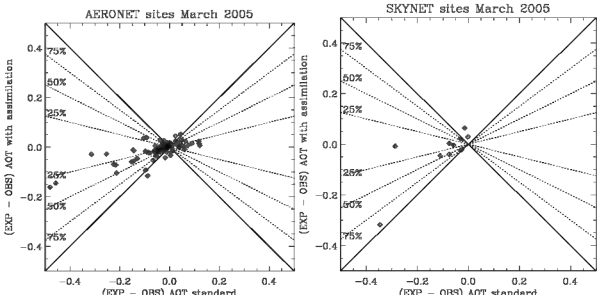

Figure 2: Monthly biases for standard simulation and assimilation for the AERONET and SKYNET sites.

At the moment, there are two different applications of the resulting assimilated aerosol fields. First, such fields can be used to initialize cloud-resolving models that study

the interrelation of aerosols and meteorological conditions in cloud formation. Fig. 3 shows an example of the simulated water cloud distribution over Asia using assimilated aerosol fields in the Japan Meteorological Agency Non-Hydrostatic Model (JMA-NHM) with spectral bin cloud microphysics.

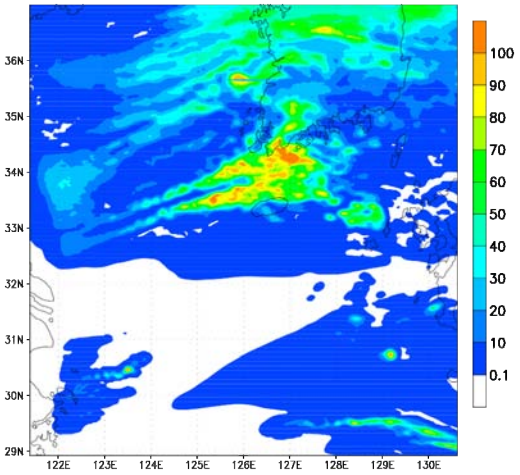

Figure 3: Distribution of water cloud optical thickness in a cloud model with bin-resolved cloud microphysics.

These cloud simulations may subsequently be compared to MODIS observations for verification (ongoing work).

Second, the assimilated aerosol fields can be used to study vertical profiles of aerosols. In Fig. 4, we show 4 examples of averaged (March-May 2005) attenuated backscatter profiles in Asia. As is clear from Fig. 2 (left panel), the original simulation already provided AOT and AE quite close to the SKYNET observations. Yet the LIDAR observations by ADnet are clearly different. This suggests a problem with the extinction-to-backscatter ratio, or in other words, the aerosol scattering properties (ongoing work).

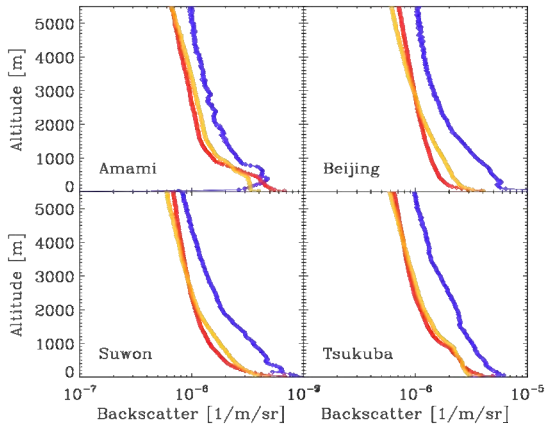

Figure 4: LIDAR profiles over Asia; observed (blue), standard simulation (red) or assimilation (orange).

6. Assimilation of SSA

In principle, there is no problem in assimilating SSA as an independent piece of information. Assimilating SSA is actually very interesting, as it will allow the distinction of carbon and sulfate aerosol. More-over, SSA is an important parameter in the calculation of direct aerosol radiative forcing. Yet, there are a few issues that make assimilation of SSA more daunting than the assimilation of AOT or AE. The first is the poorly constrained (imaginary) refractive index of carbon aerosols (this issues includes the difficult question of their mixing state). According to [9], carbon absorptive characteristics vary over a large range. But to simulate observations from the model ensemble, it is necessary to choose a characteristic value. Secondly, correct assimilation requires a realistic estimate of the error in observed SSA. After all, it is the weighting between observational error and model prediction error that determines how much the assimilation system will modify the state because of a certain observation.

Finally, there is the issue of source location. Our assimilation system in effect assumes source locations and then adjusts source strengths based on observations. However, forest fires are spatially and temporally highly variable. Correct assimilation of SSA, with the purpose of improving carbon simulation, would benefit greatly from improved emission source locations based on fire maps (e.g. from MODIS).

7. Summary

We have discussed current and future use of SKYNET observations for an aerosol assimilation system. Since SKYNET fills a geographic data gap of surface based aerosol observations in an important natural and man-made aerosol source region (Asia), its importance can not be overstated. On the contrary, it would be beneficial if the network is expanded, in particular into India. Finally, for optimal assimilation it is desirable that more efforts at observational error characterization are made, either through comparison with co-located AERONET sites or through radiative transfer simulations.

Acknowledgements

Part of this research was supported by funds from MOE/GOSAT, MOE/GER fund B- 083, JST/CREST, JAXA/EarthCARE, MEXT/VL for climate diagnostics, and MEXT/Innovative Program of Climate Change Projection

as well as the NIES GOSAT project team.

References

1) Gong S.L.: A parametrization of sea-salt aerosol source function for sub- and super-micron particles, Glob. Biochem. Cycles 17, 2003.

2) Streets D.G., Yan F., Chin M., Diehl T., Mahowald N., Schultz M., Wild M., Wu Y., Yu C.: Anthropogenic and natural contributions to regional trends in aerosol optical depth, J. Geophys. Res. 114, 2009.

3) Bouttier F., Cortier P.: Data assimilation concepts and methods, ECMWF training course, 1999.

4) Hunt, B., Kostelich, E., and Szunyogh, I.: Efficient data assimilation for spatiotemporal chaos: a Local Ensemble Transfom Kalman Filter, Physica D, 230, 112–126, 2007.

5) Takemura, T., Okamoto, H., Maruyama, Y., Numaguti, A., Higurashi, A., and Nakajima, T.: Global three-dimensional simulation of aerosol optical thickness distribution of various origins, J. Geophys. Res., 105, 17,853–17,873, 2000.

6) Takemura, T., Nakajima, T., Dubovik, O., Holben, B., and Kinne, S.: Single-scattering albedo and radiative forcing of various aerosol species with a global three-dimensional model, J. Clim., 15, 333–352, 2002.

7) Schutgens N.A.J., Miyoshi, T., Takemura, T., Nakajima, T.: Applying an ensemble Kalman filter to the assimilation of AERONET observations in a global aerosol transport model, ACP 10, 2010.

8) EA team: Data report on the acid deposition in the East Asian region, Tech. rep., Network center for EANET, http://www.eanet.cc/, 2005.

9) Bond T.C., Bergstrom R.W.: Light absorption by carbonaceous particles: an investigative review, Aer. Sci. & tech. 40, 27-67, 2006.

Estimation of radiation budget using geostationary satellites

Hideaki Takenaka, Munehisa K Yamamoto, Masamitu Hayasaki, Atsushi. Higuchi, Naoko Saitoh, Hiroaki Kuze, Fumihiko Nishio, Tamio Takamura (1)**,**
Satoru Fukuda, Teruyuki Nakajima (2)**,**
Arata Okuyama, Yuki Kosaka, Ryuichiro Nakayama, Hiromi Owada,
Kenji Date, Tomoaki Ono (3)

(1) C*enter for environmental remote sensing, Chiba university*
(2) *Atmosphere and Ocean Research Institute, Tokyo university*
(3) *Meteorological Satellite Center, Japan Meteorological Agency*

Abstract

SW radiation budget is estimated using geostationary satellites (GMS-5, GOES-8, GOES-10, METOSAT-5, METEOSAT-7). Each satellite data are calibrated, and optics properties of the cloud are retrieved. An accurate calibrated data propose the better accuracy for analysis of cloud and radiation budget. In this study, cloud and SW radiation budget analysis are done by CAPCOM algorithm and EXAM SYSTEM. On the other hand, aerosol optical thickness is retrieved by L-REAP algorithm. We discuss the possibility of aerosol-cloud-radiation interaction in north Pacific ocean and north Atlantic ocean.

Keywords **:** Radiation budget, Aerosol, Cloud, Radiation, Interaction

1. Introduction

Clouds can cool the Earth by reflecting solar radiation and also can keep the Earth warm by absorbing and emitting terrestrial radiation. They are important in the energy balance at the Earth surface and the Top of the Atmosphere (TOA) and are connected complicatedly into the Earth system as well as other climate feedback processes. Aerosols reflects solar radiation and cools the earth, and it is called a direct effect. Moreover, aerosols influences the condensation of the cloud particles by indirect effect. Thus, cloud and aerosol are one of the important element in Earth energy system, and it's important to be estimate radiation budget to better understand climate and environmental change.

Wetherald and Manabe discussed the cloud feedback process using a General Circulation Model (GCM) [Wetherald and Manabe, 1988]. Tsushima and Manabe tested the cloud feedback sensitivity to global mean surface temperature based on explicit definition of feedback processes. GCM has strong sensitivity for global mean surface temperature although analysis of sensitivity based on observations are negligible [Tsushima and Manabe, 2001]. Cloud modeling is a big uncertainty for the climate model and long term analysis for the global change would be estimated. It is important to evaluate the influence of cloud for Earth's radiation budget based on observations.

Geostationary satellite observations are useful for estimating the upward and downward radiation budget at the surface and the TOA over wide regions and at high temporal resolution. We develop a vicarious calibration technique for the global analysis. An accurate calibrated data propose the better accuracy for analysis of cloud and radiation budget. (In this study, four satellites: GMS-5, GOES-8, GOES-10, METOSAT-5, METEOSAT-7 are used for analysis). An accurate calibrated data propose the better accuracy for analysis of cloud and radiation budget. Additionally, the possibility of aerosol-cloud-radiation interaction is discussed.

2. Methods

2.1.Calibration of satellites observation data

The geostationary satellite has a big advantage for estimation of radiation budget because of highly time-resolved data. One of key factors in the estimation is a

sensor calibration. It has some issues in the calibration procedures. In this study, five geostationary satellites (GMS-5, GOES-8, GOES-10, METEOSAT-5, METEOSAT-7) is used for radiation budget analysis. Each satellite were calibrated by Global Space based Inter-Calibration System (GSICS) proposed method based on three component using the radiative transfer code RSTAR6. The satellites data calibrated in high accuracy achieves a accurately radiation budget analysis.

2.2.Retrieval of cloud optical properties

We used the Comprehensive Analysis Program for Cloud Optical Measurement (CAPCOM) [Nakajima and Nakajima, 1995; Kawamoto et al., 2001]. This algorithm was also adopted as one of the standard algorithms for the Advanced Earth Observing Satellite II/Global Imager (ADEOS-II/GLI) products [Nakajima, 1999]. we applied CAPCOM to five geostationary satellites data to retrieve only the cloud optical thickness using the VIS channel

2.3.Estimation of radiation budget

We develop a high speed and accurate algorithm based on Neural Network (NN). The advantages of the NN approach are to be speed of the computations and allows to produce numerous parameters since it does not require a large data base. Figure 1 indicates a three layers network structure. Neuro-link Network solver (NN solver) is built by improved learning algorithm “Dist.-BP” that has an anti-local minimum and a survival rule of neuron depending on nerves activities [Takenaka et al., 2009; 2010]. The NN approach is one of the solution to following problems. In general, satellite based estimate methods often use a Look-up Tables (LUT). Since pre-calculated values are used, the LUT methods are effective for large amount of data processing. However, if the effects of absorbing gasses and the particle optical characteristics are incorporate dprecisely, LUT becomes huge volume. An increase in parameter needs not only the increase of LUT volume but also complex interpolation of LUT. The NN solver traces radiative transfer code System for Transfer of Atmospheric Radiation (RSTAR) [Nakajima and Tanaka, 1986, 1998] for high speed and accurate computation. The Extreme speed and Approximation module Multiple drive System (EXAM SYSTEM) controls NN solvers by multi-threading. EXAM SYSTEM applies to MTSAT-1R, estimates the solar radiation at the TOA and the surface with semi-real time, and evaluated against in situ observations. The EXAM SYSTEM uses eight Central Processing Unit (CPU) cores, And logically sliced target area

3. Result and discussion

Radiation budget product is generated based on five geostationary satellites (Fig 2). Each satellites products are smoothly connected by accurate calibration (Fig. 3). In past report, we pointed out the possibility of aerosol-cloud-radiation interaction in north Pacific ocean [Takenaka, 2009; 2010]. It indicate aerosol and thin cloud has a same pattern. They kept by strong diffuse component in
the east Asian to North Pacific ocean region. On the other hand, those characteristics (direct and diffuse component) showed the same trend in North Atlantic Ocean in ADEOS-II/GLI result [Takenaka, 2009; 2010]. In this study, we focus the North Atlantic Ocean region using developed radiation product. Figure 4 and Figure 5 indicate the downward SW flux at the surface diffuse component and direct component (June and September, 2002). We found the strong diffuse component in north Atlantic ocean in June 2002, And direct component is blocked. Those trend are not shown in September. Figure 6 shows the influence of cloud on downward SW flux. Diffuse and direct component trend are caused by low optical thickness cloud. Moreover, aerosol optical thickness increases in north Atlantic ocean (Fig.7). These trends shows the same trend in east Asia to North Pacific ocean.

- Formation of a Virtual Laboratory for Diagnosing the Earth's Climate System -

In order to diagnose the earth's climate system under severe stress such as a global warming, the cooperative research centers (CCSR, HyARC, CAOS, and CEReS,) construct "Virtual Laboratory", and research climate and environmental studies cooperatively with properties of each center. CEReS activities are Geostationary satellites global data archives and construction of Satellite information data base. Moreover, development of atmospheric radiation budget product. We aim at the contribution to a climate model and the better understanding of the climate

system.

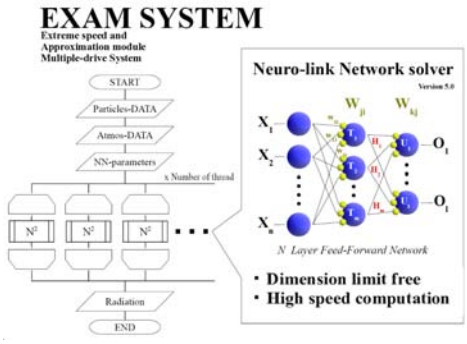

Figure 1: Schematic illustration of EXAM SYSTEM. NN solvers traces radiative transfer calculation.

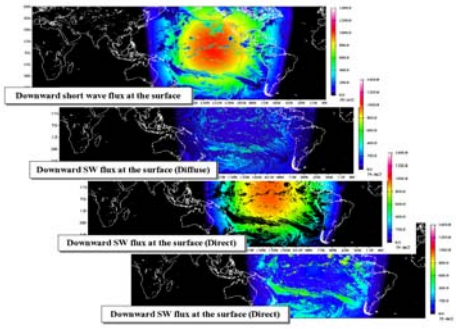

Figure 2: Test product of SW radiation budget product using five geostationary satellites. September 2-3 , 2002.

References

Wetherald, R. T. and S. Manabe (1988), Cloud feedback processes in a general circulation model , J. Atmos. Sci., 45(8), 1397-1415.

Tsushima, Y. and S. Manabe (2001), Influence of cloud feedback on annual variation of global mean surface temperature , J. Geophys. Res., 106(D19), 22,635-22,646.

Nakajima, T. Y., and T. Nakajima (1995), Wide-area determination of cloud microphysical properties from NOAA AVHRR measurements for FIRE and ASTEX regions, J. Atmos. Sci., 52, 4043-4059.

Kawamoto, K., T. Nakajima, and T.Y. Nakajima, (2001), A global determination of cloud microphysics with AVHRR remote sensing, J. Climate, 14, 2054-2068.

Nakajima, T., and M. Tanaka (1986), Matrix formulations for the transfer of solar radiation in a plane-parallel scattering atmosphere, J. Quant. Spectrosc. Radiat. Transfer,35, 13-21.

Nakajima, T., and M. Tanaka (1988), Algorithms for radiative intensity calculations in moderately thick atmospheres using a truncation approximation, J. Quant. Spectrosc. Radiat. Transfer, 40, 51-69.

Takenaka, H., T. Y. Nakajima, A. Higurashi, A. Higuchi, T. Takamura, R. T. Pinker, and T. Nakajima 2010: Estimation of Solar radiation using a Neural Network based on Radiative Transfer, J. Geophys. Res., (second revised)

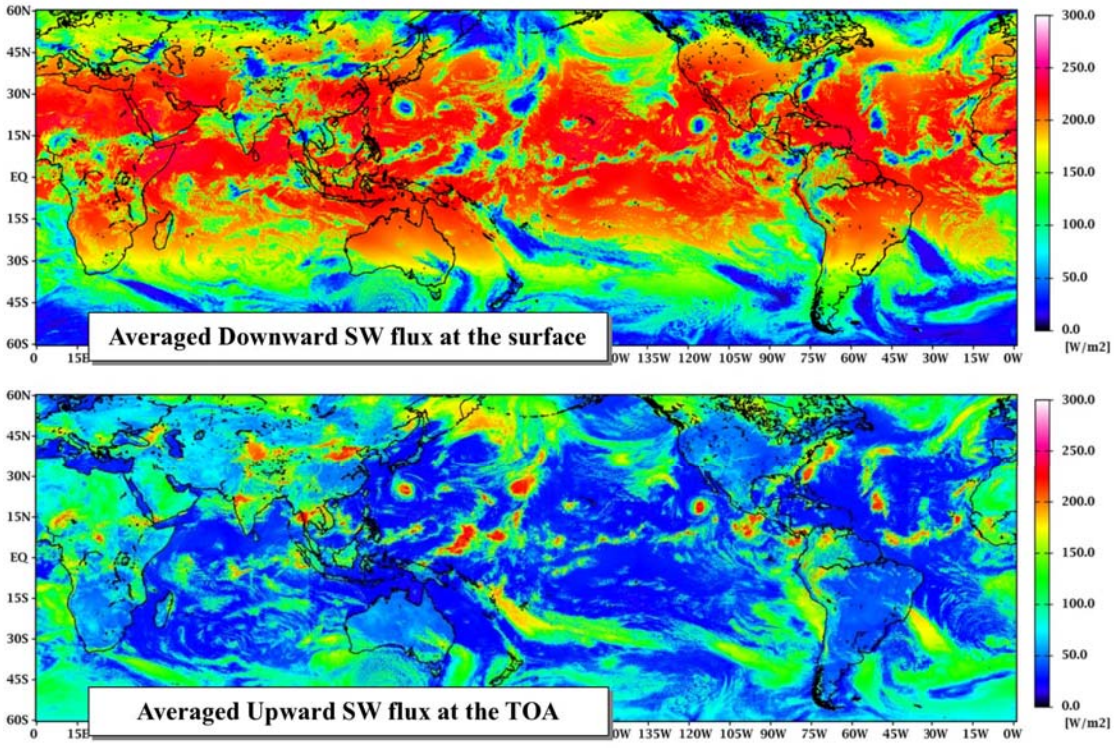

Figure 3: Averaged Downward SW flux at the surface and Upward SW flux at the TOA.

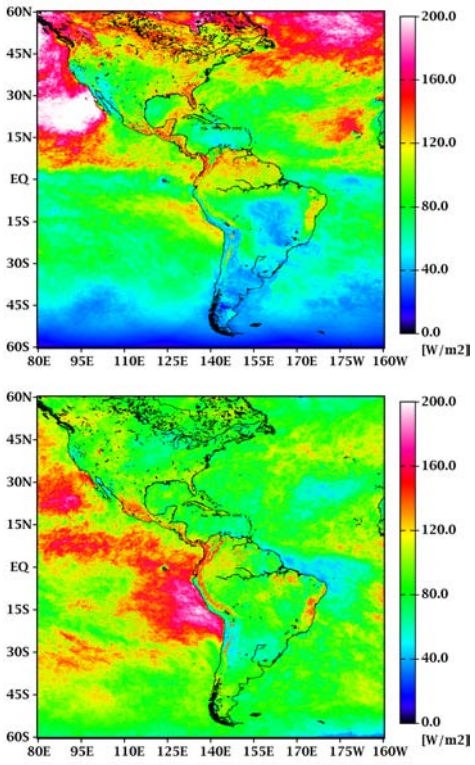

Figure 4: Downward SW flux at the surface diffuse component. Upper side: June 2002. Lower side: September 2002.

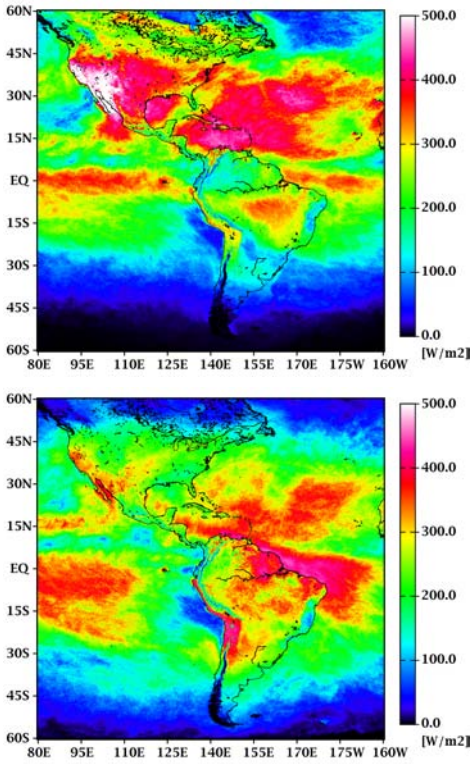

Figure 5: Downward SW flux at the surface direct component. Upper side: June 2002. Lower side: September 2002.

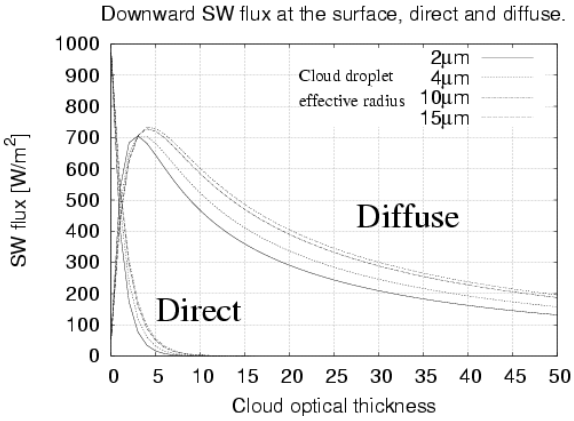

Figure 6: Influence of cloud on downward SW flux at the surface direct and diffuse component.

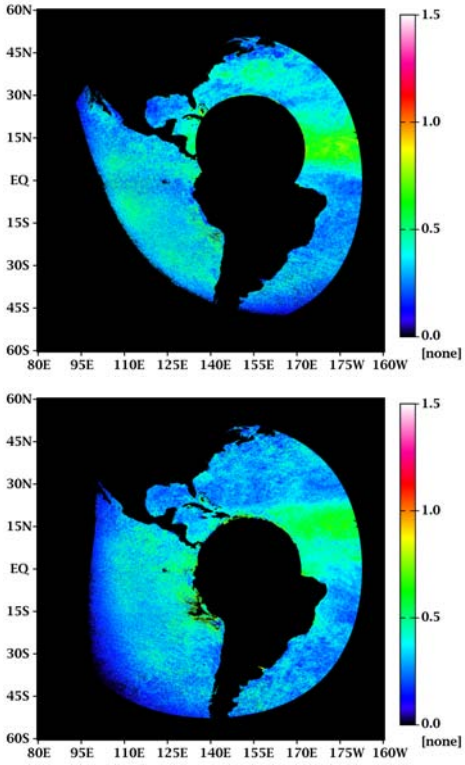

Figure 7: Aerosol optical thickness retrieved from GOES-8. Upper side: June 2002. Lower side: September 2002.

Retrieval methods of microphysical and optical properties of cloud vertical profiles from radiances measured by ground- based observations at a specific point

T. Sakami, A. Uchiyama, A. Yamazaki, and R. Kudo
Meteorological Research Institute, Japan Meteorological Agency,
1-1, Naganine, Tsukuba, Ibaraki, JAPAN 305-0052.
E-mail:tsakami@mri-jma.go.jp

Abstract

To estimate microphysical and optical properties of cloud vertical profiles from radiances measured by ground-based observations at a specific point, retrievals of the Bayesian estimate using the maximum likelihood method and estimate using the Kalman filter are developed. In addition, the estimate system based on these developed retrievals is expanded in principle from one estimate cycle to four estimate cycles. Through ideal experiments, it is founded out that a coupling among different retrieval methods is likely to improve the accuracies of estimates.

***Keywords* :** sky radiometer; radiance; microphysical property; optical property; cloud vertical profile; Kalman filter; Bayesian estimate; maximum likelihood method

1. Introduction

The Meteorological Research Institute (MRI, Japan) has developed the basis of technology to understand climate change in atmospheric radiative properties to be caused by clouds and aerosols. Through guessing microphysical and optical properties of clouds by some radiances at some visible and near-infrared wavelengths, azimuth angles and zenith angles measured by a Sun-sky scanning photometer called i-skyradiometer, manufactured by PREDE Co. Ltd. (product name POM02), their properties of clouds linked with observations contribute to estimates of uncertainties of the radiative forcing in the present climate or the projection using climate models. Furthermore, through guessing their properties of cloud vertical profiles, their properties of cloud vertical profiles linked with observations could contribute to the data assimilation system in the weather prediction model.

To estimate microphysical and optical properties of cloud vertical profiles from information of radiances measured by ground-based observations at a specific point, various retrieval methods are developed. Moreover results of ideal experiments are showed using these developed retrievals.

2. Methods

To estimate microphysical and optical properties of cloud vertical profiles from radiances measured by ground-based observations at a specific point corresponds to solving the inverse problem to a one-dimensional vertical atmospheric radiative transfer model. In this study, to solve its inverse problem, some retrievals of the Bayesian estimate using the maximum likelihood method and estimate using the Kalman filter are newly developed. In addition, the estimate system based on these developed retrievals is expanded as showed by Fig.1. $\{x_l^\lambda\}_{\lambda\in\Lambda,\, l\in Z}$ is a set of variables to estimate, Λ and Z are index sets. Λ represents a set of physical variables, such as cloud liquid water mixing ratio, cloud ice mixing ratio, mode radius and standard deviation of cloud droplet or ice crystal distribution. Z represents a set of atmospheric heights at which variables to estimate are deposited. $\{A_k\}_{k\in K}$ is a set of new variables through a basis transform. K is a index set linked with Λ and Z through a basis transform. N represents a truncated index number. The over-bar and over-tilde represent sets to which $\{A_k\}_{k<N}$ and $\{A_k\}_{k\geq N}$ are mapped by an inverse basis transform. The superscript, *estimate* represents a set which is estimated from solving the inverse problem. It is the standard estimate that $\{x_l^\lambda\}_{\lambda\in\Lambda,\, l\in Z}$ is mapped to $\{\ln x_l^\lambda\}_{\lambda\in\Lambda,\, l\in Z}$, $\{\ln x_l^\lambda\}^{estimste}_{\lambda\in\Lambda,\, l\in Z}$ is deduced from solving the inverse problem using $\{\ln x_l^\lambda\}_{\lambda\in\Lambda,\, l\in Z}$, is mapped to $\{x_l^\lambda\}^{estimste}_{\lambda\in\Lambda,\, l\in Z}$, $\{x_l^\lambda\}_{\lambda\in\Lambda,\, l\in Z}$ is equal to $\{x_l^\lambda\}^{estimste}_{\lambda\in\Lambda,\, l\in Z}$, and until estimated radiances are close to measured radiances, this process is repeated. A series of this process is called estimate cycle. $\{\ln x_l^\lambda\}_{\lambda\in\Lambda,\, l\in Z}$ is transformed to new variables $\{A_k\}_{k\in K}$ by a basis transform. Then, a new estimate cycle to pass $\{A_k\}^{estimate}_{k\in K}$ is introduced in the estimate system. $\{A_k\}_{k\in K}$ is divided between $\{A_k\}_{k<N}$ and $\{A_k\}_{k\geq N}$. This means that dominant component and anomaly component are represented in the estimate system. In this study, the former is preserved, and the latter is estimated. Then, two estimate cycles to pass $\{A_k\}^{estimate}_{k\geq N}$ or $\{\ln \tilde{x}_l^\lambda\}^{estimste}_{\lambda\in\Lambda,\, l\in Z}$ are newly introduced in the estimate system.

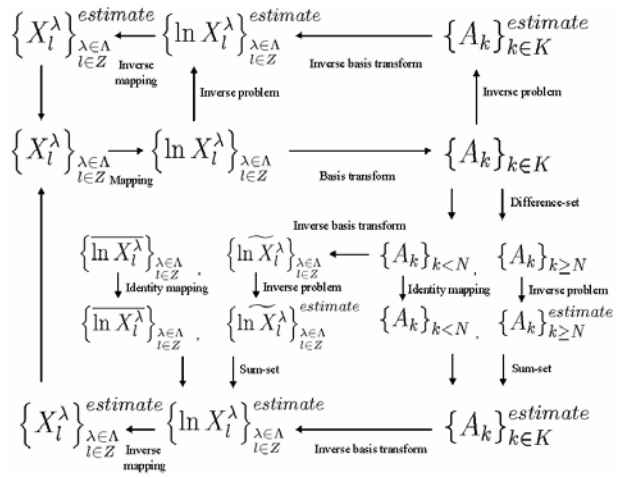

Fig.1 Schematic overview of the expanded estimate system. Variables to estimate are transformed to a vector spanned by a basis set, and the vector filtered out is estimated as new variables.

3. Experimental design

Two different cases are experimented that the cloud liquid water is deposited at 4 levels (2km, 3km, 4km, and 5km), and the cloud liquid water and cloud ice are deposited at 2 levels (2km and 3km). In these cases, some radiances at wavelengths of 0.315nm, 0.34nm, 0.5nm, 0.675nm, 1.627nm, and 2.2nm and zenith angles of 0° and 60° are measured. The true values to estimate are assumed such as the cloud mixing ratio is 5.0×10^{-4} kg/kg, the mode radius and standard deviation of the log-normal distribution are 1.2×10^{-3}cm and 1.6 with respect to the cloud liquid water, 3.0×10^{-3} cm and 1.6 with respect to the cloud ice. For the radiative transfer model which is forward model, RSTAR6B (Nakajima and Tanaka, 1986) is used. The experimental numbering is made as follows.

1.The maximum likelihood method.
2.The maximum likelihood method including the Fourier transform as a basis transform for estimated variable.
3.The maximum likelihood method including the Fourier transform as a basis transform and high-pass filter for estimated variables.
4.The Kalman filter.
5.The Kalman filter including the Fourier transform as a basis transform for estimated variables.
6.The Kalman filter including the Fourier transform as a basis transform and high-pass filter for estimated variables.
7.Average over all methods.

4. Results and Discussion

Fig.2 shows estimates of the cloud mixing ratio, standard deviation, and mode radius. In these experiments, the maximum likelihood method poorly has the accuracies of estimates, and the Kalman filter estimates the standard deviations better. Each retrieval method does not highly have the accuracies of estimates for all variables to estimate. However, by averaging over all methods, the estimates trend to come close to the true values. Some coupling methods among different retrieval methods, named ensemble retrieval method are likely to improve the accuracies of estimates.

（a）

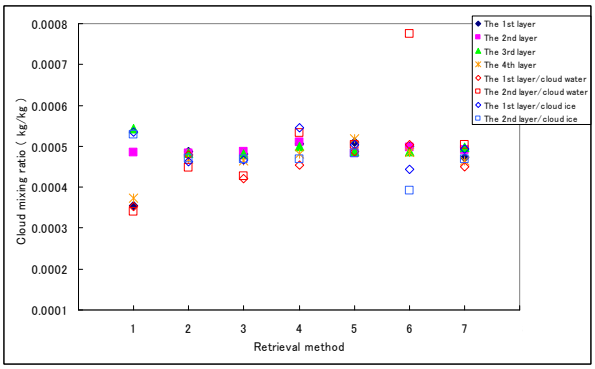

（b）

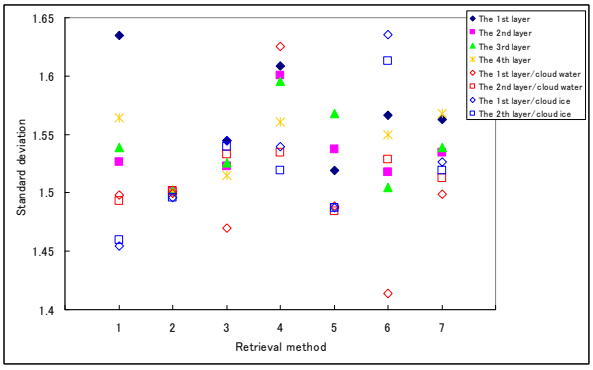

（c）

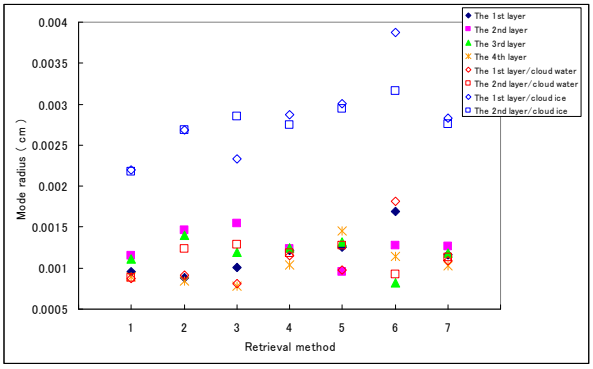

Fig.2 Estimates using various retrieval methods, (a)cloud mixing ratio(kg/kg), (b)standard deviation, (c)mode radius (cm).

Reference

Nakajima, T., and M. Tanaka (1986), Matrix formulation for the transfer of solar radiation in a plane-parallel scattering atmosphere, J. Quant. Spectrosc. Radiat. Transfer, 35, 13– 21.

High Resolution Doppler Observations of Clouds with the Millimeter-wave CPR FALCON-I

TAKANO Toshiaki[1], YAMAGUCHI Jun[2], ABE Hideji[1], SUZUKI Yohei[1], MORIYA Shusuke[1], NISHINO Daichi[1], KAWAMURA Yohei[1], NAKANISHI Yuji[3], and TAKAMURA Tamio[3]

[1]*Graduate School of Engineering, Chiba University; Inage, Chiba 263-8522, Japan, takano@faculty.chiba-u.jp*

[2]*Japan Aerospace Exploration Agency*

[3]*Center for Environmental Remote Sensing, Chiba University*

Abstract

High resolution Doppler Observations of clouds have been done with the millimeter-wave cloud profiling radar (CPR) FALCON-I developed at Chiba University. FALCON-I operated at 95 GHz has a high spatial resolution of 15 m in the ranging direction and of 0.2° in the perpendicular directions. Precise observations of melting layers at the bottom of clouds reveal that rain drops whose diameters would be around 1 mm are generated and accelerated up to 7 m/s downward in quite thin layer of about 200 m. Doppler Observations of interior of cumulonimbus suggest existence of small structures of about 1 km in which abrupt up and downward flow occurs. These results will be useful to investigate characteristics of clouds in various places and oceans in order to make global model of atmosphere.

Keywords : Cloud Profiling Radar, Millimeter Wave Radar, Cloud Properties, Height Distribution of Clouds, Structure of melting layer, dynamics of interior clouds, Global Model of Atmosphere.

1. Introduction

It is getting more important to know the global environment and the global change of climate for the human beings. It is necessary to know balance of solar energy coming to the Earth and cycle of water for the comprehension and to solve severe problems such as the greenhouse warming, the drying, the ozone holes and so on. One of the most significant features to know them is cloud. Information on 3-dimensional structures of clouds, sizes and distribution of cloud particles, dependence on size of optical characteristics of cloud particles, motions of particles in clouds, and so on are all desirable to determine the role of clouds.

Fig.1. Cloud profiling radar FALCON-I. It has two 1-m diameter antennas which transmit and receive radio waves at 95 GHz.

Observations of clouds with radars would be the most powerful method to derive the information because of the following advantages: a) radio waves do not suffer from heavy extinction such as visible light, and consequently can investigate the interior of clouds, b) the radar technique, which is an active sensing method, has great advantage to investigate interior structures of clouds to passive methods such as total power observations of irradiance of clouds, c) Doppler measurements of clouds is applicable only to radio frequency waves.

We have originally designed and developed a cloud profiling radar at 95GHz. We adopt a frequency-modulated continuous wave (FM-CW) radar rather than a pulse radar because the former can easily achieve more sensitive and high-resolution system than the latter. Whole view of the developed radar, which is named “FALCON-I” is shown in Fig.1 and its parameters and performance of are summarized in Table 1. Detail of FALCON-I is described in the papers [1]-[4].

Table 1. Parameters and performance of FALCON-I.

Antenna Diameter	1 m × 2
Frequency	94.79 GHz
Output Power	0.5 W (+27 dBm)
Beam Width	0.18 degree
Range Resolution	15 m
Direction of Antennas	Zenith
Polarization	1 Linear
Temporal Resolution	1 msec (Typical)
Sensiutivity (at 5 km)	-32 dBZ (Typical)
Doppler Velocity Range	±3.2 m/sec (Typ)

2. Observations with FALCON-I

Using FALCON-I, we observed clouds in various regions, at Chiba (Fig.2), at cape Hedo in Okinawa (Fig.3), and oceans on board MIRAI (Fig.4): a Japanese scientific research vessel operated by Japan Agency for Marine-Earth Science and Technology (JAMSTEC). FACLON-I is a mobile facility which is able to operate through the internet connection with the commercial power supply of about 100V 15A. During these observations, FALCON-I worked stable and well and showed good performance [5]-[7].

3. Observations of cumulonimbus

3-1. Reflectivity profiles

We continuously observed clouds in summer 2010 at Chiba University. High resolution Doppler Observations of clouds have been obtained as well as reflectivity profiles for several large cumulonimbus during the period.

Fig.5. shows time-height diagram of reflectivity for a cumulonimbus on July 25, 2010. The anvil of the cumulonimbus began to be seen around 9:30 UT (18:30 JST) from about 12 km in height and gradually came down to lower height. The main part of the cumulonimbus was shown in 10:40-11:20 UT at 4-9 km in height. Abrupt increase of observed reflectivity by going lower height is shown at 4 km. This increase of reflectivity should be caused with growth of diameters of raindrops in the melting layer. At lower frequency, for example, X-band (10 GHz) observations, strong enhancement of reflectivity called “bright band is usually recognized in the melting layer. At 95 GHz, however, bright enhancement cannot be seen but abrupt increase of reflectivity is only seen.

Fig.2. FALCON-I installed on a truck in the campus of Chiba University. The container behind the truck is housing of FALCON-I with two Teflon sheet windows on the ceiling for MIRAI observations (see Fig.4).

Fig.3. FALCON-I set in the Cape Hedo Station in Okinawa, Japan, of National Institute for Environmental Studies during the campaign in spring, 2008.

Fig.4(a). Japanese scientific research vessel, MIRAI, operated by Japan Agency for Marine-Earth Science and Technology (JAMSTEC).

Fig.4(b). Container of FALCON-I settled on the upper deck of MIRAI.

3-2. High resolution Doppler observations

Fig.6 shows Doppler spectral diagrams of the cumulonimbus on July 25, 2010 observed with FALCON-I at Chiba University. This cumulonimbus was generated several hours before observations in the northwest direction and moved toward Chiba area. We obtain one Doppler spectral diagram in every minute with 250 ms observations. Because Doppler velocity is derived by measuring phase shift of return signal scattered by objects, there are ambiguities of 2π. This causes that, for example, an echo observed to be 0 m/s may have real vertical velocity of $\pm 6.38 \times n$ m/s, where n is an integer.

We found, first, the anvil of the cumulonimbus around 9:30 UT at about 12 km in height. Vertical velocity of the anvil was about 0 to -1.5 m/s at 10:08 UT, where negative velocity means downward motion of the matter. Such range of small negative velocities is usually observed even for quiet and stable clouds. This fact can be explained that only largest cloud particles would be able to detect with FALCON-I, which have slight downward velocities about 1 m/s. In the lower part of the anvil shown at 10:29 UT, thin up and downward structures were seen projected form the main echo of the cloud. Thin upward cloud of 0 to +1 m/s was revealed at the height of 8.0 km as well as thin downward clouds of -1.5 to -2.5 m/s at 7.3 km and -2 to -3 m/s at 8.3 km. These clouds are as thin as about 100 m in the vertical direction. We can find such thin structures in other temporal data in this cloud and these do not maintain its structure in the next minute data. These facts suggest that these thin structures have also horizontal sizes of about 100 m if we assume the horizontal velocity is 1 to 2 m/s and/or life time of the structure is less than 1 minute.

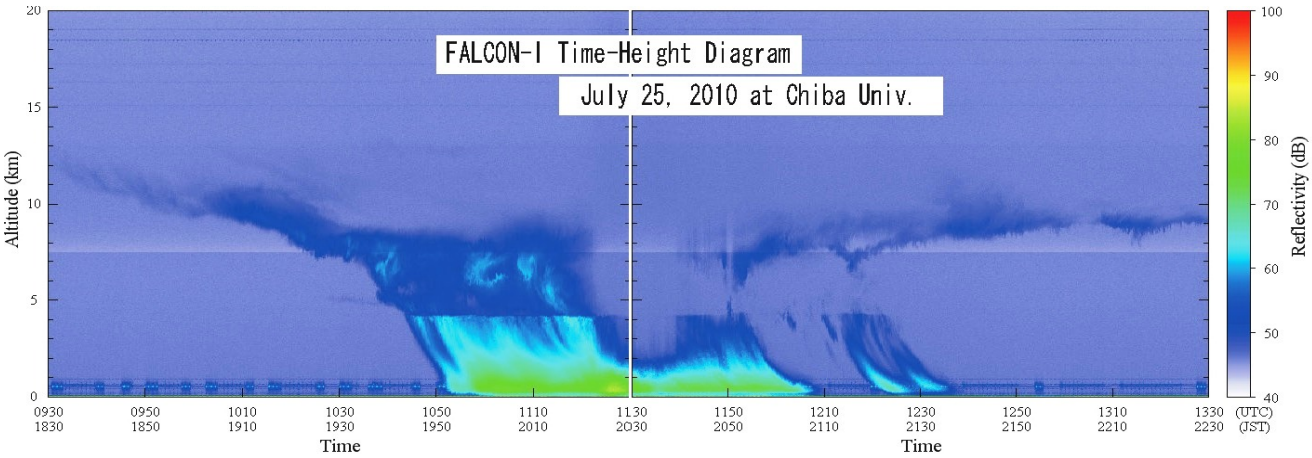

Fig.5. Time-height diagram of reflectivity observed with FALCON-I on July 25, 2010 at Chiba University. The anvil of the cumulonimbus began to be seen around 9:30 UT (18:30 JST) from about 12 km in height and gradually came down to lower height. The main part of the cumulonimbus was shown in 10:40-11:20 UT at 4-9 km in height. Rain started around 10:50. The intensity scale is dB in an arbitral unit.

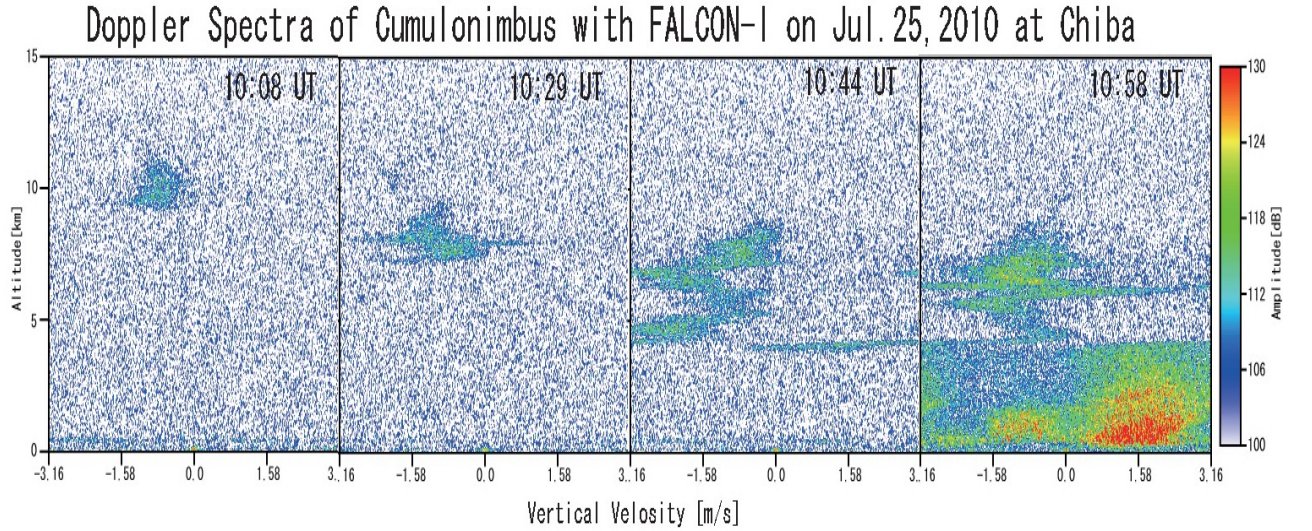

Fig.6. Doppler spectral diagrams of the cumulonimbus shown in Fig.5 observed with FALCON-I on July 25, 2010 at Chiba University. Panels show the velocity structure of matter in the anvil at 10:08 UT, lower part of the anvil at 10:29 UT, at start of the rain at 10:44 UT, and during hevy rain at 10:58 UT.

Rain started at around 10:44 UT as shown in Fig.5 and corresponding Doppler spectral diagram is the third panel in Fig.6. We can see thin line structure of a few hundred meters of vertical width at 4.2 km in height whose vertical velocities are from -0.7 to +3.16 m/s in Doppler diagram at 10:44 UT. It is obvious that this thin line is the echo of the very beginning of precipitation when we look successive spectral diagrams. The real vertical velocities of this line structure should be from -7 to -3.16 m/s instead of from –0.7 to +3.16 m/s, i.e. $2\pi = 6.32$ m/s should be subtracted. The line structure should be connected to the left end of the panel and continued to the bottom of the main body of cumulonimbus. We notice a small velocity gradient in the line structure in the vertical direction: the height of the line is about 3.9 km at the lowest velocity of -7 m/s, and is about 4.2 km at the velocity of -3.16 m/s. The whole structure of the thin line is followings: it starts from about -2 m/s on the bottom of the cumulonimbus at 4.3 km in height, and continues up to -7 m/s at 3.9 km. Turbulent up and down ward motions of $\pm$few m/s also exist in the main body of the cumulonimbus as shown in the Doppler diagrams at 10:44 and 10:58 UT.

3-3. Discussion

Observing frequency ν of FALCON-I is 94.79 GHz which correspond to the wavelength $\lambda = 3.16$ mm. For the wavelength, spherical particles whose diameter D is smaller than about 1 mm scatter the radio wave with Rayleigh scattering region, in which scatter cross section σ is in proportion to ν^4. Particles larger than 1 mm scatter the wave with Mie scattering region, in which σ changes up and down resonating with the particle diameter and converges in its geometric cross section. A rough estimation of the raindrop size distribution N(D) would be in proportion to D^{-3} if we assume total volume of each size is constant. We may, therefore, consider that the most effective diameters of raindrops for scattering the wave of FALCON-I are 1 ± 0.5 mm.

The thin and sharp line structure shown in Fig.6. at 10:44 UT, which is the echo by the beginning of the precipitation, suggests following facts as well as related structures. Rain drops of about 1 mm diameter are rapidly generated in the thin sheet of less than 100m thick in the melting layer at the bottom of the cumulonimbus. They are accelerated from -2 up to -7 m/s during 400 m drop, where this downward velocity corresponds with a usual terminal velocity for 1 mm diameter raindrops. The up and down motions in the anvil and the main body of the cumulonimbus suggest the existence of turbulences of several 100m in size in cumulonimbus

Acknowledgements

The authors thank KOBAYASHI Fumiaki of National Defense Academy for presenting information about cumulonimbus during the collaborative observations in summer 2010. This work was supported with GEOSS (Global Earth Observation System of Systems) by the Japanese Ministry of Education, Culture, Sports Science and Technology (MEXT), and with the Grant-in-Aid for Scientific Research by MEXT #14380241, #18310006 and #20310005. It was also supported with Research Projects for Promoting Technological Seeds by Japan Science and Technology Agency (JST) Innovation Satellite Ibaraki in 2007, 2009, and 2010.

References

1) TAKANO Toshiaki, YAMAGUCHI Jun, ABE Hideji, FUTABA Ken-ichi, YOKOTE Shin-ichi, KAWAMURA Yohei, TAKAMURA Tamio, KUMAGAI Hiroshi, OHNO Yuichi, NAKANISHI Yuji, NAKAJIMA Teruyuki; “Development and Performance of the Millimeter-Wave Cloud Profiling Radar at 95 GHz: Sensitivity and Spatial resolution”, IEEJ Trans., FM, Vol.128, No.4, pp.257-262, 2008 (in Japanese), translated to Electronics and Communications in Japan, Vol.93, No.3, 2010.

2) ABE Hideji, YAMAZAKI Fumihiro, YAMAGUCHI Jun, KAWAMURA Yohei, NAKANISHI Yuji, TAKANO Toshiaki, TAKAMURA Tamio, OHNO Yuichi; “Doppler Observations with the Millimeter-Wave Cloud Profiling Radar FALCON-I”, IEEJ Trans., FM, Vol.129, No.4, pp.177-182, 2009 (in Japanese).

3) YAMAGUCHI Jun, TAKANO Toshiaki, NAKANISHI Yuji, ABE Hideji, KAWAMURA Yohei, YOKOTE Shin-ichi, KUMAGAI Hiroshi, OHNO Yuichi, HORIE Hiroaki; “Evaluation of Radar Reflectivity (Z) for FMCW Millimeter-Wave Cloud Radar FALCON-I”, IEEJ Trans., FM, Vol.129, No.4, pp.183-189, 2009 (in Japanese).

4) YAMAGUCHI Jun, TAKANO Toshiaki, TAKAMURA Tamio, NAKANISHI Yuji, KAWAMURA Yohei, ABE Hideji, HORIE Hiroaki, OHNO Yuichi; “Evaluation of Parallax on the Dual-Antenna 95 GHz MMCR FALCON-I”, IEICE Trans, Vol.J92-C, No.12, pp.806-812, 2009 (in Japanese).

5) TAKANO Toshiaki, FUTABA Ken-ichi, ABE Hideji, YAMAGUCHI Jun,HIRAI Akihito, KAWAMURA Youhei, KUMAGAI Hiroshi, OHNO Yuichi, FUJIYOSHI Yasushi, and OKAMOTO Hajime; “Observations of Clouds on MIRAI in the Pacific Ocean with the Millimeter-wave FM-CW Radar at 95GHz”, The International Society of Optical Engineering, Vol.6362, No.30, pp.636230・1-8, 2006.

6) G.Pandithurai, T. Takamura, J. Yamaguchi, K. Miyagi, T. Takano, Y. Ishizaka, S. Dipu, A. Shimizu; “Aerosol effect on cloud droplet size as monitored from surface-based remote sensing over East China Sea region, Geophysical Research Lett., VOL.36, L13805, doi:10. 1029/2009 GL038451, 2009.

7) J.Suzuki, M.Fujiwara, A.Hamada, Y.Inai, J.Yamaguchi, R.Shirooka, F.Hasebe, T.Takano; “Cloud-Top Height Variability Associated with Equatorial Kelvin Waves in the Tropical Tropopause Layer during the Mirai Indian Ocean Cruise for the Study of the MJO-Convection Onset (MISMO) Campaign”, SOLA (Scientific Online Letter on the Atmosphere), Vol.6, pp.097-100, 2010.

Evaluation of Cloud Observations by FMCW CPR FALCON-I at Hedo Station

Jun Yamaguchi[1], Toshiaki Takano[2], G. Pandithurai[3], Hideji Abe[2], Youhei Kawamura[2]
Hideaki Takenaka[4], Tamio Takamura[4], Toshiyoshi Kimura[1], Yutaka Ishizaka[5]
[1]*JAXA, Tsukuba Space Center, Sengen 2-1-1, Tsukuba, Ibaraki, Japan, yamaguchi.jun@jaxa.jp*
[2]*Chiba University Graduate School of Engineering, Yahoichou 1-33, Inage, Chiba, Japan*
[3]*Indian Institute of Tropical Meteorology, Dr. Homi Bhabha Road, Pashan, Pune 411008 India*
[4]*Chiba University CEReS, Yahoichou 1-33, Inage, Chiba, Japan*
[5]*Aichi Gakuin University,, Yoshiike 12, Iwasaki, Nisshin, Aichi,, Japan*

Abstract

CPR (Cloud Profiling Radar) is expected to reveal the inside structure of clouds. Using vertical profiles of radar reflectivity factor, vertical profiles of cloud microphysical properties (e. g., cloud effective radius, liquid water content, cloud optical depth) can be retrieved with data of other instruments, which leads to better understanding of cloud radiative forcing and the earth's energy balance. Chiba University has developed the solid-state ground-based FMCW CPR FALCON-I to achieve higher range and time resolution with lower power. In this study, sensitivity and accuracy of FALCON-I are evaluated at the Hedo observation in 2008.

Keywords **:** CPR (Cloud Profiling Radar), radar reflectivity factor, microphysical properties, FMCW, FALCON-I, radiative forcing

1. Introduction

It is clearly reported in IPCC AR4 that clouds and aerosols are one of the important components of radiative forcing of the earth for better understanding of global warming [1]. Although the contributions to radiative forcing from carbon dioxide and methane known as the greenhouse gas are estimated with small error bars from numerical simulation, it is very difficult to estimate the contributions from cloud and aerosols [2]. They are many types of aerosols, and the combined aerosols direct radiative forcing is estimated at -0.50 ± 0.40 Wm^{-2}, and cloud albedo radiative forcing is -0.7 Wm^{-2} as the median with a 5 to 95% range of -0.3 to 1.8 Wm^{-2}. There are still much to study to solve aerosol indirect effect. Making a progress of this estimation needs filling the gap between observation works and modeling in spatial and temporal distribution. Both of more frequent observation of aerosols and clouds in global and local scales are expected.

CPR is the one of most effective remote sensing instrument to study cloud inside structure by observing cloud vertical profiles of radar reflectivity factor and doppler velocity, which supply important information for cloud distribution and cloud microphysical properties. Since the concept of CPR in millimeter-wavelength was proposed in 1981 to detect nonprecipitating clouds [3], several CPRs at 35 GHz, 78 GHz and 95 GHz have been developed in the U.S., the U.K., Germany and Japan. Observation from Spaceborne CPR called CloudSat has began in 2006 by NASA (National Aeronautics and Space Administration) and CSA (Canadian Space Agency) to map 3D distribution of cloud in global scale [4]. EarthCARE project, which is conducted by JAXA (Japan Aerospace Exploration Agency), NICT (National Institute of Information and Communications Technology) and ESA (European Space Agency), will be a next big step for aerosol and cloud observation. JAXA and NICT are developing 95 GHz CPR for EarthCARE project which is the first spaceborne doppler CPR at 95 GHz [5]. Chiba University in Japan has developed a solid-state ground-based FMCW 95 GHz CPR named as FALCON-I (FMCW Radar for Cloud Observations) since 1999, evaluated theoretically [6] and systematically [7]. FMCW system achieves high range resolution, and FALCON-I is expected to reveal more detailed cloud vertical structure than pulsed CPR. FALCON-I is also expected to calibrate the CPR of EarthCARE as one of the ground calibration system. FALCON-I is expected to contribute to cloud microphysics which reveals the physical process from formation, growth, precipitation and extinction of cloud.

The primary aim of this study is to evaluate the sensitivity of FALCON-I, comparing cloud vertical profiles with CloudSat. The second aim of this study is to evaluate cloud microphysical properties retrieved from radar reflectivity factor to estimate FALCON-I's accuracy by comparing the estimated downward radiation flux from FALCON-I and the observed downward radiation flux by Pyranometer. In this paper, we evaluated correlation of the estimated cloud

TABLE I
SPECIFICATIONS OF FALCON-I

Range Resolution	15 m
Temporal Resolution	1minute (at Z mode)
Transmitting Power	27 dBm (0.5 W)
Antenna System	Bistatic Cassegrain
Antenna Beamwidth	0.18 deg (Full Angle)
Sensitivity	-30 dBZe at 5 km

TABLE II
SPECIFICATIONS OF CLOUDSAT

Range Resolution	485 m
Temporal Resolution	0.16 s
Transmitting Power (Peak, Mean)	1800 W, 25 W
Antenna System	Monostatic Offset
Antenna Beamwidth	0.108 Deg
Sensitivity	-30 dBZe

TABLE III
SPECIFICATIONS OF WVR-1100

Liquid Water Sensing Channel	
Frequency	31.4 GHz
Bandwidth	0.4 GHz
Beamwidth (3dB)	4.6 deg
Common Characteristics	
Temporal Resolution	3 min

optical thickness by FALCON-I and the observed shortwave downward radiation by Pyranometer for the evaluation as a first step. We also evaluated retrieved cloud droplet effective radius, using cloud cendensation nuclei observed by CCN counter.

2. Instrumentation

We used Z (radar reflectivity factor) of FALCON-I to retrieve cloud microphysical properties in this study. FALCON-I operates at 94.79 GHz with 20 MHz frequency modulation. The specifications of FALCON-I are shown in Table 1, and the outlook is shown in Figure 1. FALCON-I achieved long range observation upto 20 km with high range resolution (about less than 20m) with FMCW system. FALCON-I also has doppler velocity observation function [8]. Although bistatic antenna system causes reduction of receiving power, it is corrected with correction index [9]. Atmospheric attenuation, multi-scattering effect and attenuation in clouds were ignored to estimate radar reflectivity factor.

NASA developed a spaceborne CPR at 94.05 GHz, loaded on CloudSat which launched in 2006. CloudSat is orbiting as a member of A-Train with Aura, Glory, PARASOL, CALIPSO, Aqua and OCO with approximate altitude of 700km [4]. The specifications of CloudSat are in Table 2.

Microwave radiometer is used to measure emission at micrometer, millimeter and sub-millimeter wavelength. WVR-1100 manufactured by Radiometrics Corporation has two channels; the channel of 23.8 GHz to estimate column-integrated amounts of water vapour (g/cm^2), the channel of 31.4 GHz to estimate the amounts of liquid water (g/cm^2), and the specifications of MVR-1100 are shown in Table 3 [10]. In this study, the channel of 31.4 GHz is used to observe LWP (Liquid Water Path), and it is operated in Hedo Station by Chiba University CEReS. It is said that typical retrieval uncertainties of LWP is 25-30g/m^2.

CCN is a particle that can form into a cloud droplet. The CCN counter CCN-100 can measure CCNs at several supersaturations manufactured by Droplet Measurement Technology [11]. Aichi Gakuin University operated the CCN counter during Feb.-Apr. in 2008. The specifications of CCN-100 are: 1) continuous flow, 2) single supersaturation and 30 seconds supersaturation change, 3) supersaturation range 0.1 - 2.0%.

Pyranometer is the instrument to measure the upward and downward solar irradiance on a planar surface to estimate the solar radiation flux density (W/m^2). The pyranometer CM21 manufactured by Kipp & Zonen is operated for a whole year by Chiba University CEReS. The specifications of CM21 are: 1) spectral range 305-2800 nm (50% points) and 335-2200 nm (95% points), 2) sensitivity 7-17 $\mu V/Vm^2$, 3) directional error $10W/m^2$, 4) viewing angle 2π sr [12].

3. Methodology

Cloud observations were done at CHAAMS (Cape Hedo Aerosol and Atmosphere Monitoring Station) owned by NIES (National Institute for Environmental Studies) which locates on 26.87° N, 128.26° E in Cape Hedo, Kunigami, Okinawa, Japan [13]. Okinawa normally experiences temperatures above 20°C for most of the year, categorized in subtropics.

Although WVR-1100 and CM21 operate for whole year, FALCON-I and CCN-100 joined observation at CHAAMS for a short term. FALCON-I operated at this station from February 17th until May 4th in 2008 and CCN-100 operated from February 18th until April 18th in 2008. Temporal resolution is 1 minute at FALCON-I, 3 minutes at

WVR-1100, 30 minutes at CCN-100, and 10 seconds at CM21.

Re (cloud droplet effective radius) is retrieved from Z and cloud droplets number concentration (N) as below:

$$r_e(h) = \frac{1}{2}\left(\frac{Z(h)}{N(h)}\right)^{1/6} \exp(-0.5\sigma_x{}^2), \quad (1)$$

where h is height, and σ_x is the logarithmic spread of the cloud droplet size distribution and is 0.34 in this study which is the average spread of marine stratus clouds [14]. In case of stratus clouds, although CCN-100 was set on the ground, we can assume N as CCN number concentration which is constant with height [15], [16], [17].

Although we cannot avoid assuming that N and σx are constant with height, the effective radius can be also retrieved in terms of variable h by using vertical profiles of Z and Q (LWP) as shown by Eq. 2 [14]:

$$R_e(h) = \frac{Z^{1/6}(h)}{2Q^{1/3}}\left(\frac{\pi\rho}{6}\right)^{1/3}\left(\sum_{i=1}^{i=m} Z^{1/2}(h_i)\Delta h\right)^{1/3} \exp(-2\sigma_x{}^2), (2)$$

where ρ is the water density, hi is height, i represents measurement bin of Z, Δh is the range of 1 bin (9.155 m at FALCON-I).

LWC (Liquid Water Content) q_i can also be retrieved from Z and LWP shown by Eq. 3 [18]:

$$q_i = \frac{QZ_i^{1/2}}{\sum_{i=1}^{m} Z_i^{1/2}\Delta h}, \quad (3)$$

COT (cloud optical thickness) τ can be written in terms of Q and Re by Eq. 4 [19]:

$$\tau = \frac{3}{2}\left(\frac{Q}{R_e}\right), \quad (4)$$

Thus, we get cloud optical depth at each radar observation bin and integrated COT retrieved from Z of FACLON-I.

4. Comparison of Ze from Simultaneous Observation

CloudSat has passed over 5 times within a 5 km radius of CHAAMS while FALCON-I was operating. The both CPRs detected clouds in 4 of 5 cases, and the 4th case at 4:54, April 11th (UTC), showed high consistency of the profiles of Ze shown in Fig. 1. The green dots are the Ze of CloudSat from 2B-GEOPROF file of CloudSat data set with correction of gas attenuation, the yellow dots are the Ze of

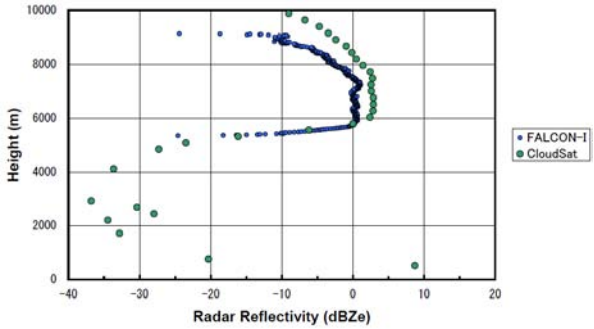

Fig. 1. Comparison of Z_e verical profiles of FALCON-I and CloudSat at 4:54Z, April 11th, 2008 at CHAAMS.
1) Blue dots: Z_e of FALCON-I
2) Green dots: Z_e of CloudSat

FALCON-I, and the blue dots are the Ze of FALCON-I with gas attenuation correction of CloudSat. The cloud observed by the both CPRs is single layered ice cloud with thickness of approximate 5 km, high homogeneous in temporal and spatial. The starting location of the CloudSat's path of this profile is 624 m apart, and the ending location is 470 m apart from CHAAMS. The both profiles match well at the cloud bottom and inside of the cloud, whereas FALCON-I's gradient of the profile is steeper than CloudSat. This conflict is not understood and still under consideration.

5. Retrieval of Microphysical Properties

The temporal changes of Q, N, Z, Re and aerosol size distribution were discussed [20]. Fig. 2 (a) shows the temporal change of the vertical profiles of retrieved effective radius at 8:00Z on April 10th, with the black dots and 10:00Z with the red dots by the method of Z and N shown in Eq. 1. The most important differences of the two profiles are that the size of radius increased at any height from 8:00Z to 10:00Z. Although cloud bottom height rose up about 70 m and the cloud top height rose up about 100 m from 8:00Z to 10:00Z, the geometrical thickness didn't change much. N at 7:56Z was 276 cm-3 and 306 cm-3 at 9:56Z. On the other hand, Q was 0.036 g/cm2 at 7:58Z and 0.0312 g/cm2 at 9:59Z. The increment of N was 10.9% and of Q was -8.7%.

Increase of CCN number retrains cloud droplets to grow bigger if liquid water amount is constant because each droplets scramble for water. In this case, Q decreased from 8:00Z to 10:00, which can encourage miniaturization of droplets, and this can explain the change of the profiles of retrieved effective radius in Fig. 2 (a).

Fig. 2 (b) shows the change of aerosol size distribution at 8:00Z in the black line and dots and 10:00Z in the red line and dots. The OPC (Optical Particle Counter) Model 237B of Pacific Scientific Instruments is operated by Chiba University CEReS at CHAAMS. The OPC has 5 channels

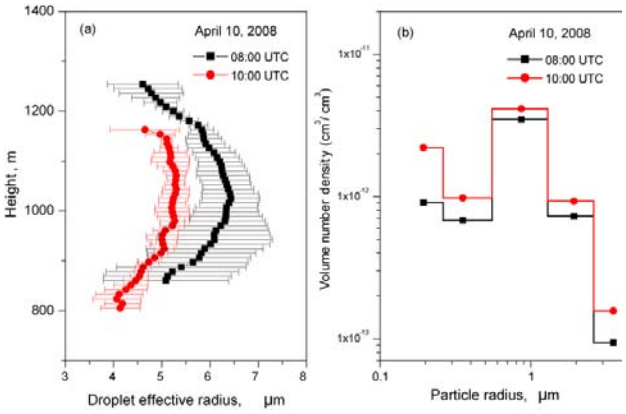

Fig. 2. Vertical Profiles of Retrieved Droplet Effective Radius and Observed Aerosol Particle Radius Distribution [20]:
1) Black dots: at 8:00Z, April 10th
2) Red dots: at 10:00Z, April 10th
3) Fig. (a): Averaged effective radius proflies during 20 minutes with standard deviation
4) Fig. (b): Aerosol radius distribution with 5 channels by OPC

of size resolution. From the temporal change from the black dots to the red dots, it is clear that the number of aerosol increased at any size from 8:00Z to 10:00Z. This aerosol increase corresponds to the increase of CCN in this case, and it implies the Aerosol Indirect Effect.

COT from cloud bottom to cloud top were estimated under the condition of single layered, non-precipitating and liquid water cloud. We compared the estimated COT with observed SWD by the pyranometer to evaluate the estimated microphysical properties by FALCON-I. We had 4 cases of steady clouds which matches all conditions in daytime: Term 1 is Feb. 24th 08:00-10:00Z, Term 2 is Feb. 25th 08:00-11:30, Term 3 is Feb. 28th 09:00-11:00, Term 4 is Mar. 30th 14:00-17:00. Fig. 3 shows the correlation of the estimated COT and the observed SWD.

The observed intensity after a cloud path I can be written with the variable τ:

$$I = I_0 e^{-\tau} \qquad ,(5)$$

where I_0 is the intensity of radiation source.

Thus correlation between SWD and COT should show the relation expressed by Eq. (5), Fig. 3 shows that SWD is an exponential function with variable COT. Spread of the plots and overestimation of COT should be evaluated carefully. Temporal change of SWD was relatively steady, comparing with temporal change of COT. Estimation of noise floor of FALCON-I and MVR-1100 influences values of estimated microphysical properties, and it might cause the instability of COT. This matter is under study, focusing errors of LWP and Z of raw data.

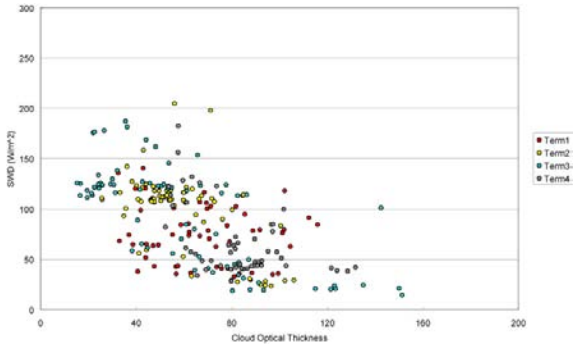

Fig. 3. Correlation of the Retrieved Cloud Optical Thickness of FALCON-I and the Short-wave Downward Flux Observed by Pyranometer:
1) Term1: 08:00-10:00 (JST), February 24th
2) Term2: 08:00-11:30 (JST), February 25th
3) Term3: 09:00-11:00 (JST), February 28th
4) Term4: 14:00-17:00 (JST), March 30th

6. Conclusion and future work

In this study, vertical profiles of Re were retrieved from Z observed by FALCON-I with CCN number concentration by CCN counter and LWP by microwave radiometer. Temporal change of the retrieved Re was discussed with the change of aerosol, which implies aerosol indirect effect. The increase of CCN number concentration and aerosol size distribution and the decrease of liquid water path were relevant to the temporal change of the profiles in the case. Estimated COT from retrieval of LWC and Re was evaluated by comparing correlation with observed SWD. Although it showed a theoretical relation of exponential, spread of the distribution is large, thought to be derived from error range of LWP and Z.

Although the several steady cases from the CHAAMS observation were discussed and evaluated in this study, this discussion has to be evaluated statistically with enough amounts of data and cases. Especially, systematic errors of the each instrument must be considered and separated from the discussion of microphysical phenomenon.

Acknowledgements

The authors wish to acknowledge the support of NIES for providing us an opportunity of cloud observation at the CHAAMS. The authors also thank the students of Prof. Takano, Prof. Takamura and Prof. Ishizaka who arranged and set the instruments and data acquisition.

References

1) Forster P. and V. Ramaswamy (as the coordinating lead authors), “The Physical Science Basis - Chapter 2 Changes in Atmospheric Constituents and in Radiative Forcing,”

IPCC Fourth Assessment Report, Working Group I Report, 2005.
2) Le Treut H. and B. McAvaney, “A Model Intercomparison of Equilibrium Climate Change in Response to CO2 Doubling,” Note du Pole de Modelisation de l'IPSL 18., Oct. 2000.
3) Lhermitte R., “Millimeter Wave Radar,” AMS, 20th Conference on Radar Meteorology, pp.744-748, Nov.-Dec. 1981.
4) Stephens G. L., D. G. Vane, S. Tanelli, E. Im, S. Durden, M. Rokey, D. Reike, P. Partain, G. G. Mace, R. Austin, T. L'Ecuyer, J. Haynes, M. Lebsock, K. Suzuki, D. Waliser, D. Wu, J. Kay, A. Gettelman, Z. Wang and R. Marchand, “CloudSat Mission: Performance and Early Science after the First Year of Operation”, AGU, Journal of Geophysical Research, Vol.113, D00A18, pp.1-18, Dec. 2008.
5) Takahashi N., T. Kimura, Y. Ohno, H. Horie, H. Nakatsuka, Y. Seki, K. Sato, K. Okada and Y. Sakaide, “Current Status of EarthCARE/CPR Development,” IEICE, Technical Report, Vol.109, pp.13-17, 2010.
6) Takano T., J. Yamaguchi, H. Abe, K. Futaba, S. Yokote, Y. Kawamura, T. Takamura, H. Kumagai, Y. Ohno, Y. Nakanishi and T. Nakajima, “Development and Performance of the Millimeter-wave Cloud Profiling Radar at 95GHz -Sensitivity and Spatial Resolution-,” IEEJ Trans., Vol.128, No.5, Apr. 2008, pp.132-139.
7) Yamaguchi J., T. Takano, Y. Nakanishi, H. Abe, Y. Kawamura, S. Yokote, H. Kumagai, Y. Ohno and H. Horie, “Evaluation of Radar Reflectivity (Z) for FMCW Millimeter-Wave Cloud Radar "FALCON-I",” IEEJ Trans, vol. 129, No. 4, Apr. 2009, pp.183-189.
8) Abe H., Yamazaki F., Yamaguchi J., Kawamura Y., Ohno Y., Nakanishi Y., Takano T. and Takamura T, ”Doppler Observations with the Millimeter-Wave Clouds Profiling Radar FALCON-I”, IEEJ, FM, Vol. 129, No.4, April 2009, pp.177-182.
9) Yamaguchi J., Takano T.,Takamura T., Nakanishi Y.,Kawamura Y., Abe H., Horie H. and Ohno Y., ”Evaluation of Parallax on the Dual-Antenna 95GHz MMCR FALCONI”, IEICE, C, Vol. 92-C, Dec. 2009, pp.806-812.
10) Liljegren J. C., “Two-Channel Microwave Radiometer for Observations of Total Column Precipitable Water Vapor and Cloud Liquid Water Path,” AMS 5th Symposium on Global Change Studies, Jan. 1994, pp.262-269.
11) Roberts G. C. and A. Nenes, “A Continuous-Flow Streamwise Thermal-Gradient CCN Chamber for Atmospheric Measurement,” Aerosl Science and Technology, Vol.39, Issue 3, Mar. 2005, pp.206-221.
12) Kipp & Zonen, “Instrunction Manual CM21 Precision Pyranometer,”
http://www.eol.ucar.edu/isf/facilities/isff/sensors /kippzonen/manual_cm21.pdf
13) National Institute for Environmental Studies, “Cape Hedo Aerosol and Atmosphere Monitoring Station,” http://www.nies. go.jp/asia/hedomisaki/outline_e.html.
14) Frisch A. S., Shupe M., Djalalovaf I., Feingold G. and M. Poellot, “The Retrieval of Stratus Cloud Droplet Effective Radius with Cloud Radars,” Journal of Atmospheric and Oceanic Technology, vol. 19, Issue 6, pp. 835-842, June 2002.
15) Davidson K. L., Fairrall C. W., Jones Boyle P. and Schacher G. E., “Verification of an Atmospheric Mixed-Layer Model for Coastal Region,” Journal of Climate and Applied Meteorology, vol. 23, Issue 4, pp. 617-636, April 1984.
16) Nicholls S. and Leighton J., “An Observational Study of the Structure of Stratiform Cloud Sheets. Part I,” Quarterly Journal of the Royal Meteorological Society, vol. 112, pp. 431-460, 1986.
17) Nicholls S., “A Model of Drizzle Growth in Warm, Turbulent, Stratiform Clouds,” Quarterly Journal of the Royal Meteorological Society, vol. 113, pp. 1141-1170, 1987.
18) Frisch A. S., C. W. Fairall, T. Uttal and J. B. Snider, “On Cloud Radar and Microwave Radiometer Measurements of Stratus Cloud Liquid Water Profiles,” AGU, JGR, vol. 103, No. D18, pp.23,195-23,197, Sep. 1998.
19) Stephens G. L., “Radiation Profiles in Extended Water Clouds. II: Parameterization Schemes,” AMS, Journal of the Atmospheric Science, vol.35, Issue 11, pp.2123-2132, Jul. 1978.
20) Pandithurai. G, T. Takamura, J. Yamaguchi, K. Miyagi, T. Takano, Y. Ishizaka, S. Dipu and A. Shimizu, “Aerosol Effect on Cloud Droplet Size as Monitored from Surface-based Remote Sensing over East China Sea Region,” AGU, GRL, vol. 36, L13805, Jul. 2009.

The analysis of Skyradiometer observation data by using SKYRAD.PACK and MRI-MLM

Akihiro YAMAZAKI[1], Akihiro UCHIYAMA[1], Eriko KOBAYASHI[2], Rei KUDO[1], and Tomonori SAKAMI[1]

[1] *Meteorological Research Institute, Japan Meteorological Agency, 1-1 Nagamine, Tsukuba 305-0052, JAPAN, akyamaza@mri-jma.go.jp, uchiyama@mri-jma.go.jp, reikudo@mri-jma.go.jp, tsakami@mri-jma.go.jp*

[2] *Aerological Observatory, Japan Meteorological Agency, 1-2 Nagamine, Tsukuba 305-0052, JAPAN, eriko-kobayashi@met.kishou.go.jp*

Abstract

SKYNET is the aerosol-cloud monitoring network in East Asia which uses PREDE skyradiometer. The aerosol optical properties which skyradiometer observes are retrieved by SKYRAD.PACK in SKYNET. We developed the software (MRI-MLM) to apply the inversion method to the maximum likelihood method based on SKYRAD.PACK version 4.2. We analyzed skyradiometer data observed in Tsukuba, JAPAN by using SKYRAD.PACK and MRI-MLM, and investigate the difference of retrieved results.

Keywords **:** skyradiometer, SKYNET, aerosol, maximum likelihood method

1. Introduction

Aerosol optical properties are very important in the studies of global and regional climate changes. SKYNET (Nakajima et al., 2003) ground based observation network is well known aerosol-cloud monitoring network in East Asia which uses skyradiometer (POM-01 or POM-02 manufactured by PREDE Co., Ltd.) for the purpose of aerosol radiative forcing studies. The aerosol optical properties which skyradiometer observes are retrieved by SKYRAD.PACK (Nakajima et al., 1996).

We improved SKYRAD.PACK version 4.2 and developed software (MRI-MLM) to apply the inversion method to the maximum likelihood method (Kobayashi et al., 2006). In this study, we compare the aerosol optical properties retrieved by using SKYRAD.PACK and MRI-MLM, respectively.

2. Skyradiometer observation data

PREDE skyradiometer POM-02 was installed and started observation in 2002 at Meteorological Research Institute (MRI) in Tsukuba (36.056N, 140.125E), Japan. Skyradiometer has been calibrated by inter-comparing it to the spetctoradiometer (SVC GER2600 manufactured by Spectra Vista Co., Ltd.) in every winter season. The spectroradiometer was calibrated annually by the Langley method using the data obtained at Mauna Loa Observatory (MLO), NOAA ESRL-GMD.

2. Data analysis

We analyzed skyradiometer data observed at MRI from 2004 to 2010 by using SKYRAD.PACK version 4.2 and MRI-MLM version 1.1, respectively. The analysis of skyradiometer needs the total ozone amount and the surface pressure to take account of ozone absorption and Rayleigh scattering of air molecules. The monthly averaged total ozone amount for 39 years (from 1971 to 2009) is taken from Aerological Observatory close to MRI. The surface pressure is taken from SYNOP data from same site.

The cloud affected data was detected by CSSR version 1.0 (Khatri and Takamura, 2009).

3. Intercomparison of aerosol optical properties

The intercomparisons of aerosol optical properties at wave length 400, 500, 675, and 870nm between SKYRAD.PACK and MRI-MLM were based on 12594 retrieved data. Figure 1 (a), (b) and (c) show scatter plots of aerosol optical thickness (AOT@500) at wavelength 500nm, Ångström exponent and single scattering albedo (SSA@500) at wavelength 500nm, respectively. AOT@500 has significant linear relationship (R=0.99, Slope=0.99, Intercept=0.01) between SKYRAD.PACK and MRI-MLM. There is good linear correlation for Ångström exponent between them. On the other hand, the retrieved single scattering albedo SSA@500 is little dispersed. $SSA@500_{MRI\text{-}MLM}$ is underestimate in the case of $SSA@500_{SKYRAD.PACK}>0.86$ and $SSA@500_{MRI\text{-}MLM}$ is overestimate in the case of $SSA@500_{SKYRAD.PACK}<0.86$, respectively.

Linear correlations of aerosol optical thickness, single scattering albedo, and Ångström exponent between SKYRAD.PACK and MRI-MLM are shown in Table 1. Aerosol optical thickness at each wavelength has highly significant linear relationship with correlation coefficient

lager than 0.99 between SKYRAD.PACK and MRI-MLM. Calculated Ångström exponents by the results of MRI-MLM are similar to those of SKYRAD.PACK. Correlation coefficients of single scattering albedo at all wavelengths are little dispersed. Single scattering albedo from MRI-MLM ($SSA_{MRI-MLM}$) is underestimate in the case of that of SKYRAD.PACK($SSA_{SKYRAD.PACK}$) is larger than around 0.87 at each wavelength and $SSA_{MRI-MLM}$ is overestimate in the case of $SSA_{SKYRAD.PACK}$ is less than around 0.87 at each wavelength , respectively.

Acknowledgement

We are grateful to Open CLASTR project for using SKYRAD.PACK version 4.2 in this research.

References

1) Nakajima, T., Sekiguchi, M., et al.: Significance of direct and indirect radiative forcings of aerosols in the East China Sea region, J. Geophys. Res., 108(D23), 8658, doi:10.1029/2002JD003261, 2003.

2) Nakajima, T., Tonna, G., Rao, R., Holben, B.N.: Use of sky brightness measurements from ground for remote sensing of particulate polydispersions, Appl. Opt., 35, 2672–2686, 1996.

3) Kobayashi, E., Uchiyama, A., et al.: Application of the Statistical Optimization Method to the Inversion Algorithm for Analyzing Aerosol Optical Properties from Sun and Sky Radiance Measurements, J. Meteor. Soc. Japan,Vol. 84, No.6, 1047-1062, 2006.

4) Khatri, P. and Takamura, T.: An Algorithm to Screen Cloud-Affected Data for Sky Radiometer Data Analysis, J. Meteor. Soc. Japan, Vol. 87, No. 1, 189-204, 2009.

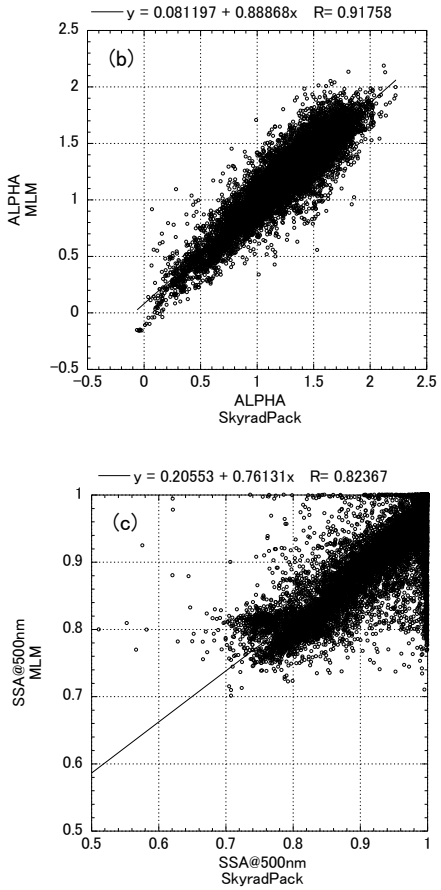

Fig. 1. Scatter plots of aerosol optical thickness (AOT) at wavelength 500nm (a), Ångström exponent (ALPHA) (b), and single scattering albedo (SSA) at wavelength 500nm (c) between SKYRAD.PACK and MRI-MLM.

Table 1. Regression curves coefficients of aerosol optical thickness (AOT), single scattering albedo (SSA), and Ångström exponent (ALPHA) between SKYRAD.PACK and MRI-MLM.

	Slope	Intercept	R
AOT@400	0.986	0.005	0.999
AOT@500	0.996	0.008	1.000
AOT@675	0.996	0.007	0.998
AOT@870	0.996	0.007	0.998
SSA@400	0.793	0.180	0.833
SSA@500	0.761	0.206	0.824
SSA@675	0.724	0.236	0.818
SSA@870	0.663	0.300	0.744
ALPHA	0.889	0.081	0.918

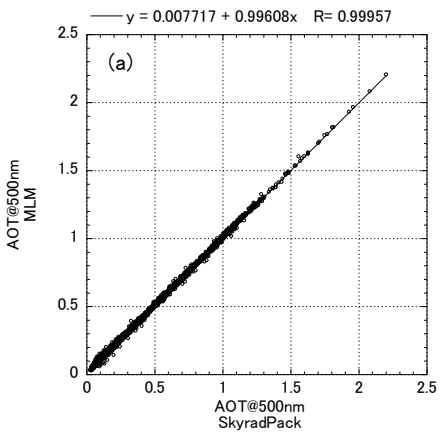

Seasonal variation of aerosol optical properties in Qingdao

Li-Fang SHENG[1], Akihiro YAMAZAKI[2], Akihiro UCHIYAMA[2], and Guang-Yu SHI[3]

[1] *Ocean University of China, 238 Songling Road , Qingdao 266100, CHINA, shenglf@ouc.edu.cn*

[2] *Meteorological Research Institute, Japan Meteorological Agency, 1-1 Nagamine, Tsukuba 305-0052, JAPAN, akyamaza@mri-jma.go.jp, uchiyama@mri-jma.go.jp*

[3] *Institute of Atmospheric Physics, Chinese Academy of Sciences, Beijing 100029, CHINA, shigy@mail.iap.ac.cn*

Abstract

Aerosol optical properties are very important in the studies of global and regional climate change. Skyradiometer is a useful instrument to obtain the ground based monitoring of aerosol optical properties. We analyzed skyradiometer data observed in Qingdao, China by using SKYRAD.PACK version 4.2 and investigate the retrieved aerosol optical properties.

Keywords **:** skyradiometer, aerosol, SKYNET

1. Introduction

Aeolian Dust Experiment on Climate impact (ADEC) was conducted from 2000 to 2004 to investigate physical and chemical properties of aeolian dust by the collaboration of China and Japan of the observation network. In this project, a skyradiometer POM-02 (manufactured by PREDE Co., Ltd.) was installed at Ocean University of China (OUC), Qingdao in 2002 and started observation to measure aerosol optical properties (Uchiyama et al., 2005). After ADEC project, OUC and Institute of Atmospheric Physics (IAP) have continued to collaborate with Meteorological Research Institute (MRI), JAPAN, and observed continuously by skyradiometer in Qingdao. On the other hand, SKYNET (Nakajima et al., 2003) has supported our continuous observation from 2008.

This paper presents preliminary results of retrieved aerosol optical properties in Qingdao.

2. Instrumentation

PREDE skyradiometer POM-02 was installed and started observation in 2002 at OUC (36.070N,120.333E) which located near Yellow Sea in Qingdao, China. Skyradiometer has been calibrated by inter-comparing it to the spetctoradiometer MRI calibrated annually by the Langley method using the data obtained at Mauna Loa Observatory (MLO), NOAA ESRL-GMD.

2. Data analysis

We analyzed skyradiometer data observed at OUC in Qingdao from 2002 to 2009 by using SKYRAD.PACK version 4.2 (Nakajima et al., 1996). In the analysis of skyradiometer observation data, we need the total ozone amount and the surface pressure. They take account of ozone absorption and Rayleigh scattering of air molecules, respectively. The monthly averaged total ozone amount for 10 years (from 2000 to 2009) is taken from Institute of Atmospheric Physics, Chinese Academy of Sciences which is a site (STN208) of World Ozone and Ultraviolet Radiation Data Centre (WOUDC). The surface pressure is taken from SYNOP data from Meteorological Observatory in Qingdao.

We use CSSR version 1.1 developed by SKYNET (Khatri and Takamura, 2009) for cloud-screening procedure in this study.

3. Retrieved aerosol optical properties

In this study, we show preliminary results of retrieved aerosol optical properties from skyradiometer observation data in Qingdao.

Figure 1 shows scatter plots in the respective season between aerosol optical thickness at wavelength 500nm (AOT@500nm) and Ångström exponent. And Table 1 shows seasonal mean values of aerosol optical thickness at wavelength 500nm (AOT@500nm) and Ångström exponent.

Higher AOT@500nm was observed in summer, and lower AOT@500nm was observed in winter. Ångström exponent was almost observed more than 0.5 for 3 seasons (JJA, SON, and DJF). Low Ångström exponent have relatively higher optical thickness in spring (MAM).

Acknowledgement

Observation of skyradiometer has been supported by

SKYNET from 2008.

We are grateful to Open CLASTR project for using SKYRAD.PACK version 4.2 in this research.

References

1) Uchiyama, A., Yamazaki, A., et al.: Characteristics of Aeolian dust observed by sky-radiometer in the ADEC Intensive Observation Period 1 (IOP1), J. Meteorol. Soc. Japan, 83A, 291-305, 2005.

2) Nakajima, T., Sekiguchi, M., et al.: Significance of direct and indirect radiative forcings of aerosols in the East China Sea region, J. Geophys. Res., 108(D23), 8658, doi:10.1029/2002JD003261, 2003.

3) Nakajima, T., Tonna, G., Rao, R., Holben, B.N.: Use of sky brightness measurements from ground for remote sensing of particulate polydispersions, Appl. Opt., 35, 2672–2686, 1996.

4) Khatri, P. and Takamura, T.: An Algorithm to Screen Cloud-Affected Data for Sky Radiometer Data Analysis, J. Meteor. Soc. Japan, Vol. 87, No. 1, 189-204, 2009.

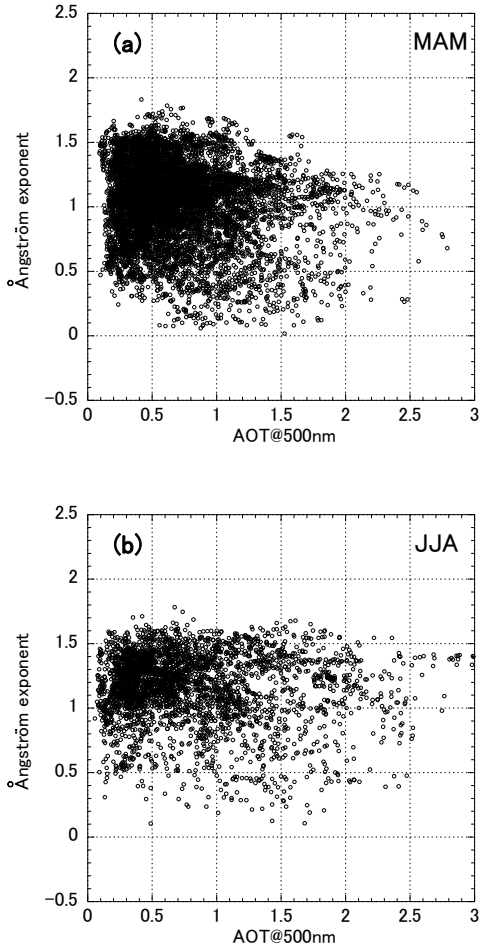

Fig. 1. Scatter plots of aerosol optical thickness at wavelength 500nm (AOT@500nm) and Ångström exponent in the respective season.
(a) Spring (MAM), (b) Summer (JJA), (c) Autumn (SON), and (d) Winter (DJF).

Table 1. Seasonal mean values (*Mean*) and standard deviation values (σ) of aerosol optical thickness at wavelength 500nm (AOT@500nm) and Ångström exponent in the respective season.

	MAM		*JJA*		*SON*		*DJF*	
	mean	σ	mean	σ	mean	σ	mean	σ
AOT@500nm	0.69	0.40	0.80	0.55	0.55	0.40	0.43	0.29
Ångström Exp.	1.04	0.31	1.16	0.27	1.33	0.23	1.29	0.26

Current Status of Cloud-Resolving Model for Simulations of High-Impact Weather Systems

Kazuhisa Tsuboki
Hydrospheric Atmospheric Research Center (HyARC), Nagoya University
Furo-cho, Chikusa-ku, Nagoya, 464-8601, JAPAN
e-mail: tsuboki@rain.hyarc.nagoya-u.ac.jp

1. Introduction

One of the most important objectives of regional models is a high-resolution simulation of high-impact weather systems, which can be used for detailed studies and accurate predictions. High-impact weather systems are most significant phenomena in the atmosphere and sometimes cause huge disasters to human society. Understanding their mechanisms and structures is necessary for prediction and prevention/reduction of disasters. Most high-impact weather systems that cause heavy rainfalls and/or violent winds consist of cumulonimbus clouds and their organized systems. They are usually embedded within a larger weather system and occasionally have a multi-scale structure, ranging from cloud-scale to synoptic-scale systems. These weather systems in East Asia include the Baiu front, typhoons, and winter snowstorms associated with a cold-air outbreak.

In order to perform simulations and numerical experiments of high-impact weather systems, we have been developing the cloud-resolving numerical model named CReSS. Since the multi-scale structure of the weather systems has a wide range of horizontal scales, a large computational domain and a very high-resolution grid to resolve individual classes of the multi-scale structure are necessary to simulate the evolution of the weather systems. In particular, an explicit calculation of cumulonimbus clouds is important for a quantitative simulation of precipitation associated with the high-impact weather. It is also required to formulate accurately cloud physical processes as well as the fluid dynamic and thermodynamic processes. For this type of computation, a large parallel computer with a huge memory is necessary.

The purpose of the present-day research is to explicitly simulate clouds and their organized systems in a large domain (larger than 1000 x 1000 km) with resolved individual clouds using a very fine grid system (less than 1 km horizontally). This will clarify a detailed structure of the high-impact weather systems and permits a more quantitative prediction of the associated precipitation. It will contribute to the accurate prediction of precipitation and the reduction of disasters caused by the high-impact weather systems.

2. Brief description of CReSS

The formulation of CReSS is based on the non-hydrostatic and compressible equation using terrain-following coordinates. Prognostic variables are 3-dimensional velocity components, perturbations of pressure and potential temperature, water vapor mixing ratio, sub-grid scale turbulent kinetic energy (TKE), and cloud physical variables. A finite difference method is used for the spatial discretization. The horizontal domain is rectangular, and variables are set on a staggered grid: the Arakawa-C grid in the horizontal and the Lorenz grid in the vertical. For time integration, the mode-splitting technique (Klemp and Wilhelmson 1978) is used. Terms related to sound waves of the basic equation are integrated with a small time step, and other terms with a large time step.

Cloud physical processes are formulated by a bulk method of cold rain, which is based on Lin et al. (1983), Cotton et al. (1986), Murakami (1990), Ikawa and Saito (1991), and Murakami et al. (1994). The bulk parameterization of cold rain considers water vapor, rain, cloud, ice, snow, and graupel. The microphysical processes implemented in the model are described in Fig.1.

Parameterizations of the sub-grid scale eddy motions in CReSS are one-order closure of Smagorinsky (1963) or the 1.5-order closure of turbulent kinetic energy (TKE). In the latter parameterization, the prognostic equation of TKE is used. All numerical experiments in this textbook use three-dimensional 1.5-order closure scheme. The surface process of CReSS is formulated by a bulk method, whose bulk coefficients are taken from Louis et al. (1981).

Several types of initial and boundary conditions are available. For a numerical experiment, a horizontally uniform initial field provided by a sounding profile will be used with an initial disturbance of a thermal bubble or random temperature perturbation. The boundary conditions are one of the following types; rigid wall, periodic, zero normal-gradient, and wave-radiation types.

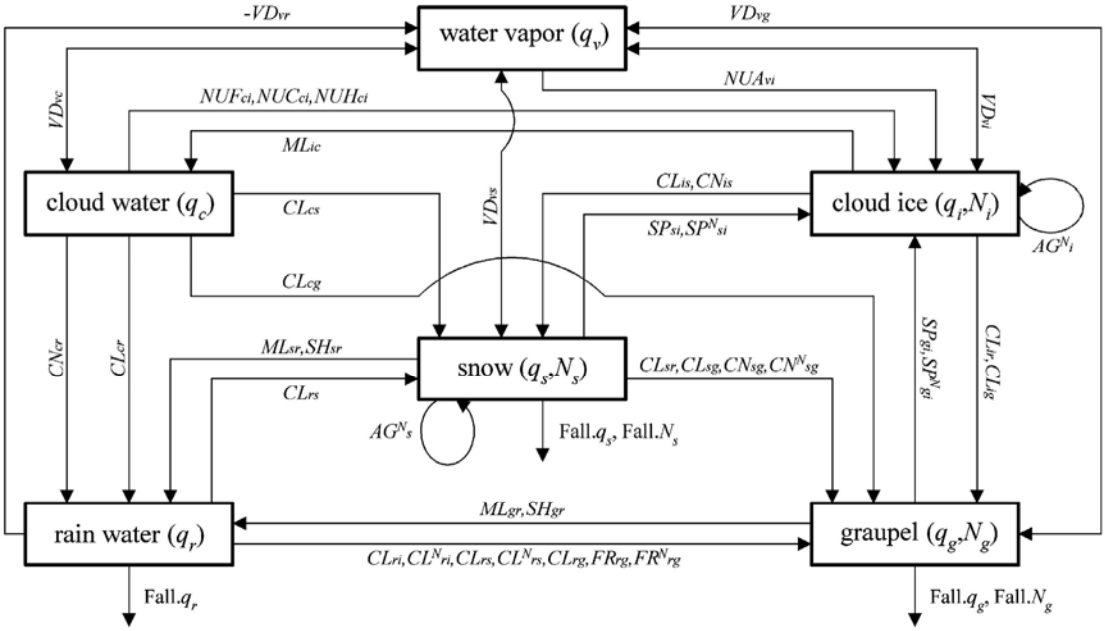

Fig.1: Diagram describing water substances and cloud microphysical processes in the bulk scheme of CReSS

CReSS can be nested within a coarse-grid model for a prediction experiment. In such an experiment, the initial field is provided by interpolating grid-point values and the boundary condition is provided by the coarse-grid model. For a computation within a large domain, conformal map projections are available, which include the Lambert conformal projection, the polar stereographic projection, and the Mercator projection.

For parallel computing of a large computation, CReSS provides two-dimensional domain decomposition in the horizontal direction (Fig.2). Parallel processing is performed using the Massage Passing Interface (MPI). Communications between individual processing elements (PEs) are performed by exchanging data of the two outermost grids. The OpenMP is also available.

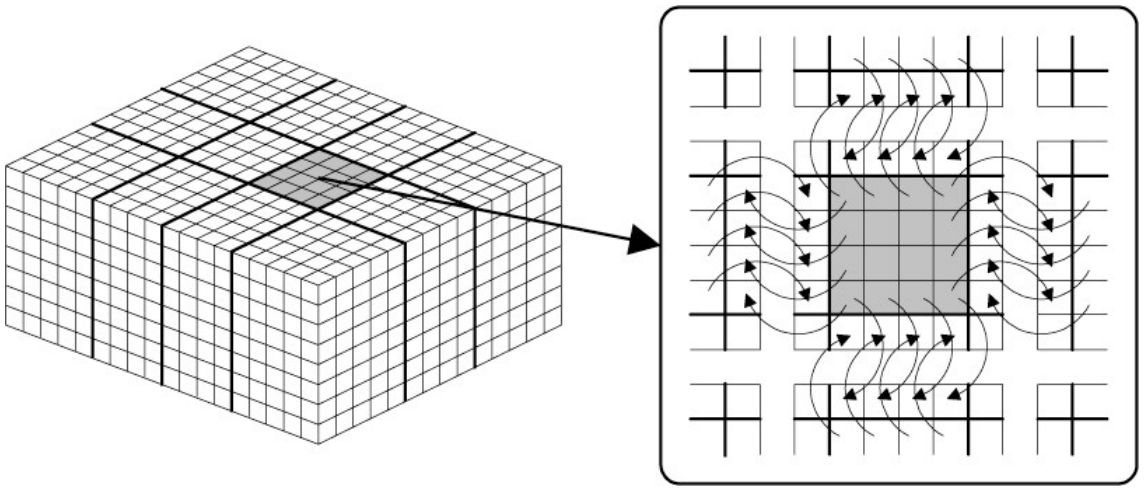

Fig.2: Schematic representation of two-dimensional domain decomposition and the communication strategy for parallel computations using MPI.

3. Simulation of Tornado within a Supercell

The supercell is highly three-dimensional and its horizontal scale is several tens of kilometers. A large domain in the order of 100~km is necessary to simulate a supercell using a cloud model. A tornado, on the other hand, has a horizontal scale of a few hundred meters. The simulation of the tornado requires fine horizontal grid spacing in the order of 100~m or less. In order to simulate a supercell and its associated tornado by a cloud model, a huge memory and high-speed CPU are crucial.

Numerical experiments of a supercell thunderstorm using a cloud model have been performed during the past 20 years (Wilhelmson and Klemp, 1978; Weisman and Klemp, 1982, 1984). Recently, Klemp and Rotunno (1983) attempted to increase the horizontal resolution to simulate the fine structure of a meso-scale cyclone within the supercell. An intense tornado occasionally occurs within a supercell thunderstorm. It is, however, more difficult to resolve a tornado. To overcome this difficulty, Wicker and Wilhelmson (1995) used an adaptive grid method, a two-way nesting technique, to simulate tornado genesis. Their grid spacing of the fine mesh was 120 m. Grasso and Cotton (1995) also used a two-way nesting procedure of a cloud model to simulate a tornadic vorticity. Nesting methods introduce complications of communication between the coarse-grid model and the fine-mesh model at the boundary. A cloud-resolving model does not require any nesting methods. We simulate both the supercell and the tornado using a uniform grid, therefore avoid any complication of the boundary communication. The computational domain of the present simulation is about 50 x 50 km and the grid spacing is 100 m. The integration time is about 2 hours.

The basic field is give by a sounding at Shionomisaki, Japan at 00 UTC, 24 September 1999. The initial perturbation is a warm thermal bubble placed near the surface, which can induce an initial convective cloud. One hour from the initial time, a quasi-stationary supercell is simulated by CReSS (Fig.3). The hook-shaped precipitation area and the bounded weak echo region (BWER), which are characteristic features of a supercell, are formed in the simulation. An intense updraft occurred along the surface flanking line. At the central part of BWER or of the updraft, a tornadic vortex was formed 90 minutes from the initial time.

A close view shows closed contours in the central part of the vorticity. The diameter of the vortex is about 500 m and the maximum vorticity is about 0.1^{-1}, similar to the observed tornado. The pressure perturbation also shows closed contours that correspond to those of the vorticity. This indicates that the flow in the vortex is in cyclostrophic balance. The vertical cross section of the vortex shows that the axis of the vorticity and the associated pressure perturbation is inclined to the left hand side and extends to a height of 2 km. At the center of the vortex, the downward extension of cloud is simulated.

Though this is a preliminary result of a supercell and tornado, some characteristic features of the observation are successfully simulated. The important point of this simulation is that both the supercell and the tornado are simulated with the same grid size. The tornado is produced purely by the physical processes in the model. A detailed analysis of the simulation will provide us important information on tornado genesis within a supercell

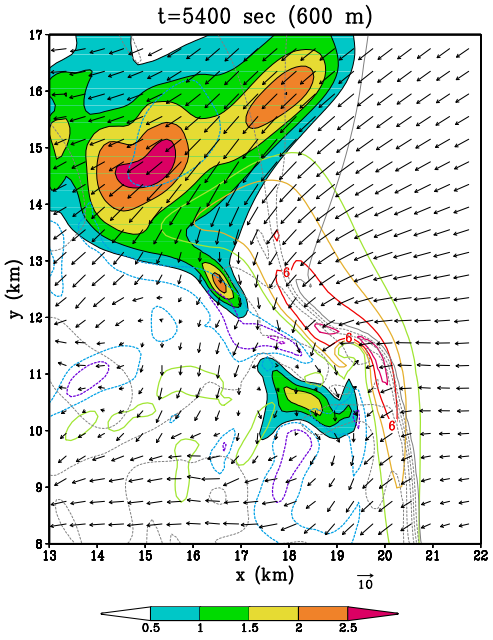

Fig.3 Horizontal display at 600~m of the simulated supercell at 5400 seconds from the initial. Mixing ratio of rain (gray scales, g kg^{-1}, vertical velocity (thick lines, m s^{-1}, the surface potential temperature at 15m (thin lines, K) and horizontal velocity vectors.

4. Typhoons and the associated heavy rainfall: T0418 and T0423

Typhoons develop by close interaction between a large-scale disturbance and embedded intense cumulonimbus clouds. The horizontal scale of typhoons ranges from several 100 km to a few 1000 km while that of the cumulonimbus clouds is an order of 10 km. Typhoons often bring a heavy rain and a strong wind. The heavy rain is usually localized in the eyewall and spiral rainbands which

develop within typhoons. Since cumulonimbus clouds are essentially important for typhoon development, the cloud-resolving model is necessary for a detailed numerical simulation of typhoons.

Some typhoons usually attain Japan and its surroundings and cause severe disasters. In particular, ten typhoons landed over the main lands of Japan in 2004. In the present section, we show two simulation experiments of the typhoons. One is the typhoon T0418 which brought a very intense wind and caused huge disasters due to the strong wind. The other is the typhoon T0423 which brought heavy rainfalls and caused severe floods.

Typhoon T0418 moved northwestward over the northwest Pacific Ocean and passed Okinawa Island on 5 September 2004. Its center passed Nago City around 0930 UTC, 5 September with the minimum sea level presser of 924.4 hPa. When T0418 pass over Okinawa Island, double eyewalls were observed. This is a distinctive feature of the typhoon. T0418 was characterized by strong winds and caused huge disasters due to the strong winds over Japan.

The main objectives of the simulation experiment of T0418 are to study the eyewall as well as spiral rainbands, and to examine structure of the strong wind associated with the typhoon around Okinawa Island. The simulation experiment of T0418 started from 0000 UTC, 5 September 2004. The simulation experiment shows very detailed structure of the eye and the spiral rainbands (Fig.4). Individual cumulus clouds are resolved. They are simulated within the eyewall and along the spiral rainband. A weak precipitation forms around the central part of the eye. The maximum tangential velocity is present along the eyewall and at a height of 1 km. It is larger than 70 m $^{-1}$. The high-resolution experiment shows detailed structure of the cloud and precipitation systems associated with the typhoon, and simulates the overall structure of the typhoon and its movement.

Typhoon T0423 moved along the Okinawa Islands on 19 October 2004 and landed over Shikoku Island on 20 October. In contrast to T0418, T0423 is characterized by heavy rainfall over Japan. Heavy rainfalls associated with T0423 occurred in the eastern part of Kyushu, Shikoku, the east coast of the Kii Peninsula, and the Kinki District. They caused severe floods and disasters in these regions.

The purpose of the simulation experiment of T0423 is to study process of the heavy rainfall. At the initial time of 1200 UTC, 19 October 2004, T0423 was located to the NNE of Okinawa.

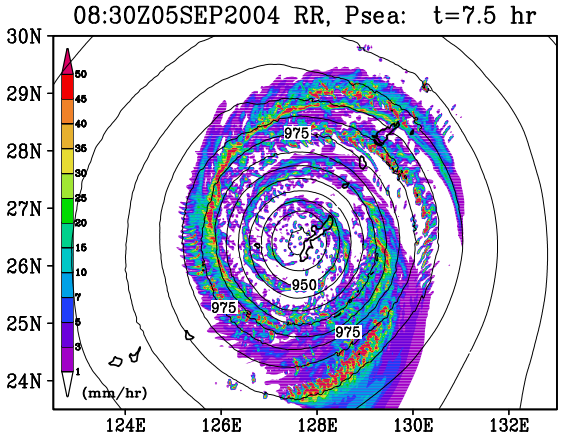

Fig.4: Surface pressure (contour lines; hPa) and rainfall intensity (color levels; mm hr^{-1}) of the simulated Typhoon T0418 at 0830~UTC, 5 September 2004.

The movement of T0423 and the rainfall were successfully simulated. In the simulation, a northward moisture flux is large in the east side of the typhoon center. When the large moisture flux reaches to the Japanese Islands, heavy rainfalls occur along the Pacific Ocean side. The heavy rainfall moves eastward with the movement of the typhoon from Kyushu to Shikoku. When the typhoon reaches to the south of Shikoku, heavy rainfall begins in the Kinki District (the rectangle in Fig.5) and intensifies at 0630 UTC, 20 October (Fig.5). The distribution and intensity of precipitation well correspond to those of the radar observation.

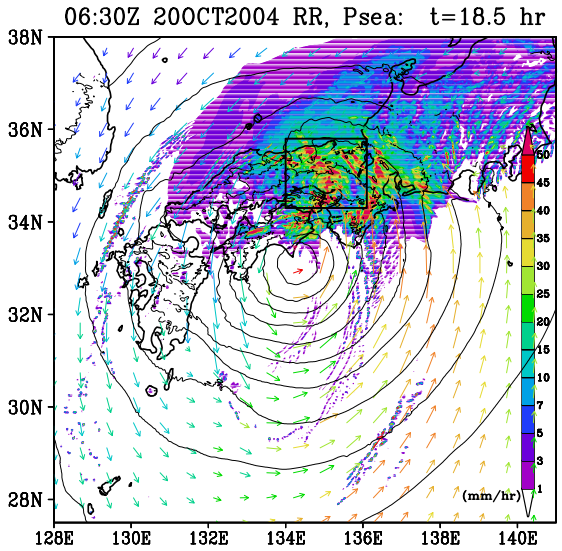

Fig.5: Same as Fig.4 but for the Typhoon T0423 at 0630~UTC, 20 September 2004. Arrows are horizontal wind velocity at a height of 974 m and warmer colored arrows means moister air. The rectangle indicates the region of Fig. 6

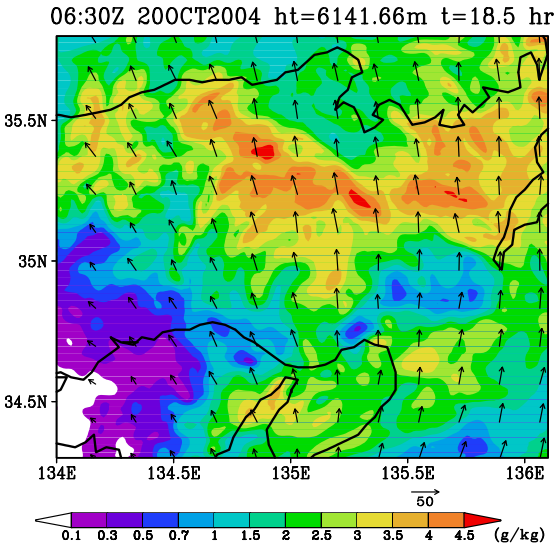

Fig.6: Mixing ratio of precipitation (color levels;g kg^{-1}) and horizontal velocity (arrows) at a height of 6142~m at 0630~UTC, 20 September 2004.

The close view of northern Kinki shows that a large amount of solid precipitation is present around a height of 6 km (Fig.¥ref{fig:T0423_small}). The heavy rainfall in the region forms below the large mixing ratio of the solid precipitation. The heavy rainfall along the Pacific Ocean side moved eastward, while that in the Kinki District lasted until 12 UTC, 20 October. After the typhoon moved to the east of the Kinki District, the northeasterly was intensified significantly. Consequently, orographic rainfall formed in the northern Kinki District. As a result, the accumulated rainfall became a large amount and the severe flood occurred.

5. Localized heavy rainfall

Precipitation systems associated with the Baiu front occasionally show a multi-scale structure. The Baiu front extends zonally for several thousand kilometers while a localized heavy rainfall has a horizontal scale of a few hundred kilometers. To clarify the water circulation process and the role of each class of the multi-scale systems, we performed a simulation experiment of the heavy rainfall in a large domain and with a high resolution. The explicit representation of cumulonimbus clouds in the model is essentially important for accurate and quantitative simulation of the localized heavy rainfall.

The localized heavy rainfall occurred in Niigata and Fukushima prefectures on 13 July 2004. Radar observation of the Japan Meteorological Agency (JMA) showed that an intense rainband extended zonally and maintained for more than 6 hours. The Baiu front was present to the north of Niigata and a sub-synoptic scale low (SSL) moved eastward along the Baiu front.

The initial and boundary condition were provided by the JMA Regional Spectral Model (RSM). Initial time is 1200~UTC, 12 July 2004. The simulation showed that the SSL moved eastward along the Baiu front.

Figure 7 shows that the SSL reaches Japan at 0020~UTC, 13 July 2004. Moist westerly wind is intense to the south of the SSL. Large precipitation extends to the east of the SSL. On the other hand, a very intense rainband forms to the south of the SSL. Enlarged display (Fig.8) of the rainband shows that it extends from the northern part of the Noto Peninsula and reaches Niigata with intensification. The rainband forms between the southwesterly and westerly winds at the low level. The rainband is composed of intense convective cells. It maintains until the SSL moves to the Pacific Ocean. The long time maintenance of the intense rainband results in the severe flood in Niigata Prefecture.

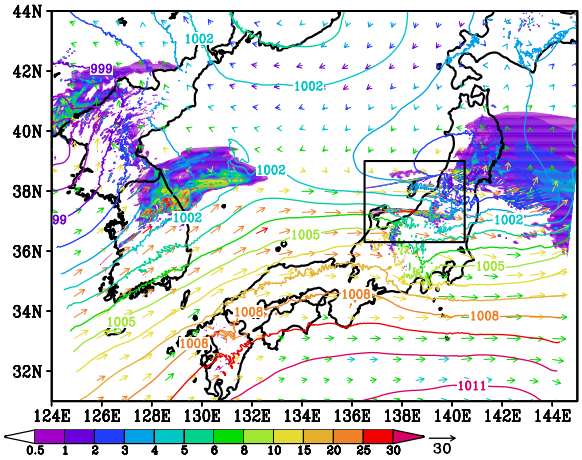

Fig. 7: Surface pressure (contour lines; hPa) and rainfall intensity (color levels; mm hr-1) and horizontal velocity (arrows) at a height of 1610 m at 0020 UTC, 13 July 2004. Warmer colored arrows mean moister air. The rectangle indicates the region of Fig. 8.

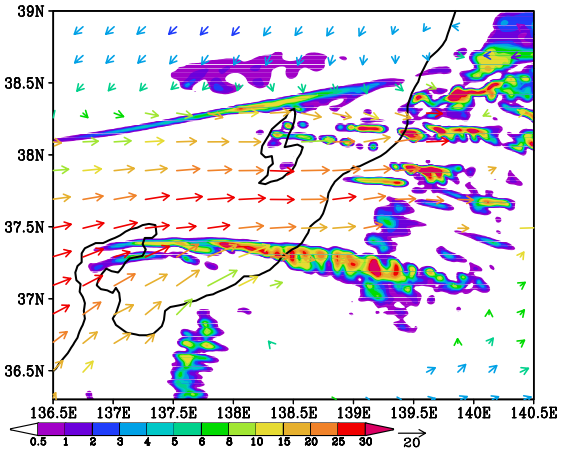

Fi.8: Same as Fig.7 but for the region of the rectangle in Fig.7 and at a height of 436 m.

6. Summary

High-impact weather systems occasionally cause huge disasters to human society owing to heavy rainfall and/or violent wind. They consist of cumulonimbus clouds and usually have a multi-scale structure. High-resolution simulations within a large domain are necessary for quantitatively accurate prediction of the weather systems and prevention/reduction of disasters. For the simulations, we have been developing a cloud-resolving model named the Cloud Resolving Storm Simulator (CReSS). The model is designed and optimized for a parallel computer. The purpose of the present research is high-resolution simulations of high-impact weather systems in a large calculation domain with resolving individual cumulonimbus clouds using the CReSS model. Characteristic high-impact weather systems in East Asia are the Baiu front, typhoons, and winter snowstorms. The present paper describes simulations of these significant weather systems. We have chosen for the case study of the Baiu front the Niigata-Fukushima heavy rainfall event on 13 July 2004. Typhoons for simulations are T0418 which caused a huge disaster due to strong wind, and T0423 which caused severe flood over the western Japan in 2004. These experiments clarified both the overall structures of weather systems and individual clouds. The high-resolution simulations resolving individual clouds permit a more quantitative prediction of precipitation. They contribute to accurate prediction of wind and precipitation and to reduction of disasters caused by high-impact weather systems.

Acknowledgements

The present study of CReSS development is supported by the KAKUSHIN program. The simulations of the present work were performed by the Earth Simulator and mainframe computer of the computer center at Nagoya University.

References

Tsuboki, K. and A. Sakakibara, 2002: Large scale parallel computing of Cloud Resolving Storm Simulator. *High Performance Computing, Springer*, H. P. Zima et al. Eds, 243-259.

Tsuboki, K., 2008: High-resolution simulations of high-impact weather systems using the cloud-resolving model on the Earth Simulator. *High Resolution Numerical Modeling of the Atmosphere and Ocean, Springer, New York, Kevin Hamilton and Wataru Ohfuchi (Eds)*, 141-156.

Liu. A. Q., G. W. K. Moore, K. Tsuboki and I. A. Renfrew, 2006: The effect of the sea-ice zone on the development of boundary layer roll clouds during cold air outbreaks. *Boundary-Layer Meteorology*, **Vol.118, No.3**, 557 - 581.

Maesaka, T., G. W. Kent Moore, Liu, A. Q., and K. Tsuboki, 2006: A simulation of a lake effect snowstorm with a cloud resolving numerical model. *Geophysical Research Letters*, **Vol.33**, L20813.

Wang, C. C., G. T. J. Chen, T. C. Chen and K. Tsuboki, 2005: A numerical study on the effects of Taiwan topography on a convective line during the Mei-yu season. *Monthly Weather Review*, **Vol.133**, 3217 - 3242.

Diurnal variation of cloudiness over South Asia using satellite observations

B. C. Bhatt[1], T.-Y. Koh[1], M. K. Yamamoto[2], K. Nakamura[3]

[1]*Nanyang Technological University, 9th storey BorderX block, RTP, 50 Nanyang Drive Singapore 637553*

bcbhatt@ntu.edu.sg

[2]*Chiba University, 1-33 Yayoi-cho, Inage-ku, Chiba 263-8522, Japan*

mkyamamoto@faculty.chiba-u.ac.jp

[3]*Nagoya University, Furo-cho, Chikusa-ku, Nagoya 464-8601 Japan*

nakamura@hyarc.nagoya-u.ac.jp

Abstract

The climatological features of the diurnal cycle of cloudiness were investigated over three convective centers of interest over South Asia: over the Himalayas; north India and the Bay of Bengal (BOB). Three hourly blackbody brightness temperature (TBB) data from the METEOSAT-5 and rainfall data (3B42) from the Tropical Rainfall Measuring Mission (TRMM) were utilized. Analysis was concentrated on pre-monsoon and the summer monsoon season. Two methods were used to detect cloudiness: one method counted cloud clusters (CC) and utilized cloud tracking technique to identify time clusters (TC); and the other method computed cloud cover frequency (CCF). CC was defined as a contiguous area of pixels with TBB lower than the threshold of 219 K. The CCF was derived using 235 K as the threshold.

From the analysis, it was noted that there were many CC over north India in the pre-monsoon season especially during the late afternoon hours. But deep convective activity was weaker over the region during the summer monsoon season. Bimodal diurnal cycle in CC occurrence was noted over the Himalayas during the summer monsoon season. It was noted that the peak convective activity occurred at 6 LT for the Bay of Bengal during both the summer monsoon and the pre-monsoon season. The life cycle of cloud clusters during summer monsoon season was also investigated. The diurnal cycle varied with location. There appeared a gradual delay in the preferred time of initiation, attainment of maximum area and dissipation as one progresses northward from BOB region through north India to the Himalayas.

Keywords: diurnal variation; climatology; South Asia

1. Introduction

Atmospheric convection seems ubiquitous over South Asia. The widespread cloud and precipitation activity during monsoon period has long been recognized over the region. The frequency of convection is modulated by a variety of phenomena including monsoon depressions, intraseasonal active-break phases and the local diurnal circulations such as land-sea breezes and mountain-valley winds.

Changes in convective activity on the diurnal time scale have been observed in many places around the globe. If we examine the South Asian region covered by previous cloud/precipitation studies, Indian Ocean have been explored more than the adjoining landmasses (Gambheer and Bhat 2001). Convective activity over domains within South Asia has not been sufficiently researched, although there were some studies on diurnal variations. Kodama et al. (2005) reported maximum lightning activity over the east coast and north part of India during the pre-monsoon season. In the Himalayas, bimodal diurnal cycle of rainfall has been reported from limited ground-based and satellite observations (e. g., Bhatt and Nakamura 2006). Over the northwest side of Bay of Bengal (BOB), Zuidema (2003) documented a high degree of convective activity with morning maximum in cloudiness in the summer monsoon season. The monsoon depressions from BOB usually move northward or northwestward accompanied by the onshore transport of moist air. There is substantial convective organization. The associated rainfall is distributed across three regional maxima centered separately in BOB, north India and the southern slopes of the Himalayas (Xie et al. 2006). The diurnal variability over the centers of heavy

rainfall in BOB, north India and the Himalayas has not been sufficiently researched and deserve further attention. Based on the observations reported by Xie et al. (2006), three convective centers of interest (Fig. 1) are identified for this work: region A in the Himalayas; region B in north India and region C in the BOB to examine fine-scale variations of convective activity.

The aim is to delineate the climatological diurnal convective activity over three convective centers during the pre-monsoon and especially in the summer monsoon seasons. We use high spatial resolution infrared (IR) data denoting cloud fields from METEOSAT-5. We also performed a simple validation of METEOSAT results with Tropical Rainfall Measuring Mission (TRMM) data from over ten years.

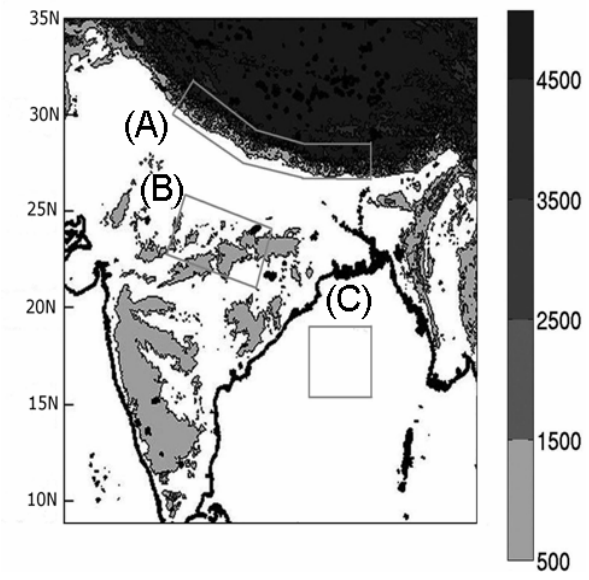

Figure 1: Terrain height (units: m) over South Asia. The three regions used to study cloud diurnal variations are: region A, region B and region C.

2. Data and Method

Two sets of satellite data were used. One was TRMM rain product (3B42) available on 0.25º x 0.25º grid with temporal resolution of 3 hours from 1999 to 2008. This product is from multiple satellite microwave and infrared measurements (Huffman et al. 2007). The other was METEOSAT-5 IR brightness temperature (TBB) data available with spatial resolution of 5 km and temporal resolution up to 1 hour for 1999 and 2000 but data at hand was limited to 0, 3, 6, 9, 12, 15, 18 and 21 Local Times (LT) to be comparable with the TRMM dataset. Local times are defined as Universal Time Coordinate (UTC) + 6 hours. 12 months of data from both datasets were divided into two seasons: pre-monsoon season for March, April and May (MAM); and summer monsoon season for June, July and August (JJA).

Two methods were used to detect cloudiness from METEOSAT-5 data. One utilized cloud cluster (CC) technique while the other computed cloud cover frequency (CCF). In the CC technique, deep convective clouds were detected as patches of very low TBB. A CC was defined as a contiguous area larger than 2000 km2 and with a brightness temperature lower than 219 K. The cloud tracking procedure used here was similar to the one described by Williams and Houze (1987). To detect convective clouds in the CCF technique, it was assumed that cloudy sky has not only cooler but also less homogeneous distribution of TBB than clear sky. The CCF was derived using 235 K as the threshold.

3. Results and Discussion

3.1 METEOSAT-5 data

The selected two years, 1999 and 2000 are not exceptional with regards to inter-annual climatic variations in the region. The space-time variability of deep convective clouds during the pre-monsoon and summer monsoon will be described. We examined areal representation of the diurnal cycle of cloudiness without considering each CC's life span over South Asia in the three regions. Figure 2a shows the diurnal variation of the normalized number of CC over a day for the pre-monsoon season. The average number of CC in every 3-hour interval in local time has been normalized by the respective total number of CC in a day for each region so that the relative variation stands out. The peak occurrence of CC over region B and the region A is in the mid-afternoon (15 LT). On the other hand, in region C, the maximum occurs in the early morning (6 LT). Thus, the phase of the diurnal cycle differs greatly between land and sea. The enhanced CC distribution over north India including region B was nearly oriented in NE-SW direction as it was noted in the spatial distribution of CC (not shown).

Figure 2b shows the diurnal variation of the normalized number of CC over a day for the summer monsoon season. The peak appears earlier in this season at 12 LT over region B, while the region A peak remains at 15 LT. The shift in the time of maximum convective activity from early afternoon in the region B to late afternoon over the region A may

suggest northward migration of deeply convecting MCSs. It is remarkable that the peak convective activity occurs at 6 LT for region C during both the summer monsoon and the pre-monsoon. These results are in agreement with diurnal cycle studies by Ohsawa et al. (2001), Yamamoto et al. (2008) and Zuidema (2003) over the BOB region. From the spatial distribution, it was noted that deep convective activity was weak during the summer monsoon (not shown).

We further focused on the summer monsoon season and investigated the life time of cloud clusters over three domains (Fig. 3). For the Himalayan region, time cluster (TC) mostly form in the early afternoon (12-15 LT), attain their maximum area around 15 LT and then decay away by the early evening (18-21 LT). In region B, initiations tend to occur in the early morning (6-9 LT) but maximum area is only attained around noon (12 LT) followed by dissipation in the early afternoon (12-15 LT). The region C stands out among the three regions in that initiation, attainment of maximum area and dissipation all tend to take place before noon (around 3-6 LT, 6 LT and 9-12 LT respectively).

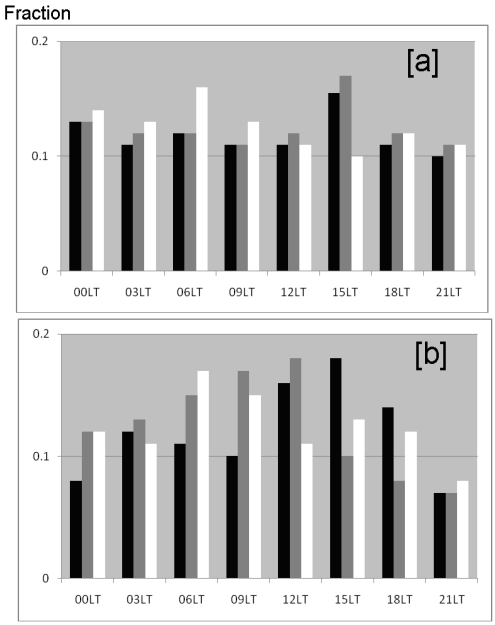

Figure 2: Diurnal variation of the number of CC normalized by the total number of CC over a day for each region during MAM 1999-2000 (a) and during JJA 1999-2000 (b). The black, gray and white bars denote results for the regions A, B and C respectively.

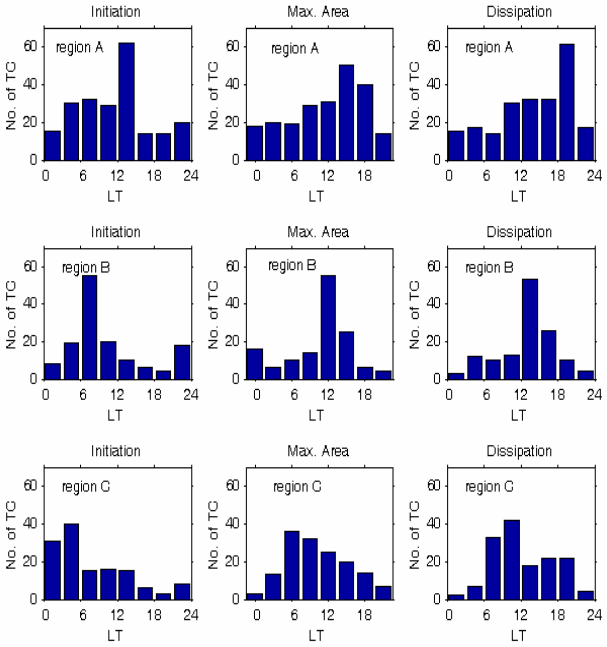

Figure 3: The number of TC distributed over their local time of initiation (left column), attainment of maximum area (middle column) and dissipation (right column) in JJA 1999-2000. The first, second and third rows correspond to the regions A, B and C respectively.

3.2 TRMM data

Ten years of TRMM 3B42 rainfall data (1999-2008) was analyzed. The findings have the statistical significance to establish the robustness of the same phenomena that was revealed in the shorter METEOSAT-5 dataset. The spatial distribution of normalized differential rainfall index (NDRI) during MAM and JJA of 1999-2008 is computed (Yamamoto et al. 2008). Moderate to large NDRI over region C suggests relatively strong diurnal variations (Fig. 4). Over regions A and B, the NDRI values are more variable. During the pre-monsoon season in region A, the low nighttime rainfall in the TRMM observations does not correspond with the high nighttime occurrence of CC noted in Meteosat-5 results. For the summer monsoon season, there is concentration of nighttime intense rainfall over the region A. The nighttime occurrence of CC, which could imply the likelihood of rain, is evident in the METEOSAT-5 data analysis. Results from Meteosat-5 for region B and C also agree well with TRMM rainfall analysis.

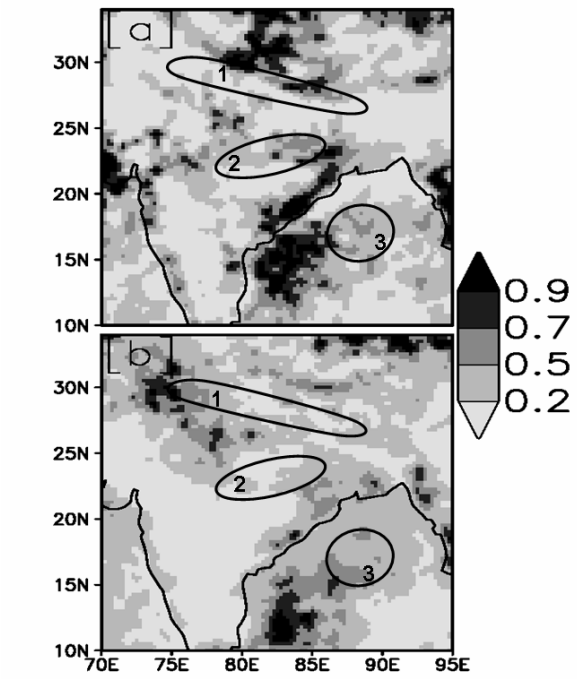

Figure 4: Normalized Difference Rainfall Index (NDRI) derived from TRMM (3B42) dataset: (a) for MAM 1999-2008, and (b) for JJA 1999-2008. Regions marked 1 to 3 represent regions A, B and C respectively.

4. Summary

The climatological features of the diurnal cycle and spatial variability of cloudiness were investigated over South Asia using data from the METEOSAT-5 during March-May and June-August of 1999 and 2000. Analysis of ten years of TRMM rainfall product (3B42) was performed to enhance the confidence in 2-year METEOSAT-5 results. Three convective centers of interest were investigated: region A in the Himalayas; region B in north India and region C in the Bay of Bengal (BOB). For pre-monsoon season, the preferred region of occurrence of CC was over region B. In the pre-monsoon season, there are many CC over region B and the region A in the mid-afternoon (15 LT). In the summer monsoon season, the peak occurrence of CC appears around 12 LT over the region B and still around 15 LT over the region A. For region C, CC is most numerous around 6 LT in both seasons, showing clear contrast with the other two land regions.

The life cycle of cloud clusters during summer monsoon is worthy of note: statistically speaking, there is a gradual delay in the preferred time of initiation, attainment of maximum area and dissipation as one progresses northward from regions C through B to A.

Acknowledgements

This symposium is sponsored by the Ministry of Education, Science, Sports and Culture, Japan (MEXT), and National University Corporation Chiba University.

References

1) Bhatt, B. C. and K. Nakamura, 2006: A climatological-dynamical analysis associated with precipitation around the southern part of the Himalayas. *J. Geophy Res*. 111, D02115

2) Gambheer, A. V., and G. S. Bhat, 2001: Diurnal variation of deep cloud systems over the Indian region using INSAT-1B pixel data. *Meteorol. Atmos. Phys*. 78, 215-225.

3) Huffman, G. J., R. F. Adler, D. T. Bolvin, G. Gu, E. J. Nelkin, K. P. Bowman, Y. Hong, E. F. Stocker, and D. B. Wolff, 2007: The TRMM multi-satellite precipitation analysis: quasi-global, multi-year, combined-sensor precipitation estimates at fine scale. *J. Hydrometeor*. 8, 38-55.

4) Kodama, Y.-M., A. Ohta, M. Katsumata, S. Mori, S. Satoh, and H. Ueda, 2005: Seasonal transitions of predominant precipitation type and lightning activity over tropical monsoon areas derived from TRMM observations. *Geophys. Res. Lett*. 32 (L14710).

5) Ohsawa, T., H. Ueda, T. Hayashi, A. Watanabe, and J. Matsumoto, 2001: Diurnal variations of convective activity and rainfall in tropical Asia. *J. Meteorol. Soc*. 79, 333-352.

6) Williams, M. and R. A. Houze Jr., 1987: Satellite-observed characteristics of winter monsoon cloud clusters. *Mon. Wea. Rev*. 115, 505-519.

7) Xie, P., H. Xu, N. H. Saji and Y. Wang, 2006: Role of narrow mountains in large-scale organization of Asian monsoon convection. *J. Climate* 19, 3420-3429.

8) Yamamoto, K. M, F. A. Furuzawa, A. Higuchi and K. Nakamura, 2008: Comparison of diurnal variations in precipitation systems observed by TRMM PR, TMI, and VIRS. *J. Climate* 21, 4011-4028.

9) Zuidema, P., 2003: Convective clouds over the Bay of Bengal. *Mon. Wea. Rev.* 131, 780-798

Validation of cloud detecting algorithm CLAUDIA using CALIPSO and Cloudsat cloud mask

Takashi Matsui[1], Haruma Ishida[2], Takashi Y. Nakajima[1]

[1]*Reasearch and Information Center, Tokai University, 2-28-4 Tomigaya, shibuya-ku, Tokyo 151-0063, Japan*
pine@tokai-u.jp, nkjm@yoyogi.ycc.u-tokai.ac.jp

[2] *Yamaguchi University Faculty of Engineering, 2-16-1 Tokiwadai, Ube, Yamaguchi 755-8611, Japan*
ishidah@yamaguchi-u.ac.jp

Abstract

CLAUDIA is a cloud detection algorithm developed for the arbitrary multispectral imagers. A validation of CLAUDIA using the CALIPSO and Cloudsat observations is presented. A comparison between CLAUDIA and MODIS cloud mask algorithm (MOD35) is also presented. The validation reveals about the accuracy of the cloud masks generated by CLAUDIA and the dependency of the detection accuracy on several surface types. The result indicates that CLAUDIA identifies the clear pixels more accurately than MOD35 and CLAUDIA is more neutral than MOD35. In other word, CLAUDIA is not biased to either clear or cloudy.

Keywords **:** cloud mask, MOD35

1. Introduction

The cloud mask is one of the standard products produced from the satellite imagers. It is used as the preprocessing for the high-order products. Cloud and Aerosol Unbiased Decision Intellectual Algorithm (CLAUDIA) is a cloud detection algorithm developed for the arbitrary multispectral imagers[1)]. It is now used to generate the cloud mask products from the GOSAT/CAI observations and will be adapted to the Japanese future Earth observing missions, GCOM-C/SGLI and EarthCARE/MSI. In this study, the validation of CLAUDIA using the CALIPSO and Cloudsat observations are presented. The comparison of CLAUDIA with MOD35 is also presented.

2. CLAUDIA

The CLAUDIA was developed under the concept of the neutral cloud detections. "Neural" means the discriminations are not biased either clear or cloudy. It consists of several pixel-by-pixel threshold tests that output the Clear Confidence Level (CCL) that indicates the probability of cloud existence through a value from 0.0 (cloudy) to 1.0 (clear) (Fig.1). CLAUDIA calculates the final CCL from the CCL values of the tests using the following formulation:

$$Q_1 = 1 - \sqrt[m]{(1-q_{11})(1-q_{12})\cdots(1-q_{1m})} \quad (1)$$

$$Q_2 = \sqrt[n]{q_{21}\cdot q_{22}\cdots q_{2n}} \quad (2)$$

$$Q_{final} = \sqrt{Q_1 \cdot Q_2} \quad (3)$$

where q_{gi} is the CCL of the i-th threshold test in group-g. Q_g represents CCL values of the group-1 or 2. Q_{final} is the final CCL of CLUAIDA. The group-1 consists of the suitable tests for detecting the clear pixels (Table 1) and Eq. (1) is considered to be "clear conservative''. In contrast, the group-2 consists the suitable tests for detecting the cloudy pixels and Eq. (2) is considered to be ''clear conservative.''

The concept of the CLAUDIA is referred to that of MOD35. MOD35 also calculates CCL values, but the formulation to combine the CCL values and the concept of the grouping are different from CLAUDIA[2)]. The formulation of MOD35 tends to bring "cloudy bias" .

3. Validation of CLAUDIA using CALIPSO-Cloudsat

The radar and lidar satellite can be used to validate the cloud masks generated from imager data because the detections by the former are generally more accurate than the latter. For example, Ackerman *et al*. used the CALIPSO observations to validate MOD35[4)]. In this study, the cloud masks generated using CLAUDIA from Aqua/MODIS data in January 2008 to November 2008 are validated based on the combined Cloudsat-CALIPSO cloud masks[6)]. Aqua/MODIS, Cloudsat and CALIPSO consist the "A-train" and the their observations are overlapped. The MOD35 overlapped with them are also validated.

The outputs of Cloudsat-CALIPSO cloud mask are the cloud existences in each vertical bin. For this validation, the pixels are labeled as "cloudy" if one or more cloudy bins exist. The outputs of MOD35 are "Cloudy", "Probably cloudy", "Probably clear", or "Clear". For the comparison with MOD35, 0-0.25, 0.25-0.5, 0.5-0.75, 0.75-1.0 of the

CLAUDIA CCL values were labeled as “Cloudy”, “Probably cloudy”, “Probably clear” or “Clear”, respectively.

The occurrence rate images according to CLAUDIA and MOD35 outputs when the Cloudsat-CALIPSO cloud masks indentified as “Clear (Cloudy)” were shown in Fig. 3 (Fig.4). In Fig.3 CLAUDIA and MOD35 identified the 78% and 55% pixels as “Clear” and misidentified the 10% and 17% pixels as ”Cloudy” on average. In Fig.4 CLAUDIA and MOD35 identified the 70% and 89% pixels as “Cloudy” and misidentified the 14% and 6% pixels as ”Clear” on average. The result indicates that the discrimination of MOD35 tend to be biased to “Cloudy” whereas CLAUDIA can identifies both “Clear” and “Cloudy” in almost the same accuracy. Therefore CLAUDIA is more neutral than MOD35.

The images and histograms of the averaging NDVI calculated referring to Cloudsat-CALIPSO, CLAUDAI or MOD35 are shown in Fig.5. The histogram of CLAUDIA is more similar to that of Cloudsat-CALIPSO than that of MOD35.

References

1) Ishida, H. and T. Y. Nakajima (2009), Development of an unbiased cloud detection algorithm for a spaceborne multispectral imager, *J. Geophys. Res.*, *114*, D07206, doi:10.1029/2008JD010710.

2) Ackerman, S. A., K. I. Stabala, W. P. Menzel, R. A. Frey, C. Moeller, and L. E. Gumley (1998), Discriminating clear sky from clouds with MODIS, *J. Geophys. Res.*, 103, 32,141–32,157, doi:10.1029/ 1998JD200032.

3) Ackerman, S. A., R. E. Holz, R. Frey, E. W. Eloranta, B. Maddux, and M. J. McGill (2008), Cloud detection with MODIS: Part II. Validation, *J. Atmos. Oceanic Technol.*, *25*, 1073–1086.

4) Hagihara, Y., H. Okamoto, and R. Yoshida (2010), Development of a combined CloudSat•CALIPSO cloud mask to show global cloud distribution, *J. Geophys. Res.*, *115*, D00H33, doi:10.1029/2009JD012344.

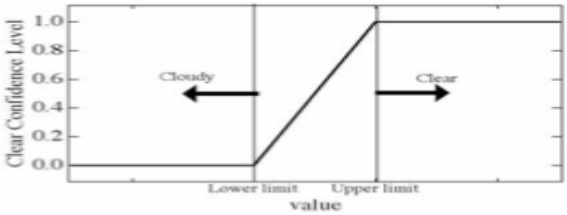

Fig. 1 The concept of the clear confidence level in tests

Table 1 Threshold tests in CLAUDIA and main targets

Group	Threshold tests	Main target
1	R(0.86μm)	Optically thick clouds over ocean
	R(0.66 μm)	Optically thick clouds over land
	R(0.86μm)/ R(0.66μm)	Optically thick clouds
	NDVI	Clouds over deep forests
	R(0.86μm)/ R(1.6μm)	Clouds over bright desert
2	BT(10.8μm)	High clouds
	R(1.38μm)	Thin cirrus
	BT(10.8μm)- BT(3.9μm)	Optically thick clouds

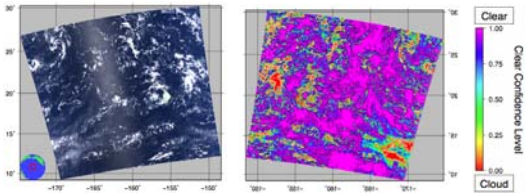

Fig. 2 An example of CLAUDIA outputs. (left : MODIS RGB, right : CLAUDIA out put)

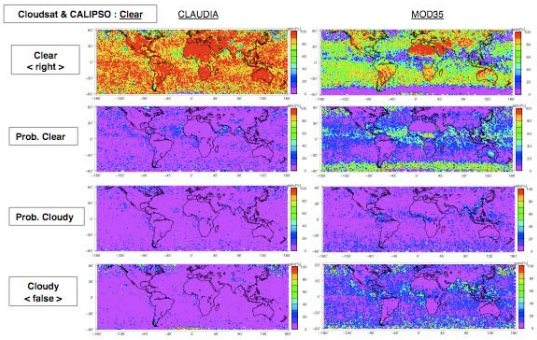

Fig. 3 The occurrence rate images according to CLAUDIA and MOD35 outputs for “Clear” pixels.

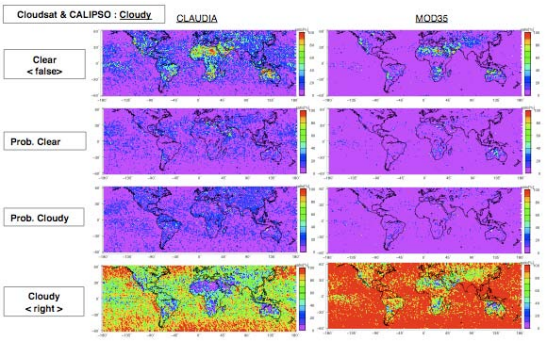

Fig. 4 The occurrence rate images according to CLAUDIA and MOD35 outputs for “Cloudy” pixels.

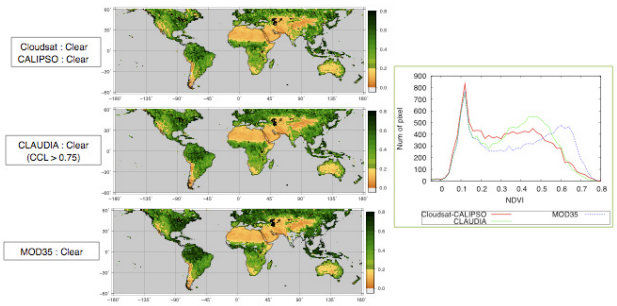

Fig.5 The images and histogram of NDVI made referring to Cloudsat-CALIPSO, CLAUDAI or MOD35 cloud masks.

A statistical analysis for the characteristics of cloud/precipitation system from Cloudsat data

Munehisa K. Yamamoto, Atsushi Higuchi, and Masamitsu Hayasaki

Center for Environmental Remote Sensing, Chiba University, Japan, mkyamamoto@faculty.chiba-u.jp

Abstract

Global distributions of cloud largely effect earth radiation budgets. The heating / cooling effect differs depending on a type of cloud due to the differences of the characteristics of radiative process. Thus, it is important to understand cloud distributions classified into some cloud types. A cloud type classification method has been developed using multiple bands in visible and infrared using geostationary satellite. However, it was hard to classify the cloud types because of limit of information from optical thickness and cloud top height.

In 2006, Cloudsat satellite carrying the Cloud Profiling Radar (CPR) was launched, and its observation enables us to find vertical distributions of cloud globally. This study tried to characterize cloud / precipitation characteristics and classify cloud types from vertical distributions of clouds observed by Cloudsat CPR. This study applied a base of vertical-method of the Tropical Rainfall Measuring Mission (TRMM) Precipitation Radar (PR) 2A23 algorithm to the vertical distributions of reflectivity factor (Z) from CPR in order to detect the bright band height (BBH) and cloud types. The detected BBH exists under 250-500 m from freezing height derived from a re-analysis data. The cloud types were classified into convective with large Z, stratiform with BBH, and others.

In this presentation, we will also report the characteristics of global cloud distributions with / without precipitation, with shallow or anvil, and so on.

Keywords **:** Remote sensing, Cloudsat CPR, cloud distribution

1. Introduction

Recently, the global warming attracts big attention. One of the biggest concerns is the change of the global cloud distributions. Global distributions of cloud largely effect earth radiation budgets. The heating / cooling effect differs depending on a type of cloud due to the differences of the characteristics of radiative process such as reflection from short wave radiation and absorption and emission from long wave radiation. Since these processes depend on a cloud thickness and cloud temperature, it makes difficult to estimate and predict the global radiation budget. Therefore, it is important to understand cloud distributions classified into the cloud types.

A cloud type classification method has been suggested using multiple bands in visible and infrared using geostationary and low-orbit satellites. For example, Inoue (1987) developed a simple cloud type classification based on split-window technique. Brightness temperature difference between visible and infrared channels has good relation to some cloud types. However, it was hard to classify the cloud types because of limit of information from optical thickness and cloud top height. Using precipitation radar technique, on the other hand, rain type classification method has been developed to estimate precipitation because drop size distributions are largely different with rain types. The Tropical Rainfall Measuring Mission (TRMM) provides standard products of rain characteristics from three-dimensional radar reflectivity. In 2006, Cloudsat satellite carrying the Cloud Profiling Radar (CPR) was launched, and its observation enables us to find vertical distributions of cloud globally. This study tried to characterize cloud / precipitation characteristics and classify cloud types from vertical distributions of clouds observed by Cloudsat CPR.

This study presents the characteristics of global cloud precipitation distributions and the classification of cloud types from Cloudsat CPR.

2. Data

This study mainly used Cloudsat CPR 2B-GEOPROF product provided by the Cloudsat Data Processing Center for June-July August (JJA) 2007–2009. This product provides radar reflectivity factor and significant echo and cloud flag observed by CPR, MODIS, and ECMWF data. In order to compare the simultaneous observation data between Cloudsat CPR and TRMM PR, we used 2D-CLOUDSAT-TRMM product. This product summarizes a basic nearest-neighbor interpolation of the TRMM data on to the Cloudsat data's along track resolution, and generated for intersects with an overpass time difference of 50 minute or less.

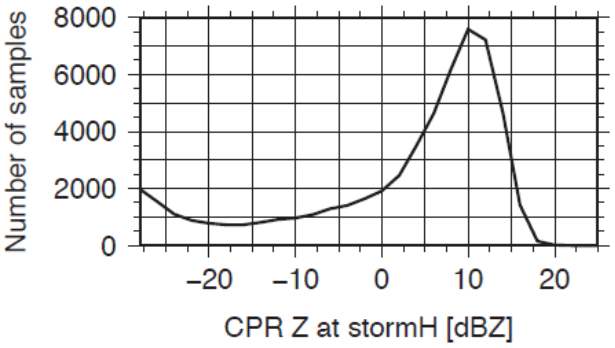

Fig. 1 Appearance number of CPR radar reflectivity factor at TRMM stormH.

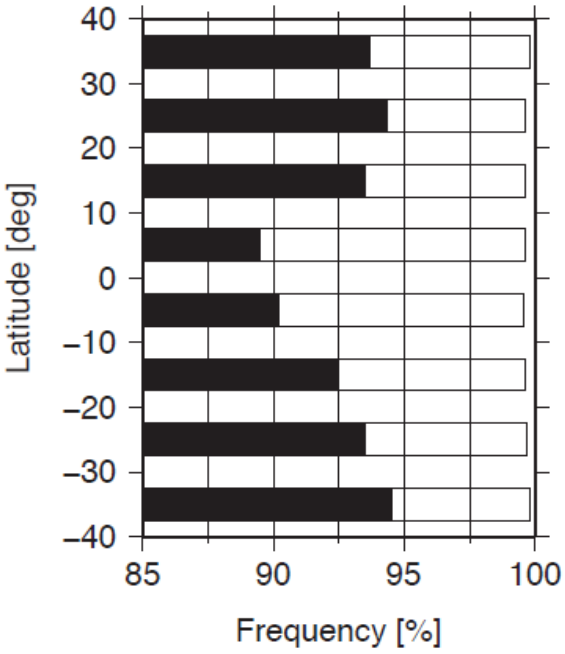

Fig. 2 Appearance frequency of cloud / rain detected pixels with Cloudsat CPR (black) and with both CPR and TRMM PR (white) displayed by cumulative bar chart.

3. Results

3.1 Instantaneous Cloudsat CPR vs TRMM PR

Radar reflectivity factor Z is given by the sixth-powers of the diameters of all the drops contained in a unit volume of space. However, equivalent radar reflectivity factor (Z_e), Z derived from radar received power, is affected by precipitation attenuation depending on radar frequency. Under the simultaneous observation, Z_e from Cloudsat CPR and TRMM PR should be different value. When storm top height (stormH as the top height of precipitation) is identified from Cloudsat CPR, this difference must be considered. According to the appearance number of Cloudsat CPR Z_e at the stormH from TRMM PR (about 17 dBZ) in the simultaneous observations (Fig. 1), Z_e is concentrated around 10 dBZ. This difference is explained by the radar frequency, horizontal resolutions, and overpass time difference. From this result, hereafter stormH from Cloudsat CPR is defined by the top height of 10 dBZ.

Figure 2 shows the appearance frequency of radar echo from Cloudsat CPR and TRMM PR at the same pixel. When both of the echoes are detected in the pixel, cloud with precipitation would exist. If the Cloudsat CPR only observes radar echo, this pixel would contain non-precipitating cloud. There are few pixels just TRMM PR echo detected. Over 90% of the radar echo detected pixels exists non-precipitating clouds except for tropics. The appearance frequency of precipitating clouds in the tropics is higher than those in the mid-latitude regions. This implies that shallow and weak precipitation frequently occurs in the mid-latitude ocean.

3.2 Global distributions of cloud / precipitation parameters

Historically cloud type and cloud top height detections from satellite sensors have been used by visible and infrared channels. However, it is hard to estimate them precisely due to lack of vertical resolutions. Moreover, it is not easy task to match up simultaneous data of both of cloudH and stormH unless TRMM PR and VIRS observations. Assuming the correspondence of stormH from Cloudsat CPR mentioned the precious subsections, relationship between stormH and cloudH should be further understood.

Figure 3a shows mean cloudH from Cloudsat CPR. Over ocean, cloudH over 12 km appears over the maritime continent, the Bay of Bengal, and the west coast of the Mexico. High cloudH regions correspond to large amount of rainfall. Over land, cloudH also exceed 10 km over tropical Africa and south-east Asia. However, cloudH over land is generally lower than that over ocean. From the difference between the ascending and descending passes (Fig. 3b), cloudH over ocean (land) in the early-afternoon pass is higher (lower) than that in the mid-night pass due to diurnal variations of cloud activity. Mean stormH distributions (Fig. 3c) apparently similar to the mean cloudH. However, high stormH regions are relatively different particularly over land (e.g. the Tibetan Plateau, western India, and North America). The ascending-descending contrast between land and ocean is apparently obscured, but stormH over the Rocky Mountains is dominant in nighttime. These diurnal variations correspond to those from TRMM PR and VIRS (Yamamoto et al. 2008).

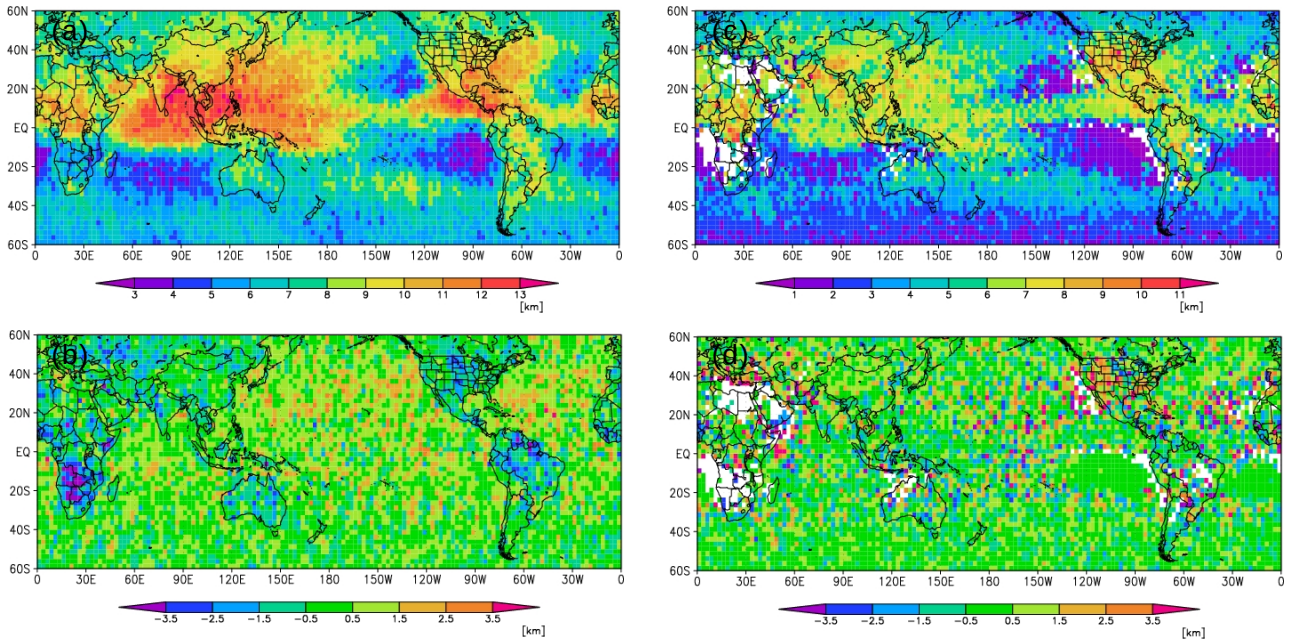

Fig. 4 Horizontal distributions of (a) Mean cloudH in the daily passes (b) difference of mean cloudH between the daily pass and nocturnal pass, and (c) (d) those for mean stormH observed by Cloudsat CPR in 2007-2009 JJA.

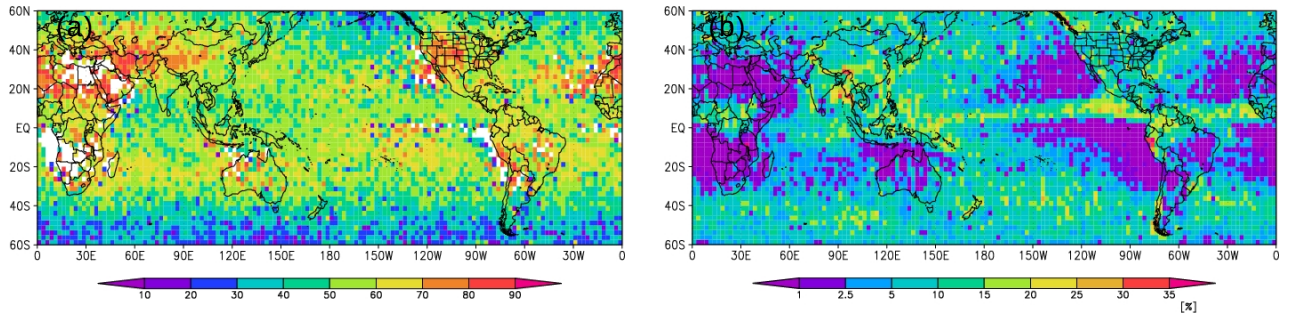

Fig. 5 Horizontal distributions of (a) median of stormH / cloudH and (b) occurrence frequency in stormH / cloudH in the daily pass observed by Cloudsat CPR in 2007-2009 JJA.

Frequency of occurrence with stormH to cloudH is shown in Fig. 4. The high frequency regions where cloud system is likely to cause precipitation occur over the Bay of Bengal and the west coast of Mexico. Over the mid-latitude region, large differences of the frequency are not found.

As convective system develops, storm height generally increases. A ratio of stormH to cloudH would be one of the indices of convective activity. Figure 4 illustrates median of all pixels with stormH / cloudH. StormH reaches above 80% of cloudH in the Sahara, Middle-east, the Tibetan Plateau, and Rocky Mountains. Over ocean, tropic region becomes higher ratio than in mid-latitude. Regions with relatively the high ratio such as south Indian Ocean and south-east Pacific correspond to small precipitation amount.

3.3 Cloud type classification from Cloudsat CPR

In order to identify further cloud / precipitation characteristics, a classification method based on the V-method of TRMM PR2A23 algorithm (Awaka 2007) was applied to the Cloudsat CPR data except for some modifications (Table 1). For the freezing height estimation vertical distributions of temperature and geopotential height from the Japanese 25-year Reanalysis (JRA-25) and JMA Climate Data Assimilation System (JCDAS) data instead of monthly mean surface temperature and constant lapse rate.

Figure 6 shows vertical distributions of radar echoes with freezH, BBH, and cloud type observed by Cloudsat CPR and those observed by TRMM PR at a case of overpass. BBH exists under 250-500m from freezH with small variations. From the vertical distributions of radar echoes BBH is reasonably detected. Compared to the rain type from TRMM PR, further cloud type characteristics are detected due to finer resolution.

In the cloud type classification by infrared sensors, it is

Table 1 Parameters from Cloudsat CPR developed in this study and modifications from PR2A23 standard product.

TRMM PR	Cloudsat CPR	Modification
rainFlag	cloudFlag	Cloud certain / possible was idenitfied from CPR_Cloud_mask
rainType	cloudType	V-method was only applied to cloudType. Convective cloud was identified from Zmax > 15 dBZ
freezH	freezH	JRA25 data instead of monthly mean surface temperature
HBB	HBB	freezH1km, Zmax > 10 dBZ
stormH	cloudH	The highest altitude of CPR_Cloud_mask

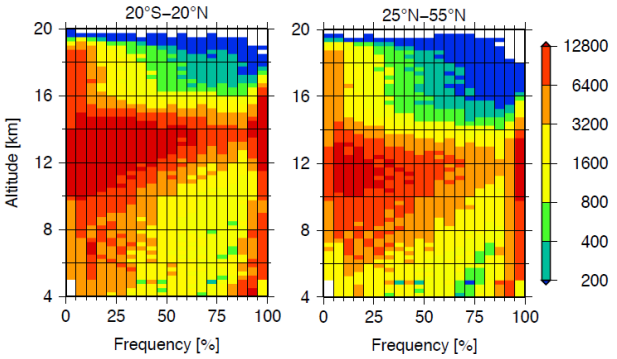

Fig. 3 Contoured appearances of altitude diagram of fulfillment ratio from cloudH observed by Cloudsat CPR in 2008 over ocean in 20ºS–20ºN (left) and 25º–55ºN (right).

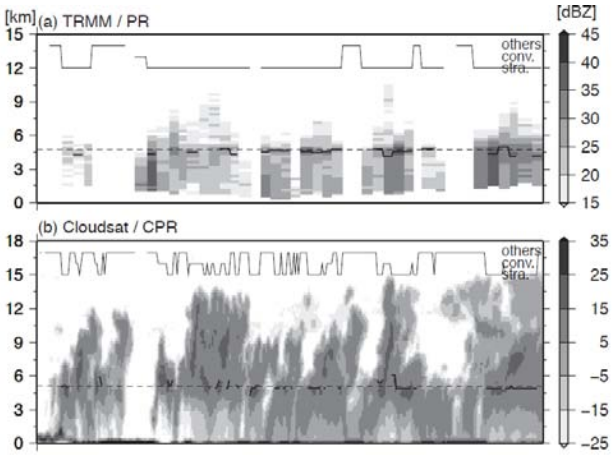

Fig. 6 Vertical distributions of radar reflectivity factor in (a) TRMM PR and (b) Cloudsat CPR (gray image), freezH (dotted lines), bright band height (bold solid lines), and rain (cloud) type (solid line in the upper part of each panel) over 16° N and 96° E at 19:25UTC overpass in 1 September, 2007.

hard to distinguish between cirrus and cumulus cloud due to similar low brightness temperature from high cloudH. On the contrary, since cloud radar can detect vertical distributions of cloud echoes, their classification would be easier. Figure 5 shows relationship between cloudH and fulfillment ratio of radar echo from the surface. Over the tropical ocean (Fig. 5a), large amount of pixels concentrates less than 30% and more than 90% of fulfillment ratio regardless of the cloudH. 10-14 km of cloudH, corresponding to the tropopause, fulfillment ratio has large variations. These distributions are similar to that over the mid-latitude oceans except for lower cloudH shifts.

4. Summaries

This study investigated cloudH and stormH characteristics from Cloudsat CPR. Compared to the TRMM PR and VIRS observations, more accurate relationship are obtained particularly in cloudH owing to 2-demensional (vertical) observation. Moreover, drop size distributions, attenuation from precipitation and cloud will be clarified by proceeding to the comparison.

Acknowledgements

This symposium is sponsored by the Ministry of Education, Science, Sports and Culture, Japan (MEXT), and National University Corporation Chiba University.

References

Awaka, J., T. Iguchi, and K. Okamoto (2007): Rain type classification algorithm. V. Levizzani, P. Bauer, and F. J. Turk (ed.), Measuring Precipitation from Space EURAINSAT and the Future, Advances in Global Change Research, 28, Springer, 213-224.

Inoue, T. (1987): A cloud type classification with NOAA 7 split-window measurements. J. Geophy. Res. 92, D4, 3991-4000.

Onogi, K. and co-authors (2007): The JRA-25 Reanalysis. J. Meteor. Soc. Japan, 85, 369-432.

Yamamoto, M. K., F. A. Furuzawa, A. Higuchi, and K. Nakamura (2008): Comparison of diurnal variations in precipitation systems observed by TRMM PR, TMI, and VIRS. J. Climate, 21, 4011-4028.

The 16th CEReS International Symposium on Climate Change
21-23 October 2010, Nago, Okinawa, Japan

SKYNET Activities in Korea

B.J. Sohn
Seoul National University

1

SKYNET ARF (Data Flow)

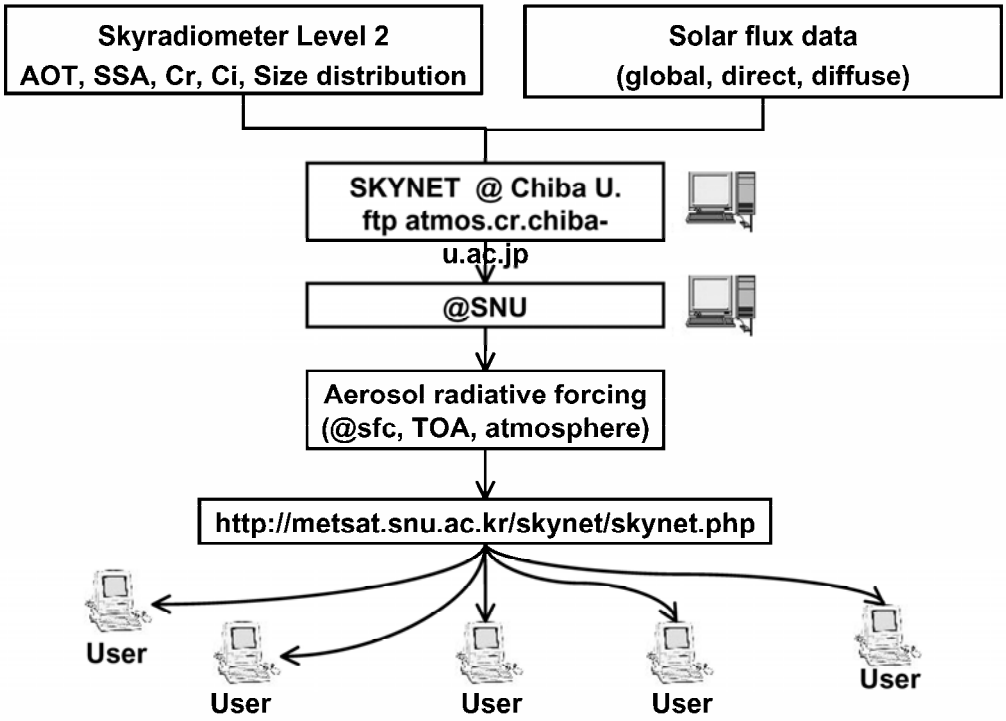

2

SKYNET ARF

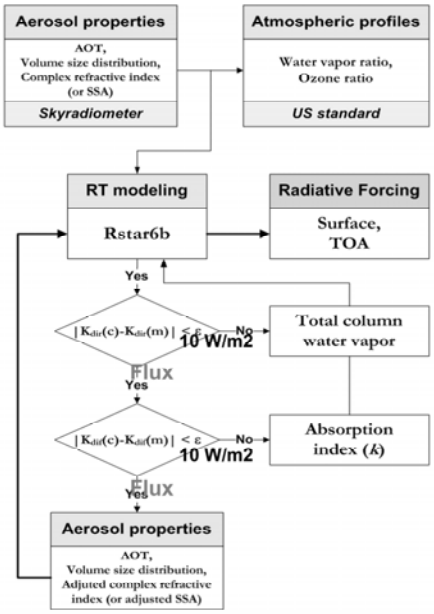

Kim, Sohn, Nakajima,Takamura (2005, JGR)

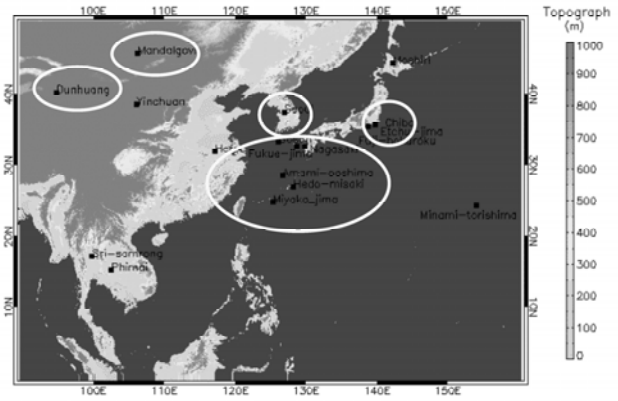

DNH(Dunhuang) : 99.09~07.01
MDG(Mandalgovi) : 98.08~98.10, 01.03~07.12
SNU(Seoul): 08.03~10.03
CHI(Chiba) : 05.09~10.03
FKE(Fukue-jima) :06.03~10.03
CHD(Hedo-misaki): 05.07~10.03
MYK(Miyako-jima): 05.02~10.03

Web display (ARF)

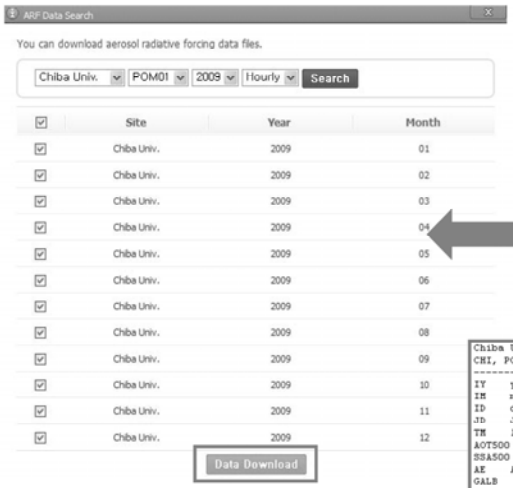

Zip file

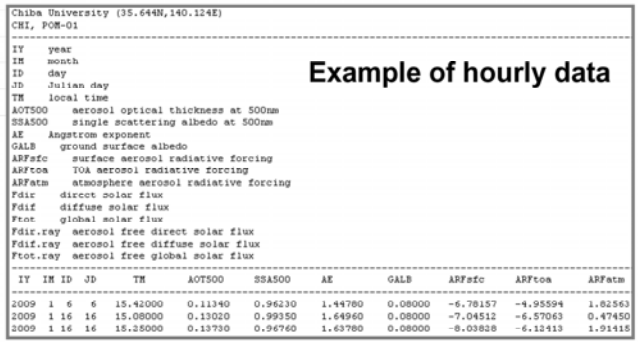

Example of hourly data

http://metsat.snu.ac.kr/skynet/skynet.php

ARF at the surface

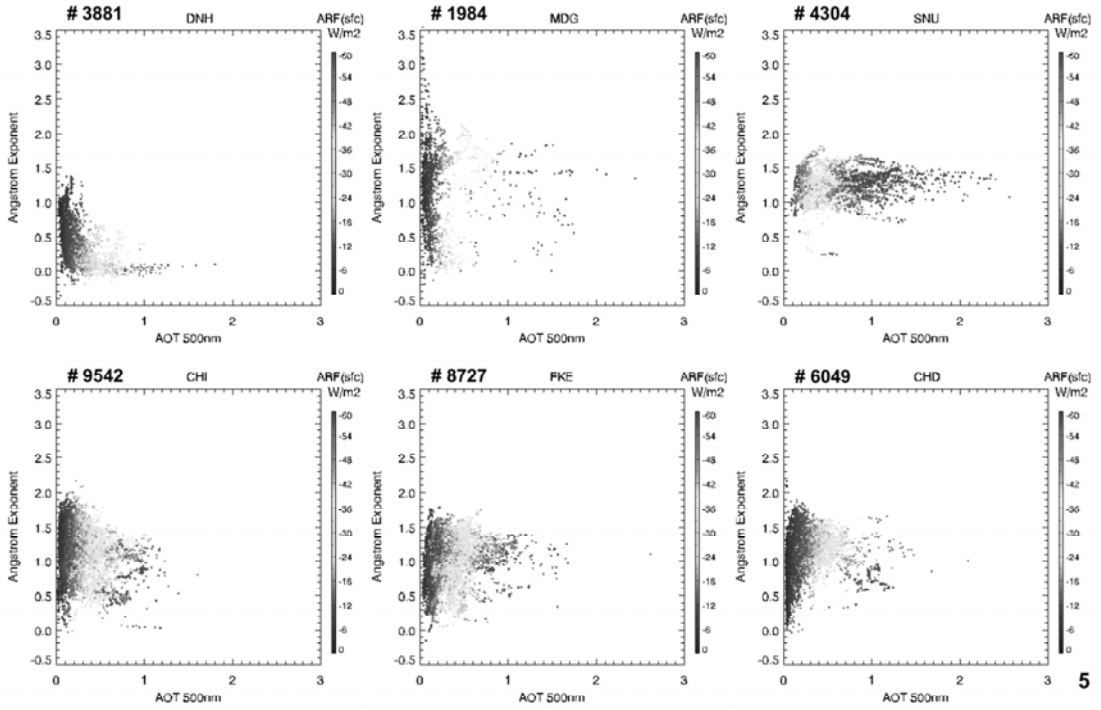

5

ARF at the atmosphere

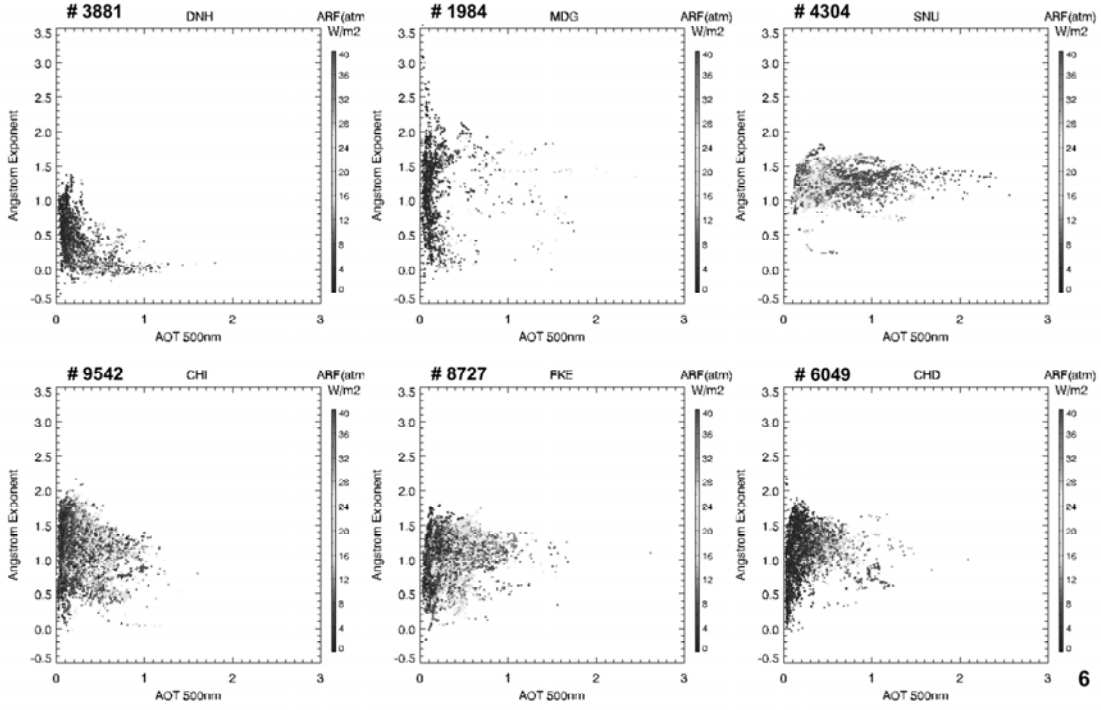

6

ARF at the TOA

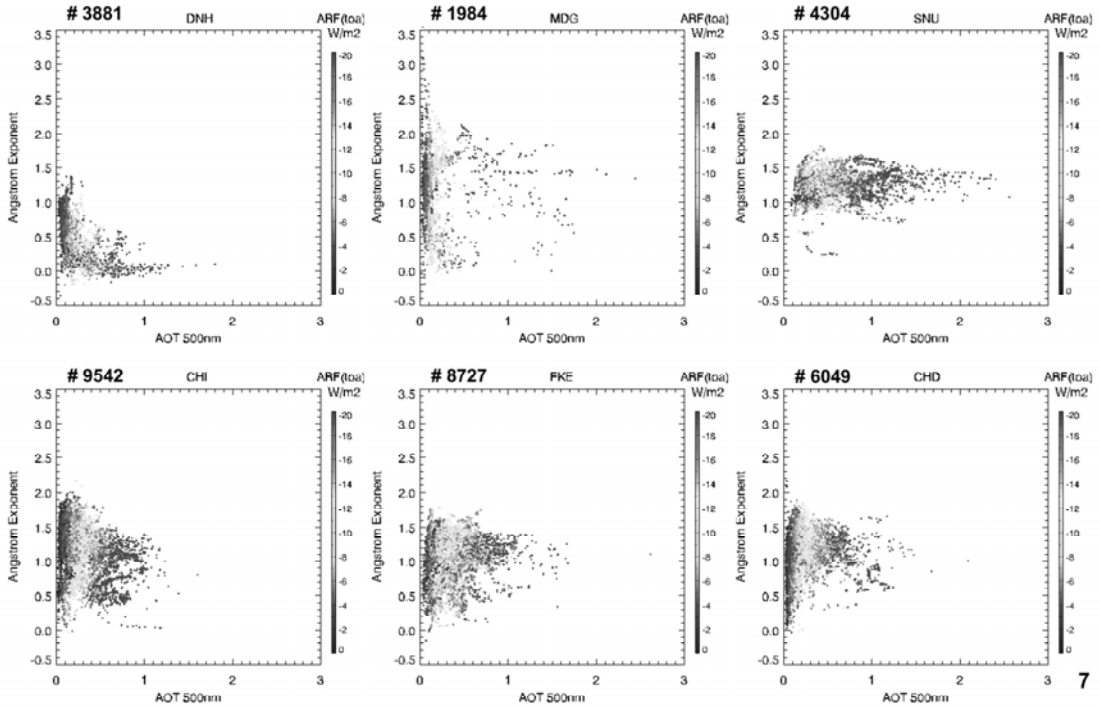

7

Clear, Dust, and Haze ARF (SNU)

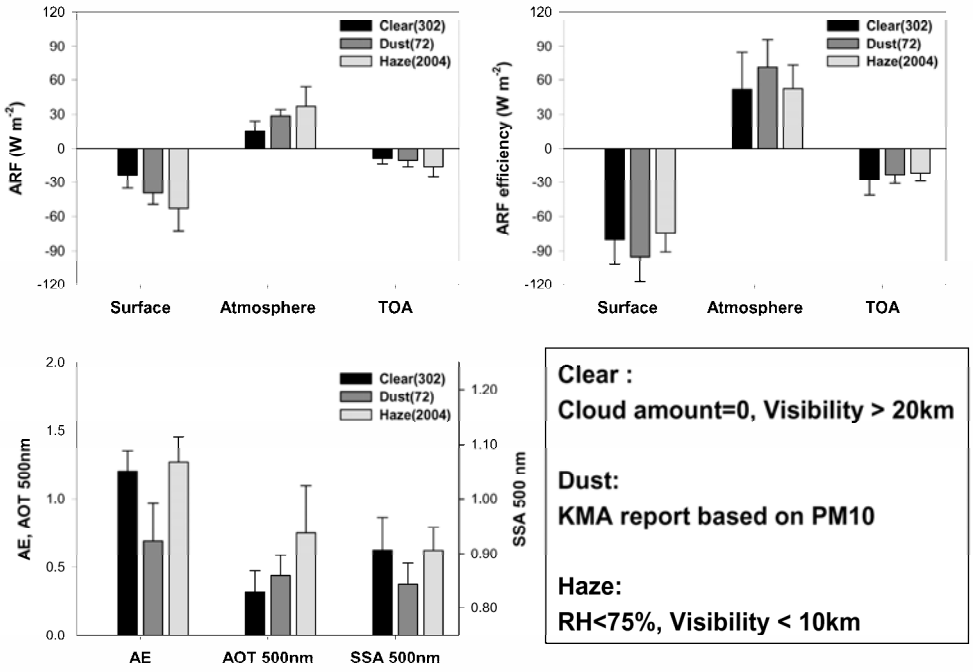

Clear :
Cloud amount=0, Visibility > 20km

Dust:
KMA report based on PM10

Haze:
RH<75%, Visibility < 10km

8

Korea Skyradiometer Network (KSNET)

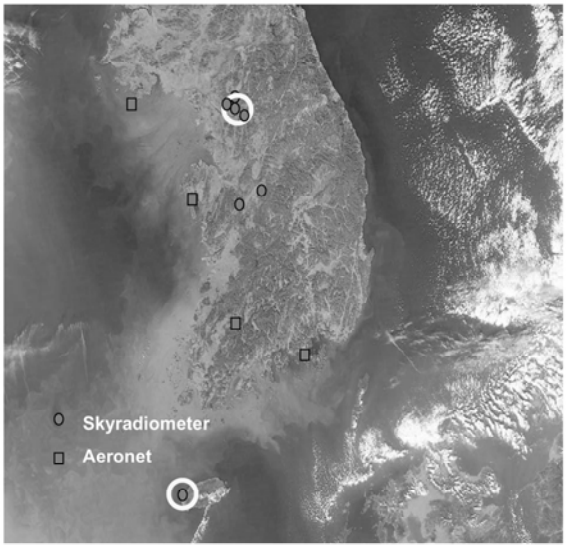

- Seoul and surroundings
  SNU (B.J. Sohn)
  Yonsei Univ(Jhoon Kim)
  HUFS (Y.S. Kim)
- Daejoen: Energy R. Institute
- Kongju Univ. (M.S. Seo)
- Gosan/SNU (B.J. Sohn)

KNMRI **Skyradiometer**

- Solar/IR flux measurements
- Pyranometer CMP21 (0.31 ~ 2.8 μm)
- Pyrheliometer CH1 (0.2 ~ 4.0 μm)
- Pyrgeometer CGR4 (4.5 ~ 42 μm)
- Suntracker ASTX-2
- Flux instruments are mounted with a sh ading ball system

- Direct plus sky radiation measurements
- POM-01: 315, 400, 500, 675, 870, 940, 1020 nm
- Direct (1 min) Diffuse (10 min interval)
- Collocated with an NIES Lidar

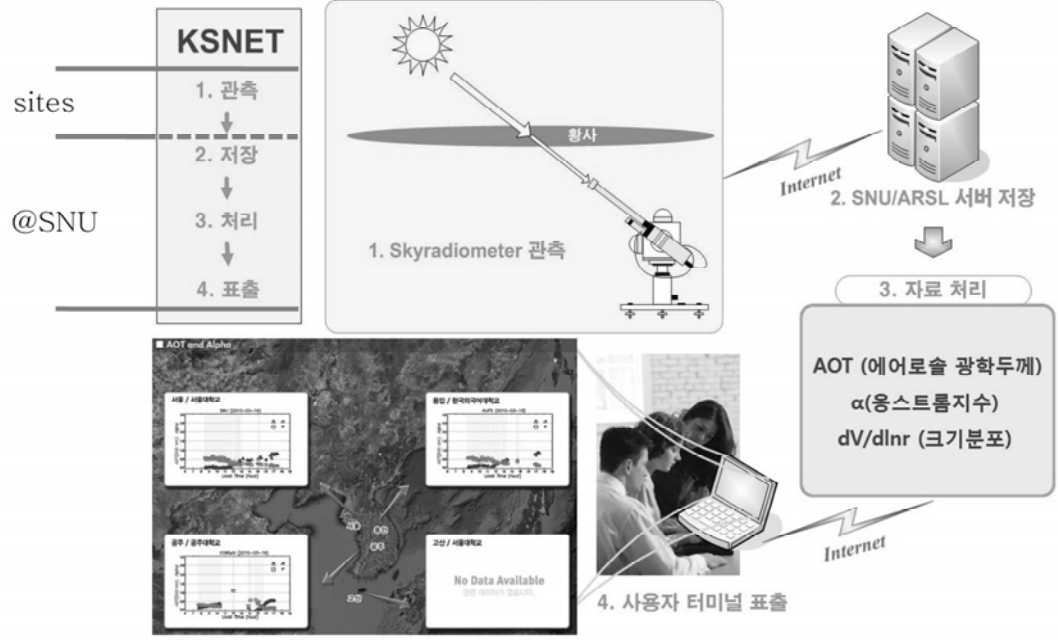

11

Real time dust monitoring

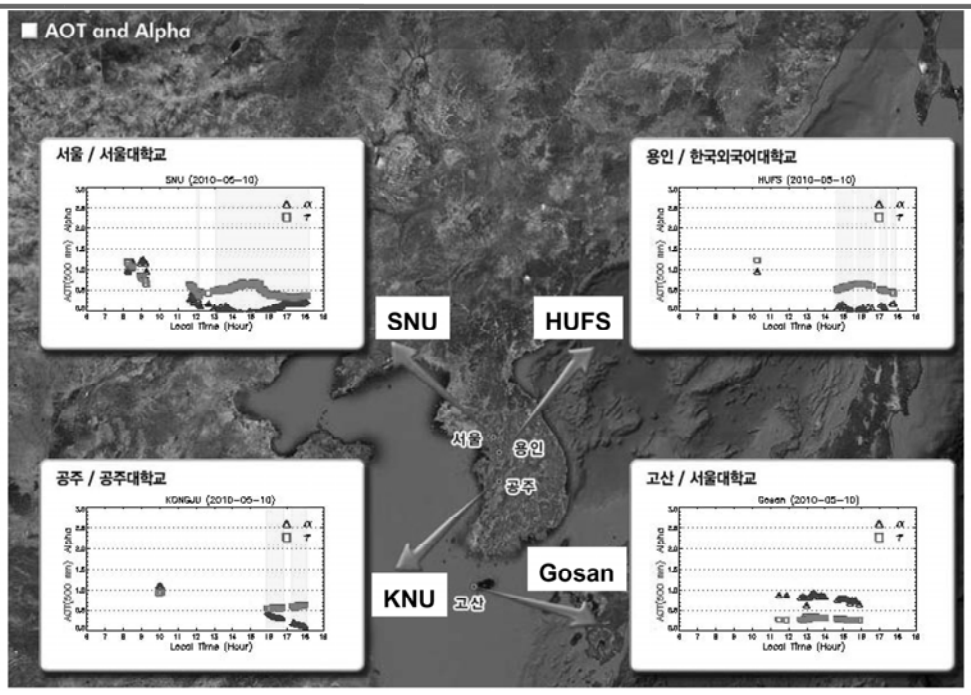

http://metsat.snu.ac.kr/ksnet/data.php

12

Real time dust monitoring

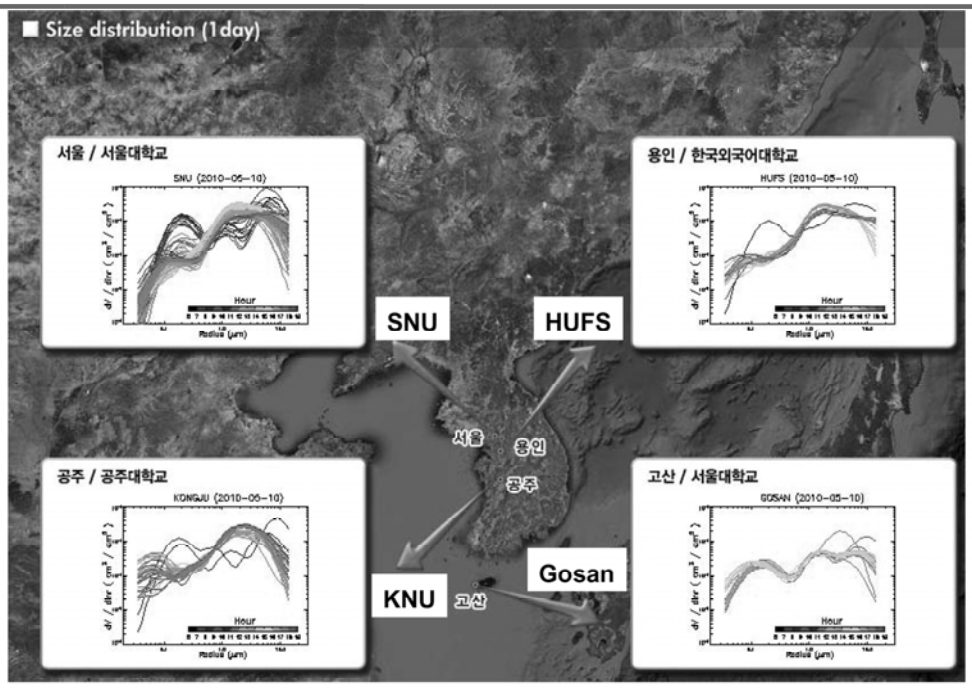

http://metsat.snu.ac.kr/ksnet/data.php

13

Two-day backward trajectories for haze events (SNU)

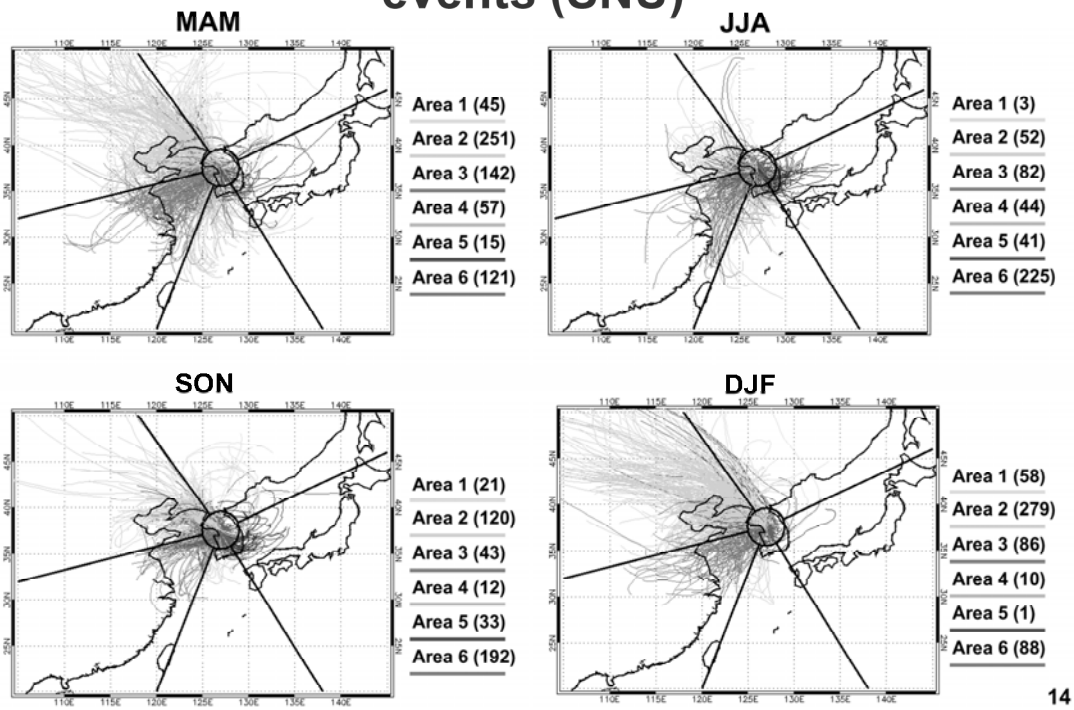

14

Radiative forcing for haze cases (SNU)

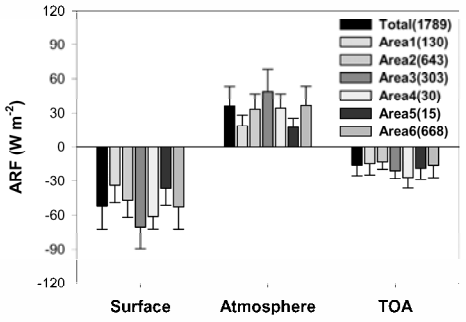

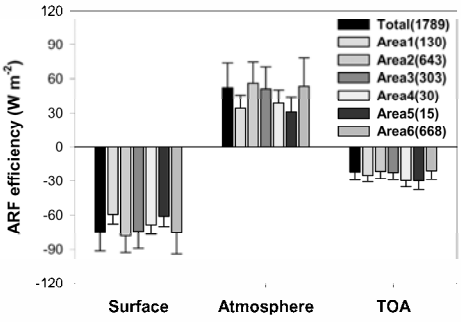

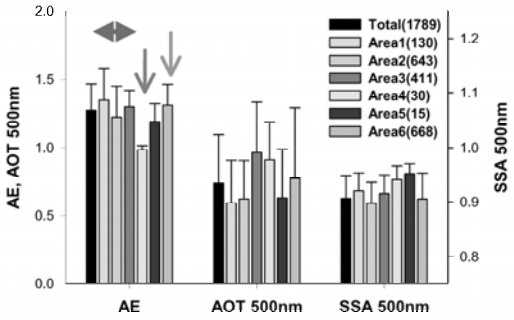

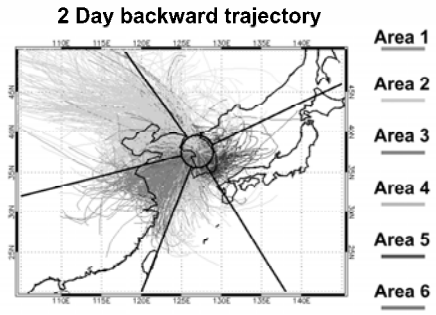

15

Optical properties for haze cases from MODIS

MODIS Data Analysis

ASMR=Aerosol Small Mode Ratio

Haze

Seoul	
Mean AOT	Mean ASMR
0.861	0.590

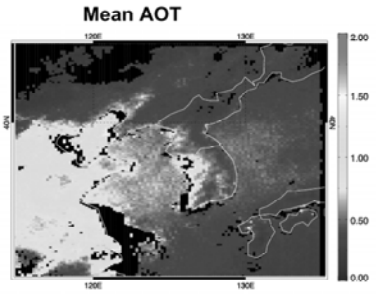

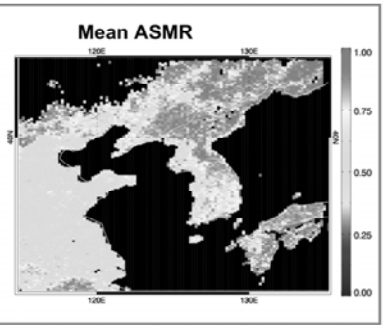

Dust

Seoul	
Mean AOT	Mean ASMR
0.897	0.190

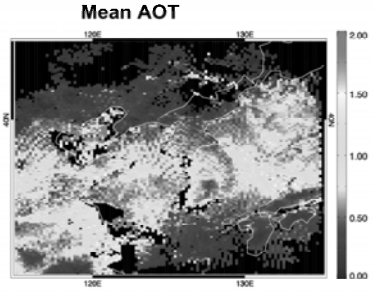

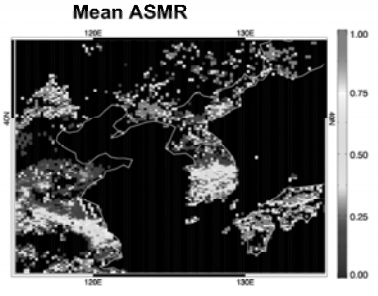

16

AOT distributions for haze cases (MODIS)

Region 2

-2day -1 Day Haze Day

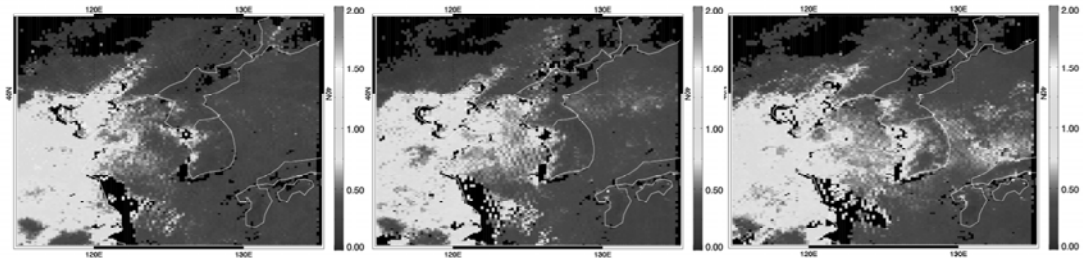

Region 3

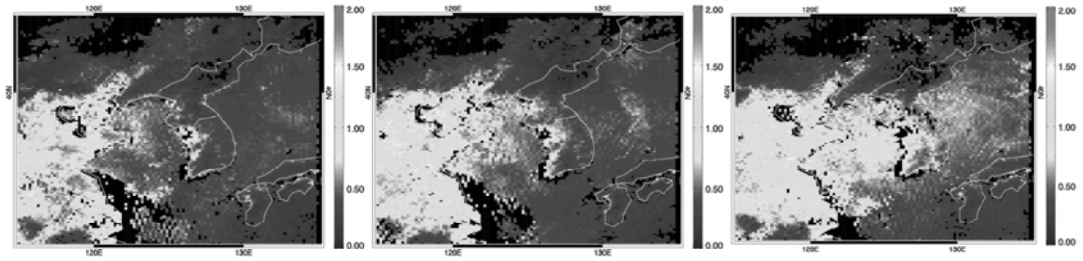

17

Mean vertical distributions (CALIPSO)

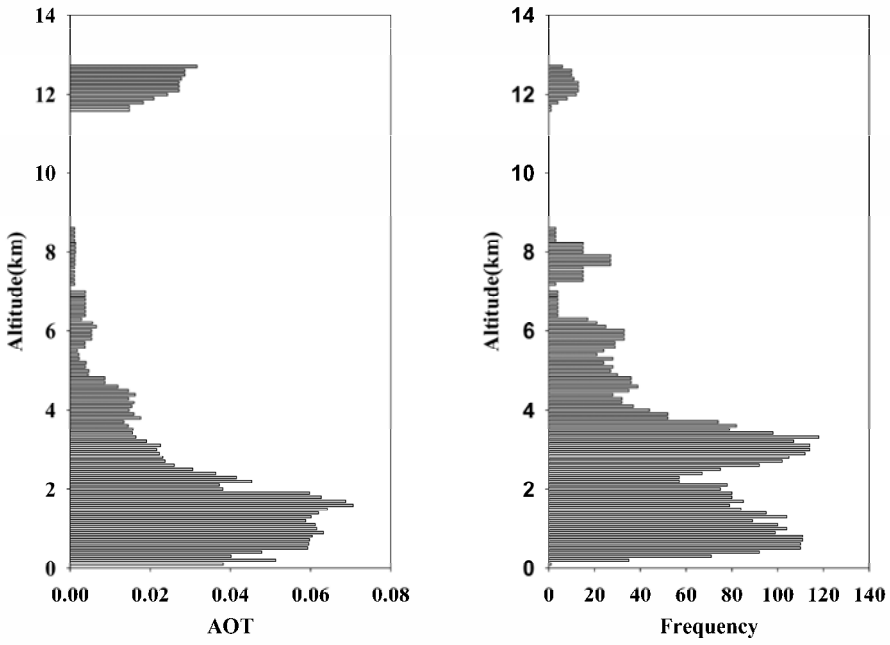

18

Thank you!


The SKYNET observation in Mandalgobi semiarid region

Jadamba Batbayar[1], Nas-Urt Tugjsuren[2]

[1]Mongolian University of Science and Technology, E-mail: tchbayar@yahoo.com

[2]Mongolian University of Science and Technology, P.O.B-157, Ulaanbaatar-46, Mongolia, E-mail: tugjsurn@must.edu.mn

Abstract

As for today, there are a number of uncertainties of atmospheric aerosols physical and optical properties due to insufficient observation network over Mongolia. However, one of the observation sites of the ground-based Skyradiometer Network (SKYNET) for Eastern-Asia has been operating since 1997 in Mandalgobi province of Mongolia. This study focused on more detailed analyses aerosol characteristics (Optical thickness, Angstrom exponent, Single scattering albedo etc.) using data sets collected at Mandalgovi sites (45.711N, 106.265E) of the Skyradiometer Network. For this purpose, Skyradiometer observation data are processed and analyzed. In addition, some preliminary results of aerosol properties analyses of the skyradiometer observation in Mongolia are presented.

1. Introduction

The atmospheric radiation and related atmospheric parameters are of fundamental importance to climate change studies. Ground based network effort promotes a large number of fundamental researches on the atmospheric parameters in any given region. SKYNET is an observation network to understand aerosol-cloud-radiation interaction in the atmosphere. SKYNET has maintained Sky radiometer observation site since 1997 at Mandalgobi, Mongolia, in collaboration with the Chiba University. This site has been instrumented mainly a sky radiometer and radiation instruments for continuous measurements of atmospheric parameters such as aerosol, cloud and radiation. The SKYNET project aims at a better understanding of long-term variability in the radiation budget and atmospheric parameters over the eastern Asia and its attributes based on the analysis of ground-network data. As for this objective, both regional and local analyses are needed to investigate the aerosol effects on climate change. SKYNET data at Mandalgobi site provide us with valuable information of earths and atmospheric parameters. The data are also important for extracting precise knowledge on the Earth atmosphere, as well as on physical processes of aerosol-cloud-radiation interactions.

Accurate information of aerosol optical properties defined by analyses using data collected by the sky radiometer of SKYNET network has been involved research activities in the semiarid region of Mongolia. These efforts has allowed an opportunity to obtaining comprehensive information of aerosol optical properties that will helpful to recognize the aerosol effects on regional climate change and future climate scenarios.

2. Data and study site description

The data used in the present study are from the Skyradiometer observations at Mandalgobi (45.711N and 106.265E) for spring, 2007. The data observed at Mandalgobi site are compiled and archived in the SKYNET server in Chiba University. The data provided from SKYNET server of Chiba University have been treated with data quality control procedure. We used Level 2.0 data including retrieved parameters such as Aerosol optical thickness (τ), Angstrom Exponent (α) and Single scattering albedo (ω) at wavelengths of 500nm.from SKYNET archive at Chiba University (http://atmos.cr.chiba-u.jp).

The observation site of SKYNET is located in the Mandalgobi. The Mandalgobi is one of the administration unite in the central part of Mongolia and is lifted at relatively high altitude 1,393m above the sea level.

3. Results and discussion

The aerosol optical properties data used in the present study were compiled from the skyradiometer data of Mandalgobi SKYNET site; the data are being archived at Chiba University. Table 1 summarizes statistical characteristics of the aerosol optical properties in Mandalgobi semiarid region which analyses have been performed in the current study. It is gave an opportunity to evaluate the background characterization aerosol optical thickness, Angstrom exponent and Single scattering albedo in semiarid region of Mongolia.

The optical thickness is with mean values of τ (500nm)

Table 1. Statistical characteristics of Aerosol optical thickness, Angstrom exponent and Single scattering albedo

Year/Months	N	τ	σ_{τ}	α	σ_{α}	ω	σ_{ω}
March, 2007	5	0.18	0.07	1.28	0.42	0.94	0.03
April, 2007	18	0.17	0.04	1.27	0.31	0.99	0.02
May, 2007	24	0.18	0.05	0.78	0.18	0.96	0.03

around 0.17-0.18 and standard deviation of 0.04 to 0.07. The Angstrom exponent ranging 0.78 to 1.28 with standard deviation 0.18- 0.42 and single scattering albedos are around 0.94-0.99 at 500nm with standard deviation 0.02-0.03.

Figure 1 illustrates the daily averaged aerosol optical thickness (a), Angstrom exponent (b), single scattering albedo (c) and standard deviations of daily τ_a (500nm) (d) for period from March to May in 2007 at Mandalgobi SKYNET site. From Figure 1a the daily average aerosol optical thickness values at 500 nm are higher in the second half of the spring season than first half. The aerosol optical thickness values are generally, between 0.05 and 0.20, however some cases has exceed this values. As for the monthly variation of the daily average aerosol thickness showed maximum value 0.53 in the first decade of May. Thus, daily mean values of τ_a (500nm) over Mandalgobi show the spring seasonal peaks in May, 2007. In the majority of cases the computed standard deviations of daily τ_a (500nm) range below less than 0.07, however, occasionally can far exceed this value (Fig.1d).

Figure 1b presents the daily averaged values of Angstrom exponent, α for Mandalgobi site. The Angstrom exponent values showed significant variability which values from 0.13 to 1.89 while AOT values are between 0.05 and 0.60 and large day to day variation in the study period.

Furthermore, the optical observation data collected in Mandalgobi SKYNET site provides by single scattering albedo data for this study. As for daily average single scattering albedo ω, at 500nm, values range from 0.87 to 0.99 (Fig.1c). However, mostly values of single scattering albedo observed in the range between 0.95 and 0.99. These values

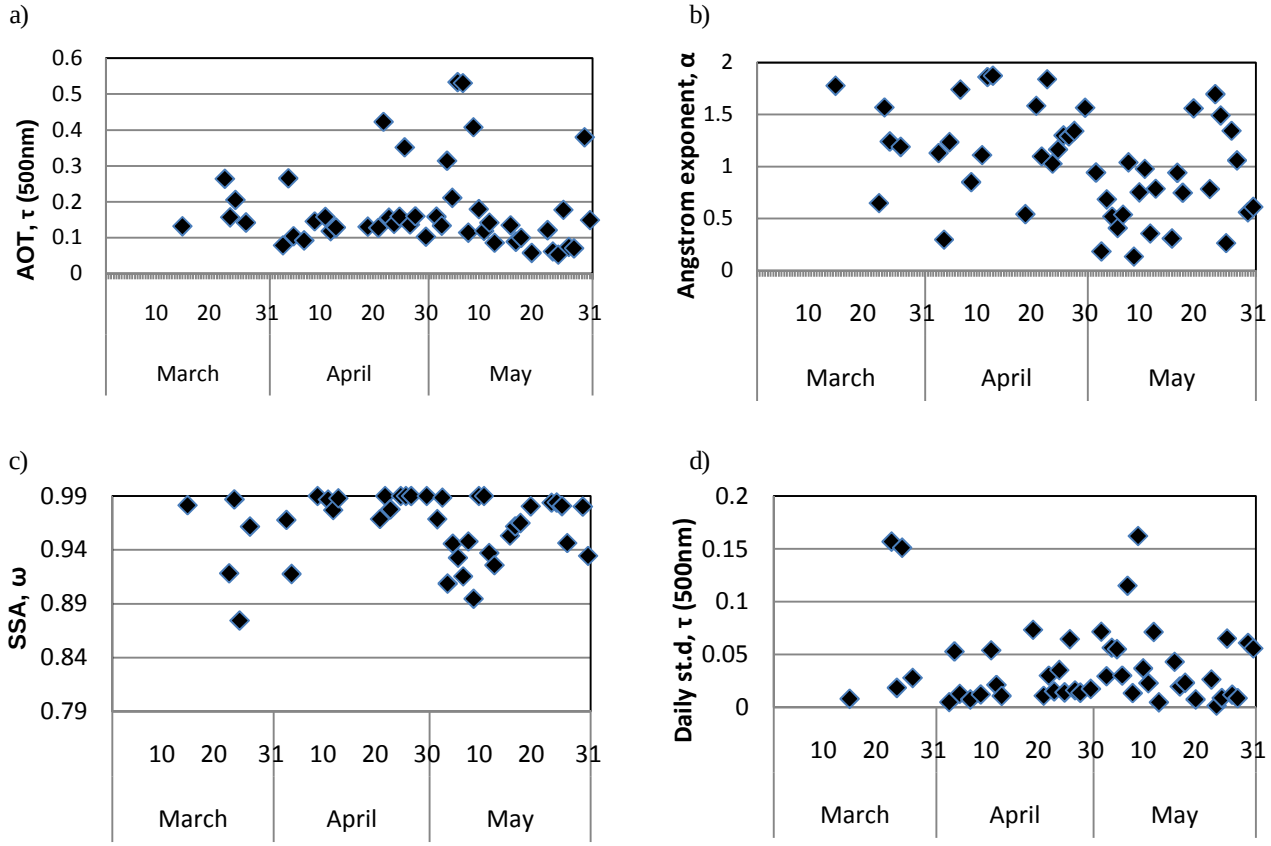

Figure 1. Daily mean values of aerosol thickness at 500nm (a), daily mean values of Angstrom exponent (b), daily mean values of single scattering albedo (c), daily standard deviations of τ (500nm) (d) for Mandalgobi site (45.711N, 106.265E)

indicate that are close to values in clean region. The single scattering albedo obtained in this region at 500nm is similar to 0.95 in Nagasaki (Nakajima et al., 1989). But some values of single scattering albedo as well as 0.87 and 0.89 obtained some times for this period that are similar to 0.89 in Dunhuang (Kim, D-H. et al., 2005).

The frequency of occurrence distributions for aerosol optical thickness τ, and Angstrom exponent α are presented in Figure 2. The frequency histograms of τ (500nm) for Mandalgobi site demonstrate the majority of values (75%) are less than 0.20 (Fig.2a) and other values (25%) are around 0.30-0.60. The most frequently occurring values of τ (500nm) are about 0.20 for this site in spring 2007.

The Angstrom exponent frequency for Mandalgobi site shows relatively broader distributions. The frequency histogram has higher Angstrom exponent's peak frequency around between 0.7 and 1.3.

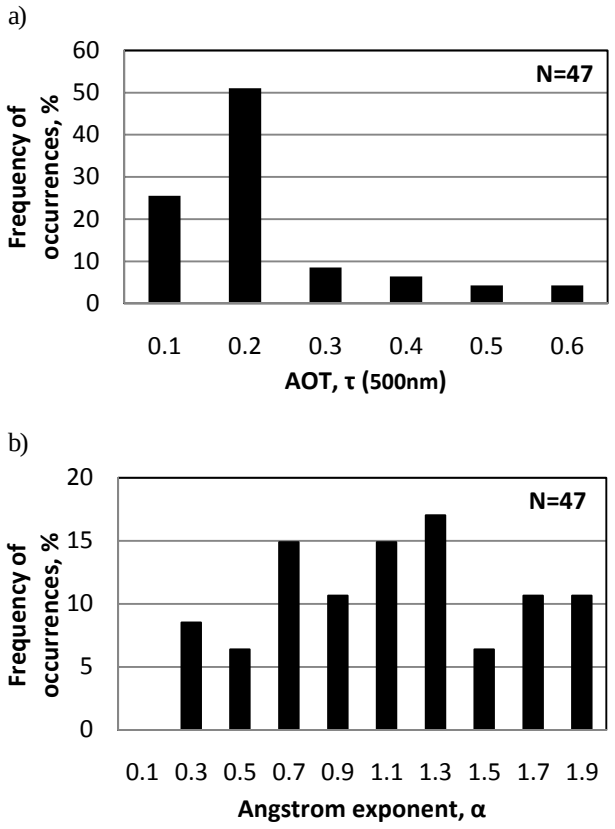

Fig. 2. Frequency of occurrences of aerosol optical thickness at 500nm (a) and Angstrom exponent, α (b) for Mandalgobi site.

The scattergrams of Angstrom exponent, α versus aerosol optical thickness, τ (500nm) for spring, 2007 are shown in Fig. 3. As shown on these scattergrams for Mandalgobi site has a wide range of Angstrom exponent values (0.13-1.89) at low aerosol optical thickness (0.05-0.20). It shows a reasonable trend of increasing values of Angstrom exponent, α as τ (500nm) decreases over study site. There is a most large variation of aerosol optical thickness values when Angstrom exponent values are smaller than about 0.8 in spring season. Therefore, Mandalgobi site shows negatively correlation between AOT and Angstrom exponent.

Lastly, the analysis of the aerosol optical properties should be continued with the more continuous observational data and to elaborate and improve the analyses for different seasons and more optical and physical parameters such as volume size distributions and refractive index.

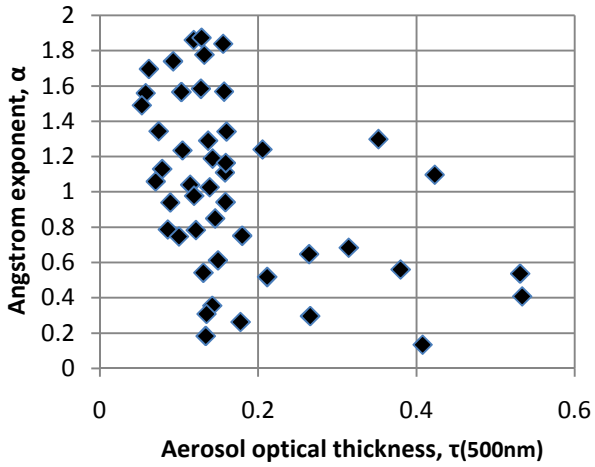

Figure 3. Scattergram of Angstrom exponent versus Aerosol optical thickness in spring, 2007 for Mandalgobi site.

4. Conclusion

The conclusions of this analysis are summarized as follows:

1. Aerosol optical properties (aerosol optical thickness, Angstrom exponent, and single scattering albedo) over semiarid region were analyzed for spring, 2007, using measurements of the Skyradiometer Network (SKYNET). The aerosol optical thickness values are generally, between 0.05 and 0.20, however some cases has reached up to 0.53 in spring. Mandalgobi site has large Angstrom exponent ranging between 0.13 and 1.89 due to fine particles. And there also exist dust particles with Angstrom exponent values around 0.13-1.00. The single scattering albedo values mostly range from 0.95 to 0.99. These values indicating close to the values in relatively clean region.
2. Future work is needed to better utilize the SKYNET observation data for more detailed aerosol optical properties analysis, such as volume size distributions and refractive index.

References

1. Dubovik, O., B. N. Holben, T. F. Eck, A. Smirnov, Y. J. Kaufman, M. D. King, D. Tanre and I. Slutsker, 2002: Variability of absorption and optical properties of key aerosol types observed in worldwide locations, J. Atmos. Sci., 59, 590-608.
2. Kim, D-H., J.Sohn, T. Nakajima, T.Takamura, Toshiko Takemura, Byoung-Cheol Choi, and Soon-Chang Yoon, 2004: Aerosol radiative forcing over East Asia determined from ground based sky radiation measurement. J. Geophys. Res., Vol. 109
3. Nakajima, T., M. Tanaka, M. Shiobara, K. Arao, and Y.Nakanishi, 1989: Aerosol optical characteristics in the yellow sand events observed in May, 1982 at Nagasaki-part II. Models. J. Meteor.Soc. Japan, 67, 279-291
4. Takamura, T., Nakajima, T., Okada, I., Uchiyama, A., Sugimoto, N., Shi, G.Y., Zhou, J., 2002: Aerosol-cloud-radiation study using the SKYNET data. The first ADEC Workshop, Tokyo, Japan; http://www.aeoliandust.com.
5. Xuehua Fan, Hongbin Chen, Philippe Goloub, Xiango Xia, Wengxing Zhang and Bernadette Chatenet., 2006: Analysis of column-integrated aerosol optical thickness in Beijing from AERONET observations, China Particuology, Vol. 4, No. 6, 330-335.

Characterics of atmospheric aerosols at the Observatory for Atmospheric Research at Phimai, Thailand, a station of SKYNET

Boossarasiri Thana[1], Thawatchai Sudjai[1], Jinchula Chotpitayasunon[1], Haruo Tsuruta[2], Tamio Takamura[3], Teruyuki Nakajima[2]

[1] *Department of Geology, Chulalongkorn University, Phayathai road, Bangkok 10330, THAILAND: boossara@geo.sc.chula.ac.th, thawatchai@geo.sc.chula.ac.th, share7@hotmail.com*

[2]*: Center for Climate System Research, The University of Tokyo, 5-1-5 Kashiwanoha, Kashiwa, Chiba, JAPAN*: *haru2004@ccsr.u-tokyo.ac.jp*

[3]*Center for Environmental Remote Sensing (CEReS), Chiba University, 1-33 Yayoi-cho, Inage-ku, Chiba 263-8522, JAPAN, takamura@faculty.chiba-u.jp*

Abstract

Aerosols play an important role in the global climate, the radiative forcing of the climate, and the Earth's radiative balance. The aerosols were measured at the Observatory of Atmospheric Research, in Phimai, Thailand where is a member of SKYNET, during 2006-2008. The amount aerosols were much higher in the dry seasons than in the wet seasons due to monsoon. The aerosols were collected during 2007-2008 and the records of fine particles found that ammonium sulfate, and elementary and organic carbons were major components especially in dry season. Aerosol optical depth by sky radiometer was about 0.90 in wet seasons, and much higher than in the dry seasons. In dry season were many fires activity due to the biomass burning from agricultural harvest almost all over Thailand. These results clearly indicate that the aerosols emitted from biomass burning could affect on atmospheric.

Keywords **:** Aerosol, aerosol optical depths, single scattering albedo, biomass burning, chemical composition

1. Introduction

Aerosols influence both direct and indirect the radiation balance. Direct scattering and absorbing interaction between atmospheric aerosols and incoming solar radiation may influence the radiative forcing. The aerosol scattering and absorption depend on their chemical physical properties. The important of aerosol types such as black carbon from agriculture or human activities are key of climate changing. Chemical and optical properties of atmospheric aerosols in a regional scale are expected to be much differences because there are many different sources of aerosols in natural and anthropogenic area. The purpose of this study focus on the results from the aerosol measurements at Phimai (15.18^{o}N ,102.56^{o}E), Thailand, in Southeast Asia where affected by the aerosols emitted by biomass burning of crop residues in regional scale.

2. Methods

Atmospheric aerosols were observed at the Observatory for Atmospheric Research in Phimai which is SKYNET station in Southeast Asia. This station is located in northeastern Thailand surrounding with agricultural activities. The location is located on Korat platau where the main component of rock is called rock salt. The optical properties were measured by Skyradiometer (POM-02). The instrument was manufactured by PREDE. The optical properties data were screened cloud-affected analysis by Khatri and Takamura (2009). Some uncertainties will be introduced. Columnar aerosol optical depths (AODs) were estimated and to determine the Ångström exponent, a basic measure related to the aerosol size distribution will be investigated. In general, the Ångström exponent ranges from 0.0 to 2.0, with smaller Ångström exponents corresponding to larger aerosol particle sizes [Dubovik et al., 2002; Kim et al., 2004]. During June 2006 through August 2008, the chemical properties were measured. The samples were collected twice a day within three days continuously every two weeks by using multi-nozzle cascade impact (MCI) samplers on the filter of 47 mm in diameter (d). The sizes of aerosols were collected as d < 1.0μm, 1.0μm < d < 2.5 μm, 2.5μm < d < 10 μm, and 10 μm < d in respectively. In this paper will be focus only on $PM_{2.5}$. Chemical analysis

was made for OC and EC by optical thermal OC/EC analyzer.

3. Results and Discussion

To reduce uncertainties in the quantitative assessment of aerosol effects on regional climate and environmental changes, extensive measurements of aerosol optical properties were made with skyradiometer at Phimai observatory for atmospheric research at Phimai were used during 2006-2009.

The variations of atmospheric aerosol is large difference in concentration. The daily average of aerosol optical depth (AOD) were between 0.2-0.7 in winter (dry season) and the AOD increasing at the end of dry season in summer cause of wind direction changed. The AOD were higher than 0.5 up to 1.4 in summer. Meanwhile the AOD is lower than 0.5 during rainy season of 2006, but the value is higher and increase nearly to 1.0 in 2007 and 2008. Figure 1 shows the time series of daily mean AOD at 500 nm . At Phimai, a range of AOD, implying different types of aerosols. There were an increasing in small aerosol particles from winter to summer due to regional biomass burning. In the summer seasons, large sea salt aerosol particles seems to be dominated. This suggests that more than one type of aerosol are mixed in the climatic effects.

The increasing AOD in summer may cause of biomass burning activities. The Ångström exponent during wet season was clear that the value is larger than 1.3. On the other hand during dry period, the value of Ångström exponents were variety from near zero up to 2.0. The Ångström exponent is often used as a qualitative indicator of aerosol particle size (Angstorm, 1929), with values greater than 2 indicating small particles associated with combustion by products, and values less than 1 indicating large particles like sea salt and dust. Values of Ångström exponent ≤1 indicate size distributions dominated by coarse mode aerosols (radii ≤ 0.5 mm) that are typically associated with dust and sea salt, and values of Ångström exponent ≥ 2 indicate size distributions dominated by fine mode aerosols (radii ≥ 0.5 mm) that are usually associated with urban pollution and biomass burning [Eck et al., 1999; Westphal and Toon, 1991]. Therefore the size distribution in this area were mixed between coarse and fine particle during dry season especially in summertime as show in figure 2 which is the daily average of AOD and Ångström exponent. The graph shows that the fine parcels caused of increasing AOD.

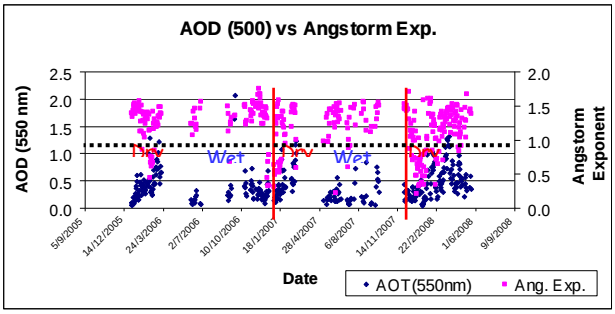

Figure 1. Time series of daily mean aerosol optical depth and Ångström exponent at 500 nm during 2006-2008.

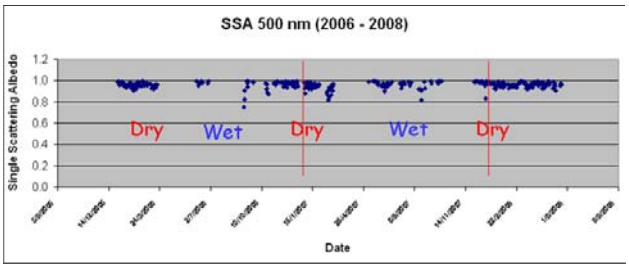

Figure 2. Time series of daily mean single scattering albedo 500 nm during 2006-2008.

The single scattering albedo (SSA: ω) is the important optical characteristic of absorbing properties of aerosol particles, which determines the ratio between scattering and absorption in the total extinction: $\omega = \sigma / (\sigma + \alpha)$ where σ is the scattering coefficient, and α is the absorption coefficient. In figure 2. shows the time series of daily mean SSA at 500 nm. are not much different. SSA is between 0.9-1.0 except some value in rainy season, the SSA decreased to 0.7-0.8. It means that most of particles scattered the radiation. For the decreasing values of SSA may cause from the difference type of aerosol came to the area. For example in 2006 the difference particles appeared during the end of wet season (figure 2). SSA is about 0.7. It seems to be that the single scattering albedo is slightly difference in wet season as the increasing humidity in the atmosphere.

By using the backward trajectory model to track the air masses arrived at Phimai as shows in figure 3. (HYSPLIT Trajectory: http://www.arl.noaa.gov/ready/hysplit4.html). The movement majority route of the aerosol came from the different ocean in both monsoon seasons. Even though the wind blew from the difference direction. Except the SSA values were sometimes decreased, it might regard to the activity that happen locality. For example as shown in figure 2, at the end of wet season in 2006, SSA decreased significantly. An alternative reason is the variation of southwest monsoon. In Phimai, there are substantially more biomass burning and adding more absorbing soot and organic aerosols to the atmospheres.

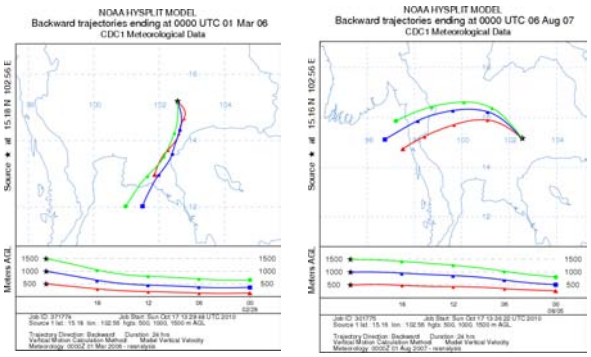

Figure 3. The backward trajectory for 2 different monsoon.

The SSA values are not clear that the aerosol type are not so difference properties between dry and wet season.

During mid 2007 to early 2008, the chemical experiment was done. The samples were collected for 72 hours continuously twice a month. The period for collecting data is 11 months by multi-nozzle cascade impact samplers with speed 20 liters per minutes. The chemical compositions of aerosols were determined by and optical thermal OC/EC analyzer for organic carbon (OC) and elementary carbon (EC). The daily mean EC and OC concentration in dry season was clearly shown that the value was much higher than in the wet season (Figure 4 and 5), the mean total concentration of OC was about 3.5 times higher than that of EC in the whole period. The mean EC in $PM_{2.5}$ were about 90 and 95 % of the mean total concentration in the wet and dry season, respectively, while the mean OC in $PM_{2.5}$ had about 65 and 80 % of the total in the wet and dry season, respectively (Tsuruta et al.; 2008). During rainy season the aerosol concentration were washed out from the atmosphere. This result is shown the increasing of $PM_{2.5}$ again after winter monsoon onset completely. The ratio of aerosol in the whole periods are the same as mention above. This result corresponds to the main activities in this area where is agriculture such as cassava. Therefore the aerosols in this area were emitted by biomass burning of crop residuals especially in dry season. Phimai is located in Korat Platau where the main rock in this area is rock salt then the aerosol samples tend to be large size from salt.

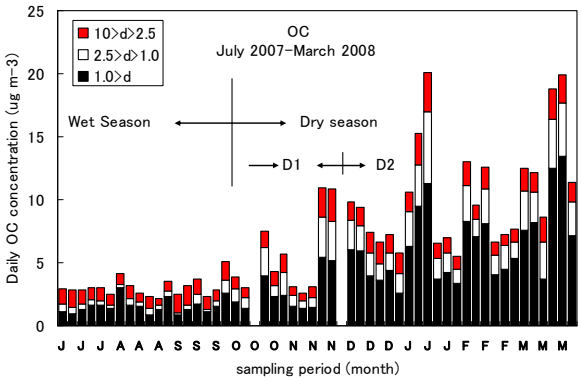

Figure 4. Daily mean OC concentrations in PM2.5 in Phimai (July 2007- March 2008)

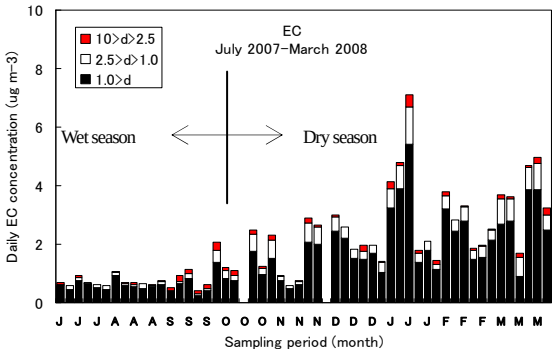

Figure 5. Daily mean EC concentrations in PM2.5 in Phimai (July 2007- March 2008)

Phimai affected by two difference direction of monsoon. In summer, the southwest monsoon from Indian ocean will dominate. Then the seasalt aerosol will be transport to the region. The opposite direction is the northeast monsoon from east Asian continent during winter. The source of wind direction will be the cause of particle types.

Conclusion

The aerosol particle in Phimai is almost the same type except at the end of southwest monsoon season. The optical properties were changed from scattering property to a more absorption. This result was confirmed by the size of aerosol which is more variety during the same period. The chemical component was shown the large concentration of organic carbon much more than elementary carbon. The size of PM2.5 in elementary carbon were high concentration in both winter and summer. The changing of monsoon affected to the type of aerosol in the region.

Acknowledgements

We would like to express our great thanks to many staffs in Department of Geology, Chulalongkorn University, Thailand for an excellent implementation of the Observatory of Atmospheric Research at Phimai and also the SKYNET project which their techniques and financial support and cloud screening data which we use in this paper.

References

1) Angstrom, A. (1929), On the atmospheric transmission of Sun radiation and on dust in the air, Geogr. Ann., 11, 156– 166.
2) Dubovik, O., B. N. Holben, T. F. Eck, A. Smirnov, Y. J. Kaufman, M. D. King, D. Tanre, and I. Slutsker (2002), Variability of absorption and optical properties of key aerosol types observed in worldwide locations, J. Atmos. Sci., 59, 590– 608..
3) Eck, T., B. N. Holben, J. Reid, O. Dubovik, A. Smirnov, N. O'Neill, I. Slutsker, and S. Kinne (1999), Wavelength dependence of the optical depth of biomass burning, urban, and desert dust aerosols, J. Geophys. Res., 104(D24), 31,333– 31,349.
4) Khatri, P. and T. TAKAMURA (2009), An Algorithm to Screen Cloud-Aﬀected Data for Sky Radiometer Data Analysis, J. Met. Soc. of Japan, Vol. 87, No. 1, pp. 189—204. DOI:10.2151/jmsj.87.189.
5) Kim, D.-H., B.-J. Sohn, T. Nakajima, T. Takamura, T. Takemura, B.-C. Choi, and S.-C. Yoon (2004), Aerosol optical properties over east Asia determined from ground-based sky radiation measurements, J. Geophys. Res., 109, D02209, doi:10.1029/2003JD003387.
6) Mattoo, S., and B. N. Holben (1994), Size distribution and scattering phase function of aerosol particles retrieved from sky brightness measurements, J. Geophys. Res., 99(D5), 10,341– 10,356.
7) Tsuruta, H., J. Chotpitayasunon, B. Thana, P. Khatri, T. Takamura, Hayasaka, T. Nakajima. (2008), Characterization of atmospheric aerosols at the Observatory for Atmospheric Research at Phimai, Thailand, a station of SKYNET. presented in CEReS International Symposium/ SKYNET Workshop, Chiba University, Nov. 13-14, 2008.
8) Westphal, D., and O. Toon (1991), Simulations of microphysical, radiative, and dynamical processes in a continental-scale forest fire smoke plume, J. Geophys. Res., 96(D12), 22,379–22,400.

An investigation of SSA retrieval using simulated SKYNET observations

Makiko Hashimoto[1] and Teruyuki Nakajima[2]

[1] *Atmosphere and Ocean Research Institute, 5-1-5 Kashiwanoha, Kashiwa, Chiba 277-8568,Japan.*

[1]*m_hashi@aori.u-tokyo.ac.jp*, [2]*teruyuki.nakajima@aori.u-tokyo.ac.jp*

Abstract

Single scattering albedo (SSA) is a key parameter to estimate aerosol direct radiative forcing and to understand earth's climate. This study focused on SSA retrieval by a software package, SKYRAD.pack, which has been developed by University of Tokyo but shown a tendency of overestimates of retrieved SSA suggested by comparison with AERONET results in Beijing. In order to investigate the origins of the errors, we did sensitivity tests for various parameters (ground albedo, calibration constant, gas absorption) associated with the algorithm program in SKYRAD.pack. The results showed that overestimate of retrieved SSA is attributed by underestimate of calibration constant and/or ground surface albedo. The consideration of gas absorption is not a possible reason of the error but an important step for SKYRAD.pack to more accurately retrieve SSA.

Keywords **:** SSA; SKYRAD.pack; algorithm

1. Introduction

Aerosol optical properties observed by SKYNET are retrieved using a software package, SKYRAD.pack, developed by the University of Tokyo. However, it has been pointed out that the value of the single scattering albedo (SSA) in Beijing site was systematically larger than that of AERONET (Che et al., 2008). A close intercomparison of the SKYNET and AERONET results indicates that SSA from SKYNET has a tendency to rapidly become unity with increase in wavelength, when SSA value is close to unity. And there is also a tendency of larger size distribution for coarse mode aerosols with radius larger than several microns. The same happened in Phimai observation site (Tsuruta, *personal communication*, 2010).

There are several candidates for the cause: Ignorance of gaseous absorption by SKYRAD.pack; the minimum observable scattering angle (3 degrees) is not small enough for retrieving the coarse mode aerosol size distribution; error in the improved Langley method (Nakajima et al., 1996); error in the solid angle measurement and so on. We, therefore, made a numerical experiment using the Rstar6b radiative transfer code to simulate observed data of PREDE skyradiometer and investigate the effects of various observational and instrumental parameters that affect the SKYNET retrievals.

2. Methods

Observation data was simulated by the radiation model assuming the gaseous constituent profiles of "US standard atmosphere" and the optical properties of "Rural aerosol type" with a solar zenith angle of 60 degree, and ground surface albedo of 0.2. The rural aerosol type includes water-soluble (70 %) and dust-like particles (30 %). We used five channels at 400, 500, 670, 870, and 1020 nm. In the analysis, we gave normal random errors of ±5%, ±10%, and ±50% to the ground surface albedo and ±1%, ±3% and ±5% to the calibration constant for the test data to be analyzed by SKYRAD.pack. We also changed the minimum observable scattering angle from 1.5 to 3 degrees. Furthermore, we made experiments with and without gas absorption in the inversion.

3. Results and Conclusions

From Figs. 1 and 2, SSA was overestimated when the calibration constant or ground surface albedo given in the analysis was lower than in reality. Particularly, a small difference in the calibration constant had a significant impact on the SSA retrieval. It was also found that the smaller minimum observable scattering angle improved the retrieval of the volume size distribution for large particles (*not shown*), but the retrieved SSA rarely changed its value. From Fig. 3, SSA was improved when gas absorption is included in the analysis, but the improvement is small and difficult to explain the large difference in the retrieved SSA values between SKYNET

and AERONET. That is, it is considered that a cause of large SSA in Beijing is underestimate of calibration constant and/or ground surface albedo. In the future study, we will investigate impacts of other candidates to retrieved SSA, especially in terms of the differences in SSA between different wavelengths.

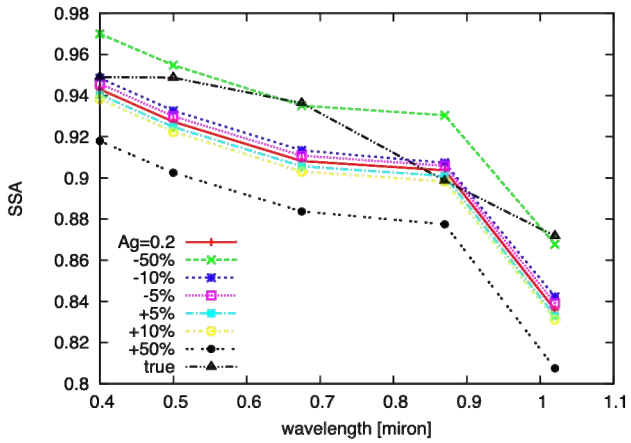

Fig. 1 SSA dependence on wavelengths ranging from 0.4 to 1.02 micron for various ground albedo (Ag) values

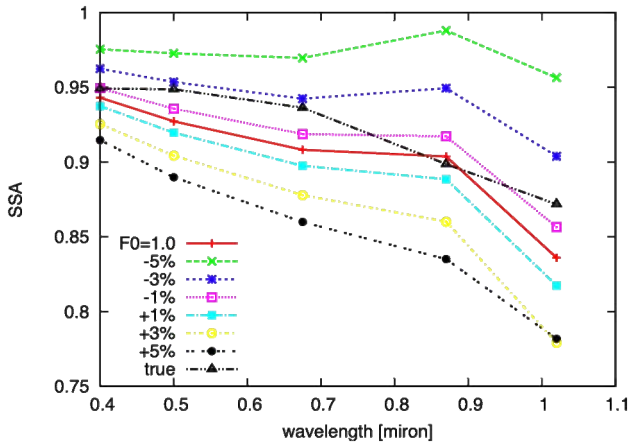

Fig. 2 Same as in Fig 1, but for various calibration constant (F0) values

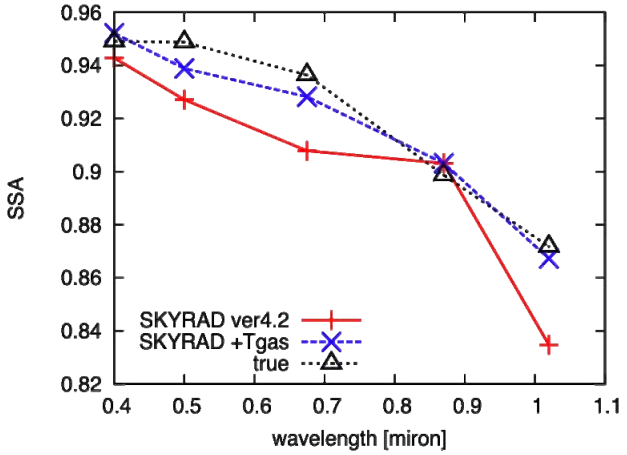

Fig. 3 Same as in Fig 1, but for gas absorption effects

Acknowledgements

We would like to thank SKYNET and SKYRAD.pack developers, especially Miho Yamano and Kathri Pradeep. We were supported by projects from JAXA/EarthCARE, MEXT/VL for Climate System Diagnostics, MOE/Global Environment Research Fund B-083, NIES/GOSAT and JST/CREST.

References

Che, H., G. Shi, A. Uchiyama, A. Yamazaki, H. Chen, P. Goloub, and X. Zhang, 2008: Intercomparison between aerosol optical properties by a PREDE skyradiometer and CIMEL sunphotometer over Beijing, China. Atmos. Chem. Phys., 8, 3199–3214.

Nakajima, T., G. Tonna, R. Rao, Y. Kaufman, and B. Holben, 1996: Use of sky brightness measurements from ground for remote sensing of particulate polydispersions. App. Opt., 35, 2672-2686.

Development of SKYNET community aerosol inlet and SSA Obtained from Surface Aerosol Data at Cape Hedo and Fukue Island Sites

Naoki Kaneyasu
National Institute of Advanced Industrial Science and Technology
16-1 Onogawa, Tsukuba 305-8569, Japan, kane.n@aist.go.jp

Abstract

A community inlet was deployed at each SKYNET supersite by 2007 for the *in-situ* monitoring of surface aerosol optical/microphysical properties Periodical calibration of Integrating Nephelometers have been carried out since 2008. Upgrading of the monitoring infrastructure enabled us to compare the measured aerosol optical data at different sites in SKYNET. As a case study, single scattering albedos of surface aerosols at Cape Hedo and Fukue Island are calculated after addressing several correction procedures.

Keywords **:** optical properties, aerosol inlet, single scattering albedo, absorption coefficient, scattering coefficient

1. Introduction

Data obtained from SKYNET *in-situ* surface aerosol monitoring instruments had been used for the calculation of aerosol optical properties. However, air inlets that introduce ambient air into aerosol monitoring instruments were different site by site in design and shape. They are not properly characterized in particular for their size separation abilities. In addition, Integrating Nephelometers in SKYNET sites have not been calibrated periodically before 2007 except that in Miyako site. Data obtained from filter-based absorption photometers such as PSAP need to be corrected for multiple scattering by filter fibers, particles retained on the filter fibers, and the "shadowing" effect of deposited particles. Previous calculations for aerosols optical parameter such as single scattering albedo (SSA) from SKYNET *in-situ* data did not consider these problems.

The author designed a common inlet system for SKYNET and has installed it in super sites (Cape Hedo, Fukue Is., Miyako Is. Hefei, and Phimai) since 2007 (Kaneyasu et al., 2009). Periodical calibration of Integrating Nephelometers has been carried out since 2008. Addressing above issues enables us to compare the data at different SKYNET sites. The design of SKYNET community aerosol inlet is briefly described here. In addition, preliminary results of SSA calculation at Cape Hedo and Fukue are compared.

2. SKYNET community aerosol inlet

SKYNET community aerosol inlet is designed in accordance with the guideline proposed by World Meteorological Organization/Global Atmosphere Watch project. The basic structure consists of a vertical pipe installed through the roof of the laboratory so that the air is brought from the inlet top (>4.5 m from ground level) to the air splitter attached at the bottom of pipe with minimal bending parts (Fig.1).

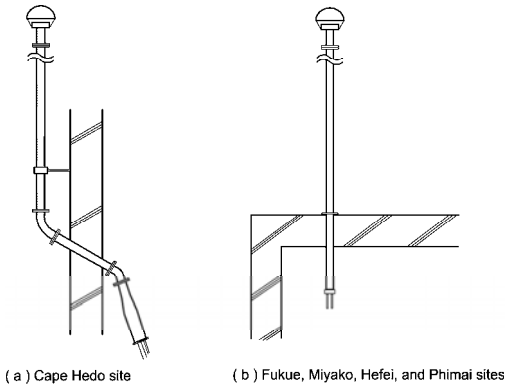

Fig.1 Basic structure of SKYNET community inlets installed at (a) Cape Hedo site, and (b) Fukue, Miyako, Hefei, and Phimai sites. *

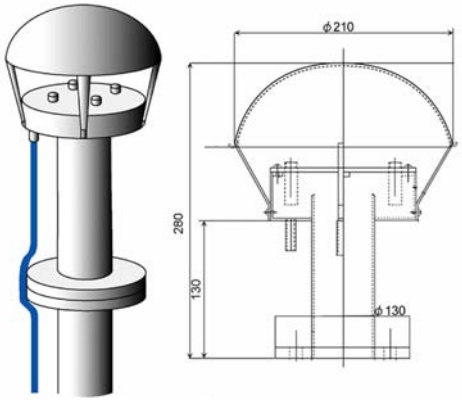

Fig. 2 Illustrative schematics of PM_{10} impactor-head of SKYNET community aerosol inlet (Left), and its cross-sectional drawing (Right). *

Aerosols are pre-separated at the inlet top with a PM_{10} impactor head newly designed for SKYNET super sites (Fig. 2). The size separation characteristic of the inlet was tested with poly-dispersed fly-ash particles in a factory. The experimentally determined 50% cut-off point was 9.4-10.3 μm in aerodynamic diameter. Air splitters that distributes air into each aerosol instruments are designed as iso-kinetic type which adjust the air speed in main pipe and in narrow tubes connected to each aerosol instruments (Fig.3). This enables to avoid unwilling size separation of particles at the splitter

Fig. 3 Iso-kinetic air splitter of SKYNET community aerosol inlet.

3. A case study: calculation of SSA at Fukue and Hedo sites.

Integrating Nephelometers physically integrate the scattered light by particles inside a cavity column. However, they cannot measure scattered light at forward extreme and backward extreme angles that leads to an error in the measurement of aerosol light scattering coefficient. This is called *truncation error*. Truncation error is well characterized for TSI 355x/356x series nephelometers (*e.g.*, Anderson et al., 1996). For the aerosol light scattering coefficient at Cape Hedo, data from a TSI nephelometer is used and corrections for the truncation error were applied according to this paper.

On the other hand, the evaluation of truncation error for Radiance M903 nephelometer is rather limited (Heintzenberg et al, 2006). The author theoretically evaluated the truncation error of Radiance nephelometer, which is often deployed in SKYNET sites. Mie scattering calculations were made with aerosol size distributions measured at Cape Hedo site with an Aerodyne Aerosol Mass Spectrometer (A. Takami, personal correspondence) and with the refractive index of sulfate ammonium. Aerosol light scattering coefficient in Fukue measured with a Radiance nephelometer is corrected for truncation error in this manner.

In Cape Hedo and Fukue, *in-situ* aerosol absorption has been continuously measured with Aethalometers (Magee AE-32). A numbers of correction schemes have been proposed to retrieve aerosol absorption coefficient from the attenuation data by Aethalometer. In this study, the correction scheme of Coen et al.(2009) was applied. Fig.4 compares the monthly average aerosol SSA (dry state) at Cape Hedo and Fukue in April 2009, April 2010, and August 2010. Regardless of the large difference in pollution concentrations between two sites, dry SSA of surface aerosols at Cape Hedo and Fukue does not differ greatly.

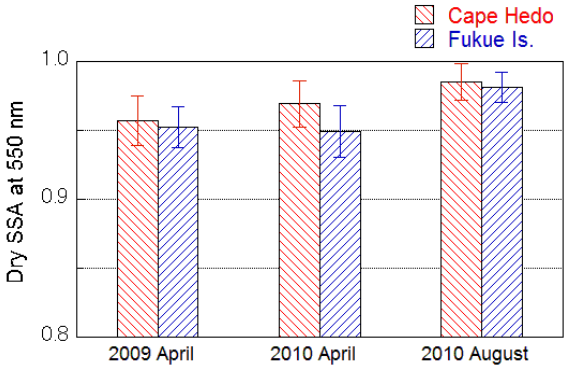

Fig. 4 Comparison of monthly average single scattering albedos at Cape Hedo and Fukue sites in April 2009, April 2010, and August 2010.

Acknowledgements

This study was conducted under GEOSS/SKYNET program funded by the Ministry of Education, Science, Sports and Culture, Japan (MEXT). Figures marked with * are reproduced from figures in Kaneyasu et al.(2009).

References

Anderson, T. L. et al., Performance characteristics of a high-sensitivity, three-wavelength total scatter/backscatter Nephelometer, *J. Atmos. Oceanic Tech.* 13, 967-986 (1996).

Ceon, M. C. et al., Minimizing light absorption measurement artifacts of the Aethalometer: evaluation of five correction algorithms, *Atmos. Meas. Tech. Discuss.*, 2, 1726-1770 (2009).

Kaneyasu, N. et al., Designing of GEOSS-SKYNET aerosol inlet and its evaluation using poly-disperse fly-ash particles, *J. Jpn. Assoc. Aerosol Sci. Tech.*, 24, 201-208, *in Japanese* (2009)

Heintzenberg, J. et al., Intercomparisons and aerosol calibration of 12 commercial integrating Nephelometers of three manufactures, *J. Atmos. Oceanic Tech.* 23, 902-914 (2006).

The influence of meterological parameters and PM_{10} concentrations on visibility of Kathmandu Valley

Shashank Pandey (1), Sanjay Nath Khanal (2) Dhiraj Giri (3), Ashish Singh (4)
Corresponding Author address: sanjay@ku.edu.np

1. *VSBK/CESEF Project, Nepal(Government of Nepal/Swiss Developement Cooperation),Kathmandu Nepal*
2. *Department of Environmental Science and Engineering, Kathmandu University, Kathmandu, Nepal*
3. *Department of Natural Science, Kathmandu University, Kathmandu, Nepal*
4. *Environment and Public Health Organization, Kathmandu, Nepal*

Abstract

Increasing experience of periods of impaired visibility is assumed to be due to increased air pollution in Kathmandu valley. It is observed that the number of clear days in Kathmandu Valley is decreasing since the past two decades. In Nepal, very few studies have focused on the status of visibility in Kathmandu Valley. This study tries to find a linkage between Visibility, Particulate matter 10 (PM_{10}) and Meteorological parameters in the Kathmandu valley.

In this study we have considered daily 24-hour average PM_{10} concentration recorded in six air monitoring site in Kathmandu Valley as the PM_{10} concentration of Kathmandu Valley. The duration of the PM_{10} data ranges from 2003 to 2005. Similarly, meteorological data were obtained from the weather monitoring station of the Department of Hydrology and Meteorology located at Tribhuvan International Airport (TIA) for the period 2003 to 2005. For better representation of the influence of PM_{10} and meteorological parameters, only those days were considered with data from 6 air monitoring sites, and meteorological data from the weather station.

The trend in the mean visibility is increasing as we go from 2003 to 2005 i.e. 7.5467 km to 8.1267 km respectively. The mean visibility is highest in monsoon 8.6131 km, which decreases with post monsoon 7.8781 km, pre monsoon 7.0356 km and winter 6.5363 km respectively in a descending order. The Chi-square test of independence at 0.05 level of significance, reveled that mean visibility in the Kathmandu Valley depends on the different seasons of Kathmandu Valley. In the case, of variation of visibility, with the time of the day, it was found to increase gradually with the commencement of day peaking at 2:45 P.M and declining with the onset of night. Irrespective of season, it is observed that as the day progresses the temperature increases, the wind becomes turbulent, humidity decreases and foggy weather disappears. This might be the reason for highest visibility during the noon time. The analysis of variance of mean visibility with different time of the day shows that the mean visibility was found to differ significantly with the different time of the day. Meteorological parameters like temperature (minimum and maximum), rainfall, wind speed, pressure, total cloud and humidity were also found to affect mean visibility.

Keywords **:** PM, Visibility, Meteorology, Kathmandu.

Introduction

Besides, the unequivocal admission of health effects of increasing air pollution levels in Kathmandu Valley, increasing experience of periods of impaired visibility is also assumed to be due to increased air pollution. It is observed that the number of clear days in Kathmandu Valley is decreasing since the past two decades. Aesthetically, for the resident of the Valley, such impaired visibility and appearance of haze, is perhaps the most obvious adverse effect of air pollution.

Visibility impairment is perhaps one of the most well understood effects of air pollution, occurring when particles and gases in the atmosphere scatter and absorb light. Generally fine particles from anthropogenic sources are commonly responsible for visibility impairment. Through complex chemical reactions, gases react to form such fine particles, e.g. sulphur dioxide reacts to form ammonium sulphate, nitrogen oxides react to form ammonium nitrate and hydrocarbon gases can convert into carbon particles. Some of these particles are hygroscopic in nature, and absorbing water enhances their ability to impair visibility. Hence, when relative humidity is high, the visibility impairment capability of certain particles such as sulphates increases. Correspondingly, Visibility is a good and simple

indicator for air quality. Increase in the amount of fine particulate and gases in the atmosphere are associated with reductions in the ability of the human eye to see through the atmosphere or identify an object at a distance. Commonly applied measurement of visibility degradation is visual range in miles or km, (higher values mean better visibility). It can be measured easily even without aid of any instruments.

Numerous studies carried out all over the world have given ample evidence that visibility impairment is largely due to the light scattering of ambient aerosols for which concentrations are governed by meteorological conditions and the emission source strength. Visibility impairment, which results from the scattering and absorption of light by particles and gases in the atmosphere, is considered as a direct effect of air pollution. Many have shown correlation between meteorological parameters, particulate matters and visibility. In Nepal, very few studies have focused on visibility in Kathmandu Valley. This study examines the influence of meteorological parameters such as, maximum and minimum temperature, rainfall, relative humidity, atmospheric pressure, total cloud coverage, wind speed, wind direction and PM_{10} concentration on visibility.

Materials and Methods

Study area

KathmanduValley

Kathmandu Valley is an oval shaped, flat bottomed basin which occupies about 351 square kilometer. It is about 1300m above mean sea level and is surrounded by high hill range whose altitude from the valley floor varies from 500m to 1400m. The cross section of the oval structure of the Kathmandu Valley extends 20 km from north to south and 30 km from east to west. Kathmandu Valley is influenced by monsoon. The general pattern is characterized by a windy hot and humid climate in March to May, followed by a well-defined monsoon is approximately from June to the middle of September. About 82 per cent of the rain falls during the period of monsoon. So, the remainder of the year is dry with cold winter in December, January and February. Autumn is the most pleasant season with the pleasant temperatures and occasional short bursts of rain; winter temperatures drop to freezing with a high level of snowfall in the mountains. Wind is ordinarily light throughout the year, but there is a strong wind in and around the March to May. Major part of the winds blowing over the valley is southwesterly and northwesterly. Wind speed lies in the range of 0.5-7.5 m/s. The relative humidity reaches more than 80 % during rainy season but decreases to about 50 % during dry season. Fog is common in the morning during the months of October to February. A high altitudinal variation with extreme diurnal radiation leads to a potentially strong cooling system in the night and a warming in the day. During the dry season, cooling in the morning and late afternoon causes the formation of deep inversion layers. When the inversion layer is deep enough, insulation may not break through the inversion. Due to topographical specificity, once the pollutants have entered into the valley, they cannot easily escape and may remain into the atmosphere for extended period of time.

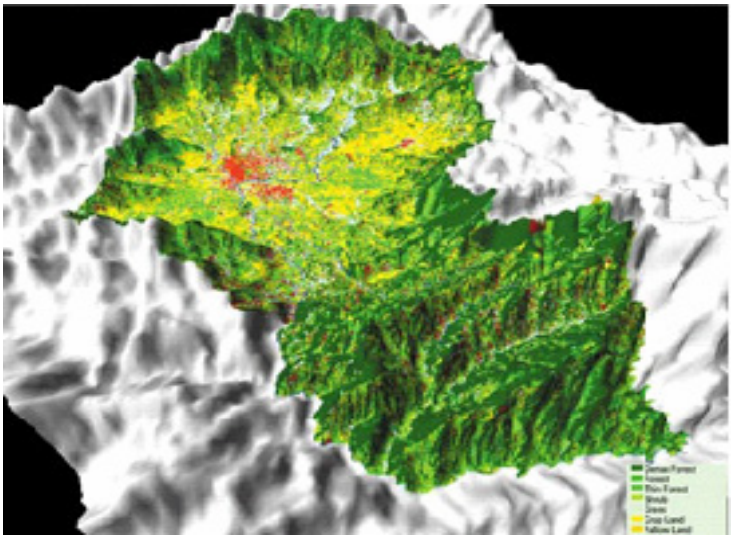

Figure 1 : Geographic View of Kathmandu Valley

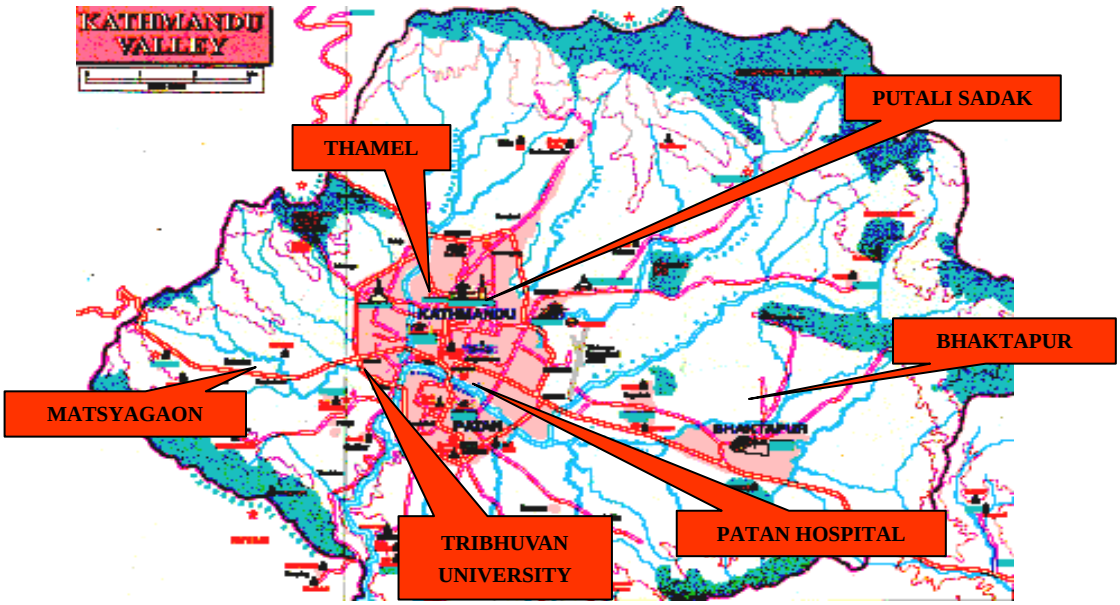

Figure 2: Air Quality Stations at Kathmandu Valley

Monitoring Sites

Air Quality Monitoring Sites

In Kathmandu Valley daily 24-hour continuous air monitoring is carried out at six permanent sampling stations, namely urban roadside station, (urban traffic place, Putalisadak and urban hospital place, Patan Hospital), urban residential station, (city core residential place, Thamel), urban background station (Tribhuvan University, and Bhaktapur) and valley background station (Matsyagaon). The air monitoring stations thus were located in all directions and represented all predominant urban areas associated with high, medium and low human activities (Figure-1). This was done as to get a better spatial representation of the valley.

Air Monitoring Instrument for PM_{10}

In these stations particulate matter concentration is monitored by standard method on daily basis. A Low Volume Sample (LVS) for PM_{10} and $PM_{2.5}$ without pneumatic movement of filters is used. The PM_{10}/$PM_{2.5}$ sampler was type M/S Instrumatic, Denmark, Model 85-02, designed according to the EN12341 standard.

Meteorological data

Meteorological data recorded by weather monitoring station at Tribhuvan International Airport (TIA), was used for the study. TIA is the only monitoring station in Kathmandu Valley that measures visibility together with meteorological variables including wind direction, wind speed, temperature, relative humidity, cloud cover, atmospheric pressure and precipitation.

Visibility

Visibility is an observational data. TIA station has developed a map of Kathmandu valley with overlaying concentric circles starting with a 500 meters radius, covering the total area of Kathmandu valley. With an increase of 500 meter, a concentric circle is present with a reference point place. The center of all circles is TIA station. In the case of visibility distance falling between the circles, approximation is done. The unit of visibility is Km.

Data

PM_{10} and meteorological data were obtained for the period of 2003 to 2005. For better representation of the influence of PM_{10} and meteorological parameters, only those days were considered with data from all 6 air monitoring sites, and meteorological data from the weather station. The main computational tools used were Microsoft Excel and statistical tool, SPSS. Means, standard deviations, correlation analysis, regression, Chi- Square and ANOVA test were done to show the statistical significance of the differences. To study nature of distribution of visibility, probability distribution curve was plotted using Best Fit tool.

Results

Temporal Variation of Visibility

Mean visibility was found increasing from 2003 (7.5467 km) to 2005 (8.1267 km) (Table: 1).

Table 1: Mean, Standard Deviation, Maximum and Minimum value, and Range

Year	N	Mean (km)	Std. Deviation	Minimum (km)	Maximum (km)	Range (km)
2003	305	7.5467	1.4428	3.66	12.53	8.87
2004	366	7.2667	1.4964	3.24	10.89	7.64
2005	347	8.1267	1.7909	2.25	12.13	9.88
Total	1018	7.6437	1.6281	2.25	12.53	10.28

Table 2: Seasonal Variation of Visibility in Kathmandu Valley

Season	N	Mean (km)	Std. Deviation	Minimum (km)	Maximum (km)	Range (km)
Pre-monsoon	276	7.0356	1.4310	3.56	11.75	8.19
Monsoon	366	8.6131	1.1340	5.44	12.53	7.08
Post-monsoon	171	7.8781	1.6896	4.12	12.13	8.01
Winter	205	6.5363	1.5198	2.25	11.38	9.13
Total	1018	7.6437	1.6281	2.25	12.53	10.28

It was recorded highest in monsoon (8.6131 km), followed by post monsoon (7.8781 km), pre monsoon (7.0356 km) and winter (6.5363 km) respectively. It can be inferred that different season has an effect on the mean visibility in Kathmandu Valley. Monsoon season is recorded with highest rainfall and with the lowest value of PM_{10} as well. Winter season is observed to have the lowest rainfall, more fog, effect of inversion layer and highest PM_{10} value might be the reason for the lowest mean visibility. Mean visibility in the Kathmandu Valley was dependent on different seasons and differ significantly in different seasons.

Mean visibility in the Kathmandu Valley was better in the month of June (8.328 km) to October (8.5325 km). The highest mean visibility was in the month of September (8.7559 km) and lowest in the month of January (5.7753 km). Mean visibility was dependent on different months and differ significantly within the months.

Mean visibility was found to be more in Dashain and Tihar (long festival)period (8.59kms), whereas it was lowest, (7.65 km) during working days. This might be due to the decrease in PM10 concentrations by reduced vehicular movement during this time. It was to differ significantly with the different days. Visibility was found to increase gradually with the commencement of day peaking at 2:45 P.M and declining with the onset of night. Irrespective of season, it is observed that as the day progresses the temperature increases, the wind becomes turbulent, humidity decreases and foggy weather disappears. Mean visibility was found to differ significantly with the different time of the day.

Influence of Meteorological Parameters on Visibility

In Kathmandu valley, average visibility was found maximum in maximum air temperature range of 32^{o}C and above, and the visibility was lowest at the temperature range below 16^{o}C This trend was evident in every season. With the minimum temperature, maximum mean visibility of 8.6691 km was observed in the range of 20-25^{o}C, and the mean visibility reaches to a minimum of 6.3497 km when the temperature reaches the lowest range of -0.5^{o}C.

Wash out effect of particulates by rainfall is also evident with the visibility change during rainy and non-rainy periods. It is observed that the mean visibility is higher during the period of rain compared to period of no rain. However, during the rainfall period, the visibility is highest in rainfall range of (10mm - 30mm). Mean visibility was at lowest with relative humidity 40-60% (6.711 km) and as the relative humidity grows to 80% and above range, the mean visibility reaches the maximum of 7.6968 km. The amount of relative humidity in the atmosphere is found dependent on rainfall. Therefore, it can be implied that increase in humidity means increase in rainfall and which directly increase the visibility. With atmospheric pressure, the data shows inverse relationship with the visibility. Though, the trend in the data is not as clear, but the general trend seems to show that the increase in pressure causes lowering of visibility. Such inverse relationship may be due to fact that that as the pressure goes up, the atmosphere becomes a stable one, which characterizes low or no wind and rainfall.

Table 2: Average concentration values determined within selected ranges of temperature, precipitation, atmospheric pressure, wind speed and relative humidity in Kathmandu Valley

T_{max} (^{0}C)	N	Mean Vis.(kms)	T_{min} (^{0}C)	N	Mean Vis.(kms)	Rain (mm)	N	Mean Vis.(kms)	AP (mmhg)	N	Mean Vis.(kms)	Total cloud (OKTA)	N	Mean Vis.(kms)	RH (%)	N	**Mean PM_{10}**
< 11	2	5.7049	-0.5-1	8	6.3497	No rain	624	7.3017	<855.0	6	7.3417	Clear sky	2	3.7188	40.00-60.00	24	**6.7118**
11-16	8	4.4100	1-5	119	6.5958	0.001-10.0	259	8.2877	855.0-860.0	143	8.3884	0-2	186	7.5213	60.00-80.00	362	**7.6129**
16-20	81	6.0264	5-10	200	6.9683	10.0-20.0	61	8.1434	860.0-865.0	319	8.0686	2-4	281	7.1715	≥80	632	**7.6968**
20-24	194	6.9657	10-15	216	7.2794	20.0-30.0	36	8.0479	865.0-870.0	412	7.2479	4-6	283	7.8032			
24-28	306	7.7119	15-20	256	8.1294	30.0-40.0	19	7.5695	870.0-875.0	136	7.0587	6-8	262	8.1102			
28-32	393	8.2576	20-25	219	8.6691	40.0-50.0	6	7.6394	≥875.0	2	8.8750	≥8 a	4	6.6406			
≥32	**34**	**8.5320**				**≥50**	**13**	**7.8795**									

Wind Speed (m/s)	N	Mean
No wind	43	7.1309
0-2	970	7.6595
2-3	5	9.0000
Total	1018	7.6437

The relation of visibility with cloud cover elucidate that maximum mean visibility of 8.1102 kms is seen with high total cloud range of 6-8 OKTA; where as the minimum mean visibility of 3.7188 kms is seen when there is clear sky. The overall trend, however, depicts direct effect of cloud cover on visibility.

Maximum mean visibility (9.0000 km) was seen with the highest wind speed range of 2-3 m/s; where as the minimum mean visibility (7.1309 km) is seen when there is no wind. This means that wind helps in increasing the visibility, and this is due to the ability of high speed wind to blow away the particles.

It was found that wind blows mainly from two directions; west and south of the Kathmandu Valley. Irrespective of the season westerly and southerly wind was predominant. However, during the monsoon easterly wind and in winter northwesterly wind were in account. Wind direction in sixteen compass point directions for the period 2005 indicate that the highest mean visibility in Kathmandu Valley was associated with wind direction NNE (11.5 Km). However, considering different seasons, highest mean visibility was associated with wind direction NNE, SSE, WSW and WNW in pre-monsoon, monsoon, post-monsoon and winter respectively.

Similarly in Kathmandu Valley lowest mean visibility was associated with the wind direction North, ENE, SSE and ENE respectively in pre-monsoon, monsoon, post-monsoon and winter.

In general, the visibility in the Kathmandu Valley depends on the ambient air temperature, precipitation, atmospheric pressure, wind speed, relative humidity and predominant wind direction and differs significantly with these parameters.

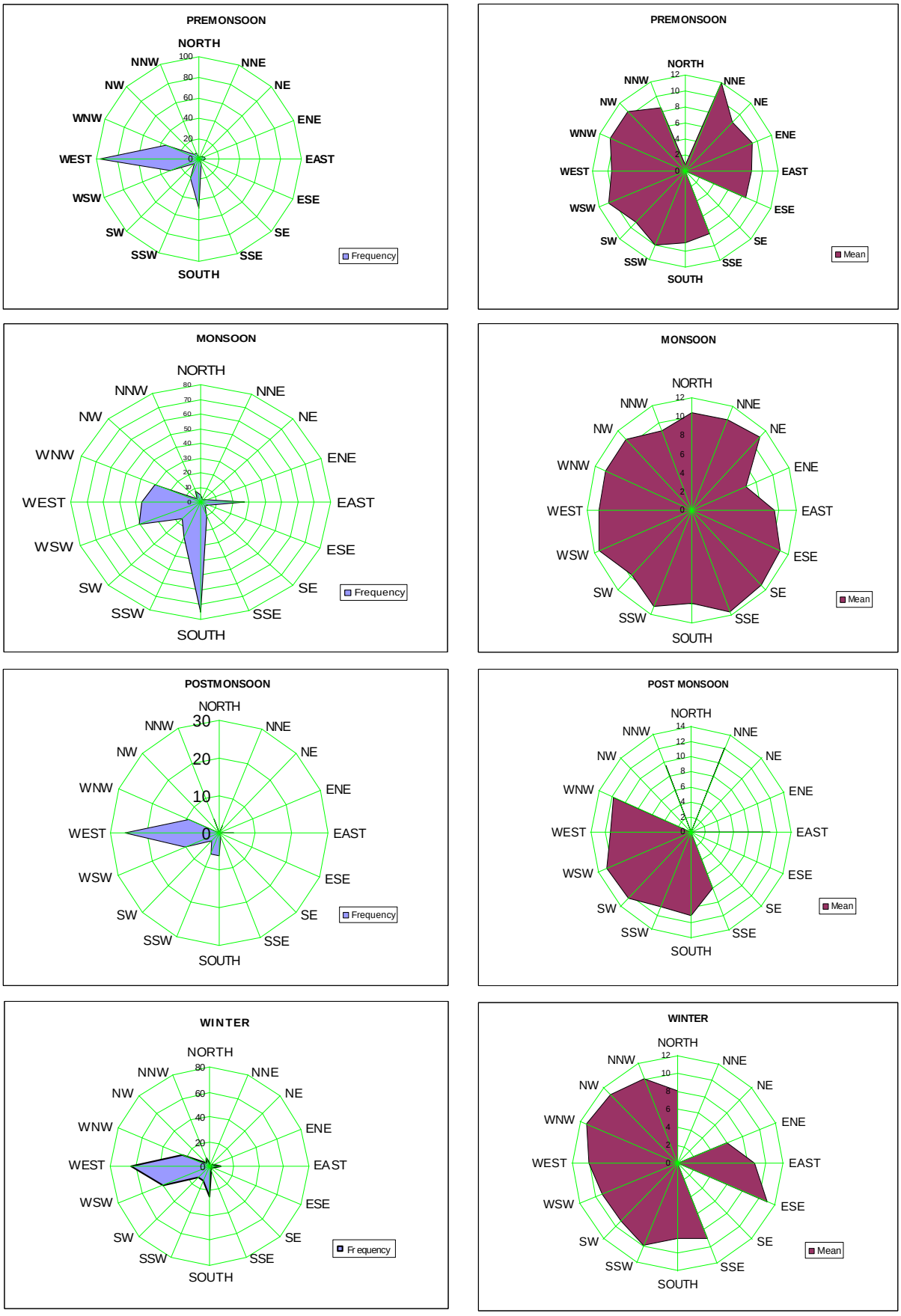

Figure 3: Prevailing wind directions in different seasons and corresponding visibility in Kathmandu Valley

Table: 3. 24 hour PM 10 data from monitoring stations of Kathmandu valley.

PM_{10} (μg/m3)	N	Mean	Std. Deviation	Minimum	Maximum	Range
Good (0 -60)	96	8.2378	1.1471	5.44	11.63	6.18
Moderate (60-120)	406	8.6414	1.2333	4.94	12.53	7.58
Unhealthy (120-350)	514	6.7638	1.4447	3.24	11.63	8.38
Very Unhealthy (350- 425)	2	2.7688	.7336	2.25	3.29	1.04
Total	1018	7.6437	1.6281	2.25	12.53	10.28

Influence of PM10 on Visibility

Government of Nepal has categorized five different types of air quality based on levels of PM_{10}. The categories prescribed are range 0-60 μg/m3 as "Good", 60-120 $\mu g/m^3$ as "Moderate", 121-350 $\mu g/m^3$ as "Unhealthy", 351- 425 $\mu g/m^3$ as "Very Unhealthy", and >425 $\mu g/m^3$ as "Hazardous". In this study the same categories have been maintained for the purposes of interpretation statistical analysis.

Table: 3 shows that the mean visibility increases with decrease in PM_{10} concentration. The mean visibility is highest i.e. 8.6414 km between 0-120 (μg/m3) of PM_{10} concentration and low i.e. 2.7688 km in highest concentration of 351-425 (μg/m3) of PM_{10}. Increase in PM_{10} density in the atmosphere results in the increased scattering of light, reducing visibility thereby. Mean visibility in the Kathmandu Valley depends on the PM $_{10}$ concentrations and it was found to differ significantly with PM_{10} concentration.

Mean visibility varies significantly with the change of PM_{10}, and also with the change of wind speed, barometer pressure, total cloud, temperature (maximum and minimum), humidity, year, month and season. However, the change in the day of the week was found not significantly affecting the visibility. From this analysis, it can be inferred that PM_{10} is not the only factor determining visibility. It can be implied that while relating PM_{10} with the visibility, the above meteorological factors play a significant role and must be considered for analysis.

Correlation Analysis

Table 4 depicts the correlation of visibility and different meteorological parameter during the study period.

Visibility in the valley has positive relationship with maximum temperature, minimum temperature, rainfall, wind velocity and total cloud. This implies that as the visibility increases, the maximum temperature, minimum temperature, rainfall, wind speed, and total cloud are higher and vice versa. However, the Pearson's coefficient is relatively strong with maximum and minimum temperature.

However, visibility in the valley has negative relationship with atmospheric pressure and PM_{10}. As the atmospheric pressure and PM_{10} increases visibility in Kathmandu Valley decreases and vice versa. R-square value of -.606, signifies a strong relation of PM_{10} with visibility.

Table 4: Pearson's Coefficient of Correlation between Visibility with Selected Meteorological Parameter and PM10

		MAX. TEMP.	RAINFALL	HUMIDITY	ATMOSPHERIC PRESSURE	WIND VELO.	TOTAL CLOUD	MIN TEM	PM_{10}
Visibility	Pearson Correlation	.453**	.081*	.018	-.262**	.066*	.177**	.446*	-.606**
	Sig. (2-tailed)	.000	.010	.561	.000	.035	.177	.000	.000
	N	1018	1018	1018	1018	1018	1018	1018	1018

** Correlation is significant at the 0.01 level (2 -tailed)

Table 5: Pearson's coefficient of correlation between Visibility in Kathmandu Valley and selected meteorological parameter in different seasons

		MAX. TEMP.	RAINFALL	HUMIDITY	ATMOSPHERIC PRESSURE	WIND VELO.	TOTAL CLOUD	MIN TEM	PM_{10}
Visibility	Pearson Correlation	.070	.081*	.018	-.262**	.066*	.177**	.446*	-.606**
	Sig. (2-tailed)	.000	.010	.561	.000	.035	.177	.000	.000
	N	1018	1018	1018	1018	1018	1018	1018	1018

Regression Analysis

Considering that the mean visibility in Kathmandu Valley depends on maximum temperature, minimum temperature, rainfall, relative humidity, atmospheric pressure, wind speed, total cloud coverage and the PM_{10} concentration linear regression analysis was done. Regression analysis is found to be significant at 0.05 level of significance. It was also observed that except rainfall and wind speed, other meteorological parameters are found to be significant predictor of visibility. Further it was observed that R^2 value is 0.563 i.e. 56.3% of variation in dependent variable has been explained by independent variable.

Probability Distribution

The frequency distribution of visibility is useful in understanding the statistical characteristics of air quality. In Kathmandu Valley the visibility data follows the Weibull probability distribution. The probability graph shows that the mean visibility lie in the range of 4.73 km to 10.21 km with 90% confidence interval. Maximum number of observations was found between 7 to 9 kms, with a probability of around 0.25.

Table 6: Regression Coefficient

	Un-standardized Coefficients	Std. Error	Standardized Coefficients	T	Sig.
	B		Beta		
(Constant)	45.464	8.764		5.188	0.0000
Maximum Temperature	0.07	0.023	0.177	3.009	0.003
Minimum Temperature	0.004	0.02	0.015	0.191	0.849
Rainfall	-0.012	0.004	-0.081	-3.479	0.001
Humidity	-0.065	0.008	-0.313	-8.251	0.0000
Atmospheric Pressure	-0.036	0.01	-0.097	-3.554	0.0000
Wind Speed	-0.213	0.111	-0.05	-1.918	0.055
Total Cloud	-0.129	0.034	-0.165	-3.735	0.0000
Average PM_{10}	-0.024	0.001	-0.818	-26.89	0.0000

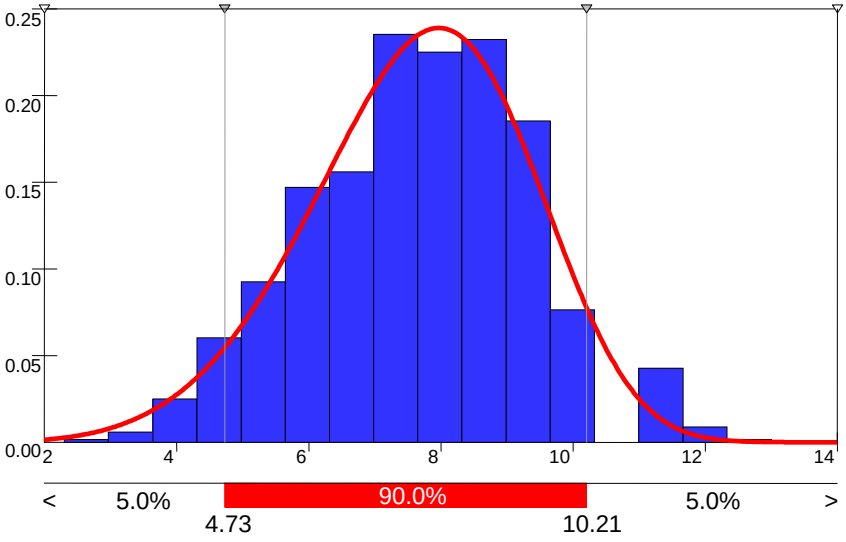

Figure 4: Frequency distribution of visibility in Kathmandu valley.

Conclusions

1. Monsoon season was found to have the highest visibility with winter having the lowest of all.
2. The mean visibility in the Kathmandu valley is better in the month of June 8.328 km to October 8.5325 km as compared with other months. Visibility was less during January (5.7753 km).
3. Mean visibility was found increased during the non-working days long festival time (Dashain and Tihar) than that of working days and week end days. Within a day, It was observed that the visibility increase gradually with the day which peaks at 2:45 P.M and declines with the onset of night.
4. Mean visibility was found dependent with different year, different seasons, and in different months.
5. Meteorological parameters like temperature (minimum and maximum), rainfall, wind speed, pressure, total cloud and humidity were found to affect mean visibility. Mean visibility is dependent on the above parameters. Change in temperature (minimum and maximum), rainfall, wind speed, pressure, total cloud and humidity changes the mean value of visibility. Visibility in the valley has positive relationship with maximum temperature, minimum temperature, Rainfall, wind velocity and Total cloud. The analysis of visibility with the wind direction for the year 2005 shows the highest mean visibility in Kathmandu Valley was associated with wind direction NNE.
6. PM_{10} concentration was found to affect mean visibility and is dependent on PM_{10}. Mean visibility varies significantly with the change of PM_{10}, and also with the change of meteorological parameter.
7. Visibility in the valley has negative relationship with atmospheric pressure and $PM_{10.}$ Except rainfall and wind speed, other meteorological parameters are found to be significant predictor of visibility. The probability distribution of the visibility was found to follow the Weibull's distribution, where maximum observed value lie in the range of 7-8 kms. This implies that maximum number of day in Kathmandu has the corresponding visibility range.

Acknowledgements

This study was funded by the Kathmandu University. We thank the Air Quality Department of the Ministry of Environment Science and Technology, Department of Hydrology and Meteorology, and Tribhuwan International Airport for assistance in technical issues and for providing pollution and meteorological data.

This paper is presented in the 16th CEReS International Symposium on climate change studies through activities of SKYNET and Virtual Laboratory for climate diagnostics (October 21-23, 2010), Chiba University, Nago, Okinawa, Japan with support from Japan Society for Promotion of Science (JSPS).

Selected References

1. Charlson, R. J. and Heintzenberg, J, (1995). Aerosol Forcing of Climate, John Wiley & Sons, Chichester, pp. 191–194.
2. Davis, J.M., Eder B. K., Nychka D., Yang Q., (1998). Modeling the effects of meteorology on ozone in Houston using cluster analysis and generalized additive models. Atmospheric Environment, 32, 2505–2520.
3. ENPHO, (1993 b). Air Quality Assessment in Kathmandu City. Environment and Public Health Organization, Kathmandu, Nepal.
4. Gautam, C., (2002). "Ambient Air Quality, Inventory of Pollutants and Future Ambient Air Quality Monitoring Programme of Kathmandu Valley", Proceedings of One Day Seminar on Air Quality Management of Kathmandu Valley: Challenges and Opportunities, Kathmandu, 2002.
5. Gautam, C, Sharma, S., and Fuglsang K., (2004). Air Quality Monitoring and Management in Kathmandu, Nepal. International Conference on Better Air Quality Management in Asia (BAQ 2004), December 2004, Agra, India.
6. Giri, D., Murthy. V. K., Adhikary, P.R., Khanal, S. N., (2007). Cluster analysis applied to atmospheric PM_{10} concentration data for determination of source and spatial patterns in ambient air quality of Kathmandu Valley, Current Science, 93, No.5.
7. Giri, D., Murthy. K., Adhikary, P.R., Khanal, S. N., (2006). Estimation of number of deaths associated with exposre to excess ambient PM10 air pollution. Int. J. Environ. Sci. Tech., 4(2), 183-188.

8. Giri, D., Murthy. K., Adhikary, P.R., Khanal, S. N., (2006). Ambient air quality of Kathmandu Valley as reflected by atmospheric particulate matter concentration (PM_{10}). Int. J. Environ. Sci. Tech., 3(4), 403-410.
9. Giri, D., Murthy. K., Adhikary, P.R., Khanal, S. N., (2004). "Spatial and seasonal variation of ambient airborne particulate matter (PM_{10}) mass concentrations in Kathmandu Valley" Proceeding of International conference on better air quality management in Asia, from December 6-8, 2004, Agra, India.
10. Lee, D.O., (1990). The influence of wind direction, circulation type and air pollution emissions on summer visibility trends in southern England. Atmospheric Environment 24A, 195–201.
11. Lee, D.O., (1994). Regional variations in long-term visibility trends in the UK, 1962–1990. Geography 79, 108–121.
12. Liou, K. N., (1996), An Introduction to Atmospheric Radiation, Academic Press, California, pp. 50–86.
13. Malm, W.C., (1999). Introduction to Visibility. Air Resources Division National Park Service.
14. MOPE, (2003). National Ambient Air Quality Standards for Nepal. Ministry of Population and Environment. HMG/ Nepal.
15. Pandey, R.K., (1987). Geography of Nepal. Center for Altitude Geography, Kathmandu, Nepal.
16. Sapkota, B.K., Sharma, N.P., Poudel K. and Bhattarai, B., (1997). "Particulates Pollution Levels in Kathmandu Valley", Environment, 3:2, Ministry of Population and Environment, Kathmandu.
17. Van de Hulst, H. C., (1987). Light Scattering by Small Particles, Dover Publication, New York, pp. 383–453.

Long-term Variation of Aerosol Optical Depth in China Based on Meteorological Horizontal Visibility Observations*
Validation and Analysis of Aerosol Optical Depth Derived from Meteorological Horizontal Visibility in China*

QIN S. G.[1,2] SHI G.Y.[2 #] CHEN L[2,3] WANG B.[2] ZHAO J. Q.[2] YU C. W.[4] YANG S.[2]

1 Meteorological Observation Center, China Meteorological Administrator, Beijing, China

2 State Laboratory of Numerical Modeling for Atmospheric Sciences and Geophysical Fluid Dynamics, Institute of Atmospheric Physics, Chinese Academy of Sciences, Beijing, China

3 National Satellite Meteorology Center, China Meteorological Administrator, Beijing, China

4 Climate Center of Hebei Province, Shijiazhuang, China

Abstract

After treating with the visibility data inhomogeneity source from inconsistent record format at the beginning of the year 1980, we obtain the long-term time series of visibility, from which atmospheric aerosol optical depth over China during 1961 to 2005 are derived. By validation, it shows well consistency with former research and observation on long-term variation of aerosol optical depth over China. It is found that aerosol optical depth over China showed an increasing trend but a slowdown upward trend in the post-1985, especially in megacity regions. The aerosol optical depth are low in the northwestern China and high in the southeastern China where aerosol optical depth is generally greater than 0.4, and the maximum of more than 0.8 locates in the Sichuan Basin.

Keywords : Visibility Aerosol Optical Depth

1. Introduction

Atmospheric aerosol plays an important role in energy balance of Earth-Atmosphere system and thus can influence the global climate change significantly through direct, semi-direct and indirect effect. Aerosol Optical Depth (AOD) is one of the primary parameters to determine the aerosol radiative effects which can be obtained through ground-based measurement and satellite retrieval (Dubovik et al., 2000; Chu DA et al., 2003), however, due to highly temporal and spatial variability of aerosols, there is still lack of long time series of AOD on global or even regional scale.

Horizontal Visibility is an indicator reflecting the atmosphere transparency which is highly negative correlated with AOD. Studies by Wang et al. (2009) indicate that AOD derived from meteorological horizontal visibility has a considerable accuracy with satellite retrieval product. This article is to validate AOD estimated with visibility data observed at routine meteorological stations and to give spatial and temporal variations of AOD over China.

2. Data and Methods

2.1 Data information

Meteorological horizontal visibility was observed in 753 routine meteorological stations from 1961 up to 2005. 639 stations more than 35 years are used in this paper, where are select to estimate AOD. Note that the visibility record format begins to change from 1980. Before 1980 visibility was divided into ten levels based on different visibility distance range while after 1980 was given the actual visibility distance (unit: km). Routine meteorological stations in China are regularly observed at least 4 times a day, at 2:00am, 8:00am, 14:00pm and 20:00pm (Beijing time, the same below). In order to eliminate the visibility target inconsistencies in night time at 2:00am and 20:00pm and possible fog influence at 8:00am, the one observed at 14:00am was chosen to represent the daily visibility in this paper. In addition, for the purpose of AOD estimating, the visibility observed in some weather conditions, such as precipitation, fog and high humidity (RH> 90%) was removed.

2.2 Visibility data processing methods

As mentioned formerly, visibility had different record format before and after 1980. If want to derive long-term time series, it is required to assign a reasonable visibility distance for level in record format before 1980. In theory,

* This article is based on a study first reported in Chinese Journal of Atmospheric Sciences, 2010, Vol. 34(2): pp449-456.

* This article is based on a study first reported in Chinese Journal of Atmospheric Sciences, 2010, Vol. 34(2): pp449-456.

Corresponding author, supervision for this study

Table 1 Visibility interval and estimation for visibility levels

Visibility Level	Visibility interval / km	Estimates for corresponding level / km
0	<0.05	0.025
1	0.05~0.2	0.1
2	0.2~0.5	0.28
3	0.5~1.0	0.7
4	1.0~2.0	1.41
5	2.0~4.0	2.67
6	4.0~10.0	6.77
7	10.0~20.0	13.58
8	20.0~50.0	29.04
9	≥50.0	54.27

daily visibility data in level format can be assigned any value in the interval corresponding to the level, e.g. the median; however, because of non-equidistance intervals for levels, it may lead to inhomogeneity for time series. In this paper, daily visibility data from 1980 to 2005 are transferred to levels format data firstly, and then under the limit of each level, daily visibility is averaged as the estimates for the ten levels (hereinafter called estimates). Table 1 gives the visibility levels, intervals and estimates for corresponding level respectively, in which estimate is median of interval for level_0, that is 0.025km. It can be seen that the estimates for a visibility level is less than the median of interval, and the level is larger, the difference is more significant.

Using the estimates to replace daily visibility data before 1980 in format of level, the monthly and annually average visibility can be obtained. Figure 1 shows long-term variation of visibility over China from 1961 to 2005 averaged by 639 stations data, in which two processing results are given at the beginning of 1980. One is to get the annual average using the visibility observations directly (the circles), the other is to convert visibility to levels, then obtain the annual average according to processing method for data before 1980 (black dots). As shown in Figure 1, the visibility data processing method used in this paper may effectively guarantee the continuity of the visibility variation over China when record format were altered from 1980, and at the same time, keep a small relative errors between the estimates to observations after 1980 with the errors range form -1.5% to 1.7%, which is the slightly influence on long-term trend analysis. In order to keep the continuity of data, later in this paper, the AOD is derived based on the visibility obtain by estimates for whole period from 1961 to 2005.

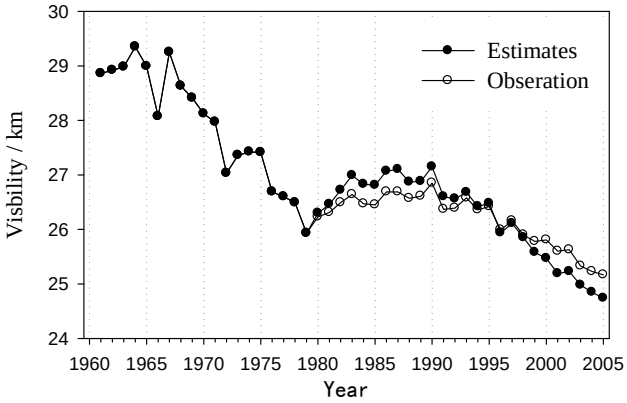

Fig.1. Variation of annually averaged visibility over China during 1961 to 2005

2.3 The method to derive AOD based on visibility

According to the definition of meteorological visibility *V*, Visibility is inversely proportional to the atmospheric extinction coefficient$\sigma_{0.55}$ at the wavelength of 0.55μm, which can be expressed by equation (1):

$$V = \frac{3.912}{\sigma_{0.55}} \qquad (1)$$

In atmospheric standard conditions (*T* = 15 ℃, *P* = 1013hPa), assuming aerosol obey Junge distribution, in terms of the relationship between atmospheric vertical attenuation with visibility in Elterman (1970), and aerosol particle concentration distribution with height inducted by McClatchey et al. (1971), AOD (τ_λ) can be derived from visibility (*V*) based on the equation (2),

in Equation (2),*Z* is the altitude of meteorological station (km), H_1=0.886+0.0222*V* km, H_2=3.77km, v^*= -2, λ=0.55μm.

In this paper, the surface vapor pressure is introduced to revise the result of AOD according to the method developed by Qiu and Lin (2001), more detail in the reference.

3. Results

According to the method introduced in section two, the daily AOD in meteorological station is derived based on visibility, thus monthly and annually average for station or China is also obtained for the period from 1961 to 2005.

$$\tau_\lambda = \left(\frac{3.912}{V} - 0.0116\right)\left(\frac{0.55}{\lambda}\right)^{2-v^*}\left[H_1\left(e^{-\frac{Z}{H_1}} - e^{-\frac{5.5}{H_1}}\right) + 12.5e^{-\frac{5.5}{H_1}} + H_2 e^{-\frac{5.5}{H_1}}\right] \qquad (2)$$

3.1 Validation of aerosol optical depth results

Two time series of annually averaged AOD from 1961 to 1990 over China are shown in Figure 2. The line with solid dots shows the result of this paper, while the line with triangles show ones in Luo et al. (2000) which is obtained by "broadband extinction method" with 44 stations direct solar radiation data in China. It can be seen that two results are highly consistent in variation characteristic with a correlation coefficient of 0.9. Annually averaged AOD in this paper is slightly higher compared to result in Luo et al. (2000) and the possible reason is that AOD in this paper is obtained at the wavelength of 0.55μm, while equivalent to wavelength of 0.75μm in Luo et al. (2000), assuming aerosol obey Junge distribution, the wavelength smaller, the AOD greater.

AERONET is a global aerosol monitoring network established under the leading of NASA, whose aim is to acquire global aerosol optical properties using the ground-based sun photometer equipped at baseline or representative regional, further to validate and assess the accuracy of satellite retrievals (Dubovik et al., 2000). Here, one of AERONET sites Beijing which has the longest available data in China is selected for validation. From the variation of monthly average AOD from January 2002 to December 2005 in Beijing given in figure 3, we can see similar variation characteristic for two series with a correlation coefficient of 0.54. There are indications that the variation of monthly average AOD in Beijing derived by visibility is mild and relative larger differences for extreme AOD values compare to sun photometer observation, probably reason is that the visibility is artificial observation, which the sensitivity and accuracy can not be compared with the sun photometer instruments.

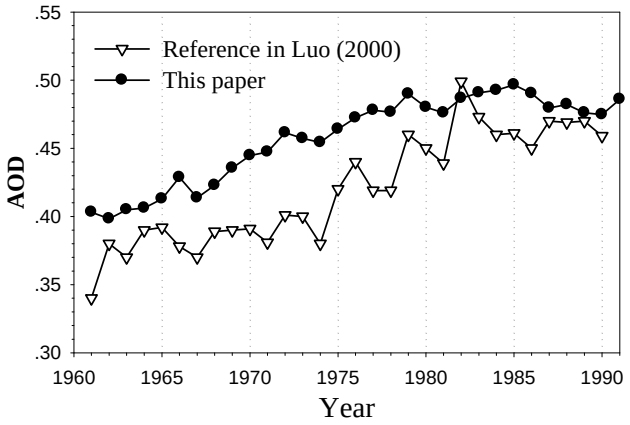

Fig.2. Variation of annually averaged AOD for 44 stations in China

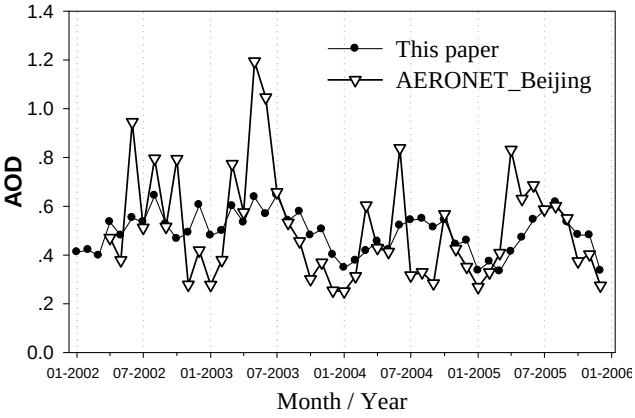

Fig.3. Variation of monthly averaged AOD in Beijing comparison to AERONET (Jan. 2001-Dec. 2005)

MODIS (Moderate Resolution Imaging Spectroradiometer) is a key instrument aboard the NASA Terra satellites which can be used to retrieve aerosol optical depth with "dark-target" method proposed and developed by Kaufman et al (1997). In this paper, the MOD 08 Level 3 monthly average AOD Gridded product from 2001 to 2005 is also used to validate the AOD derived from visibility. Figure 4 shows the scatter plots and line regressive of comparison in the spring (March, April and May), summer (June, July and August), autumn (September, October and November) and winter (December, January and February) seasons, respectively. Seen from the linear regression equations and correlation coefficients at the bottom right corner, the seasonal correlation coefficient of visibility derived AOD and MODIS AOD are all higher than 0.6, with the maximum of 0.7 in the fall, and the minimum of 0.6 in the summer which may be the reason of higher water vapor or more concurrency of clouds and rain. Further, the validation shows that visibility derived AOD is usually higher than the satellite retrieval for low AOD, while lower for high AOD. One reason may be visibility derived AOD is not satisfactory for extreme AOD as motioned formerly. Additional reasons may be that the applicability of MODIS retrieval aerosol products in China has geographical and seasonal difference (Wang et al, 2007), and the global MODIS retrieval aerosol optical depth over land is significantly higher (Xia, 2006).

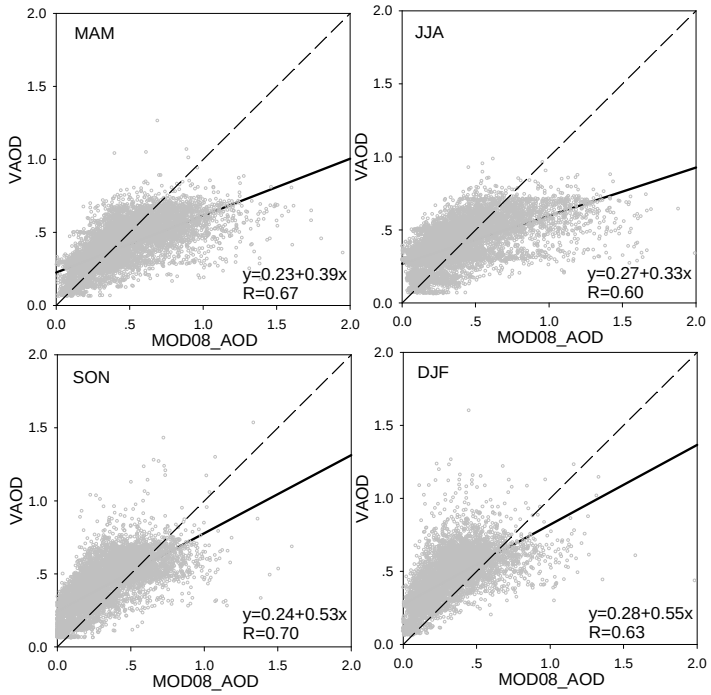

Fig. 4. Scatter plots for comparison of visibility derived AOD with MODIS retrieval AOD for each season

3.2 Temporal and Spatial characteristics of AOD in China

Using visibility derived AOD data, temporal and spatial characteristics of AOD is studied in this paper. Figure 5 shows the long-term variation characteristic of AOD over China from 1961 to 2005, in which the top figure is annually averaged by 639 stations data for more than 35 years, while the bottom figure is averaged by 31 stations data located at the capital cities of provinces, autonomous regions and municipalities on behalf of megacity mean. In figure 5, the linear trends of AOD variation for two periods (1961 to 1985 and 1986 to 2005) are also shown by solid bold line with the slope labeled on the upper left and lower right corner, respectively. It can be understand that AOD over China keep increase for the whole period from 1961 to 2005 but with a slow down increasing rate at the period of post-1986. This characteristic is especially significant in large urban areas with the rate reduces more than an order of magnitude as shown in the bottom of figure 5. Aerosols emission caused by rapid increasing fossil fuel consumption is likely account for AOD variation tendency in China. The situation is particularly evident in large urban areas before 1985, where the increase rate of AOD is largest. But with the development of the state and residents environmental awareness at the beginning of 1990s, more strength emission standards is executed for particle pollution control, which is carried out better in large urban cities than others in China, thereby cause significant difference in variation of AOD increase rate in megacity areas and other areas.

Averaged AOD distribution pattern in China is also studied in this paper using annually averaged AOD data from 2001 to 2005, and shown in figure 6. It shows that the pattern is mainly characterized by feature of a higher in southeast and a lower in northwest. There are several significant high-value areas in China such as Sichuan, Henan, North China and Yangtze River regions with AOD magnitude to 0.6 and with a maximum greater than 0.8 in Sichuan Basin. The result is consistent with Li et al (2003) study, which is obtained by the use of MODIS aerosol products.

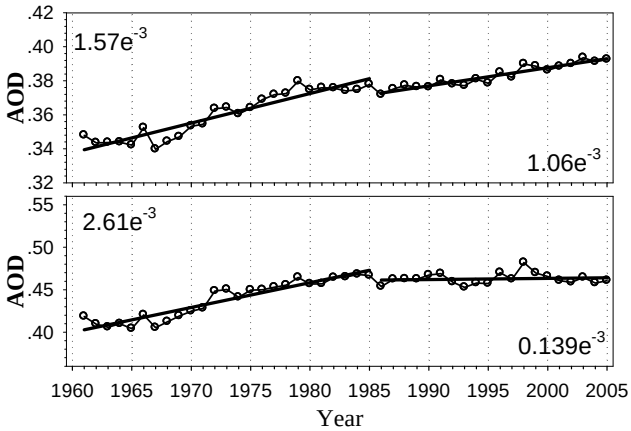

Fig.5 Variation and line trend of annually averaged AOD over China

Top: The curve is the annually averaged time series of AOD with 639 stations data for more than 35 years, the two lines are the linear trend of AOD from 1961 to 1985 and from 1986 to 2005, respectively. Their change slope is marked at upper left and lower right corner of the figure; Bottom: same with top but with 31 stations data, locate in capital cities of provinces, autonomous regions and municipalities

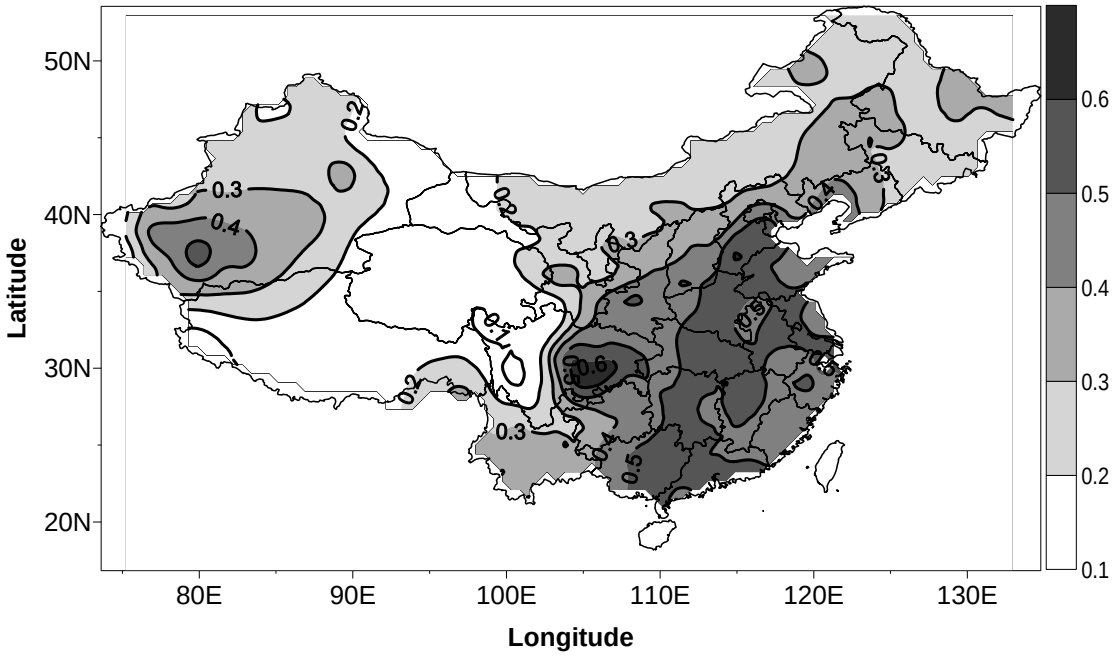

Fig.6 Distribution pattern of averaged AOD over China (2001 to 2005). The bold curve is the isoline.

4. Summary and Discussion

By using the processing method introduced in this paper, visibility data inhomogeneity source from inconsistent record format from 1980 is well disposal. Validation by former study, ground-based measurement data and satellite retrieval products are indications that it is possible to derived AOD by meteorological visibility and visibility derived AOD can well reflect distribution pattern and long-term variation characteristic

Wild et al. (2005) find that the surface solar radiation in most sites of the world has experienced a reversal tendency from reduced to increase named by from “dimming” to "brightening" at early 1990s. Shi et al. (2008) study shows that similar phenomenon is also happened in China at the beginning of 1990s. Although the reason of “brightening” needs further study, there are some evidences indicate that the reduction of atmospheric aerosol content and its interaction with the clouds is the most likely factors (Wild et al., 2005). Most solar radiation observation sites in China locate in the cities, 31 capital cities of provinces, autonomous regions and municipalities selected in this paper are actually equipped with instruments for solar radiation observations, so to some extent, “brightening” occurrence in China have a certain relationship with AOD increase rate slowing down in megacity areas. Certainly, further research is needed to verify it.

Acknowledgment

The visibility and other meteorological data used in this study are obtained from CMA/ National Meteorological Information Center, which is highly acknowledged. We also would like to thank related staff for the use of AERONET data and MODIS aerosol products.

References

Chu D A, Kaufman Y J, Iibordi G, et al. 2003. Global monitoring of air pollution over land from the Earth Observing System-Terra Moderate Resolution Imaging Spectroradiometer (MODIS). J. Geophys. Res., 108 (D21): 4661-4679.

Dubovik O , Smirnov A , Holben B N , et al . 2000. Accuracy assessments of aerosol optical properties retrieved from AERONET sun and skyradiance measurements. J. Geophys. Res., 105: 9791-9806.

Elterman L. 1970. Relationships between vertical attenuation and surface meteorogical range. Appl. Opt., 9 (8): 1804-1810.

Kaufman Y J, Tanr´e D, Gordon H R, et al., 1997. Passive remote sensing of Tropospheric aerosols and atmospheric correction for the aerosol effect. J. Geophy. Res., 102 (D14): 16815-16830.

Li C C, Mao J T, Alexis K L. 2003. Remote sensing aerosol with MODIS and the application of MODIS aerosol products. Acta Scientiarum Naturalium Universitatis Pekinensis (in Chinese), 39 (Supl): 108-117.

Luo Y F, Lu D R, Li W L, et al. 2000. Variation of atmospheric aerosol optical depth over China in recent 30 years. Chinese Science Bulletin (in Chinese), 5(5): 549-554.

Qiu J H and Lin Y R. 2001. A parameterization model of aerosol optical depths in China. Acta Meteorologica Sinica (in Chinese). 59 (3): 368-372.

Shi G Y, Hayasaka T, Ohmura A, et al. 2008. Data quality assessment and the long-term trend of ground solar radiation in China, J. Appl. Meteo. Climatol., 47: 1006-1016.

Wang L L, Xin JY, Wang Y S, et al, 2007, Valiation of MODIS aerosol products by CSHNET over China. Chinese Science Bulletin (in Chinese), 52(4):477-486.

Wang, K., R. E. Dickinson, S. Liang. 2009. Clear Sky Visibility Has Decreased over Land Globally from 1973 to 2007. Science, 323, 1468-1470.

Wild M, Gilgen H, Roesch A, et al. 2005. From dimming to brightening: Decadal changes in Solar radiation at Earth's surface, Science, 308: 847~850.

Xia X.A. 2006. Global atmospheric aerosol optical thickness with MODIS obviously higher over land. Chinese Science Bulletin (in Chines), 51(19):2297-2303.

Aerosols and Climate Changes in China

Zhanqing Li

Dept of Atmospheric and Oceanic Sciences and Earth System Science and Interdisciplinary Center
University of Maryland, College Park, MD

Abstract

As the most populated country of the world, China is a major source of aerosols which may contribute significantly to the regional climate and its changes. Following a series of extensive observation campaigns, a wealth of general and specialized measurements were acquired to allow extensive and close-up investigations of the optical, physical and chemical properties of anthropogenic, natural, and mixed aerosols; their sources, formation and transport mechanisms; horizontal, vertical and temporal variations; direct and indirect effects and interactions with the East Asian monsoon system. Particular efforts have been made to advance our understanding of the mixing and interaction between dust and anthropogenic pollutants during transport. Modeling studies were also carried out to simulate aerosol impact on radiation budget, temperature, precipitation, wind and atmospheric circulation, fog, etc. Major observation campaigns and scientific achievements towards these goals are reviewed in this paper.

1. Overview of Climate Changes in China

Perhaps the most noticeable change of climate in China is a reduction of 35% in visibility from the 1960s to the 1980s. During this period, the amount of direct solar radiation reaching the ground decreased by about 8.6% [*Luo*, 2001; *Liang and Xia*, 2005; *Shi et al.*, 2008], while global total solar radiation decreased by about 4.6% per decade [*Shi et al.*, 2008]. Sunshine duration also decreased significantly over a large portion of China in the second half of the past century [*Kaiser and Qian*, 2002].

The decrease in solar radiation is at odds with a general decrease in the annual mean cloud cover (1-3%/decade) and rainy days (1-4% /decade) observed at many ground stations [*Kaiser*, 1998; *Liang and Xia*, 2005], which is consistent with changes in the frequencies of cloud-free sky and overcast sky [*Qian et al.*, 2006]. While temperature has shown a general increasing trend over much of China, significant cooling trend was observed surrounding the Sichuan Basin and central eastern China from 1960s to 1990s [*Qian and Giorgi*, 2000; *Xu et al.*, 2006]. These studies suggest that increased atmospheric pollutants from human activities during the past several decades may have produced a fog-like haze that resulted in less sunshine and decreased solar radiation reaching the surface, reduced evaporation, and moderated the warming trend over heavily polluted areas.

Changes in precipitation follows a general trend of "southern flood and northern drought". By means of model sensitivity tests and data analysis, *Xu* [2001] and *Menon et al.* [2002] argued that the change in precipitation pattern is linked to the aerosol direct effect. By using the observed trend of AOD [*Luo et al.*, 2001] and an assumed constant of aerosol single scattering albedo (ω_o) of 0.85, *Menon et al.* [2002] obtained similar gross trends in modeled and observed temperature and precipitation trends. It is worthnoting that the ω_o as retrieved from a combination of satellite and ground observation is highly variable and the mean value across China is close to 0.90 [*Lee et al., 2007; Zhao and Li, 2007*]. Thus additional mechanisms appear to be at work as well to explain the observed climate change trends.

2. Major Observation Campaigns in China

Various observation activities have taken place since 2004 with the following overarching goals:

(1) to acquire essential aerosol and meteorological measurements for investigating the impact of aerosols on regional climate,

(2) to understand the mechanisms governing aerosol-climate interactions and how aerosols impinge on the regional impact under diverse atmospheric environments ,

(3) to examine the roles of aerosols in affecting atmospheric circulation particularly on the East Asian monsoon system.

The first observation initiative is the East Asian Studies of Tropospheric Aerosols: an International Regional Experiment (EAST-AIRE) (Li et al. 2007a). In the first phase of the study, focus has been placed on obtaining in situ

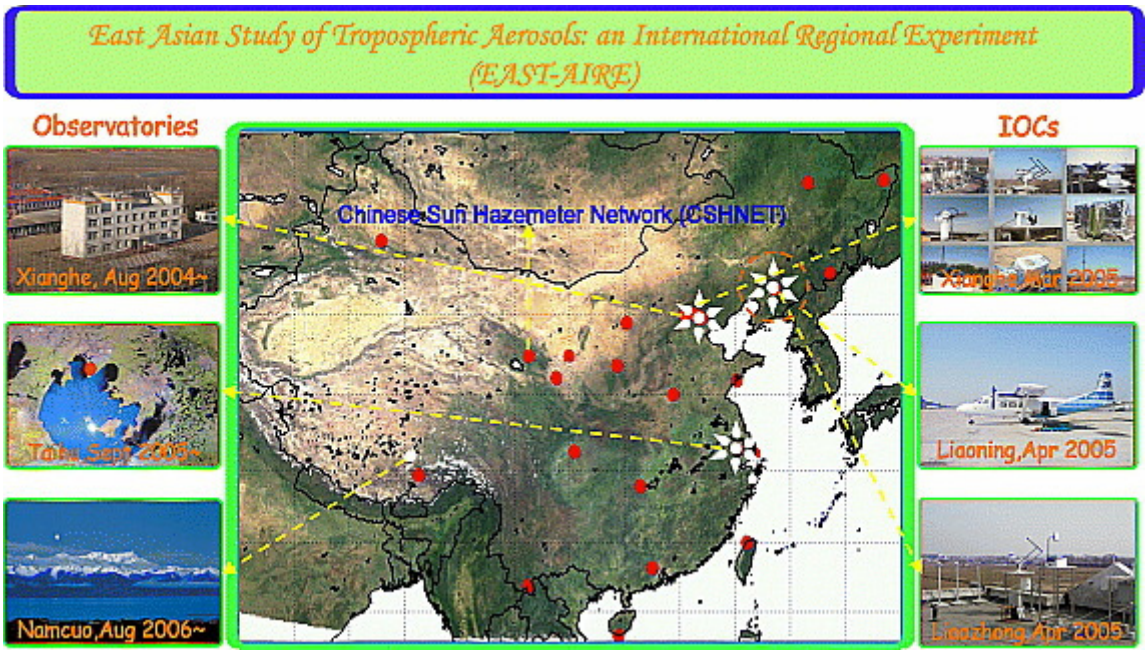

Figure 1. Observation stations and instruments for the EAST-AIRE project.

and remote sensing measurements of aerosols and pollutant gases near or down wind of major source regions throughout inland China. Both routine and intensive observation campaigns (IOC) were conducted with ground-based and airborne measurements. Extensive measurements were made at 2 baseline stations measuring aerosol, cloud and radiation quantities, 25 stations measuring AOD at multiple wavelengths; and ground-based and airborne IOCs measuring the physical and chemical properties of aerosol particles and precursor gases, and cloud and radiation quantities. The observation stations and instruments are shown in Figure 1.

The second-phase of the study was conducted from April-December 2008 at multiple sites in China with the central station equipped with the Atmospheric Radiation Measurement (ARM) Mobile Facility (AMF) at Shouxian in Anhui province of China, approximately 500 km west of Shanghai in the Jiang-Huai prairie region between the Huai and Yangzi rivers, together with three ancillary sites as shown in Figure 2.

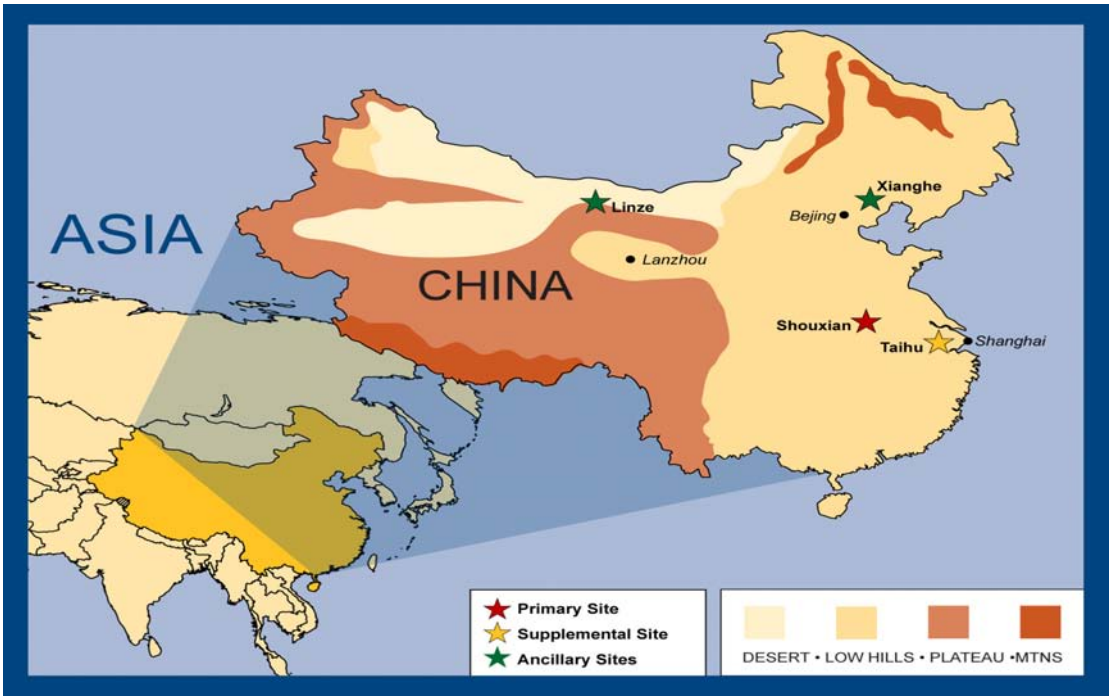

Figure 2. Observation sites in the 2nd phase of study with the ARM mobile facility at Shouxian, Anhui, China.

AMF provides virtually complete description of the state of the atmosphere, the surface and the boundary layer to help understand various atmospheric processes. It consists of a suite of in-situ, passive and active remote sensing instruments to characterize the properties, location and evolution of cloud, aerosol, and meteorological profiles. Cloud radar observes cloud location, reflectivity, particle vertical velocity, and velocity distribution above the facility. Aerosol optical/physical properties and vertical profiles were measured, together with solar/terrestrial upwelling and down-welling radiation, surface latent, sensible, and CO_2 fluxes and standard surface meteorological variables.

Thanks to the unprecedented operation of 95-GHz cloud radar in China, the vertical structure of clouds is observed for the first time. The cloud radar data are used to train and test an algorithm for estimating cloud layers using radiosonde data to detect cloud layers was tested, modified and applied to the data acquired from May to Dec., 2008 [*Zhang J. et al*., 2010]. To complement AMF's comprehensive observations, a station situated at Taihu was substantially enhanced in instrumentation. Established as an EAST-AIRE baseline station [*Li et al*., 2007b], fundamental aerosol, cloud, and radiation variables have been measured continuously since 2005. Taihu is surrounded by several large cities in the Yangtze delta region: Shanghai, Hangzhou, Nanjing, Suzhou and Wuxi (the closest).

In addition to the two southern sites, the NASA's SMART-COMMIT was deployed at two northern sites near the Gobi desert (Zhangye) and Beijing (Xianghe). SMART consists of more than 30 remote-sensing instruments measuring the optical and physical properties of aerosols, cloud, precipitation and radiaiton, while the COMMIT contains 20-some in-situ instruments to measure trace-gas concentrations, fine and coarse particle size, aerosol mass (PM_1, $PM_{2.5}$ and PM_{10}) and chemical composition. It was first deployed at Zhangye from April to June, and moved to Xianghe from June to end of October in northeastern China to enhance the observations during the Olympic Games.

3. Aerosol Properties and Radiative Forcing

Through the EAST-AIRE, we have obtained (1) the temporal and spatial distributions of aerosol loading and precursor gases [*Li C. et al*., 2007], (2) aerosol single scattering albedo (ω_o) [*Zhao and Li*, 2007; *Lee et al*., 2007; *Chaudhry et al*., 2007], (3) aerosol direct radiative effects at a few sites [*Li et al*., 2007a, *Xia et al*., 2007a,b,c], (4) validation results of satellite products [*Li et al*., 2007c; *Mi et al*., 2007], and (5) transport mechanisms [*Dickerson et al*., 2007]. *Lee et al.* [2010] proposed a new Langley method to be able retrieve AOD under variable atmospheric conditions that was applied to derive annual mean AOD at three sites during the 2008 campaign: 0.99, 0.87 and 0.84 respectively for Xianghe, Taihu and Shouxian.

Using ground-based aerosol optical depth [*Xin et al.* 2007] and single scattering albedos retrieved from a combination of satellite and ground-based observations [*Lee et al*., 2007], the first observation-based estimates of aerosol radiative forcing at the top, bottom and inside of the atmosphere were made across [*Li et al.* 2010]. On average, aerosol-induced cooling at the surface is compatible with the warming in the atmosphere, leading to virtually nil effect for the atmosphere-surface system.

An important source of sulfate was discovered in spring that has been previously overlooked [*Guo et al.* 2010] following sulfur isotope analysis and applying scanning electron microscope (SEM) imaging technique to the samples acquired in China. The same aerosol samples were analyzed in a chemical lab to study the concentrations of major elements and water-soluble ions at the Xianghe site [*Li C. et al.* 2010b], leading to a finding of unexpected high level of lead (mean: 0.28 $\mu g/m^3$) for this non-urban site. The lead was enriched by over 100 fold relative to the Earth's crust.

During the AAF field experiment in the spring of 2008, three Micro-Pulse Lidar (MPL) systems were deployed in northwestern China near the major desert source regions. Analyzing these measurements, *Huang Z. et al.* [2010] attribute the observed high-altitude dust layer over Zhangye to the site's proximity to dust sources.

Li C. et al. [2010c] investigated several trace gases and aerosol properties were measured during the AAF deployment from April to June, 2008 at Zhangye, a site located within the Hexi Corridor in northwestern China. *Logan et al.* [2010] linked air-borne dust measurements in the central Pacific to the dust observed on the ground in China, a signal of long-range transport in far downstream regions.

4. The Roles of Aerosols on Climate Changes in China

The global trend of dimming to brightening was also found in China from 1950s to 2000 *Wang and Shi* [2010]. To understand the trend, the spatial and temporal variability of sunshine duration and total/low cloud cover across China was examined in *Xia* [2010]. A significant decreasing trend (>-1%/decade) in total cloud cover was found although a slightly increasing trend in low cloud cover was seen.

Annual sunshine duration decreases by -1.7% per decade, which is consistent with the results of *Kaiser and Qian* [2002].

Given the well-established long-term trend, a key question was addressed whether current global climate models can reproduce the trend. *Dwyer et al.* [2010] found that all of the GCMs reproduce the dimming trend over China before 1990 consistent with the observations, but the magnitude of simulated trends is much less than that observed. Yet, models cannot reproduce the brightening trend after 1990. Long-term (1956 to 2005) declining trend of light precipitation was attributed to increasing aerosol loading by *Qian et al.* [2009]. *Niu et al.* [2010] revealed a doubled increase of winter fog events in central eastern China during past 30 years where aerosol loading is higher and experienced more rapid changes than many other regions. By means of controlled and experimental model (NCAR CCM3) runs, they found that increase in atmospheric aerosols can generate a cyclonic circulation anomaly to offset the predominant Siberian high-pressure system and thus reduces the flow of dry and cold air to eastern-central China, more favorable for fog to form.

In western China, previous studies found a decreasing trend for the dust events [*Qian et al*., 2002]. The reduced dust activities are corroborated with increasing precipitation in western China, as shown in *Gu et al.* [2010]. In an attempt to understand the causes for the decadal changes, they carried out model simulations and concluded that light-absorbing aerosols are the primary cause for precipitation increase which leads to the reductions in dust storm frequency and intensity [*Gu et al.* 2010].

5. Conclusions

The sources, distribution, and effects of aerosols over East Asia, particularly China, have drawn much attention over the past several years. Thanks to the intensive observation campaigns as outlined here, significant progress has been made towards better understanding of various aspects of the East Asian aerosols, including their spatiotemporal variations, optical and microphysical characteristics, and chemical composition of both anthropogenic and natural aerosols, enabling the estimation of the aerosol radiative effects. These coordinated new measurements also allow for more in-depth investigations into the key processes governing aerosol-climate interactions, long-range transport and evolution of aerosols, the interaction of various aerosol species, and the source-receptor relationship on regional scales. The data and knowledge learned from the field experiments have been proven highly valuable for conducting regional and global model simulations to address the climatic impact of East Asian aerosols on regional and global climate.

References

Bishop, J. K., R. E. Davis, and J. R. Sherman (2002), Robotic observations of dust storm enhancement of carbon biomass in the North Pacific, *Science*, 298, 817– 821.

Bréon, F.-M., D.D. Tanré, and S. Generoso, 2002, Aerosol effect on cloud droplet size monitored from satellite, *Science*, 295, 834-837.

Chaudhry, Z., J. V. Martins, Z. Li, S.-C. Tsay, H. Chen, P. Wang, T. Wen, C. Li, and R. R. Dickerson (2007), In-situ measurements of aerosol mass concentration and spectral absorption during EAST-AIRE. *J. Geophys. Res*., 112, D23S90, doi: 10.1029/2007JD009055.

DeMott, P. J., K. Sassen, M. R. Poellot, D. Baumgardner, D. C. Rogers, S. D. Brooks, A. J. Prenni, and S. M. Kreidenweis (2003), African dust aerosols as atmospheric ice nuclei, *Geophys. Res. Lett.*, 30(14), 1732, doi:10.1029/2003GL017410.

Dickerson, R. R., et al. (2007), Aircraft observations of dust and pollutants over NE China: Insight into the meteorological mechanisms of long-range transport, *J. Geophys. Res.*, 112, D24S90, doi: 10.1029/2007JD008999.

Dubovik, O., B.N. Holben, T.F. Eck, A. Smirnov, Y.J. Kaufman, M.D. King, D. Tanré, and I. Slutsker, (2002): Variability of absorption and optical properties of key aerosol types observed in worldwide locations, *J. Atmos. Sci*., **59**, 590-608 .

Duce, R. A., et al. (2008), Impacts of atmospheric anthropogenic nitrogen on the open ocean, *Science*, 320, 893–897, doi:10.1126/science.1150369.

Dutton, E. G., J. J. Michalsky, T. Stoffel, B. W. Forgan, J. Hickey, D. W. Nelson, T. L. Alberta, and I. Reda (2001), Measurements of broadband diffuse solar irradiance using current commercial instrumentation with a correction for thermal offset errors. *J. Atmos. Oceanic Technol.*, **18,** 297–314.

Dwyer, J. G., J. R. Norris, and C. Ruckstuhl (2010), Do climate models reproduce observed solar dimming and brightening over China and Japan? *J. Geophys. Res.*, 115, D00K08, doi:10.1029/2009JD012945.

Fan, X.,H. Chen, X. Xia, Z. Li, M. Cribb, (2010), Aerosol

optical properties from the Atmospheric Radiation MeasurementMobile Facility at Shouxian, China, *J. Geophy. Res*., in press.

Fu, Q., G. Zhuang, J. Li, K. Huang, Q. Wang, R. Zhang, J. Fu, T. Lu, M. Chen, Q. Wang, Y. Chen, C. Xu, and B. Hou, (2010), Source, long-range transport, and characteristics of a heavy dust pollution event in Shanghai, 2007, J. Geophys. Res., doi: 10.1029/2009JD013208, in press.

Ge, J. M., J. Su, T.P. Ackerman, Q. Fu, J.P. Huang, and J.S. Shi (2010), Dust aerosol optical properties retrieval and radiative forcing over northwestern China during the 2008 China-U.S. joint field experiment, *J. Geophys. Res*., 115, D00K12, doi:10.1029/2009JD013263.

Ginoux, P., M. Chin, I. Tegen, J. M. Prospero, B. Holben, O. Dubovik, and S.-J. Lin (2001), Sources and distributions of dust aerosols simulated with the GOCART model, *J. Geophys. Res.*, 106, 20255-20273.

Gu, Y., K. N. Liou, W. Chen, and H. Liao (2010), Direct climate effect of black carbon in China and its impact on dust storms, *J. Geophys. Res*., 115, doi:10.1029/2009JD013427.

Guo, Z., Z. Li, J. Farquhar, A. J. Kaufman, N. Wu, C. Li, R. R. Dickerson, and P. Wang (2010), Identification of sources and formation processes of atmospheric sulfate by sulfur isotope and scanning electron microscope measurements, *J. Geophys. Res.*, 115, D00K07, doi:10.1029/2009JD012893.

Hansell, R. A., K.N. Liou, S.C. Ou, S.C. Tsay, Q. Ji, and, J.S. Reid, (2008): Remote sensing of mineral dust aerosol using AERI during the UAE2: A modeling and sensitivity study, *J. Geophys. Res.*, 113, D18202, doi: 10.1029/2008JD010246.

Hansell, R. A., S.C. Tsay, Q. Ji, N.C. Hsu, M.J. Jeong, S.H. Wang, J.S. Reid, K.N. Liou, and, S.C. Ou, (2010a): An assessment of the surface longwave direct radiative effect of airborne Saharan dust during the NAMMA field campaign. *J. Atmos. Sci*., 67, 1048-1065.

Holben B. N., T. F. Eck, I. Slutsker, D. Tanre, J. P. Buis, A. Setzer, E. Vermote, J. A. Reagan, Y. Kaufman, T. Nakajima, F. Lavenu, I. Jankowiak, and A. Smirnov, (1998), AERONET - A federated instrument network and data archive for aerosol characterization, *Rem. Sens. Environ*., **66**, 1-16.

Hsu, N. C., S. –C. Tsay, M. D. King, and J. R. Herman (2006), Deep blue retrievals of Asian aerosol properties during ACE-Asia, *IEEE Trans. Geosci. Remote Sens.*, 44, 3180-3195.

Huang, J., Y. Wang, T. Wang, and Y. Yi (2006a), Dusty cloud radiative forcing derived from satellite data for middle latitude region of East Asia, *Prog. Natural Sci*., 10, 1084-1089.

Huang, J. Minnis, B. Lin, T. Wang, Y. Yi, Y. Hu, S. Sun-Mack, and K. Ayers (2006b), Possible influences of Asian dust aerosols on cloud properties and radiative forcing observed from MODIS and CERES, *Geophys. Res. Lett., 33*, L06824, doi: 10.1029/2005GL024724.

Huang, J., B. Lin, P. Minnis, T. Wang, X. Wang, Y. Hu, Y. Yi, and J. R. Ayers (2006c), Satellite-based assessment of possible dust aerosols semi-direct effect on cloud water path over East Asia, *Geophys. Res. Lett.*, 33, doi: 10.1029/2006GL026561.

Huang, J. Minnis, Y. Yi, Q. Tang, X. Wang, Y. Hu, Z. Liu, K. Ayers, C. Trepte, and D. Winker (2007), Summer dust aerosols detected from CALIPSO over the Tibetan Plateau, *Geophys. Res. Lett*., *34*, L18805, doi:10.1029/2007GL029938.

Huang, J., W. Zhang, J. Zuo, J. Bi, J. Shi, X. Wang, Z. Chang, Z. Huang, S. Yang, B. Zhang, G. Wang, G. Feng, J. Yuan, L. Zhang, H. Zuo, S. Wang, C. Fu and J. Chou (2008a) An overview of the Semi-Arid Climate and Environment Research Observatory over the Loess Plateau, *Advances in Atmospheric Sciences*, *25*(6), 1-16.

Huang, J. Minnis, B. Chen, Z. Huang, Z. Liu, Q. Zhao, Y. Yi, and K. Ayers (2008b), Long-range transport and vertical structure of Asian dust from CALIPSO and surface measurements during PACDEX, *J. Geophys. Res*., 113, D23212, doi: 10.1029/2008JD010620.

Huang, J., Q. Fu, J. Su, Q. Tang, P. Minnis, Y. Hu, Y. Yi, and Q. Zhao (2009), Taklimakan dust aerosol radiative heating derived from CALIPSO observations using the Fu-Liou radiation model with CERES constraints, *Atmos. Chem. Phys*., **9**, 4011–4021.

Huang, K., G. Zhuang, J. Li, Q. Wang, Y. Sun, Y. Lin, and J. S. Fu (2010a), Mixing of Asian dust with pollution aerosol and the transformation of aerosol components during the dust storm over China in spring 2007, *J. Geophys. Res.*, 115, D00K13, doi:10.1029/2009JD013145

Huang, K., G. Zhuang, Y. Lin, J. Li, Y. Sun, W. Zhang, and J. S. Fu (2010b), Relation between optical and chemical properties of dust aerosol over Beijing, China, *J. Geophys. Res.*, 115, D00K16, doi:10.1029/2009JD013212.

Huang, Z., J. Huang, J. Bi, G. Wang, W. Wang, Q. Fu, Z. Li,

S.-C. Tsay, and J. Shi (2010), Dust aerosol vertical structure measurements using three MPL lidars during 2008 China-US joint dust field experiment, *J. Geophys. Res.*, 115, D00K15, doi:10.1029/2009JD013273.

Huebert, B. J., T. Bates, P. B. Russell, G. Shi, Y. J. Kim, K. Kawamura, G. Carmichael, and T. Nakajima (2003), An overview of ACE-Asia: Strategies for quantifying the relationships between Asian aerosols and their climatic impacts, *J. Geophys. Res.*, 108(D23), 8633, doi:10.1029/2003JD003550.

Husar, R. B., et al. (2001), Asian dust events of April 1998, *J. Geophys. Res.*, 106(D16), 18,317– 18,330, doi:10.1029/2000JD900788.

Jacob, D. J., J. H. Crawford, M. M. Kleb, V. S. Connors, R. J. Bendura, J. L. Raper, G. W. Sachse, J. C. Gille, L. Emmons, and C. L. Heald (2003), Transport and Chemical Evolution over the Pacific (TRACE-P) aircraft mission: Design, execution, and first results, *J. Geophys. Res.*, 108(D20), 9000, doi:10.1029/2002JD003276.

Jaffe, D. A., et al. (1999), Transport of Asian air pollution to North America, *Geophys. Res. Lett.*, 26, 711 –714, doi:10.1029/1999GL900100.

Jeong, M.-J., and Z. Li (2010), Separating real and apparent effects of cloud, humidity, and dynamics on aerosol optical thickness near cloud edges, *J. Geophys. Res.*, doi:10.1029/2009JD013547, in press.

Ji, Q., (2007), A Method to correct the thermal dome effect of Pyranometers in selected hHistorical solar irradiance measurements. *J. Atmos. Oceanic Tech.*, 24, 529-536.

Ji, Q., and S.-C. Tsay (2010), A novel nonintrusive method to resolve the thermal dome effect of pyranometers: Instrumentation and observational basis, *J. Geophys. Res.*, 115, D00K21, doi:10.1029/2009JD013483.

Kaiser, D. P. (1998), Analysis of total cloud amount over China, 1951–1994, *Geophys. Res. Lett.*, 25, 3599–3602.

Kaiser, D. P. and Y. Qian, (2002), Decreasing trends in sunshine duration over China for 1954-1998: An indication of the increased haze pollution? *Geophys. Res. Lett.*, 29(21), 2042, doi: 10.1029/2002/GL016057.

Kawamoto, K. and T. Nakajima, 2003: Seasonal variation of cloud particle size as derived from AVHRR remote sensing, G*eophys. Res. Lett.*,30, doi: 10.1029/2003GL017437.

Lau, W., V. Ramanathan, G.-X. Wu, Z. Li, S. C. Tsay, C. Hsu, R. Sikka, B. Holben , D. Lu, G. Tartari, M. Chin, P. Koudelova, H. Chen, Y. Ma, J. Huang, K. Taniguchi, and R. Zhang (2008): Aerosol-hydrologic cycle interaction: A new challenge to monsoon climate research, *Bull. Amer. Meteor. Soc.*, 89, DOI: 10.1175/BAMS-89-3-369.

Lee, K. H., Z. Li, M. S. Wong, J. Xin, Y. Wang, W.-M. Hao, and F. Zhao (2007), Aerosol single scattering albedo estimated across China from a combination of ground and satellite measurements, *J. Geophys. Res.*, 112, D22S15, doi:10.1029/2007JD009077.

Lee, K. H., Z. Li, M.C. Cribb, J. Liu, L. Wang, Y. Zheng, X. Xia, H. Chen, and B. Li (2010), Aerosol optical depth measurements in eastern China and a new calibration method, *J. Geophys. Res.*, 115, D00K11, doi:10.1029/2009JD012812.

Li, Z., (2004), Aerosol and climate: A perspective from East Asia, in "*Observation, Theory, and Modeling of the Atmospheric Variability*", p501-525, World Scientific Pub. Co..

Li, Z., et al., (2007a), Aerosol optical properties and their radiative effects in northern China, J. Geophys. Res., 112, D22S01, doi:10.1029/2006JD007382.

Li, Z., et al., (2007b), Preface to special section: Overview of the East Asian Study of Tropospheric Aerosols: an International Regional Experiment (EAST-AIRE), *J. Geophy. Res.*, 112, D22S00, doi: 10.1029/2007JD008853.

Li, Z., F. Niu, K.-H. Lee, J. Xin, W.-M. Hao, B. Nordgren, Y. Wang, and P. Wang (2007c), Validation and Understanding of MODIS Aerosol Products Using Ground-based Measurements from the Handheld Sunphotometer Network in China, *J. Geophy. Res.* 112, D22S07, doi:10.1029/2007JD008479.

Li, Z., K.-H. Lee, Y. Wang, J. Xin, and W.-M. Hao (2010), First observation-based estimates of cloud-free aerosol radiative forcing across China, *J. Geophys. Res.*, 115, D00K18, doi:10.1029/2009JD013306.

Li, C., L.T. Marufu, R. R. Dickerson, Z. Li, T. Wen, Y. Wang, P. Wang, H. Chen, and J. W. Stehr (2007), In situ measurements of trace gases and aerosol optical properties at a rural site in northern China during East Asian Study of Tropospheric Aerosols: An International Regional Experiment 2005, J. Geophys. Res., 112, D22S04, doi:10.1029/2006JD007592.

Li, C., N. A. Krotkov, R. R. Dickerson, Z. Li, K. Yang, and M. Chin (2010a), Transport and evolution of a pollution plume from northern China: A satellite-based case study, *J. Geophys. Res.*, 115, D00K03,

doi:10.1029/2009JD012245.

Li, C., T. Wen, Z. Li, R. R. Dickerson, Y. Yang, Y. Zhao, Y. Wang, and S.-C. Tsay (2010b), Concentrations and origins of atmospheric lead and other trace species at a rural site in northern China, *J. Geophys. Res.*, doi:10.1029/2009JD013639, in press.

Li, C., et al. (2010c), Anthropogenic air pollution observed near dust source regions in northwestern China during springtime 2008, *J. Geophys. Res.*, doi:10.1029/2009JD013659, in press.

Liang, F., and X. Xia (2005), Long-term trends in solar radiation and the associated climatic factors over China for 1961-2000, *Annales Geophys*, 23, 2425-2432.

Liu, Y., D. Yang, W. Chen, and H. Zhang (2010), Measurements of Asian dust optical properties over the Yellow Sea of China by shipboard and ground-based photometers, along with satellite remote sensing: A case study of the passage of a frontal system during April 2006, *J. Geophys. Res.*, 115, D00K04, doi:10.1029/2009JD012684.

Logan, T., B. Xi, X. Dong, R. Obrecht, Z. Li, and M. Cribb (2010), A study of Asian dust plumes using satellite, surface, and aircraft measurements during the INTEX-B field experiment, *J. Geophys. Res.*, doi:10.1029/2010JD014134, in press.

Luo, Y., D. Lu, X. Zhou, and W. Li, (2001), Characteristics of the spatial distribution and yearly variation of aerosol optical depth over China in last 30 years, *J. Geophys. Res.*, 106, 14501-14513.

Menon, S., J. Hansen, L. Nazarenko, and Y. Luo, (2002), Climate effects of black carbon in China and India, *Science*, 297, 2250-2252.

Mi, W., Z. Li, X. Xia, B. Holben, R. Levy, F. Zhao, H. Chen, and M. Cribb (2007), Evaluation of the Moderate Resolution Imaging Spectroradiometer aerosol products at two Aerosol Robotic Network stations in China, J. Geophys. Res., 112, D22S08, doi:10.1029/2007JD008474.

Niu, F., Z. Li, C. Li, K.-H. Lee, and M. Wang (2010), Increase of wintertime fog in China: Potential impacts of weakening of the Eastern Asian monsoon circulation and increasing aerosol loading, J. Geophys. Res., 115, D00K20, doi:10.1029/2009JD013484.

Nakajima, T., et al. (2003), Significance of direct and indirect radiative forcings of aerosols in the East China Sea region, *J. Geophys. Res.*, *108*(D23), 8658, doi:10.1029/2002JD003261.

Norris, J. R. and Wild, M.: Trends in aerosol radiative effects over China and Japan inferred from observed cloud cover, solar "dimming," and solar "brightening", J. Geophys. Res., 114, 1–11, doi:10.1029/2008JD011378, 2009.

Philipona, R., (2002), Underestimation of solar global and diffuse radiation measured at Earth's surface. *J. Geophys. Res.,* **107,** 4654, doi:10.1029/2002JD002396.

Qian, Y. and F. Giorgi, (2000), Regional climatic effects of anthropogenic aerosols? The case of Southwestern China, *Geophys. Res. Lett.*, 27(21), 3521-3524.

Qian, W.H., Quan, L., Shi, S., (2002). Variations of the dust storm in China and its climatic control. Journal of Climate, 15, 1216–1229.

Qian, Y., L.R. Leung, S.J. Ghan, and F. Giorgi. (2003). Effects of Increasing Aerosol on Regional Climate Change in China: Observation and Modeling. *Tellus B*, 55(4), 914-934.

Qian, Y., D. P. Kaiser, L. R. Leung, and M. Xu (2006), More frequent cloud-free sky and less surface solar radiation in China from 1955 to 2000, *Geophys. Res. Lett.*, *33*, L01812, doi:10.1029/2005GL024586.

Qian, Y., W. Wang, L. R. Leung, and D. P. Kaiser, (2007), Variability of solar radiation under cloud-free skies in China: The role of aerosols, *Geophys. Res. Lett.*, *34*, L12804, doi:10.1029/2006GL028800.

Qian, Y., D. Gong, J. Fan, L. R. Leung, R. Bennartz, D. Chen, and W. Wang (2009), Heavy pollution suppresses light rain in China: Observations and modeling, *J. Geophys. Res.*, 114, D00K02, doi:10.1029/2008JD011575.

Ramanathan, V., et al. (2001), Indian Ocean Experiment: An integrated analysis of the climate forcing and effects of the great Indo-Asian haze, *J. Geophys. Res.*, *106*, 28,371–28,398.

Ramanathan, V., C. Chung, D. Kim, T. Bettge, L. Buja, J. T. Kiehl, W. M. Washington, Q. Fu, D. R. Sikka, and M. Wild, 2005: Atmospheric Brown Clouds: Impacts on South Asian climate and hydrological cycle. *Proc. Natl. Acad. Sci. U. S. A.*,, Vol. 102, No. 15, 5326-5333.

Rosenfeld, D., Y. Rudich, and R. Lahav (2001), Desert dust suppressing precipitation: A possible desertification feedback loop, *Proc. Natl. Acad. Sci. U. S. A.*, 98, 5975-5980.

Rosenfeld, D., et al. (2007), Inverse relation between amounts of air pollution and orographic precipitation, *Science*, 315, 1396-1398.

Shi, G., T. Hayasaka, A. Ohmura, Z. Chen, B. Wang, J. Zhao,

H. Che, L. Xu (2008), Data quality assessment and the long-term trend of ground solar radiation in China, *J. Appl. Meteor*., *47*(4), 1006-1016.

Streets, D. G., et al. (2003), An inventory of gaseous and primary aerosol emissions in Asia in the year 2000, *J. Geophys. Res.*, 108, 8809, doi:10.1029/2002JD003093.

Sullivan, R. C., S. A. Guazzotti, D. A. Sodeman, and K. A. Prather (2007), Direct observations of the atmospheric processing of Asian mineral dust, *Atmos. Chem. Phys*., 7, 1213–1236, 2007.

Sun, Y., et al. (2010), Asian dust over northern China and its impact on the downstream aerosol chemistry in 2004, *J. Geophys. Res.*, 115, D00K09, doi:10.1029/2009JD012757.

Tsay, S.-C., G.-R. Liu, N. C. Hsu, W.-Y. Sun, and et. al., (2009), Outbreaks of Asian dust storms: An overview from satellite and surface perspectives. Recent Progress in Atmospheric Sciences: Applications to the Asia Pacific Region, World Scientific, 373-401.

Wang, B., and G. Shi (2010), Long-term trends of atmospheric absorbing and scattering optical depths over China region estimated from the routine observation data of surface solar irradiances, *J. Geophys. Res.*, doi:10.1029/2009JD013239, in press.

Wang, G., J. Huang, W. Guo, J. Zuo, J. Wang, J. Bi, Z. Huang, and J. Shi (2010), Observation analysis of land-atmosphere interactions over the Loess Plateau of northwest China, *J. Geophys. Res.*, 115, D00K17, doi:10.1029/2009JD013372.

Wang, J. M., and Y. Mitsuta (1992), Evaporation from the desert - A preliminary result of HEIFE. *Boundary-Layer Meteorology*, Vol. 59, No. 4, pp. 413-41.

Wang, S.-H., N.-H. Lin, C.-F. OuYang, J.-L. Wang, J. R. Campbell, C.-M. Peng, C.-T. Lee, G.-R. Sheu, and S.-C. Tsay (2010), Impact of Asian dust and continental pollutants on cloud chemistry observed in northern Taiwan during the experimental period of ABC/EAREX 2005, *J. Geophys. Res.*, doi:10.1029/2009JD013692, in press.

Wang, T. J., S. Li, F. Shen, J. Deng, and M. Xie (2010), Investigations on direct and indirect effect of nitrate on temperature and precipitation in China using a regional climate chemistry modeling system, *J. Geophys. Res.*, doi:10.1029/2009JD013264, in press.

Wang, X., J. Huang, R. Zhang, B. Chen, and J. Bi (2010), Surface measurements of aerosol properties over Northwest China during ARM China-2008 deployment, J. *Geophys. Res.*, doi:10.1029/2009JD013467, in press.

Wild, M, H. Gilgen, and A. Roesch, (2005), From dimming to brightening: Decadal changes in solar radiation at Earth's surface. *Science*, 308, 847-850.

Xia, X., Z. Li, B. Holben, P. Wang, T. Eck, H. Chen, M. Cribb, and Y. Zhao (2007a), Aerosol optical properties and radiative effects in the Yangtze Delta region of China, *J. Geophys. Res.*, 112, D22S12, doi:10.1029/2007JD008859.

Xia, X., H. Chen, Z. Li, P. Wang, and J. Wang (2007b), Significant reduction of surface solar irradiance induced by aerosols in a suburban region in northeastern China, *J. Geophys. Res.*, 112, D22S02, doi:10.1029/2006JD007562

Xia, X., Z. Li, P. Wang, H. Chen, and M. Cribb (2007c), Estimation of aerosol effects on surface irradiance based on measurements and radiative transfer model simulations in northern China,J. Geophys. Res., 112, D22S10, doi:10.1029/2006JD008337

Xia, X. (2010a), Spatiotemporal changes in sunshine duration and cloud amount as well as their relationship in China during 1954–2005, *J. Geophys. Res.*, 115, D00K06, doi:10.1029/2009JD012879.

Xia, X. (2010b), A closer looking at dimming and brightening in China during 1961-2005, Ann. Geophys., 28, 1121-1132.

Xin, J., et al. (2007), Aerosol optical depth (AOD) and Ångström exponent of aerosols observed by the Chinese Sun Hazemeter Network from August 2004 to September 2005, *J. Geophys. Res.*, 112, D05203, doi:10.1029/2006JD007075.

Xu, Q., (2001), Abrupt change of the mid summer climate in central east China by the influence of atmospheric pollution, *Atmos. Environ*, 35, 5029-5040.

Xu, M., C. - P. Chang, C. Fu, Y. Qi, A. Robock, D. Robinson, and H. Zhang (2006), Steady decline of east Asian monsoon winds, 1969–2000: Evidence from direct ground measurements of wind speed, *J. Geophys. Res.*, 111, D24111, doi:10.1029/2006JD007337.

Zhuang, B. L., L. Liu, F. H. Shen, T. J. Wang, and Y. Han (2010), Semidirect radiative forcing of internal mixed black carbon cloud droplet and its regional climatic effect over China, *J. Geophys. Res*., 115, D00K19, doi:10.1029/2009JD013165.

Zhang, J., H. Chen, Z. Li, X. Fan, L. Peng, Y. Yu, and M. Cribb (2010), Analysis of cloud layer structure in Shouxian, China using RS92 radiosonde Aided by 95-GHz cloud radar, *J. Geophys. Res.*,

doi:10.1029/2010JD014030, in press.

Zhang, L., H. Liao, and J. Li (2010), Impacts of Asian summer monsoon on seasonal and interannual variations of aerosols over eastern China, *J. Geophys. Res*., 115, D00K05, doi:10.1029/2009JD012299

Zhang, R., G. Li, J. Fan, D. L. Wu, and M. J. Molina (2007), Intensification of Pacific storm track linked to Asian pollution, *Proc. Natl. Acad. Sci. U. S. A.*, 104, 5295–5299, doi:10.1073/pnas.0700618104.

Zhang, Y., Q. Yu, W. Ma, and L. Chen (2010), Atmospheric deposition of inorganic nitrogen to the eastern China seas and its implications to marine biogeochemistry, J. Geophys. Res., 115, D00K10, doi:10.1029/2009JD012814.

Zhao, F., and Z. Li (2007), Estimation of aerosol single scattering albedo from solar direct spectral radiance and total broadband irradiances measured in China, *J. Geophys. Res.*, 112, D22S03, doi: 10.1029/2006JD007384.

Zhao, T. L., S. L. Gong, X. Y. Zhang, and D. A. Jaffe (2008), Asian dust storm influence on North American ambient PM levels: observational evidence and controlling factors, *Atmos. Chem. Phys.*, 8, 2717–2728.

Aerosol Optical Characteristics Observed by Sky Radiometer over Loess Plateau in China during 2009

Bi J. R.[1], J. P. Huang[1], Y. Z. Liu[1], Z. W. Huang, G. Y. Shi[2], and T. Takamura[3]

[1]*Key Laboratory for Semi-Arid Climate Change of the Ministry of Education and College of Atmospheric Sciences, Lanzhou University, Lanzhou, 730000, PRC*

[2]*State Key Laboratory of Numerical Modeling for Atmospheric Sciences and Geophysical Fluid Dynamics (LASG), Institute of Atmospheric Physics, Chinese Academy of Sciences, Beijing, 100029, PRC*

[3]*Center for Environmental Remote Sensing (CEReS), Chiba University, 1-33 Yayoi-cho, Inage-ku, Chiba 263-8522, JAPAN*

Abstract

Aerosol optical characteristics observed by a POM-01 sky radiometer over Loess Plateau in China during the period from March 15th to October 31th 2009. A good agreement was implemented by the improved Langley method. The measured and retrieved AOD from the PREDE sky radiometer are very consistent with the measured by Cimel sunphotometer's results. We find that the daily average values of AOD_{500} and Ångström exponent (α) both show very large day-to-day variations, especially during the springtime. The relationship between AOD_{500} and Ångström exponent shows obvious negative correlation during the whole period. Dust aerosol particles are dominant during springtime at SACOL, and fine mode particles are predominant during summertime due to the impact of the rainy season.

Keywords **:** Aerosol optical characteristics, Loess Plateau, improved Langley method, Ångström exponent

***Corresponding Author:** Mr. Jianrong Bi, email: bijr@lzu.edu.cn

Brief instruction of the author: Jianrong Bi, Key Laboratory for Semi-Arid Climate Change of the Ministry of Education and College of Atmospheric Sciences, Lanzhou University, Lanzhou, 730000, P.R.China. (o):+86-931-5292611, E-mail: bijr@lzu.edu.cn. Now specializing in aerosol-cloud-radiation interaction with the climate change.

1. Introduction

Aerosol particles can scatter and/or absorb shortwave and long-wave radiation in the atmosphere, and then play an important role in the global and regional climate (Huang et al., 2006a,b; Li et al., 2007). There was extensive research to been conducted in climatic effects of aerosols, these studies are vital to understand the characteristics and variations of aerosol and we can evaluate more accurately the effects of aerosols on global and regional climate change in the future. However, aerosol radiative forcing and their climatic effects still contain considerable uncertainties due to both aerosol loading and properties exhibit great spatial and temporal variations (*Intergovernmental Panel on Climate Change, 2007)*. Satellite remote sensing and ground-based observations are two effective ways to understand accurately knowledge of aerosol loading and properties. Satellite retrievals need some assumptions and using ancillary meteorological data which might cause errors in the results (Takamura et al., 2009). Comparing with satellite remote sensing, ground-based measurements is more accurate and it can improve the climate model, validation of space-borne observations as well as (Huang et al., 2008).

The SKYNET is a well known ground-based observation network to understand aerosol-cloud-radiation interaction in the atmosphere (Takamura et al., 2009). The main instruments consist of a sky radiometer and radiation instruments such as a pyrenometer and pyrgeometer. SKYNET operates sky radiometers in the Asia-Pacific region for many years. The objective of this work is to examine aerosol optical characteristics over Loess Plateau in Northwester China based on continuous spectral solar direct irradiance and scattering radiance measurements by a sky radiometer during March 15th to October 31th, 2009.

2. Instrument and measurement

A sky radiometer (also known as aureolemeter) Model POM-01, produced by PREDE Co. is deployed to SACOL Observatory (Lat: 35.95°N, Lon: 104.13°E, Alt: 1970m)

over Loess Plateau in Northwestern China since March 15th 2009. SACOL is a rural site and located on the top of Tsuiying mountain, which is about 50 km southeast of Lanzhou city at the southern bank of Yellow River (Huang et al., 2008). The detailed descriptions of the instrument and data acquisition procedures were given by Aoki et al. (2003). The radiometer takes measurements of the solar direct irradiance and sky scattering radiance distributions and has seven interference filters. And we just utilize five wavelengths (400, 500, 675, 870, and 1020 nm) to retrieved aerosol optical properties.

3. Data inversion

The aerosol optical characteristics (including aerosol optical depth, Ångström exponent, volume size distribution, single scattering albedo, normalized phase function, complex refractive index of real and imaginary part) can be retrieved by using the "SKYRAD.pack Ver. 4.2" inversion algorithm developed by Nakajima et al. (1996). And a cloud screening method developed by Khatri et al. (2009) was employed firstly to eliminate the cloud contamination data and artificial observations. An important features of the inversion algorithm is that an improved Langley plot method has been used to calculate the calibration constants V_0 of instrument (Nakajima et al., 1996; Boi et al., 1999) in the equation, $V=V_0\times\exp(-m\times\tau)$, where V, m and τ represent the measured radiance, air optical mass and total extinction optical depth respectively. In the normal Langley method, the calibration constants are obtained by performing a logarithmic plot of the optical mass (m) versus measured solar direct irradiance when assuming that the aerosol optical depth remains stable during the whole calibration period. However, this is not satisfied at most locations and under most situations. Accordingly, an modified Langley method (MLM) was been developed (Tanaka et al., 1986), in which temporarily variable atmospheric turbidity was taken into account. Nakajima et al. (1996) extended Tanaka's method (MLM). Firstly, an inversion with only forward scattering intensity data (scattering angle: 3~30°) is performed. Then derived temporarily variable aerosol optical depths (AOD) are multiplied by the corresponding air optical mass (m) and used to obtained values of the abscissa for a V-($m\times\tau_a$) scattering graph. Finally, the calibration constant is obtained through a linear fit of the data points. More accurate calibration is expected since this extension allows the relative size distribution to vary with time. Hence, MLM is utilized in the study of calibrating the sun/sky radiometer.

4. Results

4.1. Calibration result of radiometer

Figure 1 illustrates an example of calibration on May 6th 2009 at SACOL. There was a large difference between the calibrations in the morning and the afternoon when normal Langley method was used (see Fig. 1a). Obviously, it was artificial since the calibrations were carried out at the same day, so the similar results should be derived. The good agreement was performed when improved Langley method was employed as shown in Figure 1b. The time series of calibration constants on the basis of MLM is depicted in

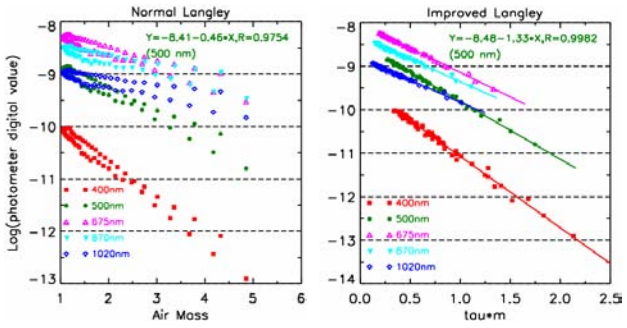

Figure 1. Calibration results obtained by using the normal Langley (left) and improved Langley (right) methods based on radiometer measurements on May 6 2009 at SACOL.

Figure 2a. indicates that the variations of V_0 at five wavelengths keep stable during the 2009. Figure 2b illustrates the corresponding monthly averaged values of V_0, which are obtained by taking running and smooth of the time series data. And there is a corresponding V_0 value for each wavelength of each month to simulate aerosol optical depths.

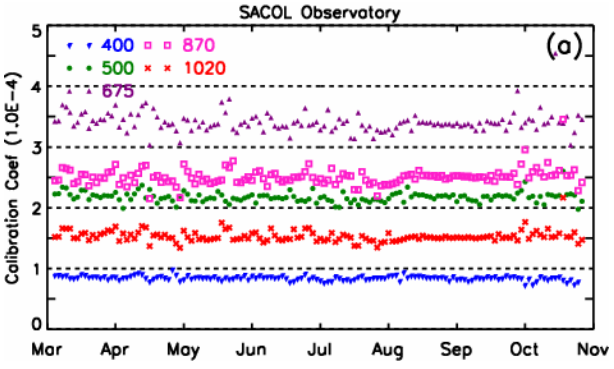

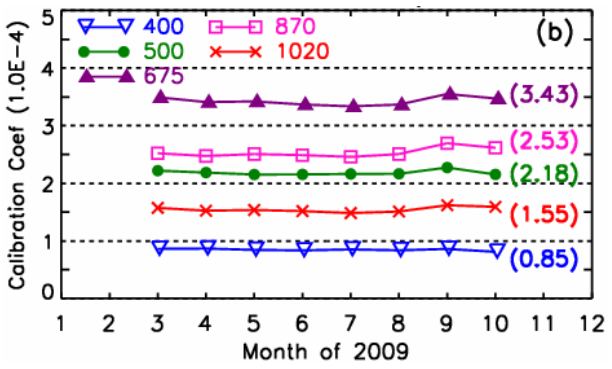

Figure 2. Time series (a) and monthly averaged (b) of calibration constants obtained by MLM. Overall average at each wavelength in parentheses in (b).

4.2. Inter-comparison with sunphotometer's result

In order to confirm the accuracy of inversion results obtained from sky radiometer, we compare between the aerosol optical depths derived from sky radiometer and sunphotometer. Figure 3 delineates a comparison between the AOD measured by a Cimel sunphotometer and the measured and retrieved AOD from the PREDE sky radiometer on April 7th 2009 at SACOL. The results show that AODs derived from PREDE sky radiometer and Cimel sunphotometer are very consistent.

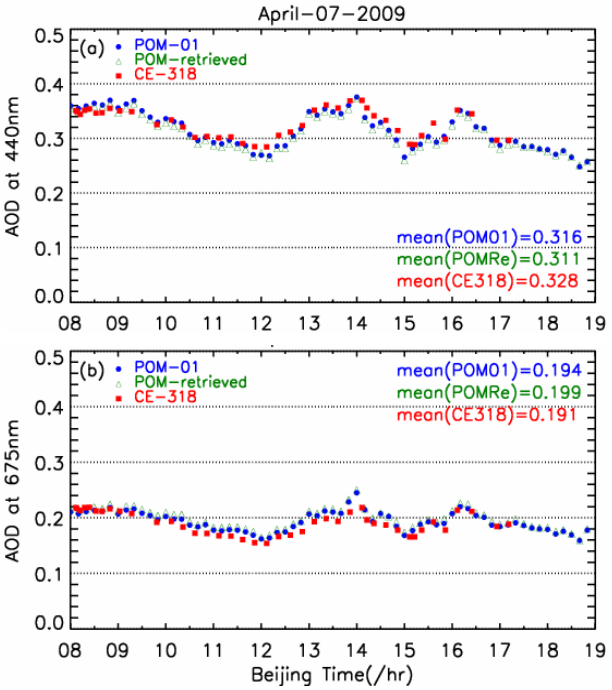

Figure 3. A comparison of AOD between sky radiometer and sun photometer at 440 nm (a) and 675 nm (b) on April 7th 2009 at SACOL

4.3. Mean daily variation

Figure 4 shows the daily mean variations of aerosol optical depth at 500 nm (AOD_{500}) and Ångström exponent (α) from the period of March 15th to October 31th 2009 at SACOL. The daily average values of AOD_{500} and Ångström exponent (α) both show very large day-to-day variations, especially during the springtime. It is also obvious that when the daily mean values of AOD_{500} are large, the daily averaged values of Ångström exponent are small, and vice versa.

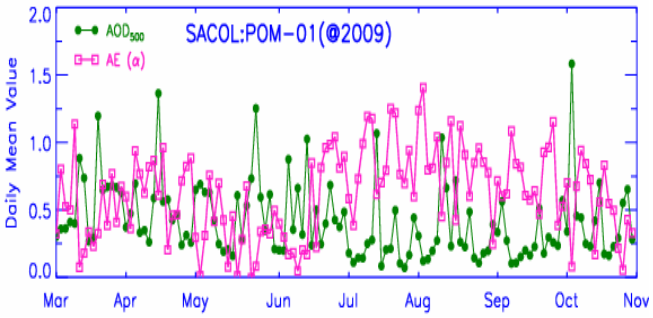

Figure 4. Mean daily values of aerosol optical depth at 500 nm (AOD_{500}) and Ångström exponent (α) during 2009 at SACOL.

4.4. Relationship between Ångström exponent versus AOD_{500}

Figure 5 depicts the relationship between Ångström exponent vs. AOD_{500} during spring and summer 2009 at SACOL. There is a significant feature that the relationship between AOD_{500} and Ångström exponent shows obvious negative correlation during the whole period. Dust aerosol particles are dominant from March to June at SACOL, and fine mode particles are predominant form July to August due to the impact of the rainy season.

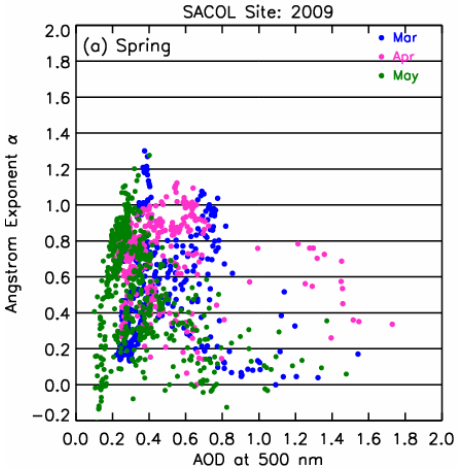

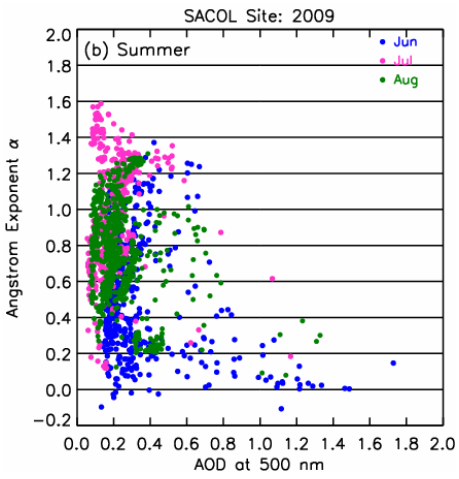

Figure 5. The relationship between Ångström exponent versus AOD_{500} during spring (a) and summer (b) 2009 at SACOL.

5. Conclusions and Discussions

Solar direct irradiance and sky scattering radiance measurements by a sky radiometer have been utilized to retrieve aerosol optical properties during 2009 over Loess Plateau in China. A good agreement was implemented by the improved Langley method. The measured and retrieved AOD from the PREDE sky radiometer are very consistent with the measured Cimel sunphotometer's results. The daily average values of AOD_{500} and Ångström exponent (α) both show very large day-to-day variations, especially during the springtime. The relationship between AOD_{500} and Ångström exponent shows obvious negative correlation. Dust aerosol particles are dominant during springtime at SACOL, and fine mode particles are predominant during summertime due to the impact of the rainy season.

Acknowledgements

SACOL was sponsored by Lanzhou University through 985 Program. We greatly appreciate Prof. Takamura and Dr. Khatri (CEReS, Chiba Univ., Japan), as well as Prof. G. Y. Shi's (LASG, IAP, CAS, China) support. We are grateful of Prof. Nakajima (CCSR, Tokyo Univ., Japan) for providing SKYRAD software. Also thanks for Dr. Z. Z. Wang (AIOFM, CAS, China). Thank you for all the people who are contributed to this job.

References

1) Huang, J., P. Minnis, B. Lin, T. Wang, Y. Yi, Y. Hu, S. Sun-Mack, and K. Ayers, 2006a, Possible influences of Asian dust aerosols on cloud properties and radiative forcing observed from MODIS and CERES, *Geophys. Res. Lett.*, **33**, L06824, doi:10.1029/2005GL024724.

2) Huang, J., Y. Wang, T. Wang, and Y. Yi, 2006b: Dusty cloud radiative forcing derived from satellite data from middle latitude regions of East Asia, *Progress in Natural Science*. **16**(10), 1084-1089.2)

3) Li Z., H. Chen, M. Cribb, R. Dickerson, B. Holben, and C. Li, et al., 2007: Preface to special section: Overview of the East Asian Study of Tropospheric Aerosols: an International Regional Experiment (EAST-AIRE), *J. Geophys. Res.* **112**, D22S00, doi:10.1029/2007JD008853.

4) Intergovernmental Panel on Climate Change (2007), *Climate Change 2007: The Scientific Basis-Contribution of Working Group I to the Fourth Assessment Report of the Intergovernmental Panel on Climate Change*, edited by S. Solomon et al., **1056** pp., Cambridge University Press, New York.

5) Takamura T., Takenaka H., Y. Cui, Nakajima T. Y., Higurashi A., Fukuda S., Kikuchi N., Nakajima T., Sano I., and R. T. Pinker, 2009:Aerosol and Cloud Validation System Based on SKYNET Observations: Estimation of Shortwave Radiation Budget Using ADEOS-II/GLI Data, *Journal of The Remote Sensing Society of Japan*, **29**(1), pp. 40-53.

6) Huang, J., W. Zhang, J. Zuo, J. Bi, J. Shi, X. Wang and Z. Chang, et al., 2008: An overview of the Semi-Arid Climate and Environment Research Observatory over the Loess Plateau, *Advances in Atmospheric Sciences*, ***25***(6), 1-16.

7) Aoki Kazuma and Yasushi Fujiyoshi, 2003: Sky Radiometer Measurements of Aerosol Optical Properties over Sapporo, Japan, *Journal of the Meteorological Society of Japan*, **81**(3), 493-513.

8) Nakajima T., G. Tonna, R. Rao, Y. Kaufman, and B. Holben, 1996: Use of sky brightness measurements from ground for remote sensing of particulate polydispersions, *Appl. Opt.*, **35**, 2672-2686.

9) Khatri, P. and T. Takamura, 2009: An algorithm to screen cloud-affected data for sky radiometer data analysis, *J. Meteorol Soc. Jpn.*, **87**, 189-204.

10) Boi, P., G. Tonna, G. Dalu, T. Nakajima, B. Olivieri, A. Pompei, M. Campanilli and R. Rao, 1999: Calibration and data elaboration procedure for sky irradiance measurements. *Appl. Opt.*, **38**, 896-907.

11) Tanaka, M., Nakajima, T., Shiobara, M., 1986: Calibration of a sunphotometer by simultaneous measurements of direct-solar and circumsolar radiations. *Applied Optics*, **25**, 1170-1176.

Characteristics of Dust Aerosol derived from sky-radiometer over Loess Plateau of Northwest China

Jianrong Bi[1],Yuzhi Liu[1], Jianping Huang[1], Guangyu Shi[2], Tamio Takamura[3], Zhong wei Huang[1], Pradeep Khatri[3], Jinsen Shi[1], Tianhe Wang[1], Xin Wang[1], Beidou Zhang[1]

[1] *Key Laboratory for Semi-Arid Climate Change of the Ministry of Education and College of Atmospheric Sciences, Lanzhou University, Lanzhou, 730000, PRC*

[2] *LASG, Institute of Atmospheric Physics, Chinese Academy of Sciences, Beijing 100029, PRC*

[3] *Center for Environmental Remote Sensing, Chiba University, Chiba, Japan*

Abstract

This study investigates the characteristics of dust aerosols over Loess Plateu of Northwest China using observation data collected in this region during 2009 and 2010. As the first part of the research, comparison of aerosol optical thickness (AOT) and single scattering albedo (SSA) measured by two independent instruments (SKYNET sky radiometer and AERONET sun photometer) is performed. We find very good agreement of AOT, whereas SSA from the former instrument is systematically higher than the latter on. The possible reasons for such differences are discussed. As the second part of the study, we study the characteristics of dust aerosols in this region. We find that strong dust events can carry high concentration of anthropogenic aerosols, such as black carbon (BC) aerosol, during their transport from the source region. This finding may provide some clues to justify absorptive Asian dust aerosols observed in the Pacific Ocean region in the past studies. The study also suggests that significant dust aerosols may exist in the atmosphere of this region even during no dust event days.

Keywords: dust aerosol, aerosol optical thickness, BC aerosol

1. Introduction

Aerosols are known to alter the atmospheric heat budget and climate by their direct (scattering and absorption of solar radiation) and indirect (modification of microphysical and optical properties of clouds). Despite the importance of aerosols on climate change, the roles of aerosols on climate change phenomenon are still not well understood. This is primarily due to short life time and variability of aerosols on space and time. In order to improve our understanding regarding aerosol effects on climate change, it is necessary to collect information of aerosols of various origins.

Among several types of aerosols, the characteristics of dust aerosols are still subject of debate (e.g.,Nakajima et al. 2007). It is likely that dust aerosols have different optical characteristics depending on geographical location. Moreover, when dust aerosols, originated from arid and semi-arid areas, transport over long distances, they mix with anthropogenic aerosols. Such mixed aerosols can have important effect on both regional and global climate. The observation data collected near the source region of dust aerosols may provide valuable clues to solve climatic effects of such mixed aerosols. As the semi-arid region of northwestern China is close to the Taklamakan and Gobi deserts, data collected at this region are of great importance to study several important aspects of dust aerosols. In view of this recognition, this study is designed to understand the characteristics of dust aerosols over Loess Plateau of Northwest China.

2. Observation site and instrumentation

Sky radiometer (Model POM-01, Manufacture: PREDE Co. Ltd. Japan) has been operated at Semi-Arid Climate Observatory and Laboratory (SACOL) (35.047^0N,104.136^0E) (http://climate.lzu.edu.cn) from March, 2009 as a part of SKYET actives of SKYNET network (http://atmos.cr.chiba-u.ac.jp). Since SACOL is a rural site, and it is located at southeast of Lanzhou city and south edge of Gobi desert, it is possible to observe various types of aerosols, including anthropogenic aerosol, natural dust, relatively background aerosol depending on the atmospheric condition and route of air masses. Due to the special geographical location and good infrastructure, it has become a super site for atmospheric study. In order to further understand the characteristics of dust aerosols in more detail, POM-02 sky radiometer was operated during an intensive field observation conducted from 20 April to 20 June, 2010 at Minqin Desert Control Research Institute (38.607^0N,102.959^0E). This study mainly uses data measured by such sky radiometers. In addition, we also used black carbon (BC) mass concentration measured by

aethalometer (Model AE-31; Manufacturer: Magee Scientific)

The detailed description of the sy radiometer instrument and data retrieval procedures can be found elsewhere (e.g., Nakajima et al., 1996; Khatri and Takamura 2009). In brief, the instrument measures spectral direct solar irradiance and diffuse sky irradiances at predefined scattering angles. Such measured data were inverted using SKYRAD.PACK (version 4.2) software (Nakajima et al., 1996) and calibration constants obtained from improved methods of Nakajima et al. (1996). The retrieved parameters are aerosol optical thickness (AOT), single scattering albedo (SSA), and refractive indices at 400nm, 500nm, 675nm, 870nm, and 1020nm for POM-01 and 340nm, 380nm, 400nm,500nm,675nm,870nm, and 1020nm for POM-02 instrument. In addition, another important retrieved parameter is volume size distribution at 20 size bins for both POM-01 and POM-02. Such retrieved parameters were further processed by using cloud screening algorithm of Khaitr and Takamura (2009).

3. Results and discussion

3.1. Intercomparison of key aerosol optical parameters obtained from SKYNET sky radiometer and AERONET sunphotometer

As SACOL was also equipped with sun photometer of AERONET network (Holben et al., 2003), which measures same optical parameters of sky radiometer of SKYNET network, it was a good opportunity to perform closure study of key aerosol parameters. Figure 1 shows comparison of AOTs at four wavelengths (400nm and 440nm, 675nm, 870nm, and 1020nm). As shown in the Figure, the comparison result is relatively good with data falling around 1:1 line. It is worth to note that the calibration constant for direct irradiances obtained from Improved Langley (IL) method using surface observation data are used for SKYNET sky radiometers (Nakajima et al., 1996), whereas as AERONET sun photometers are relied on calibration constants determined at high mountains using Normal Langley (NL) technique. The latter technique is inconvenient and economically expensive. The observed good agreement in Figure (1) may verify the accuracy of IL method adopted for SKYNET sky radiometers, and may suggest that observed AOTs in this study can be interpreted with much more confidence level. Figure (2) shows comparison of SSAs obtained from two independent instruments. In contrast to AOTs, the differences in instantaneous SSA are considerably large. The possible reasons for such poor agreement may be explained due to the difference in retrieval algorithm and measurement protocol of sky radiances. Since SSA is very sensitive to AOT, surface reflectance etc., some differences on those parameters might have also caused to differ SSA. Despite such discrepancies, two important conclusions can be drawn from Figure 2: (i) Using present versions of algorithms, SSAs from SKYNET sky radiometer are systematically higher than AERONET sun photometer (ii). The average columnar SSAs at all wavelengths are relatively small at this remote site. This indicates the transportation of light absorbing aerosols from urban atmosphere. Taking into account of the fact that this area is often under the influence of dust aerosols with higher concentration during spring season, it can be suggested that such dust aerosols can mix with strongly light absorbing aerosols transported from urban areas. Since the surface reflectance of this area is relatively high, such light absorptive aerosol mixture can trap radiation energy in the atmosphere more significantly. As a result, aerosols of this region can have very significant effect on atmospheric heat budget and regional climate. Such effects can be numerically evaluated using radiative transfer model.

3.2. Optical characteristics of aerosols during dust storm events

Figure 3 shows aerosol optical thickness at 500nm and Angstrom exponent from 22 April 2010 to 20 June 2010 at Minqin observation site. During this observation period, frequent heavy dust events were observed. The observed dust events are denoted in Figure 3(a). As shown in Figure 3(a), during such dust events, AOT at 500nm increased drastically. Such drastically increased AOTs are compensated by low values of Angstrom exponent. The indicates the dominance of coarse mode aerosols in comparison to fine mode aerosols. It is worth to note in Figures 3(a) and 3(b) that dust events are frequently observed within the gaps of few days. Another thing to be noted in Figure 3(a) is the sudden decrease of AOT after dust event. This suggests that dust aerosols are lifted by strong winds, suggesting the possibility of reaching such dust aerosols over the Pacific Ocean and beyond it. As a part of understanding the characteristics of dust aerosols in more detail, volume size distribution of one typical dust event of May 3 is compared with relatively clean observation day of May 22. Table 1 shows geometrical mean radius and volume concentration of fine and coarse mode aerosols for those two observation days. As shown in Figure 4 and Table

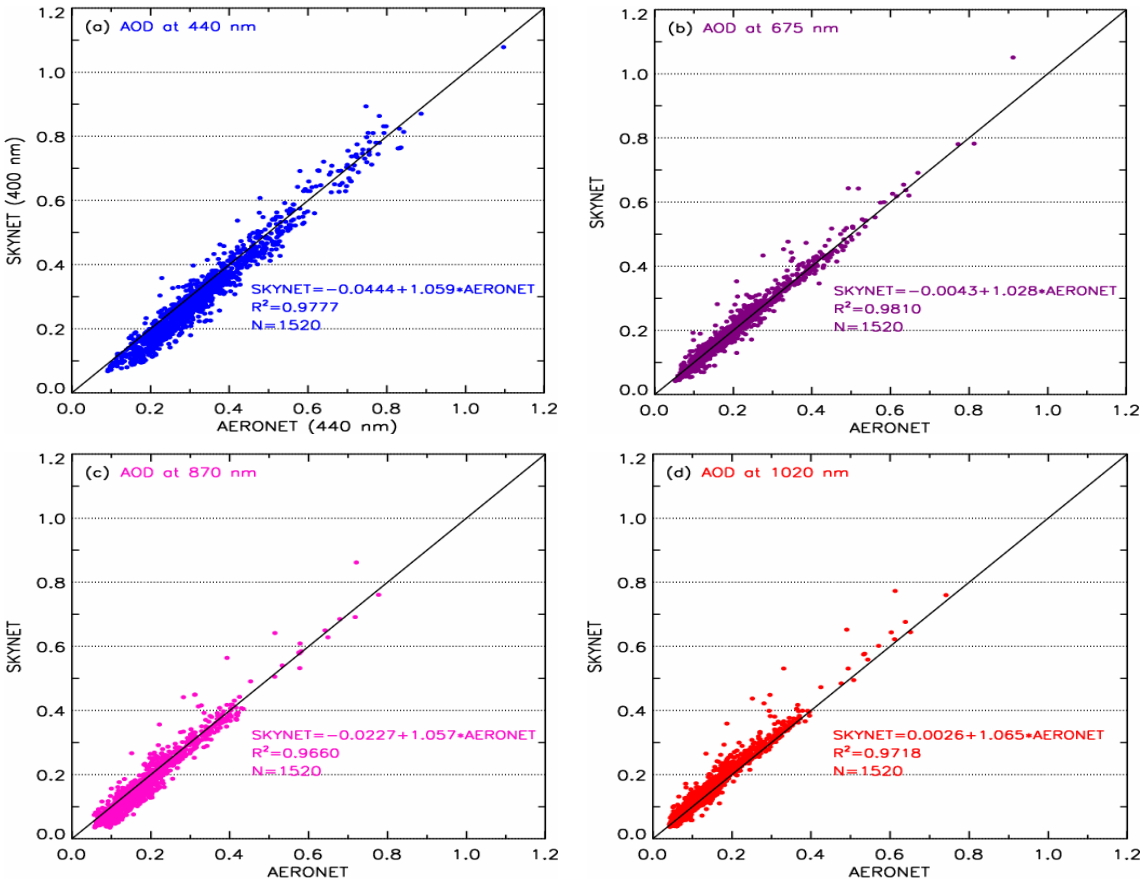

Figure 1. Comparison of AOTs between sky radiometer of SKYNET network and sun photometer of AERONET network at (a) 400nm and 440nm, (b) 675nm, (c) 870nm, and (d) 1020nm during 2009.

1 that during the dust event day of May 3, volume concentration of coarse mode aerosols largely dominate fine mode aerosols. Interestingly, Table 1 shows that coarse mode aerosols contributed more than 99.5% to total volume concentration on dust event day of May 3. Table 1 also suggests the presence of relatively large size ranged dust aerosols on May 3 in comparison to May 22. One pronouncing feature to be noted in Figure 4 and Table 1 is that even during the clear day of May 22, coarse mode aerosols large dominate fine mode aerosols. On this day, coarse mode aerosol contributed nearly 90% to total volume. This finding indicates that existence of considerable dust aerosols in the atmosphere even during no dust event cases in this region. Such result was also previously shown by Takamura et al. (2007) over Jeju island of Korea during spring season.

Another interesting result observed during intensive observation period at Minqin site is shown in Figure 5. As shown in Figure 5, during the typical dust event days, we not only observed very high concentration of dust aerosols but also very high concentration of black carbon aerosols. The very high concentration of BC mass concentration observed on April 24 at around 20 CST (Chinese standard time) is even higher than the values of BC mass concentration found in typical urban atmospheres of the world. This finding has several important implications for atmospheric research communities. There is a strong debate on light absorptive capacity of dust aerosols. Kaufman et al. (2001) suggested that Sarahan are less light absorptive, whereas as Nakajima et al. (2007) argued that Asian dust are more light absorptive. The observed result in this study may empathize that fact light absorbing capacity of Asian dusts are due to the mixture of BC and dust aerosols during the transportation of dust aerosols. Taking into account the fact that Minqin is basically the desert area, if such BC aerosols from urban areas are transported to desert areas, aerosol mixture can be more effective to influence the regional climate in comparison to other locations such as urban areas, ocean etc. Thirdly, such BC aerosols can be uplifted with dust aerosols up to high altitudes. As a result, such absorptive aerosols at high altitudes may have interaction with cloud, which may affect precipitation pattern and efficiency.

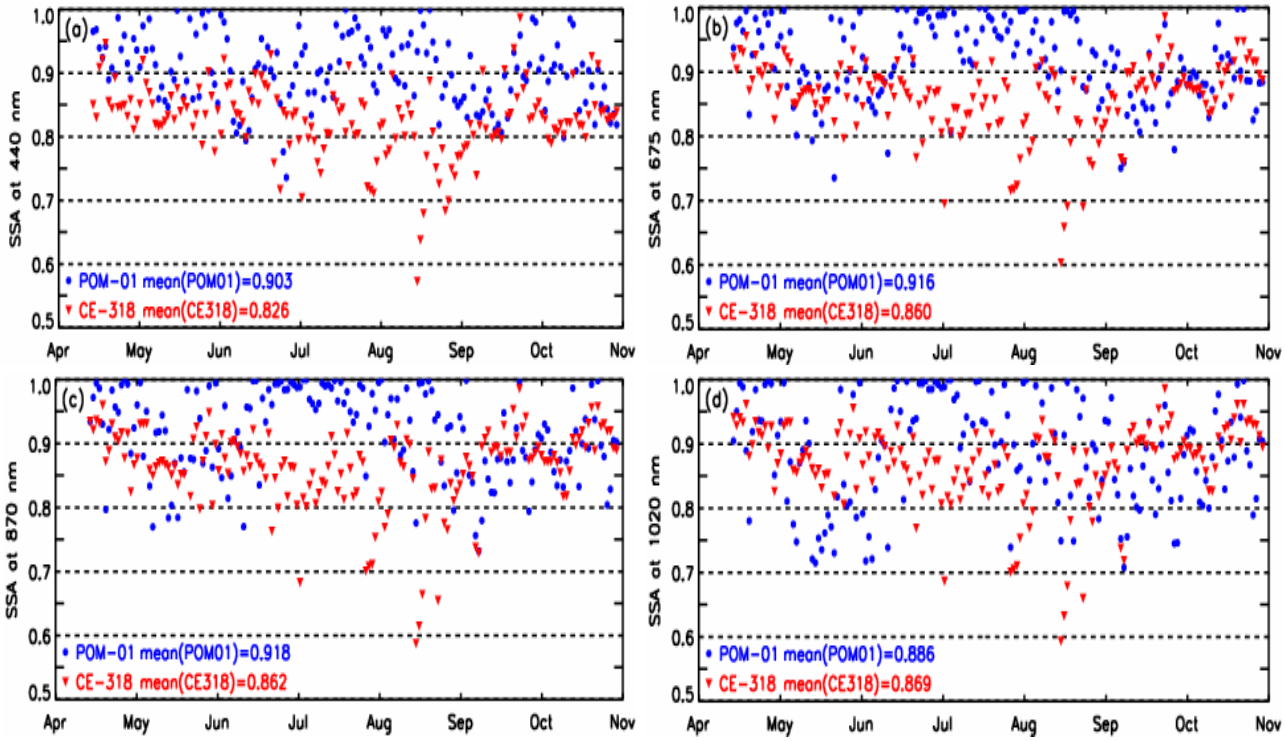

Figure 2. Comparison of aerosol SSAs between sky radiometer of SKYNET network and sun photometer of AERONET network at (a) 400nm and 440nm, (b) 675nm, (c) 870nm, and (d) 1020nm during 2009.

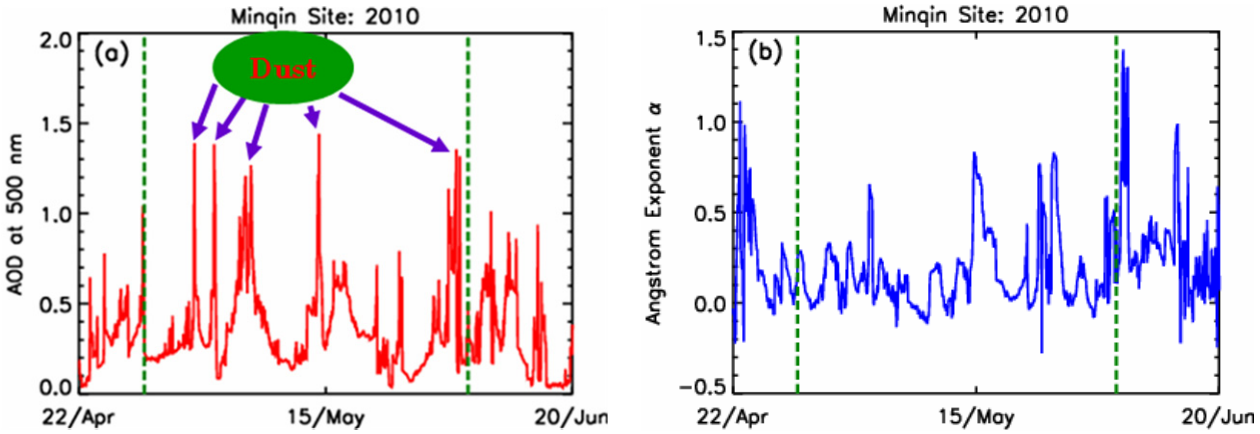

Figure 3. (a) Aerosol opt8ical thickness at 500nm and (b) Angstrom exponent at Minqin site.

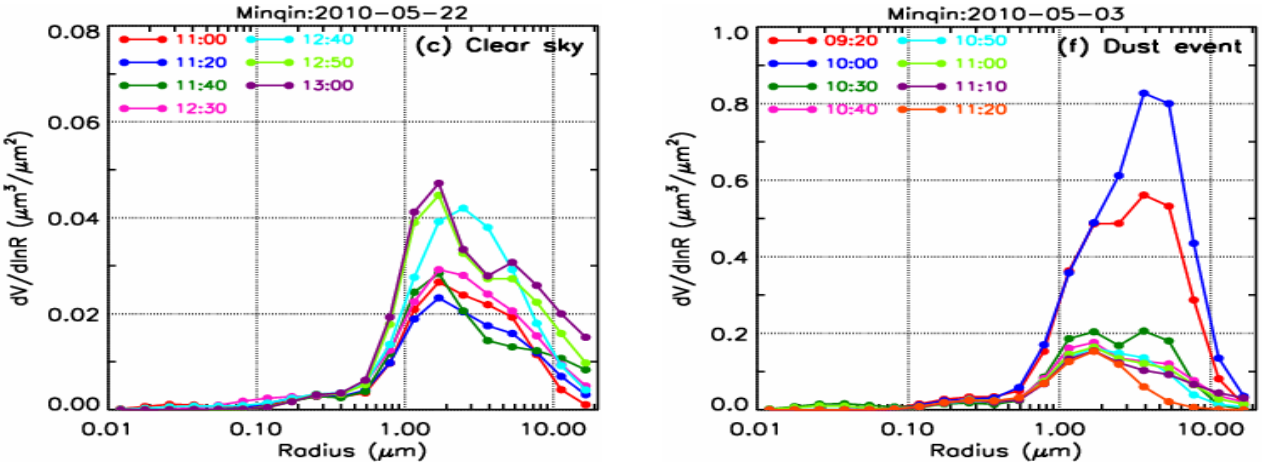

Figure 4. Volume size distribution during (a) clear sky day of 2010-05-22 and (b) dust event of 2010-05-03.

Table 1. Aerosol size distribution parameters for clear sky and dust event days shown in Figure 4.

Obs. day	$R_{m,\,fine}\,(\mu m)$	$R_{m,coarse}\,(\mu m)$	$V_{m,\,fine}\,(\mu m^3/\mu m^2)$	$V_{m,coarse}\,(\mu m^3/\mu m^2)$
Clear sky day (2010-05-22)	0.25	1.69	0.003	0.028
Dust event day (2010-05-03)	0.17	3.62	0.0024	0.83

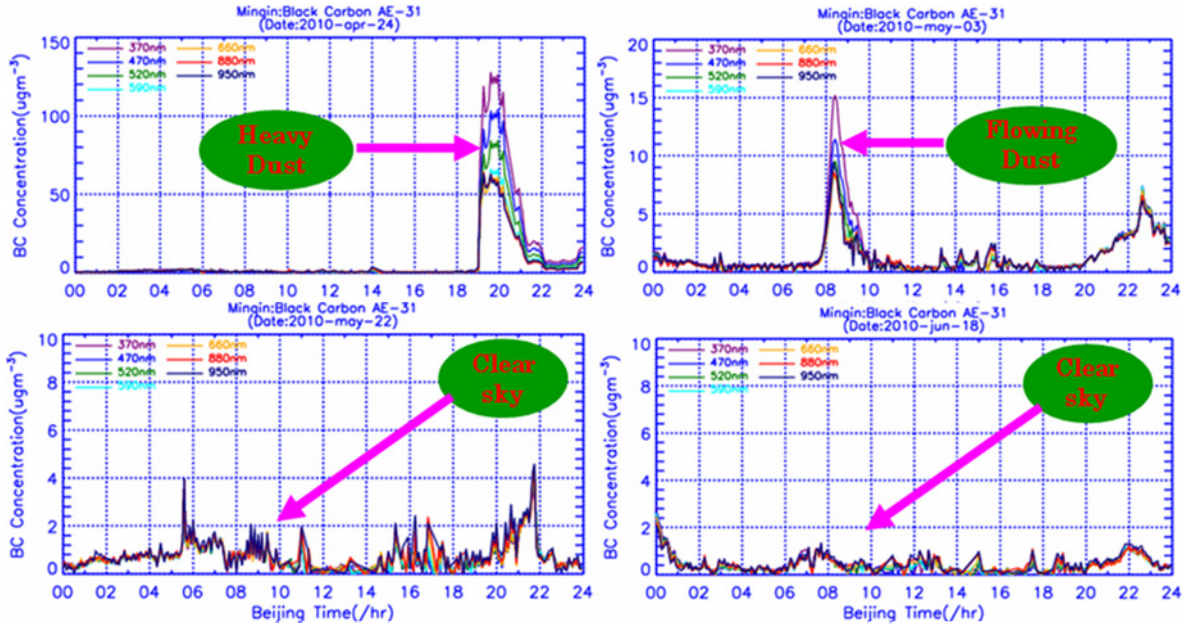

Figure 5. Black carbon mass concentration during dust event day and clear sky day

4. Summary

Dust aerosols originated from the deserts of Asia are known travel long distances around the world. As a result, such dust aerosols have strong impacts on not regional sector, but also on a global scale. This study attempts to characterize the characteristics of Asia dust aerosols near the source region over northwest China. The study mainly analyzes data measured by sky radiometer of SKYNET network. As the first part of the study, we verified by the results measured by our key instrument. After that, we discussed about the characteristics of dust aerosols by using intensive observation data. By using collocated measurements of AOTs from SKYNET sky radiometer and AERONET sun photometer, we discussed that onsite calibration protocol adopted for sky radiometer of SKYNET network is not only convenient and less expensive, but the results are also with reasonably high accuracy. In contrast to AOTs, SSAs from two independent instruments are systematically different. The possible reasons for such discrepancies are highlighted.

During the intensive observation period over Minqin in between 20 April to 20 June 2010, we observed frequent dust events with the time gap of few days. Those dust events were associated with very high AOT, low Angstrom exponent and dominant coarse mode aerosols. For the typical dust event day of May 03, we observed that coarse mode aerosols contributed more than 99.5% of total volume. For the observation days when dust events are not reported, we even observed around 90% of total volume as the volume of coarse mode aerosols. This suggests the existence of dust aerosols in considerable amount in the atmosphere even during no dust storm event. The most interesting finding of this study is the association of extremely high BC mass concentration during strong dust event cases. The observed BC mass concentration during strong dust event case is even higher than values over typical urban atmospheres of the world. The study discusses that such dust aerosols mixed with absorbing BC aerosols can have several important implications on our atmosphere. This also may help to shed light on unsolved mysteries of Asian dust aerosols.

References

Kaufman, Y. J., D. Tanre, O. Dubovik, A. Karnieli, L. A. Remer, 2001: Absorption of sunlight by dust as inferred from satellite and ground‐based remote sensing, Geo. Phys. Res., 28, 1479-1482.

Khatri, P., and T. Takamura, 2009: An algorithm to screen cloudaffected data for sky radiometer data analysis, *J.*

Meteor. Soc. Japan, **87**, 189−204.

Nakajima, T., G. Tonna, R. Rao, Y. Kaufman, and B. Holben,1996: Use of sky brightness measurements from ground for remote sensing of particulate polydispersions. *Appl. Opt.*,**35**, 2672−2686.

Nakajima, T., S. Yoon, V. Ramanathan, G. Shi, T. Takemura, A. Higurashi, T. Takamura, K. Aoki, B. Sohn, S. Kim, H. Tsuruta, N. Sugimoto, A. Shimizu, H. Tanimoto, Y. Sawa, N. Lin, C. Lee, D. Goto, and N. Schutgens, 2007: Overview of the Atmospheric Brown Cloud East Asian Regional Experiment 2005 and a study of the aerosol direct radiative forcing in east Asia, *J. Geophys. Res.*, **112**, D24S91, doi:10.1029/ 2007JD009009.

Takamura, T., N. Sugimoto, A. Shimizu, A. Uchiyama, A. Yamazaki, K. Aoki, T. Nakajima, B. J. Sohn, and H. Takenaka, 2007: Aerosol radiative characteristics at Gosan, Korea, during the Atmospheric Brown Cloud East Asian Regional Experiment 2005, *J. Geophys. Res.*, **112**, D22S36, doi: 10.1029/2007JD008506.

Influences of aerosol optical thickness and single scattering albedo on the dimming and brightening in Japan

Rei Kudo[1], Akihiro Uchiyama[1], Akihiro Yamazaki[1], Tomonori Sakami[1], and Osamu Ijima[2]

[1]*Meteorological Research Institute, Japan Meteorological Agency, 1-1 Nagamine, Tsukuba, Ibaraki 305-0052, Japan, reikudo@mri-jma.go.jp*

[2]*Chief of Radiation section, Atmospheric Environment Division, Global Environment and Marine Department, Japan Meteorological Agency, 1-3-4 Otemachi, Chiyoda-ku, Tokyo 100-8122, Japan*

Abstract

Surface solar radiation at widespread locations decreased until the mid-1980s (global dimming), and increased after the decline (global brightening). Since the transition is seen under both cloudy and clear skies, the change in aerosols is one of the dominant contributors. The radiative effect of aerosols at the surface is approximately determined by optical thickness and single scattering albedo. Long-term variations of both optical thickness and single scattering albedo are necessary to evaluate the influences of aerosols on global dimming and brightening. We have developed the method to estimate optical thickness and single scattering albedo from direct and diffuse irradiances measured by ground-based broadband radiometers. In the estimation, Junge size distribution with a fixed shaping parameter is assumed. A scaling parameter of the size distribution and an imaginary part of the refractive index are optimized to direct and diffuse irradiances. Optical thickness and single scattering albedo are calculated from these optimized parameters. The method was validated with the sky radiometer retrievals. The estimated optical thickness and single scattering albedo at 500nm agreed well with the sky radiometer retrievals. The developed method was applied to hourly accumulated direct and diffuse irradiances under clear skies from 1975 to 2008 at Tsukuba, Japan. Optical thickness increased until the mid-1980s, then decreased until the late 1990s, and was almost constant in the 2000s. Single scattering albedo was about 0.8 until the late 1980s, then increased, and was about 0.9 since the mid-1990s. The surface solar radiation calculated from estimated optical properties indicated clear dimming and brightening. The magnitude of the brightening was 12.7Wm^{-2}, of this, 8.3Wm^{-2} was due to a decrease in optical thickness, and the remaining 4.4Wm^{-2} was due to an increase of single scattering albedo.

Keywords **:** Aeorosol, Surface solar radiation

1. Introduction

Surface solar radiation at widespread locations decreased until the mid-1980s (global dimming), and then increased (global brightening). Since the transition is seen under both the clear and cloudy sky conditions, the change in aerosol optical properties is one of the dominant contributors. The radiative effect of aerosols at the surface is approximately determined by optical thickness and single scattering. Long-term variations of both optical thickness and single scattering albedo are necessary to evaluate the influences of aerosols on the global dimming and brightening.

The aerosol turbidity coefficient has been obtained from the broadband pyrheliometer, but single scattering albedo has not been obtained. In this study, we developed the method to estimate both optical thickness and single scattering albedo from broadband pyrheliometer and pyranometer. Using this method, the variations of optical thickness and single scattering albedo from 1975 to 2008 at Tsukuba, Japan were evaluated. Furthermore, the influences of them on the surface solar radiation were investigated.

2. Methods

Estimation of optical thickness and single scattering albedo are based on the parameter optimization to the measurements (broadband direct and diffuse irradiances). This method requires the forward calculation of the direct and diffuse irradiances at the surface from the aerosol parameters. The real part of the refractive index of aerosols is fixed at 1.52, and the imaginary part is estimated. The size distribution is assumed to be a Junge distribution, which is consist of a scaling parameter and a shaping parameter. The shaping parameter is related to Angström exponent, which is usually obtained from the sunphotometer measurements, but it does be obtained from the broadband pyrheliometer. Therefore, the shaping constant is fixed at 3.3, which is a normal value of the continent-urban origins. Two parameters

are optimized to the direct and diffuse irradiances by the Gauss-Newton method.

The developed method was validated with the sky radiometer retrievals. The annual means of optical thickness and single scattering albedo at 500nm in 2007 were 0.19±0.08 and 0.93±0.05 for sky radiometer, and 0.18±0.08 and 0.92±0.05 for broadband radiometers (Figure 1). Our estimated optical thickness and single scattering albedo agreed well with the sky radiometer retrievals.

3. Results

Our developed method was applied to the measurements under the clear sky conditions from 1975 to 2008 at Tsukuba, Japan (Figure 2). The optical thickness increased until the mid-1980s, then decreased until the late 1980s, and was almost constant in the 2000s. The single scattering albedo was about 0.8 until the late 1980s, then increased, and was almost 0.9 since the mid-1990s.

Using the estimated optical properties, the surface solar radiation under the clear sky conditions from 1975 to 2008 were calculated (F1 in Figure 3). The surface solar radiation under the clear sky conditions indicated more apparent dimming and brightening changes than the surface solar radiation measured under the cloudy sky conditions (F2). Therefore, the dimming and brightening at Tsukuba may be due to the changes in aerosol optical properties, not clouds.

To evaluate only the influence of optical thickness on the surface solar radiation, the surface irradiances (F1') were calculated with an average of the imaginary part of the refractive index in 1975-2008. The increase of F1 was about 12.7 Wm^{-2} from 1980-1985 to 1995-2000, of this, 8.3 Wm^{-2} was due to a decrease of optical thickness. The influence of single scattering albedo was defined by the differences between F1-F1' and was about 4.4 Wm^{-2}. The brightening under the clear sky conditions was due to both optical thickness and single scattering albedo.

4. Summary

The method to estimate aerosol optical thickness and single scattering albedo from the broadband direct and diffuse irradiances was developed, and was applied the measurements under the clear sky conditions at Tsukuba from 1975 to 2008. Optical thickness increased until the mid-1980s, then decreased until the late 1990s, and was almost constant in the 2000s. Single scattering albedo was low value until the late 1990s, then increased, and was almost constant in the 2000s. The surface solar radiation under the clear sky conditions calculated from the estimated optical properties indicated more apparent dimming and brightening than under the cloudy conditions. The magnitude of the brightening was 12.7 Wm^{-2}, of this, 8.3 Wm^{-2} was due to a decrease of optical thickness, and the remaining 4.4 Wm^{-2} was due to an increase of single scattering albedo.

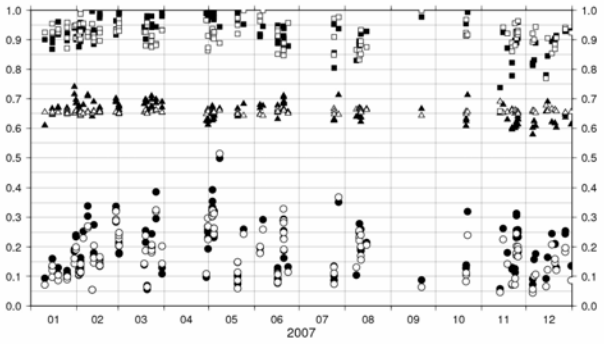

Fig. 1 Optical thickness (circles), single scattering albedo (squares), and asymmetry factor (triangles) estimated from a sky radiometer (filled) and broadband radiometers (open).

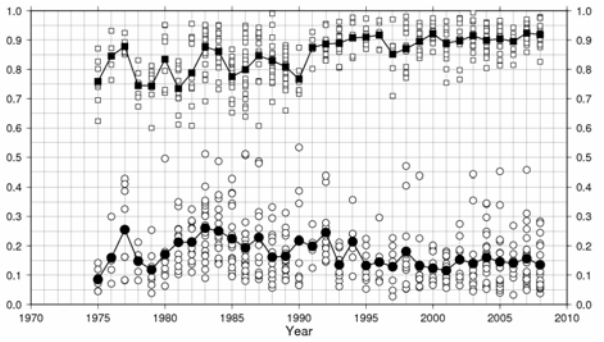

Fig. 2 Estimated optical thickness (circles) and single scattering albedo (squares) from 1975 to 2008. Open symbols are daily means and closed symbols are annual means.

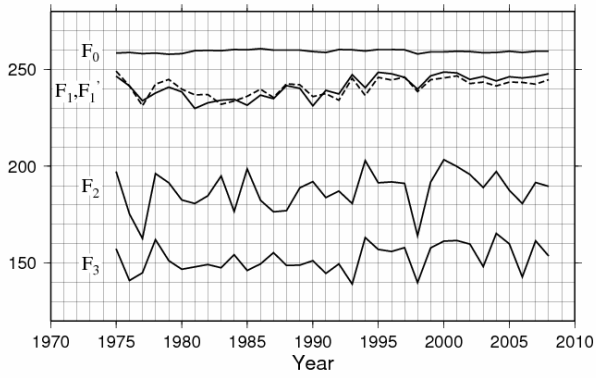

Fig. 3 Surface solar irradiances under the clear sky conditions calculated from estimated optical properties (F1), the irradiances measured under the cloudy sky conditions (F2), and the irradiances measured under the all sky conditions (F3). F1' is the irradiances calculated with an average of the imaginary part of the refractive index. F0 is the irradiances calculated without aerosols.

Spatial contrast of Asian dust concentration between windward and leeward of mountains in Japan during 1–2 April 2007

Hayasaki,[1] M., M. K. Yamamoto[1], A. Higuchi[1], A. Shimizu[2], I. Mori[2], and M. Nishikawa[2]

1: Center for Environmental Remote Sensing, Chiba University, Japan
2: National Institute for Environmental Studies, Japan

Abstract

During massive Asian dust episode for 1–2 April 2007, mass concentration of suspended particulate matter (SPM) rapidly began to increase in the morning on 1 April from coastal side of the Japan Sea. For the daytime 1 April, while rapid SPM increase and extreme high concentrations observed in Hokuriku and Tohoku, SPM concentrations in Kanto remained low level and increased from late afternoon. Ground lidar observation and rawinsonde sounding in Hokuriku show that the top height of dust layer ($\sim$ 2 km) approximately correspond to the base of temperature inversion. In Kanto, SPM increase began from east coast and then it advanced westward after 15 LT with easterly wind. The CloudSat/CPR and CALIPSO/CALIOP observations show that clouds over mainland Japan and the Japan Sea was found in the upper-level ($>$ 6 km). Continuous meteorological observations show that cloud condensation and rainfall was not observed over mountains for the daytime 1 April. These results suggest that the temporal delaying of SPM increase in Kanto was caused by an indirect dust transport.

keywords: Asian dust, indirect transport, temperature inversion

1. Introduction

During 31 March–2 April 2007, a massive dust episode observed over East Asia. The maximum PM_{10} concentration exceeded 1000 $\mu g\,m^{-3}$ in Seoul, Korea (Park et al. 2010) and 700 $\mu g\,m^{-3}$ in Banryu, western Japan (Yumimoto et al. 2008). The dust plumes brought extremely high concentration of dust, however, spatial and temporal variations of dust concentrations showed complex features in Japan.

Takahashi et al. (2010) indicate that delaying dust transport in Kanto was caused by a stably stratified layers near the ground. Tsunematsu et al. (2009) also suggest that surface-based stable layer prevent a downward transport of elevated dust to the ground level. However, their conclusion have been deduced from limited observational data and not fully discussed other processes. As shown in Han et al. (2004), wet deposition process play an important role for scavenging dust particles in a downstream area.

The main objective of this paper is to identify major cause(s) for delaying dust transport in Kanto, Japan. To show regional-scale characteristics about spatial distributions and its temporal changes of dust concentrations, we use operational air-quality monitoring data in Japan.

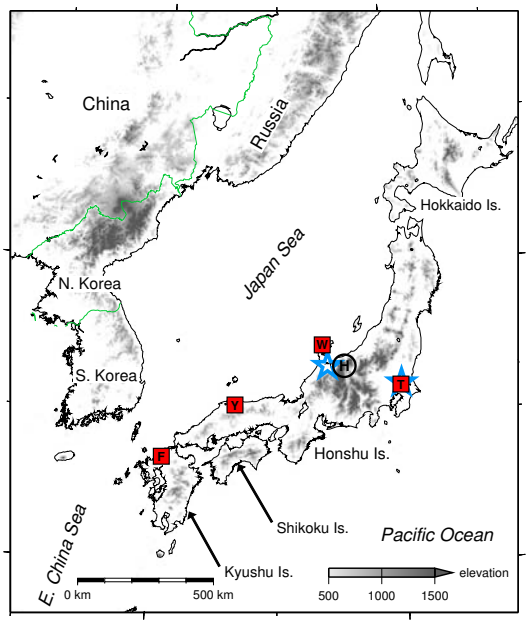

Fig. 1: Geographical locations of observatories. Square symbols: upper-air sounding sites (Fukuoka, Yonago, Wajima, Tateno (Tsukuba)); Star: Lidar observatories (Toyama and Tsukuba). "H" represents EANET site (Happo).

2. Data

Aerosol mass concentrations of SPM observed about 1300-site in Japan. Due to the difference of cut-off property of particles between PM_{10} (50% cut-off at 10 μm) and SPM (100% cut-off at 10 μm), SPM monitoring value is approximately PM_7 (Minoura et al. 2006).

The meso-scale model of grid point value (GPV-MSM) data distributed by the Japan Meteorological Agency (JMA) is used in this study. The pressure level data have 3-hourly temporal interval and 0.1° × 0.125° horizontal resolution around Japan (22.4°– 47.6°N, 120°– 150°E).

To identify a vertical profiles of cloud and dust particles, we use a combined products between CALIPSO/CALIOP and CloudSat/CPR that is provided by the Research Institute for Applied Mechanics (RIAM), Kyushu University (hereafter RIAM-CALIPSO products). The classification procedure for cloud particle types is fully documented in Yoshida et al. (2010).

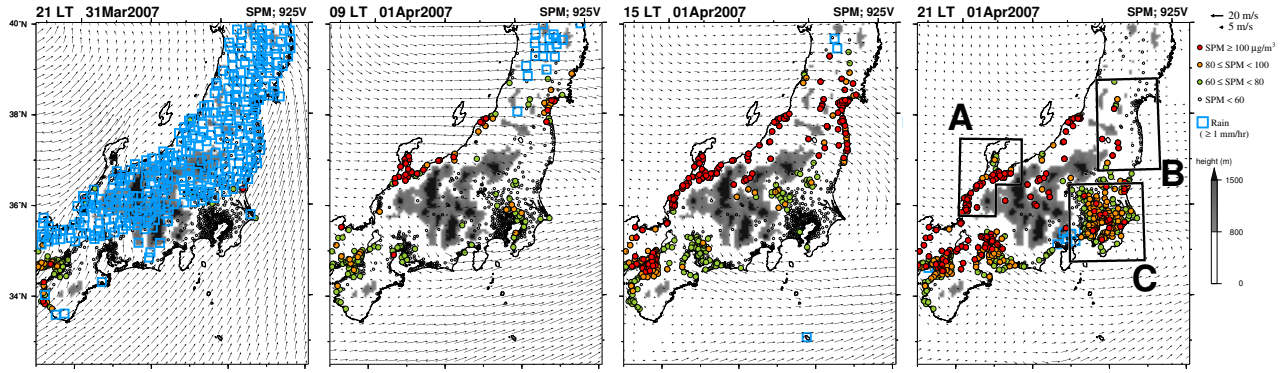

Fig. 2: Hourly SPM concentration in central Japan at (a) 21 LT on 31 March, (b) 09 LT, (c) 15 LT, and (d) 21 LT on 1 April 2007. Vectors show a 925-hPa horizontal wind of the GPV-MSM data. Rainfall intensity (light blue square) is obtained by AMeDAS observatories. Gray shade show a topography of GPV-MSM.

We also use a non-spherical (dust) extinction coefficient of ground lidar observations which is maintained by the National Institute for Environmental Studies, Japan. The algorithm and estimation scheme for separating spherical/non-spherical particles is referred from Shimizu et al. (2004).

3. Results

Figure 2 show a horizontal distribution of SPM concentrations in central Japan (Honshu island). SPM concentrations begin to increase in the morning April 1 over western Japan and coastal area along the Japan Sea after frontal rain (Figs. 2a, b). At 09 LT (Local time. 9-hour advancing from UTC) on 1 April (Fig. 2b), the maximum SPM concentration inside the area is 209 $\mu g\,m^{-3}$ in Hokuriku (Region A shown in Fig. 2d). By 15 LT on 1 April, high SPM sites (SPM $\geq$ 100 $\mu g\,m^{-3}$) advance eastward extending from western Japan, Hokuriku, and southern Tohoku (Region B). On the other hand, high SPM sites are not observed in Kanto (Region C). At 21 LT on 1 April, high SPM sites are widely observed in Kanto (Fig. 2d). The high SPM sites are firstly observed at 19 LT along the eastern part of Kanto and subsequently moved to the inland area under easterly wind condition (not shown).

Figure 3 show an areal SPM concentrations in Region A–C. The median, maximum, and 25- and 75-percentile concentrations are determined in hourly by using all observatories inside the area. Hourly rainfall intensity and surface wind at the nearest meteorological observatories from lidar site (Toyama, Sendai, and Tateno in Region A, B, and C, respectively) are also plotted. In Region A (Fig. 3a), median SPM rapidly increase from 36 $\mu g\,m^{-3}$ (08LT) to 119 $\mu g\,m^{-3}$ (10LT) within two hours. The maximum median SPM recorded 175 $\mu g\,m^{-3}$ at 19 LT and decreased gradually after that. The temporal difference between the end time of frontal rain and beginning time of SPM increase is approximately 10 hours in Region A. In Region B, which locate in approximately 300 km east of Region A and 200 km north of Region C, the median SPM concentrations have also exceeded 100 $\mu g\,m^{-3}$ at 13 LT and continued to 16 LT. The maximum median SPM in Region B is 113 $\mu g\,m^{-3}$ at 16LT 1 April. The temporal difference between frontal rain and SPM increase is approximately 8–10 hours. On the other hand, the median SPM in Region C have remained low concentration levels

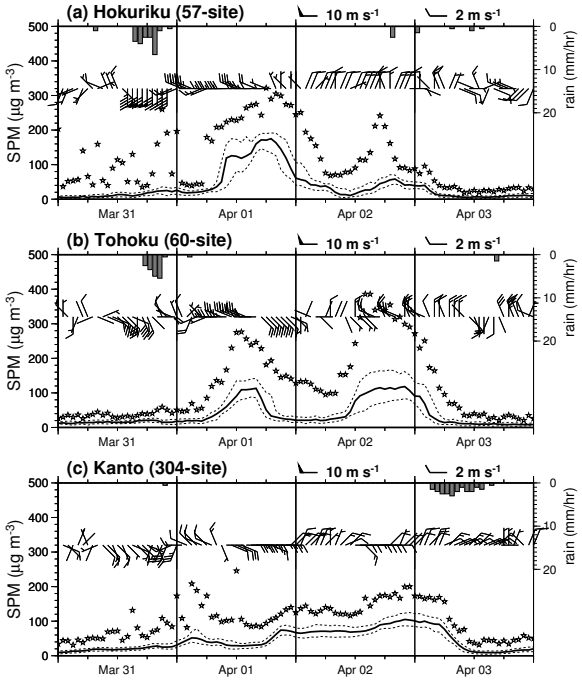

Fig. 3: SPM time series in (a) Hokuriku, (b) Tohoku, and (c) Kanto during 31 March – 3 April. Solid and dashed lines shows median, 75- and 25-percentile of SPM concentrations, respectively. Star mark: areal maximum concentration. Hourly rain intensity (downward bar) and surface wind (barb) at JMA observatory are also plotted.

around 30 $\mu g\,m^{-3}$ during the daytime and increased over 60 $\mu g\,m^{-3}$ after 20 LT (Fig. 3c).

Figure 4 show a time-height section of dust extinction coefficient at Toyama and Tsukuba. Contour lines show the potential temperature at the nearest grid point obtained from GPV-MSM. At Toyama (Fig. 4a), which locate in a coastal side of the Japan Sea, we can identify two dust layers in the daytime 1 April. The upper one locate above 3 km with weak dust extinction coefficient. The lower one can be clearly identified below 2 km that potential temperature is colder than 295 K. The dense dust layer are identified below cloud after 03 LT and then it come down the ground after 09 LT on 1 April. Meanwhile, two weak dust layers are also identified at Tsukuba (Fig. 4b) in 3–4 km ($\theta \approx 310$ K) and around 1 km above

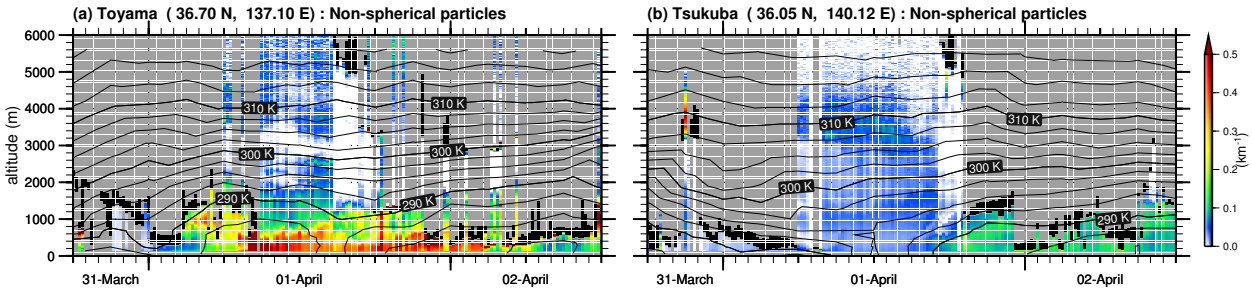

Fig. 4: Time-height section of dust extinction coefficient (color) and θ (contour; 2.5 K interval) at (a) Toyama and (b) Tsukuba during 18 LT 31 March – 12 LT 2 April 2007. black: cloud, gray: above-cloud.

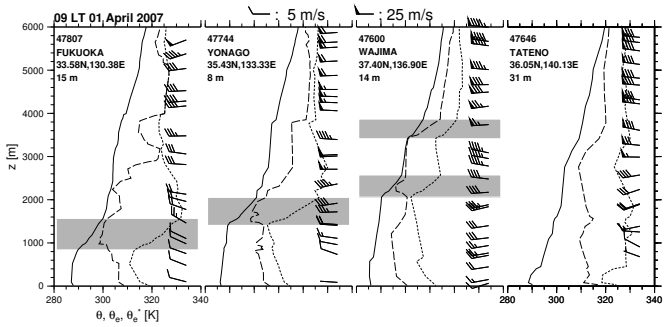

Fig. 5: Vertical profiles of θ (solid), θ_e (dashed), and θ_e^* (dotted) at four rawinsonde sites at 09 LT on 1 April. Shading represent temperature inversions ($\Delta T/\Delta z > 0$). Thin inversion layers ($\Delta z \leq 200$) are omitted.

ground ($\theta \approx 295$ K). Yumimoto et al. (2008) suggest that the upper dust layer is originated from the Taklimakan Desert. Considering a potential temperature of the lower dust layer at Tsukuba, it may be originated from the upper part of the dense dust layer in Toyama

As shown in Figs. 2 and 3, there are two interesting characteristics for SPM concentrations in Kanto: (1) SPM increase delayed compared to the adjacent area, (2) SPM remained low concentration level during the daytime 1 April. The main cause(s) of the spatial and temporal variations of SPM concentrations in Kanto will be discussed in the following section.

4. Discussion

Considering the results mentioned above and previous studies, we briefly focused on the following three processes for occurring a characteristic spatial and temporal variations of SPM in Kanto: (1) preventing downward transport of dust particles by a stably stratified layer (Takahashi et al. 2010; Tsunematsu et al. 2009), (2) wet deposition (Han et al. 2004), and (3) indirect transport going around the Central Mountains in Japan.

Firstly, we examine a possibility of a preventing downward dust transport from elevated dust layer in Kanto. As shown in Fig. 4a, potential temperature (θ) for the main dust layer at Toyama is cold below $\theta < 290$ K throughout the dust period. Moreover, the main dust layer is capped by a temperature inversion layer. Figure 5 show vertical profiles of θ, equivalent potential temperature (θ_e), and saturated equivalent potential temperature (θ_e) at 09 LT on 1 April in Japan (see Fig. 1). The inversion layers (gray shading) are identified by a vertical temperature lapse rate ($\Delta T/\Delta z > 0$) and its thickness ($\Delta z \geq 200$). Strong temperature inversions are clearly found in coastal stations along the Japan Sea. Though base heights of inversion layers increase with eastward advancing (Fukuoka: 839 m, Yonago: 1405 m, and Wajima (lower layer): 2062 m), the inversion base have same potential temperature approximately 290 K. The main dust layers are placed under the inversion base in the side of Japan Sea. Since the Central Mountains in Japan have 1500–2000 m height, most of the dust particles can not go across the mountains. Therefore, preventing vertical mixing for the daytime 1 April is not a primary cause for delaying SPM increase in Kanto.

Second, we discuss an influence of wet deposition. In the Japan Sea side, westerly wind is dominant in the dust layer. Since high mountains (approx. 2000 m) in western and northern part of Kanto blocked dust contained air-mass, dust particles may be scavenged by condensation or rainfall processes along a mountain slope. From visible satellite image, dense cloud widely covered over Japan (Fig. 6a). However, precipitation radar and ground-level rain gauges did not observe rainfall over central Japan (including Hokuriku and Kanto) during the daytime 1 April (not shown). Figure 6b show a vertical profile of clouds and dust particles. Asian dust, which is categorized as "3-D ice" in the RIAM-CALIPSO cloud particle type dataset, locate over the Japan Sea along $\theta \approx 290$K surface. On the south of Japan, water cloud can be identified in near-surface level. Height of upper clouds above mainland Japan and Japan Sea is ranging from 6 to 11-km above mean sea level. Due to a ground clutter, CloudSat/CPR can not obtain an effective signal within 1 km above ground. Therefore, CloudSat observation is hard to detect a cloud along mountain slope. Figure 7 show that time series of PM_{10}, rainfall, wind, and relative humidity (RH) at Happo (z = 1850 m). After frontal rainfall, PM_{10} increases with time on 1 April. During the daytime, a dry air-mass (RH < 30%) is observed under westerly-northwesterly wind condition. The dry air condition is also observed in the other in-situ observatories over mountainous area during the daytime (not shown). These results suggest that wet deposition is not a primary process providing a temporal delay of SPM increase in Kanto during the daytime April 1.

5. Conclusions

During the massive Asian dust episode for 1–2 April 2007, SPM concentrations in Kanto showed low-level (∼

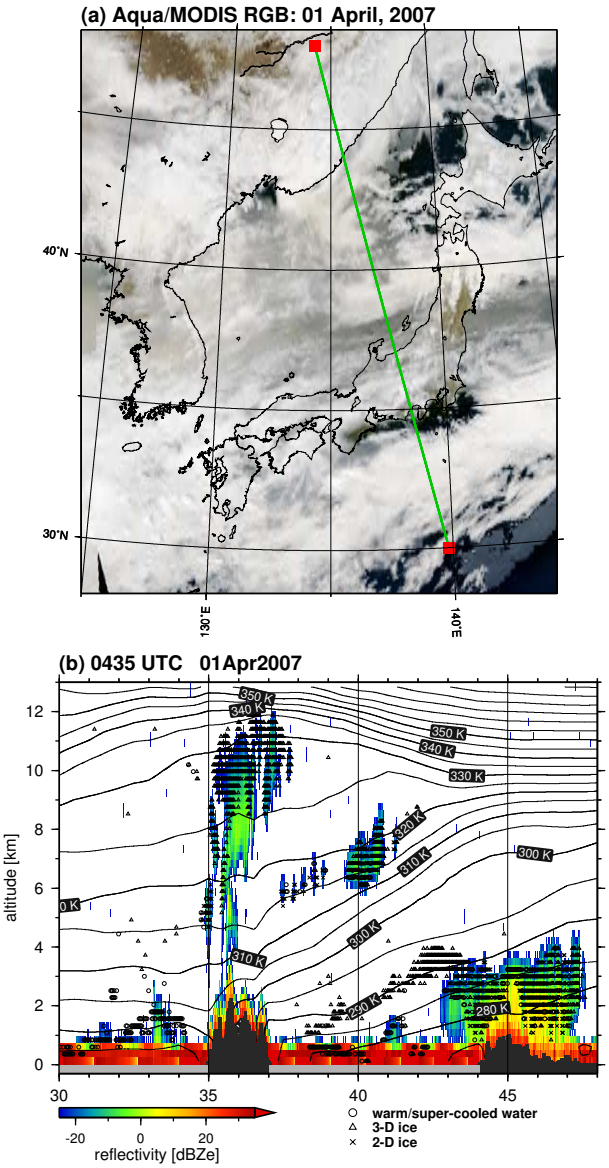

Fig. 6: (a) Aqua/MODIS visible image on 1 April, 2007. (b) Vertical profiles of radar reflectivity (color; dBZe), θ (contour), and cloud particle type (symbol; see Yoshida *et al.*, 2010) along the green line in Fig. 6a.

40 μg m^{-3}) and increased later in the evening under easterly wind condition. The main dust layer in a windward of the Central Mountains is capped by the strong temperature inversions below 2 km (Fig. 4a and 5). The capped dust layer are also reported in previous studies (e.g., Arao et al. 2006). Additionally, a dry condition inside the capped dust layer is hard to form cloud droplets and rainfall along mountain slope. These results indicate that temporal delaying of SPM increase in Kanto is caused by a indirect transport of low-level dust which is going around the Central Mountains in Japan. Since this study is just a case study, the occurrence frequency of an indirect transport can not discussed. Further studies will be required for using long-term observational data.

Acknowledgements

We thank Dr. Tsunematsu for valuable comments. The operational air-quality monitoring dataset are obtained from the C-type cooperative research project for photochemical oxidant and particulate matters (NIES, Japan). We would like to thank Dr. Y. Hagihara and Dr. H. Okamoto for offering access of the RIAM-CALIPSO products. The Generic Mapping Tools (GMT; Wessel and Smith 1998) were used for drawing the figures.

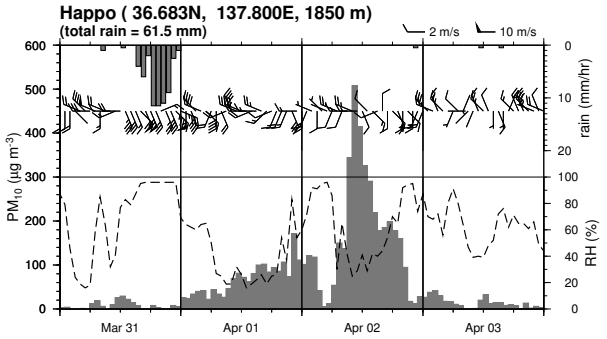

Fig. 7: Time series of PM_{10} (upward bar) and meteorological variables at Happo (36.683°N, 137.800°E; z=1850m), Japan. Dashed line: relative humidity (%), downward bar: precipitation intensity (mm/hour), barb: horizontal wind.

REFERENCES

Arao, K., J. Ishizuka, N. Sugimoto, I. Matsui, A. Shimizu, I. Mori, M. Nishikawa, K. Aoki, A. Uchiyama, A. Yamazaki, H. Togawa and J. Asano, 2006: Yellow sand dust event on 13 April 2003 over Western Kyushu, Japan. *SOLA*, **2**, 100–103.

Han, Z., H. Ueda, K. Matsuda, R. Zhang, K. Arao, Y. Kanai and H. Hasome, 2004: Model study on particle size segregation and deposition during Asian dust events in March 2002. *J. Geophys. Res.*, **109**, D19205, doi: 10.1029/2004JD004920.

Minoura, H., K. Takahashi, J. C. Chow and J. G. Watson, 2006: Multi-year trend in fine and coarse particle mass, carbon, and ions in downtown Tokyo, Japan. *Atmos. Environ.*, **40**, 2478–2487.

Park, S.-U., A. Choe and M.-S. Park, 2010: Estimates of Asian dust deposition over the Asian region by using ADAM2 in 2007. *Science of the Total Environment*, **408**, 2347–2356.

Shimizu, A., N. Sugimoto, I. Matsui, K. Arao, I. Uno, T. Murayama, N. Kagawa, K. Aoki, A. Uchiyama and A. Yamazaki, 2004: Continuous observations of Asian dust and other aerosols by polarization lidars in China and Japan during ACE-Asia. *J. Geophys. Res.*, **109**, D19S17, 10.1029/2002JD003253.

Takahashi, H., H. Naoe, Y. Igarashi, Y. Inomata and N. Sugimoto, 2010: Aerosol concentrations observed at Mt. Haruna, Japan, in relation to long-range transport of Asian mineral dust aerosols. *Atmos. Environ.*, **44**, 4638–4644.

Tsunematsu, N., H. Iwai, S. Ishii, M. Yasui, Y. Murayama and K. Mizutani, 2009: Influence of surface-based stable layer development on Asian dust behavior over Tokyo. *Boundary-Layer Meteor.*, **131**, 263–275.

Wessel, P. and W. H. F. Smith, 1998: New, improved version of Generic Mapping Tools released. *EOS Trans. Amer. Geophys. Union*, **79**, 579.

Yoshida, R., H. Okamoto, Y. Hagihara and H. Ishimoto, 2010: Global analysis of cloud phase and ice crystal orientation from Cloud-Aerosol Lidar and Infrared Pathfinder Satellite Observation (CALIPSO) data using attenuated backscattering and depolarization ratio. *J. Geophys. Res.*, **115**, D00H32, doi: 10.1029/2009JD012334.

Yumimoto, K., I. Uno, N. Sugimoto, A. Shimizu, Z. Liu and D. M. Winkler, 2008: Adjoint inversion modeling of Asian dust emission using lidar observations. *Atmos. Chem. Phys.*, **8**, 2869–2884.

Influence of Spatial Patterns of Future Atmospheric Warming on Asian Dust Emission

Nobumitsu Tsunematsu [1*], Masamitsu Hayasaki [1], Tomonori Sato [2], Feifei Cui [1], Akihiko Kondoh [1], Hiroaki Kuze [1], Kohei Sakamoto [3]

[1] *Center for Environmental Remote Sensing, Chiba University,*

[2] *Faculty of Environmental Earth Science, Hokkaido University,*

[3] *GPE-Corner, Weathernews Inc.*

[*] *E-mail: tsunematsu@faculty.chiba-u.jp*

Abstract

Spatial patterns of future atmospheric warming presented by climate model projections indicate that atmospheric temperatures of the lower troposphere will considerably increase at high latitudes in the Northern Hemisphere and also the upper troposphere at low-middle latitudes. In this study, potential impacts of the spatial patterns of future atmospheric warming on Asian dust emission were investigated by performing numerical model experiments with a dynamical downscaling of global-scale climate model (the Model for Interdisciplinary Research On Climate: MIROC V3.2-hires) projections into regional-scale atmospheric model (the Weather Research and Forecasting modeling system: WRF V3.1) simulations. After three significant Asian dust outbreaks were reproduced as the control runs using WRF-Chem, the initial and boundary conditions of the control runs were updated by adding differences in atmospheric variables between the future climate (2091-2100) and the recent climate (1991-2000) in order to execute the pseudo global warming runs. The results showed that the dust emission fluxes in the main Asian dust sources (MADSs), i.e., the Taklimakan Desert and the Gobi Desert, decrease markedly in the future climate condition. The future decreases in the dust emission fluxes would likely be caused by a combination of the relatively large increases in sea level pressures (SLPs) in MADSs and the small SLP changes to the north of MADSs, which reduces the meridional SLP gradients between those two areas and consequently decreases surface wind velocities associated with cold air outbreaks.

Keywords **:** Global warming, Asian dust emission, Dynamical downscaling, WRF, MIROC

1. Introduction

Climate model projections show spatial patterns of future atmospheric warming caused by global warming (IPCC AR4); atmospheric temperatures considerably increase in the lower troposphere at high latitudes in the Northern Hemisphere and the upper troposphere at low-middle latitudes. This leads to future changes in the meridional and vertical atmospheric temperature distributions in the Northern Hemisphere. The meridional atmospheric temperature gradients are expected to decrease in the lower troposphere and increase in the upper troposphere. Atmospheric stabilities are expected to increase at low-middle latitudes and decrease at high latitudes.

Asian dust phenomenon is one of well-known springtime atmospheric phenomena in East Asia. Asian dust particles are emitted mainly from the Taklimakan Desert and the Gobi Desert, and then transported to Korea and Japan mainly by low-pressure systems. The Asian dust emission is frequently induced by cold air surges originating from the release of Siberian air masses (e.g., sun et al., 2001). Therefore, the future Asian dust emission should be influenced by the remarkable atmospheric warming in the lower troposphere at high latitudes in the Northern Hemisphere. The future changes in atmospheric stabilities are also expected to influence the Asian dust emission, because the dust emission is closely associated with atmospheric stability (e.g., Tsunematsu et al., 2005). Nevertheless, the number of numerical studies investigating the relationship between future global warming and Asian dust emission is still rather small. This study therefore investigated potential impacts of the spatial patterns of future atmospheric warming on Asian dust emission by mainly conducting numerical model experiments.

2. Analysis of Global-Scale Climate Model Output

Output data from the Model for Interdisciplinary Research On Climate (MIROC V3.2-hires: K-1 model developers, 2004) were analyzed to obtain the spatial patterns of future global warming in the atmosphere. The MIROC model is one of global-scale climate models that are capable of reproducing past climate and predicting future climate. This model has 23 vertical levels and T106

horizontal resolution (approximately 1.125° x 1.125°).

In this study, the MIROC output data derived from results of the 20th Century Climate in Coupled Models (20C3M) experiment and the 21st century climate projection based on the Special Report on Emission Scenario (SRES) A1B were used to obtain "recent climate" for the period of 1991-2000 and "future climate" in 2091-2100, respectively. Using the monthly mean data, differences in atmospheric temperatures, geopotential heights, and u-v wind components between the future and recent climate were calculated for each grid of the MIROC model. Sato et al. (2007) named the differences "Global Warming Monthly mean Differences (GWMDs)". Months of the data used for the calculations of the GWMDs were restricted to March and April when the frequency of the Asian dust outbreaks is considerably higher than other months. The March and April monthly mean data were averaged before calculating the GWMDs. The 50°E-130°E zonal mean GWMDs at latitudes between 20°N and 80°N were prepared for each vertical level of the MIROC model (Figure 1) to downscale the future changes in the meridional and vertical distributions of atmospheric temperatures, geopotential heights, and horizontal winds into dust simulations conducted by a regional-scale atmospheric modeling system.

3. Dust Simulations by a Regional-Scale Model

The advanced research version of the Weather Research and Forecasting (WRF) modeling system V3.1 (Skamarock et al., 2008) was used for numerical experiments on dust. This modeling system provides an atmospheric chemistry model (WRF-Chem V3.1: Grell et al., 2005) that is capable of simulating the regional-scale movements of various gases and aerosol particles. This study altered source codes of WRF-Chem to simulate emission, advection, dispersion, and deposition of soil dust with the Particulate Matter up to 10 μm in size (PM10) only, after assuming the PM10 soil dust to be Asian dust particle.

Prior to performing the main numerical experiments in this study, a significant Asian dust event that occurred during the period from March 29 to April 2, 2007 was simulated by using the WRF-Chem model as the pre-experiment. The pre-experiment was conducted to confirm whether the WRF-Chem model could be applied to dust simulations. A brief outline of this Asian dust event is that the dust particles were emitted mainly from the Gobi Desert and the Taklimakan Desert and then transported to a considerably large area of East Asia including the megacities, such as Shanghai, Seoul, and Tokyo (e.g., Tsunematsu et al., 2009). In the pre-experiment, a calculation domain was given by 160 x 84 horizontal grids centered at 40°N/90°E with the grid interval of 40 km. The number of the vertical layers was set at 30. The 6-hourly global analysis data from the National Centers for Environmental Prediction-FiNaL (NCEP-FNL), which has a 1.0° x 1.0° horizontal resolution, were used for the initial and boundary conditions. An initial time of the 72 hours numerical integration was set at 0000 Universal Time Coordinated (UTC) March 29, 2007. Potential areas of emission of the soil particles were determined by the U.S. geological survey (USGS: http://www.usgs.gov) land covers categorized into barren and sparsely vegetated, shrubland, and grassland. The particles were emitted from not the ground surface but the first level of the model in this study. The height of the first level is approximately 29 m above ground level (AGL). The 29 m height difference can be disregarded because the calculation domain has a horizontal scale of several kilometers. The hourly emission mass fluxes of the PM10

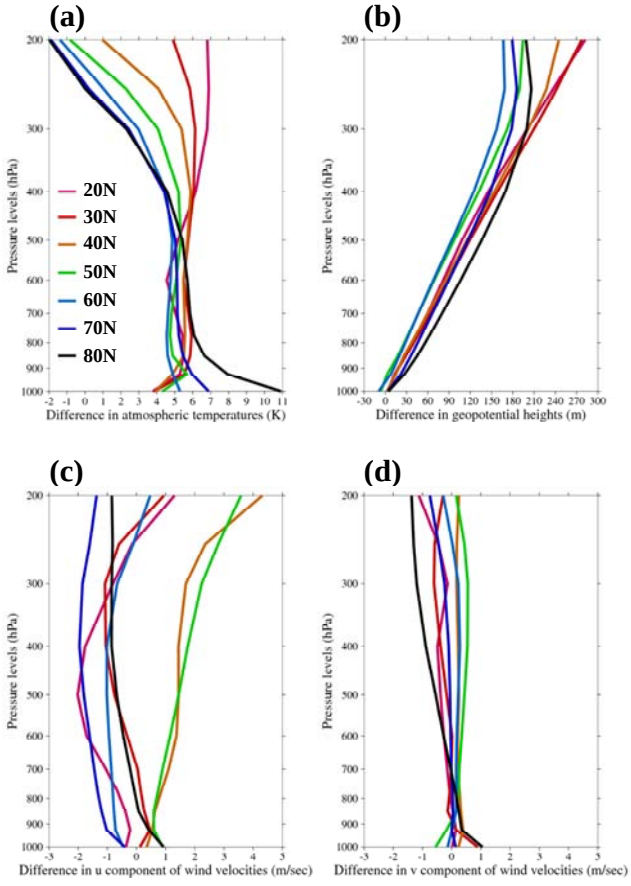

Fig. 1 Vertical profiles of the 50°E-130°E zonal mean "Global Warming Monthly mean Differences (GWMDs)" at latitudes between 20°N and 80°N of (a) atmospheric temperatures (K), (b) geopotential heights (m), (c) u component of wind velocities (m s^{-1}), and (d) v component of wind velocities (m s^{-1}).

soil dust at each grid of the model were calculated by equations presented by Mukai et al. (2004). Also, the emission mass flux was set at zero when the model grid was covered with snow. The soil moisture content and snow cover data were calculated from the NCEP-FNL data. The hourly emission of the soil particles started at the initial time plus 6 hours due to the spin-up of the model. In addition to the emission processes, the model includes calculations of both dry and wet deposition processes of the soil particles.

To show the reproducibility of the dust simulations, the spatial and temporal distributions of the simulated PM10 soil dust mass concentrations obtained from results of the pre-experiment were compared with observations of PM10 and suspended particulate matter (SPM) mass concentrations near the ground surface on the Japanese Islands, located at far from the Asian dust sources. The PM10 and SPM observation data were provided by the acid deposition monitoring NETwork in East Asia (EANET: http://www. eanet.cc/), and the Ministry of the Environment and local governments of Japan, respectively. While the PM10 data are collected from a few sites, the SPM observations are conducted at numerous sites on the Japanese Islands (Figures not shown here).

4. Pseudo Global Warming Experiment

The main numerical experiments for investigating potential impacts of the spatial patterns of future atmospheric warming on Asian dust emission were performed with another calculation domain given by 150 x 150 horizontal grids with the center of 50°N/90°E and the grid interval of 40 km. This domain is almost centered on the Asian dust sources, i.e., the arid and semi-arid regions in China and Mongolia. Also, the domain includes a large area at high latitudes where Siberian air masses develop and release cold air surges that frequently induce Asian dust emission. In the main experiments, the option of "heat and moisture fluxes from the surface" in the WRF model was turned off to remove interaction between the atmosphere and surface because this study did not consider future changes in the surface conditions. Other settings of the main experiments are the same as those of the pre-experiment.

First, we randomly selected the three significant Asian dust outbreaks, which occurred on April 14, 2002, April 16, 2003, and March 31, 2007, and then simulated those dust outbreaks as the control runs (CTL-200204, CTL-200304, and CTL-200703). The initial times of the CTLs were set at 0000 UTC April 12, 2002, 0000 UTC April 14, 2003, and 0000 UTC March 29, 2007, respectively, prior to the 72 hours numerical integration. Second, the vertical profiles of the zonal mean GWMDs of atmospheric temperatures, geopotential heights, and u-v wind components at latitudes between 20°N and 80°N, described in Section 2, were added to each variable of the 6-hourly NCEP-FNL data in proportion to the latitudes and pressure levels in order to update the initial and boundary conditions of the CTLs. Third, the updated initial and boundary conditions were used to execute the "pseudo global warming runs" (PGW-200204, PGW-200304, and PGW-200703). In the PGWs, relative humidity in the future climate was assumed to be equal to that in the recent climate because atmospheric warming can increase both the absolute amount of water vapor and the saturation vapor pressure, preventing relative humidity from largely changing. Finally, the future changes in Asian dust emission were analyzed by comparing results of the PGWs with those of the CTLs. Many previous studies adopted this dynamical downscaling method to perform numerical experiments called the "pseudo global warming experiments" [e.g., Sato et al., 2007; Kawase et al., 2009]. This downscaling method allows the spatial patterns of future atmospheric warming, derived from output data from the coarse resolution global-scale climate model (MIROC), to impact on the dust simulations by the fine resolution regional-scale atmospheric model (WRF-Chem). We can quantitatively estimate the impacts of the spatial patterns of future atmospheric warming on Asian dust emission fluxes by executing the CTL and PGW under the same background atmospheric condition and the same dust event. These are difficult for traditional dynamical downscaling methods that directly give grid point values of global-scale climate model projections to regional-scale model simulations.

Results of the experiments showed that the soil dust emission fluxes in the main Asian dust sources, i.e., the Taklimakan Desert and the Gobi Desert, decrease markedly in the future climate. In all of the three dust outbreak events, cold air outbreaks that induce Asian dust emission originated from the vicinities of Lake Baikal, the western part of Mongolia, and the Dzungaria Basin (Figures not shown). Based on the cold air outbreak routes, we can discuss a dynamical mechanism of the future decreases in the soil dust emission fluxes in the Taklimakan and Gobi deserts. Figure 2 shows mean distributions of differences in the daily total emission mass fluxes of the PM10 soil dust, the daily total column-integrated mass concentrations of the PM10 soil dust, the daily mean sea level pressures, and the daily mean surface air temperatures between the PGWs and CTLs on the three dates: April 14, 2002, April 16, 2003, and March 31,

2007. The large increases in SLPs in the Taklimakan Desert and the small SLP changes in a region ranging from the vicinity of the Dzungaria Basin to the western part of Mongolia reduce the SLP gradients between the two areas (Fig. 2c). Similarly, the large SLP increases in the eastern part of the Gobi Desert and the small SLP changes in a region ranging from the vicinity of Lake Baikal to the western part of Mongolia reduce the SLP gradients between those areas (Fig. 2c). The former SLP gradient reduction results in a weakening of the cold air surges intruding into the Taklimakan Desert, which usually move across the Tienshan Mountains or along the eastern rim of the mountains (e.g., Tsunematsu, 2005). The latter reduction leads to a weakening of the cold air surges moving to the Gobi Desert. The resultant decreases in surface wind velocities in the Taklimakan and Gobi deserts (Figures not shown) cause the remarkable reduction in the soil dust emission fluxes in those deserts (Fig. 2a). It is thus found that 1) the small SLP changes in the region located to the north of the main Asian dust sources (the Taklimakan and Gobi deserts) and 2) the large SLP increases in the main dust sources are two important factors in decreasing the future dust emission. The small SLP changes corresponded to the large increases in surface air temperatures (Figs. 2c-d).

5. Summary

Potential impacts of the spatial patterns of future atmospheric warming on the Asian dust emission were investigated by performing the pseudo global warming experiments for the three significant Asian dust outbreak events. After the three events were reproduced using WRF-Chem as the control runs, the initial and boundary conditions of the control runs were updated by adding the vertical profiles of the 50°E-130°E zonal mean GWMDs of atmospheric temperatures, geopotential heights, and u-v wind components at latitudes between 20°N and 80°N to carry out the pseudo global warming runs. The GWMDs were calculated from the MIROC outputs of the 20C3M experiment and the SRES-A1B 21st century climate projection for the periods of March and April in 1991-2000 and 2091-2100, respectively. Results of the experiments showed that the future soil dust emission fluxes in the main Asian dust sources decrease markedly, compared with the emission fluxes in the recent climate. The SLPs in the main dust sources largely increased in the future climate condition. However, the future SLP changes in the region located to the north of the main dust sources were small. The future meridional SLP gradients between the two areas therefore decreased, weakening the cold air surges that induce Asian dust emission. This mechanism can lead to reduction in the future dust emission.

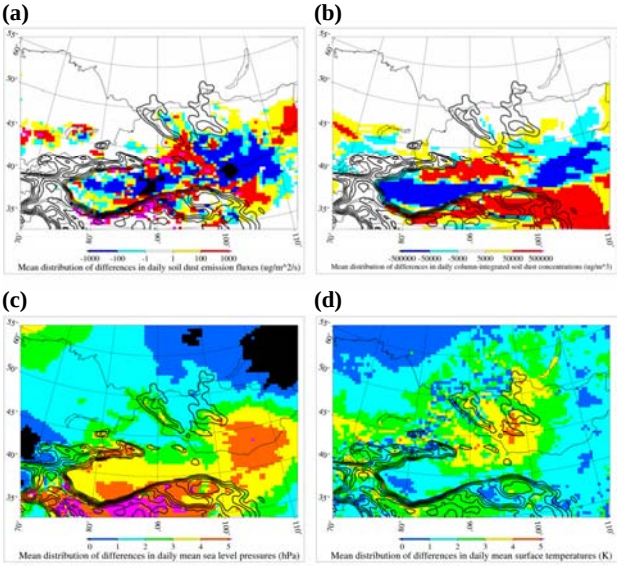

Fig. 2 Mean distributions of the differences in (a) the daily total emission mass fluxes of the PM10 soil dust (μg m^{-3}), (b) the daily total column-integrated mass concentrations of the PM10 soil dust (μg m^{-3}) in the atmosphere, (c) the daily mean sea level pressures (hPa), and (d) the daily mean surface air temperatures (K) between the PGWs and CTLs on April 14, 2002, April 16, 2003, and March 31, 2007.

Acknowledgements

This study was supported by donations from Weathernews inc. and Grant-in-Aid for Scientific Research of Ministry of Education, Culture, Sports, Science and Technology of Japan (No.20403008). The MIROC model data were provided by a project of *Formation of a virtual laboratory for diagnosing the earth's climate system with climate study-related research centers of University of Tokyo, Tohoku University, Chiba University, and Nagoya University*.

References

1)Grell, G.A, et al. (2005), *Atmos. Environ.*, **39**, 6957-6975.
2)K-1 model developers (2004), K-1 Technical Report, 1, 34pp.
3)Kawase, H., et al. (2009), *J. Geophys. Res.*, **114**, D24110.
4)Mukai, M., et al. (2004), *J. Geophys. Res.*, **109**, D19204.
5)Sato, T., et al. (2007), *J. Hydrol.*, **333**, j.jhydrol.2006.07.023.
6)Skamarock, W. C., et al. (2008), NCAR/TN-475+STR, 113 pp.
7)Sun, J., et al. (2001), *J. Geophys. Res.*, **106**, 10,325-10,333.
8)Tsunematsu, N. (2005), *Sci. Online Lett. Atmos.*, **1**, 21-24.
9)Tsunematsu, N., et al. (2005), *J. Geophys. Res.*, **110**, D21207.
10)Tsunematsu, N., et al. (2009), *Boundary Layer Meteorol.*, **131**, 263-275.

Evaluation of MODIS Aerosols Properties Based on SKYNET Ground Measurements: Implications on the Quality of Prospective Satellites' Data

Jules R. Dim [1], Tamio Takamura [2], Pradeep Khatri [2]
Nobuyuki Kikuchi [3]
[1] *Earth Observation Research Center (EORC), JAXA, Tsukuba, Japan*
[2] *Center for Environmental Remote Sensing (CEReS), Chiba University, Chiba, Japan*
[3] *National Institute for Environmental Studies (NIES), Tsukuba, Japan*

Abstract

The quality of Earth observation satellites' products can be evaluated through the comparison of these quantities with those derived from ground measurements. In the perspective of the operational start of the Global Change Observation Mission-Climate (GCOM-C) satellite carrying the Second-generation Global Imager sensor (SGLI) , the quality of aerosols properties retrieved from actual and comparable satellites, such as the Terra- and Aqua- Moderate Resolution Imaging Spectroradiometer (Terra- and Aqua-MODIS), is assessed with ground measurements from three SKYNET (observation network to understand aerosol-cloud-radiation interaction) sites, located in the southern part of Japan. In this assessment, two major aerosols properties, the aerosol optical thickness (AOT) and the Ångström exponent (Alpha), derived from skyradiometers measurements of the SKYNET sites are compared with the retrievals from two Terra- and Aqua-MODIS satellites' algorithms for a period of 2 years (2008 and 2009). Results of these comparisons show overall similarities in the monthly and seasonal variations of the aerosols quantities between these data sets. However the magnitude of this variation shows some differences between the ground data and one of the MODIS algorithms. The retrievals from this algorithm appear consistently overestimated for the AOT (thicker layers) and underestimated for Alpha (dominance of coarser particles). Possible causes of these tendencies are investigated with particular emphasis on the aerosol size distribution assumption used for the satellite retrievals and the contamination by clouds.

Keywords **:** SKYNET, Terra- and Aqua- MODIS satellites, aerosols properties, evaluation of satellite retrievals

1. Introduction

Operational remote sensing of aerosols from long-term satellites provides a means to achieve global and seasonal characterization of aerosols (Remer et al, 2005). Ground measurements, though very dispersed are generally used to evaluate and improve the quality of satellites' derived geophysical properties. In the perspective of the future launch of the GCOM-C/SGLI polar orbiting satellite, the performance of atmospheric products (the aerosol optical thickness and the Ångström exponent) derived from actual and comparable (to the GCOM-C/SGLI) satellites are evaluated with ground measurements of three SKYNET sites located in the southern part of Japan. The satellite observations used for this purpose are from Terra- and Aqua-MODIS satellites. The evaluations are aimed at highlighting and discussing the difficulties, associated with accurate aerosols retrievals, which should be addressed by the tools used to derive atmospheric properties of future satellites. The ground sites, against which the satellites' retrievals are evaluated, are located on islands and have been recording atmospheric radiation and climate data on a regular basis for at least 5 years.

2. Observation data

The aerosols properties examined in this study are the AOT and Alpha. The satellite data used to derive these properties are from the Terra- and Aqua-MODIS polar orbiters while ground measurements are obtained from three SKYNET sites located close to the sea: Fukue-jima, Hedo-Misaki, and Miyako-jima (to be called here, respectively Fukue, Hedo and Miyako). Figure 1 shows a satellite image of the AOT distribution around these sites. The AOT values here are mostly around 0.4. On these sites, skyradiometers made by PREDE, Japan as well other observation instruments record atmospheric radiation and various climate variables. The skyradiometers, measure the direct solar irradiance and diffuse sky radiances at the following wavelengths: 315, 400, 500, 675, 870, 940 and 1020 nm for the POM-01 type radiometer and at 4 additional channels (340, 380, 1627 and 2200 nm) for the POM-02 type radiometer. These skyradiometers have been calibrated by the improved Langley method at each site

(Tanaka et al., 1986; Nakajima et al., 1996a, Nakajima et al., 2003) and the error of the calibration constants is believed to be less than 2% (Nakajima et al., 2003). Aerosols properties derived from two algorithms using Terra- and Aqua-MODIS radiances are evaluated against the SKYNET sites' (to be named here Ground) measurements. These algorithms are: the National Institute for Environmental Studies, Japan algorithm (to be named here NIES) and the National Aeronautics and Service Administration, USA algorithm (to be named here NASA).

3. Description of the MODIS aerosol algorithms

The satellites' aerosols properties evaluated in this study are the products of two algorithms: NIES and NASA. Each of these algorithms is indeed two entirely independent algorithms, one for deriving aerosols over land and the second for aerosols over ocean. Over the land the aerosol optical thickness is derived using the dark target approach. The NASA land algorithm as described in Kaufmann and Tanre (1998) uses the measured radiance at 3 channels: 0.47, 0.66, and 2.13 μm channels, while over the ocean, the aerosol optical thickness is provided in seven wavelengths from 0.47 to 2.13 μm. The radiances of these channels are inverted into the aerosol optical thickness and the volume distribution (in the range of 0.08-5 μm radius). In the inversion, it is assumed that the aerosol size distribution is bi-modal log-normal. The AOT as well as secondarily-derived size parameters, among which Alpha are stored on a resolution of 10x10 pixels. The steps in the land retrievals are as follows: to determine the AOT, surface reflectance (after ozone and water vapor amount corrections) is first estimated (through reflectances at 2.13 μm). These estimated surface reflectances at 0.47 and 0.66 μm and the measured mean-of-atmosphere reflectances at 0.47 and 066 μm are used as input into the chosen model's LUT to retrieve values for the AOT, fluxes and other parameters. A full second retrieval is made from the appropriate model's LUT. The final step in the process is to interpolate the values at 0.47 and 0.66 μm using an Ångström law in order to report optical thickness and flux values at 0.55 μm.

The NIES algorithm retrieves the AOT at 0.50 μm, and Alpha from two channels (visible and NIR) radiance data (Nakajima, T., and A. Higurashi, 1997, Nakajima, T., and A. Higurashi, 1998, Higurashi, A., and T. Nakajima, 1998). Satellite-received radiances are synthesized with four look-up tables (LUTs). It is clear that the strategy for the aerosol retrieval is based, as in the NASA algorithm, on look-up the table (LUT) approach, i.e., radiative transfer calculations are pre-computed in terms of the aerosol and surface parameters. For retrievals, the ancillary data needed include wind velocity at 10 meter height, ozone and water vapor amount to correct radiance for surface reflectance, ozone and water vapor absorption. The assumption of the aerosol optical model uses a bi-modal log-normal volume spectrum for modeling the aerosol size distribution:

$$\frac{dV}{d\ln r} = \sum_{n=1}^{2} C_n \exp\left[-\frac{(\ln r - \ln r_{m,n})^2}{2\sigma_n^2}\right]$$

Where, subscript n indicates the mode number, $r_{m1} = 0.17$, $r_{m2} = 3.44$, $\sigma_1 = 1.96$, $\sigma_2 = 2.37$ are adopted for the parameters of the modeled volume spectrum, and the complex refractive index of $m = 1.5 - 0.005i$ is used in this retrieving scheme.

4. Comparisons of aerosols properties

The average aerosols quantity from daily satellite images in an area of 100*100 km surrounding each SKYNET site is chosen for the comparison with the nearest matching time ground data record. The analysis covers a period of 2 years (2008-2009). Figure 2 presents the histograms of the distribution of the aerosols properties as derived from the ground observations. The average AOT and Alpha between the sites are found to vary between 0.27 and 0.36 then 0.97 and 1.05 respectively. The distribution is mostly uni-modal to bi-modal. The AOT mode is at 0.4 for Fukue and Hedo, while the 2 modes of Miyako are at 0.7 and 0.4. The northernmost site, Fukue shows a sharper mode, while the two other sites have more flattening in the AOT distribution. The case of the latter two sites may suggest a mixture of aerosols of various origins while the former case (bell shape distribution) would indicate a more unique origin of the aerosols at that site.

Figure 3 presents the correlation between the aerosols properties measured from skyradiometers and those retrieved from the NIES and NASA algorithms. There is a better 1:1 alignment between the ground data and the MODIS-NASA properties while the MODIS-NIES retrievals constantly overestimate the AOT and underestimates Alpha. Between the three sites, the best alignment for both AOT and Alpha with the MODIS-NIES is at the northernmost site of Fukue, which has been previously identified as presenting a likely unique origin in its aerosols. The worst underestimation of Alpha values in both algorithms is at the southernmost site of Miyako (probably the most contaminated aerosols). These smaller

Alpha values of the satellite retrievals compared to the site data suggest that the aerosols detected by both algorithms are dominated by larger size particles. In both algorithms the largest AOT (>0.75) appear to be underestimated compared to the ground data. The monthly and seasonal change of AOT and Alpha reflect the differences in the magnitude of these parameters between the ground and the satellite retrievals though the short term variation trends as well as their peak and low episodes are well reflected on the satellite data.

Possible factors at the origin of these differences may range from the size distribution model assumption used in the retrieval of the aerosols properties to the cloud contamination..

5. Discussion

The differences in cloud properties between the satellite retrievals and the ground measurements are discussed in terms of the assumed size distribution used in the satellite retrievals and the cloud contamination.

As noticed earlier both NIES and NASA algorithms use a bi-modal log distribution assumption for the aerosols retrievals. There is a good correlation between the NASA data and the ground data. This would suggest that the size assumption used would be valid. This confirms also that the ground data are of high quality. A lower correlation between the ground data and the NIES retrievals was noticed earlier (Figure 2). A previous study, comparing the ADEOS-II/GLI retrievals (using a similar version of the algorithm of MODIS-NIES) with ground data (Takamura et al., 2009) confirm these tendencies and, uses the ground size distribution of the SKYNET sites to improve the initial satellite retrievals.

The cloud environment surrounding the retrieved aerosols can affect the proper detection of the aerosols properties. To study this effect, the clouds encountered in the same area where the aerosols properties are averaged are compared to these aerosols. The cloud parameters taken into account are the cloud fraction (CF), the cloud top pressure (CTP) and the cloud optical depth (COD). The examination of the clouds occurrence above the three SKYNET sites studied (Fukue, Hedo and Miyako) shows the dominance of low level clouds (63, 77 and 80% of total at the respective sites) and more specifically stratocumulus (37, 56 and 55% of total at the respective sites). At the same time, the average cloud amount estimated is 51, 55, 64% at the respective sites. It appears that the strongest discrepancies between the aerosols properties of the satellite retrievals and those of the ground occur at the most cloudy site (Miyako).

6. Conclusion

In this study, difficulties in the estimation of the atmospheric aerosols properties were examined. These pertain to the quality of the aerosol model size distribution assumption and the impact of clouds. The comparison of both the AOT and Alpha retrieved from the satellites with ground measurements showed a certain agreement in the variation trend of these aerosols properties. However the magnitude of this variation seems to differ mostly between one of the satellites retrievals and the ground measurements. And these differences do not follow a specific seasonal pattern and seem to be more accentuated in the southernmost site. The ground AOT distribution suggests there may be varied sources in the aerosol load at this site. Also it is the cloudiest of the three sites examined. This study suggests that particular attention should be paid to the size distribution model assumption and the corrective methods related to the cloud radiation scattering for aerosols retrievals from future satellites such the GCOM-C/SGLI.

References

1) Higurashi, A., and T. Nakajima, 1998: Development of a Two Channel Aerosol Retrieval Algorithm on Global Scale Using NOAA / AVHRR. J. Atmos. Sci., 56, 924-941.

2) Nakajima, T., G. Tonna, R. Rao, Y. Kaufman, and B. Holben, Use of sky brightness measurements from ground for remote sensing of particulate polydispersions, Appl. Opt., 35, 2672– 2686, 1996a.

3) Nakajima, T., and A. Higurashi, 1997: AVHRR remote sensing of aerosol optical properties in the Persian Gulf region, the Summer of 1991. J. Geophys. Res., 102(D14), 16,935-16,946.

4) Nakajima, T., and A. Higurashi, 1998: A use of two-channel radiances for an aerosol characterization from space. Geophys. Res. Lett., 25(20),3815-3818.

5) Nakajima T., M, Sekiguchi, T. Takemura, I. Uno, A. Higurashi, D. Kim, B. J. Sohn, S.-N. Oh, T. Y. Nakajima, S. Ohta, I. Okada, T. Takamura, and K. Kawamoto. 2003. Significance of direct and indirect radiative forcings of aerosols in the East China Sea region. J. Geophys. Res. 108, No. D23, 8658, doi:10.1029/2002JD003261, 2003

6) Remer L. A., Y. J. Kaufman, D. Tanre, S. Mattoo, D. A. Chu, J. V. Martins, R. –R. Li, C. Ichoku, R. C. Levy, R. G. Kleidman, T. F. Eck, E. Vermote and B. N. Holben.(2005). The MODIS aerosol algorithm, products, and validation. Journal of the Atmospheric Sciences-Special section. Vol 62. pp 947-973).

7) Takamura T., H. Takenaka, Y. Cui, T.Y. Nakajima, A. Higurashi, S. Fukuda, N. Kikuchi, T. Nanakajima, I. Sano and R.T. Pinker, Aerosol and cloud validation system based on SKYNET observations: estimation of shortwave radiation budget using ADEOS II/GLI data, J. Remote Sensing Soc. Japan, 29(1), 40-53, 2009.

8) Tanaka, M., T. Takamura, and T. Nakajima, Refractive index and size distribution of aerosols as estimated from light scattering measurements, J. Clim. Appl. Meteorol., 22, 1253– 1261, 1983.

9) Yoram J. Kaufman1 and Didier Tanré. 19998. Algorithm for remote sensing of tropospheric aerosols from MODIS (Product ID: MOD04, Revised).

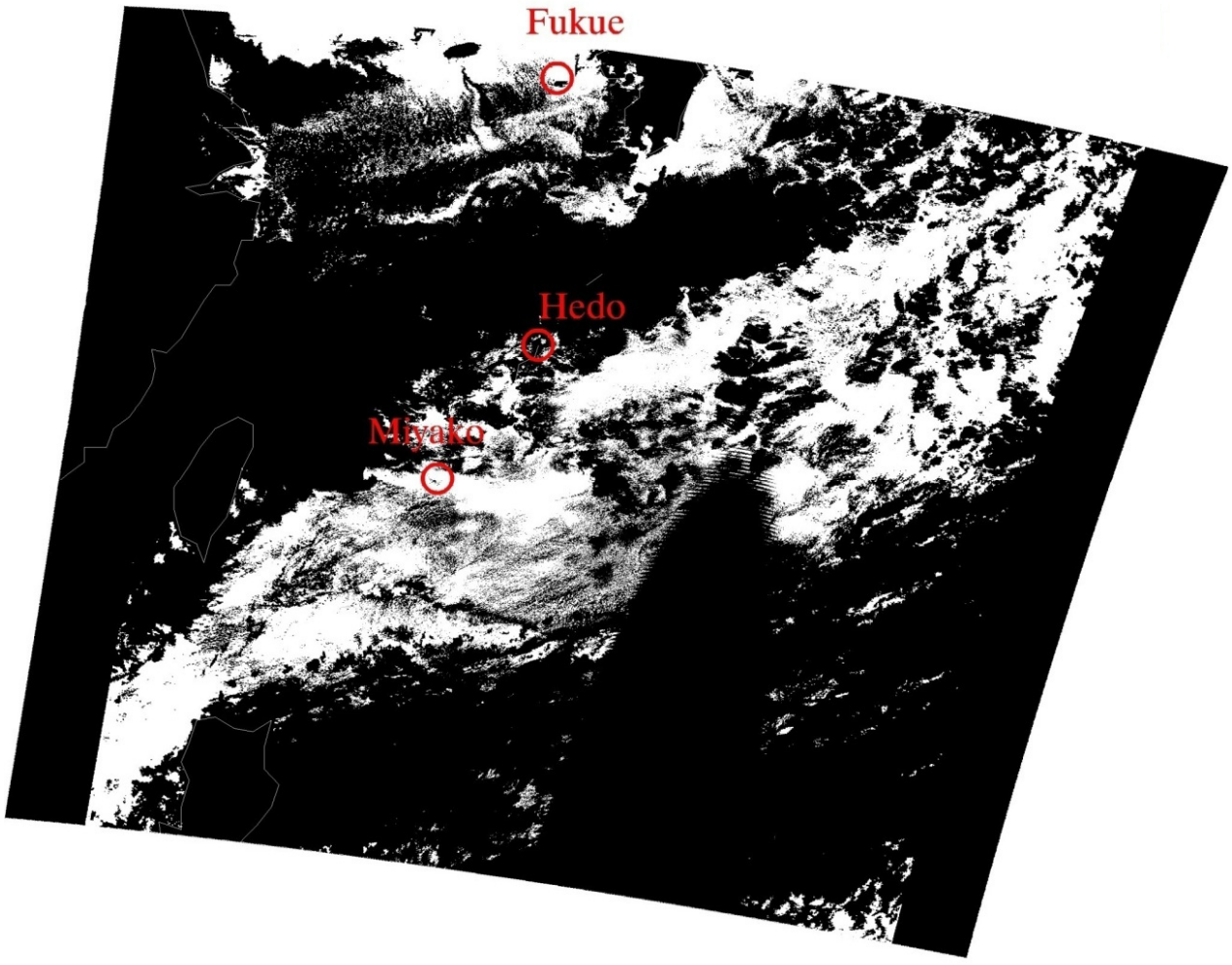

Figure 1. Satellite retrieved AOT on 2008.02.19 at 02:05 and SKYNET sites location

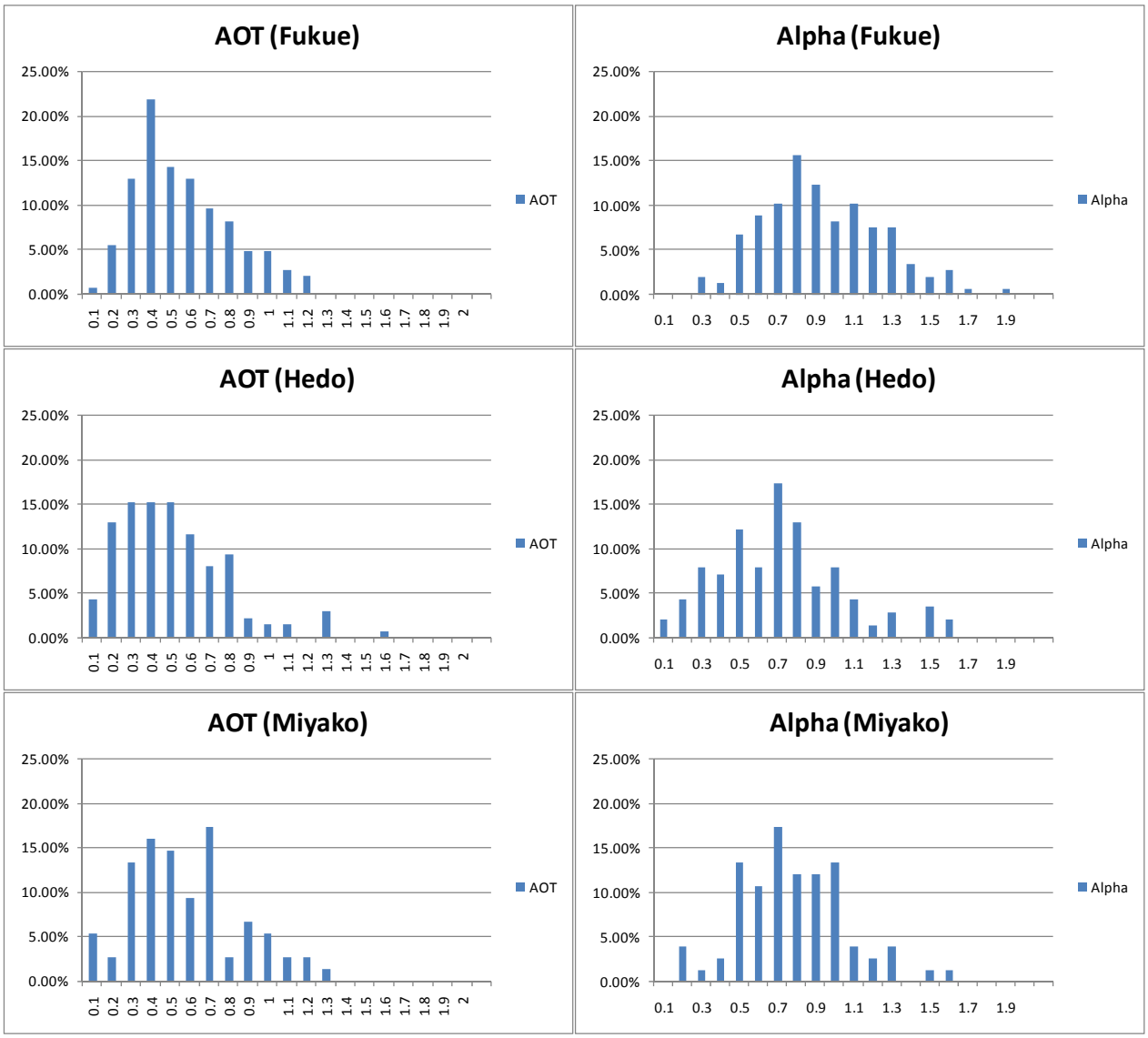

Figure 2. AOT and Alpha histogram distributions at the SKYNET sites.

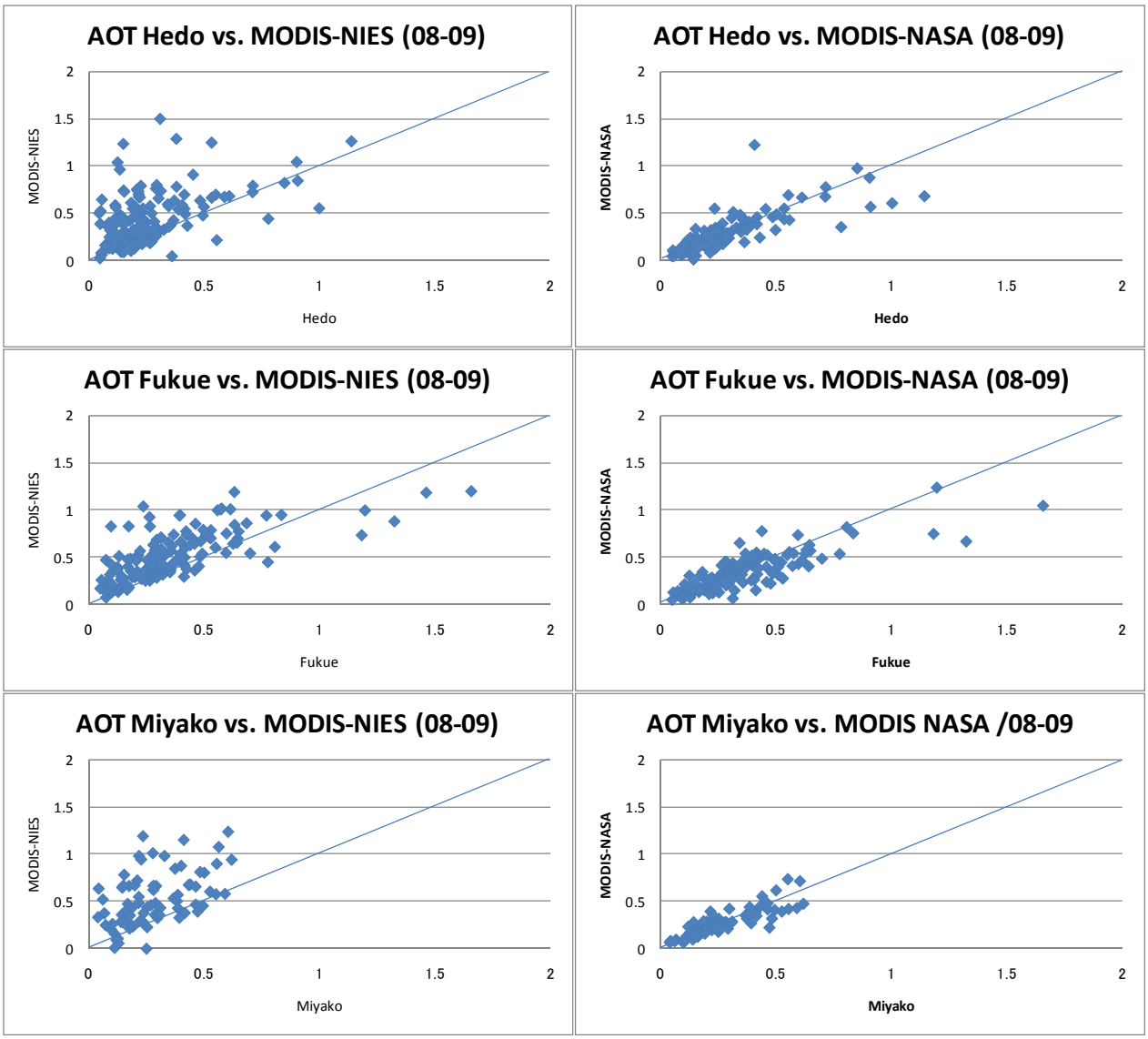

Figure 3a. AOT comparison between ground measurements (x-axis) and satellite retrievals (y-axis). .

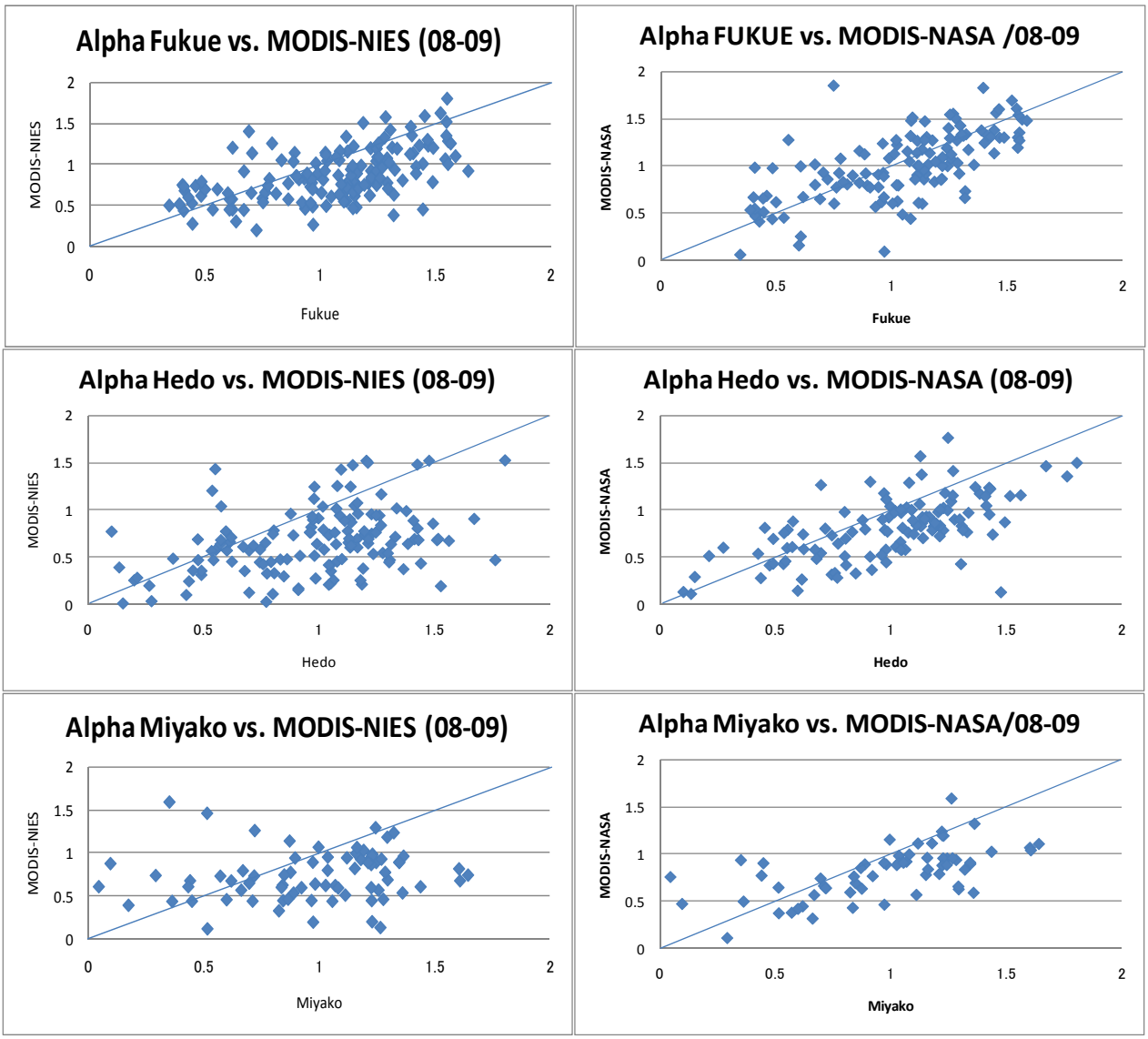

Figure 3b. Similar to figure 3a but with Alpha..

Air pollution problems in Ulaanbaatar, Mongolia

Tugjsuren Nasurt
Mongolian University of Science and Technology
E-mail: tugjsuren@must.edu.mn

Abstract

The objective of this report is to provide an analytical basis to underpin discussions on air quality in Ulaanbaatar, Mongolia and to discuss possible short and long-term strategies for reducing air pollution; given the changing demographics and growing urbanization and industrialization. These trends have spurred an increase in the demand for energy in several sectors including transport, construction, heating, industrial production and have resulted in challenges such as pollution from transport, waste disposal, and natural resource mining among others. A scenario analysis of air pollution emissions in Ulaanbaatar for the years 2010 and 2020 indicate that unless the government makes a concerted effort to address the issue at multiple levels, air pollution and its corresponding health impacts will be significant. While there is no single solution to reduce emissions, a combination of measures ranging from public education and awareness to strengthening of monitoring and enforcement, to improving technology is necessary, in order to successfully address the increasing levels of air pollution. This paper presents, multi-pollutant emissions analysis, dispersion results, impact assessment, and scenario analysis for 2010 and 2020 for Ulaanbaatar.

1. Introduction

Air pollution was one of the critical problems 20 years ago in Ulaanbaatar, but even now it has not been solved. In fact, UB is fast becoming the world's most polluted city; a remarkable achievement considering its population only hovers around the 1.2 million. The pollution is visibly worse in the wintertime. This is because coal-fueled *ger* (traditional felted tents) stoves and boilers used for heating and cooking produce toxic black smoke plumes that hover like a blanket over the often windless city. The chokingly-thick pollution is a result of a combination of factors: the poor combustion of coal in what are essentially wood stoves, the congested road traffic, the dry ground condition and industry. For about eight months of the year heating is essential for the survival of residents. 60 percent of the city's residents live in peri-urban *ger* districts; areas populated in the main by life condition not good people from Mongolia's rural areas who are arriving in a steady flow. UB's population has expanded by 70 percent over the last 20 years and unfortunately the city's infrastructure has not been able to keep up with the growth. In these areas, which are mainly located upwind of the city, the only source of heating are poor quality stoves or individual household boilers fueled by coal, wood and in some cases rubbish-varying from black tar dipped bricks to old car tires. UB's remaining citizens live in apartment buildings heated by three coal-burning heat and power stations. All forms of household heating in UB contribute to the air pollution problem.

The number of cars on the city's roads seems to be increasing daily. Drivers beep their horns impatiently and ineffectually, hoping for movement, while pumping carbon dioxide, carbon monoxide, sulphur dioxide and nitrogen oxides into the air and the faces of those braving the cold or waiting to cross the street. When cars do move, further dust is released into the air, especially in the *ger* areas where most of the roads remain unpaved.

The followings are the main causes of environmental harm and air pollution of Ulaanbaatar city and generate huge pressure against safety and healthiness.

1. *Climate and geography.* Extreme and harsh climate (Ulaanbaatar is one of the coldest capital city in the world and during the coldest months of the year), air flows and stagnancy centralize on incurved area between four mountains with affections of the air inversion in could seasons causes high densely pollution and toxin in air level of people breathing and it reached to dangerous level to the human health.
2. *Increase in demography, population migration and expansion of ger district.* As of 2009, there are 1000.0 thousand residents or 37.0 percent of total population of Mongolia accommodation in UB city, the 470.400 hectares of land. Out of 216.0 thousand families of the capital city,89.2 thousand or 41.2 percent of families live in apartments. There are 135000 families are registered in Ulaanbaatar city, which are considered to be air polluting sources among more than 130000 counted

sources in 9 districts. Moreover, each families in private houses, apartments and in gers, utilizing about 5.3 tons of coal annually which is responsible for 90 percent of air pollution in the city.

According to the information released from "Air quality Professional Agency", it is mentioned that three power plants in Ulaanbaatar city burning 3.361.510 tons of coal is utilized in 3 power stations as raw material per annum, in addition to 1378 small and middle sized low pressure furnaces utilizing 1.1 million tons, are the main generators of air pollution. 54 small and middle sized low pressure furnaces do meet the safety requirements. There are 25 schools and 18 daycares in the city which are heated by low pressure furnaces with 895000 tons of coal annually. In the last decade, the city population has increased by 300 thousand and the share of ger district families increased from 48% to 58.6%. The air polluters, in the center of the city are mostly dairy product sellers, concession standers and who burn litter for heating.

City planning and urbanization. It is challenging that industrial plants and various services are centered in Ulaanbaatar city producing large pile of wastes and ashes. As of 2007, total of 95000 vehicles, 436 motorcycles , 779 tractors and all terrain vecicles, 1626 trailers were registered in the city. However, approximately 130000 vehicles are running within the capital city. As of 2010, total of 130000 vehicles were registered in capital city. 64.6% of total vehicles in Ulaanbaatar city run on gas, 33.1% on diesel and 2.3% on liquid gas fuel. Incomplete gas burn during the traffic jam or pedaling at cross sections, causes air pollution. In addition, increasing number of gas stations and car repair shops in the city also chips in the general state of environmental pollution.

2. Air quality monitoring in Ulaanbaatar city.

There are 4 observing points measuring city air quality. There are also 22 observing points located in bigger 18 cities which measure sulfur and nitric dioxide, and conduct air monitoring and research activities. Daily average of sulfur dioxide and nitric dioxide in capital city air were higher than the standards in 12.2-34.5 percent of total observed days in 2005 and 14.0-31.0 percent in 2009. Sulfur dioxide usually increases in October thru April, due to extensive use of coal in winter time. Nitric dioxide has been observed higher than the standards all season around, usually in the area closer to bigger roads, which can be explained by use of vehicles and traffic loads. The vehicles in te capital city have increased by 3.3 times and volume ger district has increased by 2.3 times since 1995. Occasional measurement of sulfur dioxide surpassed the air quality standard (AQS) in 2007 reached to 14.6% of the total average observed, which was more with 0.6% than in 2006; occasions of nitric dioxide surpassed AQS even reached to 44% which was 12.7% higher than the 2006. How is changed this view in the last 2 years? Occasional measurement of sulfur dioxide surpassed the air quality standard (AQS) in 2009 reached to 15.5% of the total average observed, which was more with 0.64% than in 2008; occasions of nitric dioxide surpassed AQS even reached to 46% which was 13.2% higher than the 2006. As conclusion, we obviously can see that air pollution has sudden increase in last years (Fig.1-3)

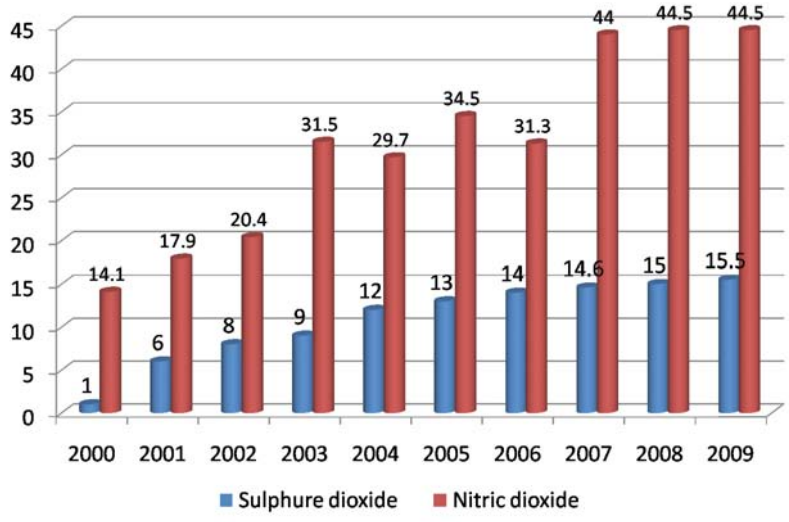

Fig.1 Number of days having higher-than-the average level of pollutant in the air (by percentage)

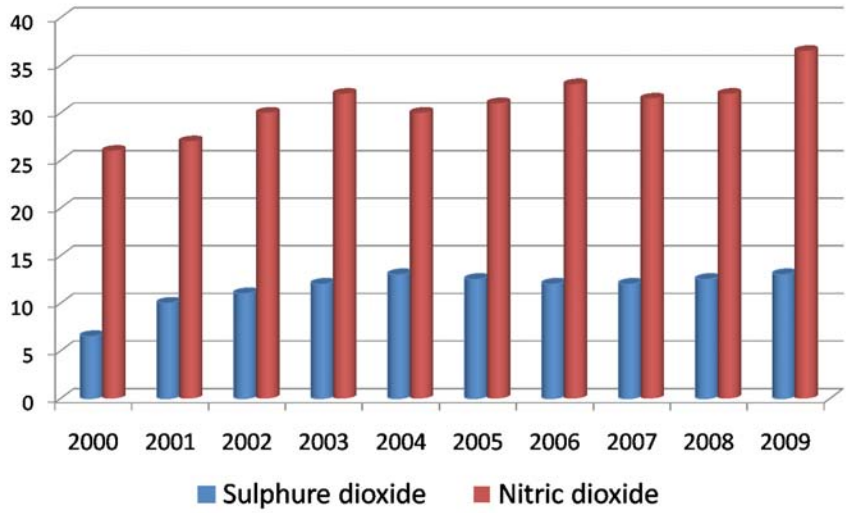

Fig.2 Statistics on Air polluting substances (mcg/m^3)

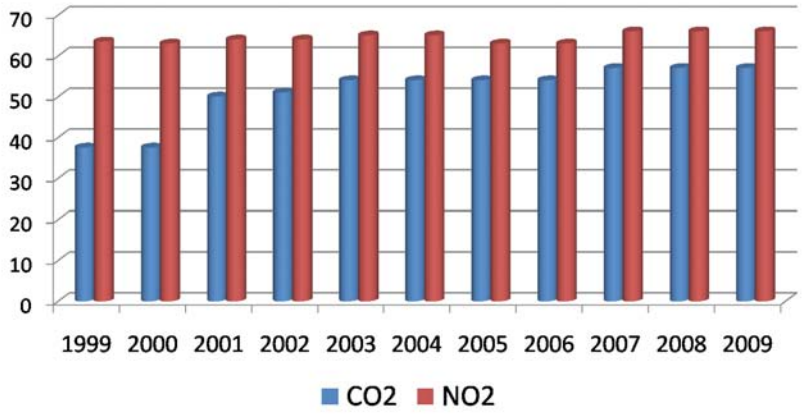

Fig.3 Annual average level of the sulfur dioxide-CO2 and nitric dioxide-NO2 in air of Ulaanbaatar city

3. Current state of air pollution in Ulaanbaatar city.

According to the research, 2009 annual average of sulfur dioxide level in the air was 12.5 mcg/m^3 and the highest or 83.0 mcg/m^3 of sulfur was recorded in January. According to the research, 2009 annual average of nitric dioxide level in the air was 37.5 mcg/m^3 and maximum daily average of 99.1 mcg/m^3 was recorded at some place in July. Ulaanbaatar city air quality information reveals that the nitric dioxide level (standard level , 40 mcg/m^3) in January 2008 was twice higher with 83mcg/m^3 at some places. Sulfur dioxide amount (standard level, 30mcg/m^3) in more air polluted areas was measured at 38-39mcg/m^3, while in other areas, the pollution was comparatively less. The above picture was observed in areas with crowded cars, cross sections, and traffic overloads. In 2007, the sulfur gas annual average in bigger cities and villages of Mongolia was 2-13mcg/m^3, the highest has been recorded in Darkhan city which was recorded at 461 mcg/m^3. The annual average level of nitric dioxide was recorded at 5-39mcg/m^3 in Darkhan city, while the highest was observed as 123mcg/m^3, which is five times higher than the average. The Government of Mongolia has issued Decree No.218 of 2007 concerning the implementation work of Parliament Resolution 46 of 28 june 2007 on Specific measures for reduction of air pollution and Presidential Directive on Specific measures for reduction of air pollution. By the order 229 of 2006 of the Minister for Nature and Environment, National Air Quality Office has been established with the purpose of implementing policies on reduction of air pollution, air quality control and research and for disseminating information. The City Mayer has issued Decree No.2/444 of September, 2006, on establishing Air Quality Unit. Issues of evaluating the current state of air pollution, measures toward reducing air pollution, required budget, and scientific estimation of implementing such measures, need to be addressed at the government

decision-making level. In connection with this, the Parliament of Mongolia has issued decree No.46 on reversing air pollution, which includes total of 13 articles.

4. Measures to reduce of air pollution in Ulaanbaatar city.

Steps are being taken to implement Point 12 of the millennium Development Goals: "to adapt sustainable development principles in the national development policies and programs and to reverse air and environmental pollution in urban areas, particularly in Ulaanbaatar city". A feasibility study has concluded that it would be efficient if plant for ecologically friendly fuel were established at Power Plant 2, a government owned joint stock company. The capacity of the plant will be processing 540 thousand tons of coal and producing 216 thousand tons of smokeless fuel annually. Calculations also show that the steam ovens converted to utilize the gas separated during the semi coking process, could generate 125.28 million kWh of electricity and 123 thousand Gcal of thermal energy. It was also concluded that coking coal is the most feasible solution to reverse air pollution in the city. Based on these conclusions, the Parliament has approved a budget of MNT 50 billion to alleviate air pollution in Ulaanbaatar city, and additional MNT 2 billion from state budget to subsidize companies that produce smokeless condensed fuel. As result of these activities, NO_2 emitted in the air will be decreased by 80-90% and poisonous chemical particles released in the environment by 95-98%, and 30 tons of particles and ashes produced by power plants annually become a history.

A family living in an average Mongolian ger with 5 walls and 2 layers will spend approximately 2.5 tons of condensed (smokeless) fuel in winter months, which will cost approximately 105 thousand tugrugs. If this is the case for 86 thousand families in Ulaanbaatar ger district, we will be able to decrease the smoke coming out of the pipe of each ger by 60 percent. Therefore, in 2007, measures have been taken toward switching low pressure furnaces that are currently being used for schools, daycares and family hospitals, with electric furnaces, and providing 20 thousand families with environmentally friendly condensed fuels, ground fuel, electric furnace and additional insulting covers. The Minister for Construction and Urban Development and The Mayor of Ulaanbaatar city signed a contract on establishing Apartment Corporation in order to implement "40000 family Apartment Project". A location of the apartment complex and corresponding urban planning , have been already selected. Moreover, it is important to seek for and increase the consumption of alternative energy sources, such as solar and wind energy, adopt new advanced technologies in the energy production and to decrease energy costs per production unit. The Ministry always holds a policy to support projects and initiatives such as utilization of gas furnace, liquid gas and utilization of inexpensive energy in night hours, production of condensed fuel, production of improved ger stove, experiment of speed fire-starter, installation of SHP-600 filter in automobiles, monitoring of automobile diagnostic centers and experiment of vehicle emission testers. In order to provide the public to live and work in healthy and safe environment and in order to legalize "polluter Pays Principle", a law on Air Payment, has been drafted and discussed at the Cabinet meeting of the Government, and consequently, submitted to the Parliament of Mongolia for final approval. With the aim of establishing legal environment for determining the roles of the state and local governments, individuals and companies, in prevention from air pollution and its increasing level, and of adopting modern technologies in reduction of air pollution, the draft law on changes and amendments to the Law on Air and on Environmental protection have been developed.

5. Conclusion

1. To increase the consumption of alternative energy sources, such as solar and wind energy, adopt new advanced technologies in the energy production and to decrease energy costs per production unit.
2. To support projects and initiatives such as utilization of gas furnace, liquid gas and utilization of inexpensive energy in night hours, production of condensed fuel and ger stove using new technologies, experiment of speed fire-starter, installation of SHP-600 filter in automobiles, monitoring of automobile diagnostic centers and experiment of vehicle emission testers. In order to provide the public to live and work in healthy and safe environment and in order to legalize "Polluter Pays Principle"
3. With the aim of establishing legal environment for determining the roles of the state and local governments, individuals and companies, in prevention from air pollution and its increasing level, and of adopting advanced technologies in reduction of air pollution

References

1. Oyun R., Jargalkhuu J., Saijaa N., N. Tugjsuren N., Mendbayar B., Sanchir I [2007]: Proseedings of "Air pollution -2007", Mongolia and Japan Joint Symposium, Nov. 24, 2007, Ulaanbaatar, Mongolia
2. Report on the state of the environment of Mongolia (2006-2007), Ulaanbaatar, 2008, Mongolia, 114 pp
3. General statistics on environmental mmpact assessments, 1998-2007, 2008-2009, Ulaanbaatar, Mongolia
4. Mongolia national action programme on climate change [2000]: Edited by Batjargal Z., Dagvadorj D., Batima P. Ulaanbaatar, 2000, 156 pp
5. Greenhouse gases mitigation potentials in Mongolia [2000]: Edited by Batima P., Dagvadorj D., Dorjpurev J. Ulaanbaatar, 2000, 144 pp
6. Tugjsuren N [2000]: Investigation of polluted cold air in the atmosphere of Ulaanbaatar city using satellite data. Proceedings of Mongolia and Russian Joint Symposium, December, 2009, Ulaanbaatar, Mongolia

Aerosol radiative properties over Hefei during 2007-2010

Zhenzhu Wang[1], Dong Liu[1], Yingjian Wang[1], Pradeep Khatri[2], Jun Zhou[1], Guangyu Shi[3], Tamio Takamura[2]

1 Key Laboratory of Atmospheric Composition and Optical Radiation, Anhui Institute of Optics and Fine Mechanics, Chinese Academy of Sciences, PO Box 1125, Hefei, Anhui 230031, China, E-mail: zzwang@aiofm.ac.cn

2 Center for Environmental Remote Sensing, Chiba University, Chiba, Japan

3 Institute of Atmospheric Physics, Chinese Academy of Sciences, Beijing, China

Abstract

Aerosol radiative properties are retrieved from the observed data using a ground based sky radiometer. The seansonal variations are discussed after a good validation using another sunphotometer. The derived results as input parameters are used to calculated aerosol radiative forcing (RF). The comparison between the measured flux and the modeled flux shows a good agreement at the surface. The mean values of RF due to aerosol at SFC, TOA, and in ATM during 2007 to 2010 are -33.9, -23.1, and 10.8 Wm-2, respectively. Because of high value in SSA, the relative RF kept in ATM is not so much though the large value of AOD over Hefei.

1. Instruction

Atmospheric aerosols have a significant impact on climate due to their imporatant role in modifying atmosphere energy budget. They are able to alter climate in direct and indirect ways. The direct effect is related to the scattering and absorption of solar and infrared radiation by aerosols, and the other one is due to changing the microphysical and chemical properties of clouds by them. The scattering of solar radiation acts to cool the planet, while absorption of solar radiation by aerosols warms the air directly instead of allowing sunlight to be absorbed by the surface of the Earth. On global scale, the direct radiatve forcing is estimated to be in the range of -0.9 to -0.1 Wm-2 for aerosols (Intergovernmental Panel on Climate Change, IPCC, 2007)[1]. Yet, these estimats are subject to very large uncertainties because of uncertainties in spatial and temporal variations of aerosols. At local scales, as aerosol properties can vary spatially and temporally, radiative forcing due to aerosols can be also very different and it can exceed the global value by an order of magnitude. Hence, there is an urgent need to obtain more informantion on aerosol properties and radiative forcing due to aerosols in different regions of climate significance especially in China.

SKYNET is an observation network to study aerosol, cloud, and radiation interaction in the atmosphere. Data collected by SKYNET network are very useful to extend our knowledge regarding the effects of aerosols on regional and global climate change. And PREDE Sky radiometer is a key instrument of this network and is useful to study aerosol properties. Also, there are other instruments implemented with, such as radiometers, microwave radiometer et al. Hefei (31.897N, 117.173E) site , as talked about in this paper, is one of the super ground-base stations in the eastern China.

In this study, aerosol properties using sky-radiometer data in Hefei are derived, and high quality data including AOD, SSA, Ang. Index in clear day are obtained. Radiative flux at the surface is calculated and compared with observed radiative flux, which is based on inversed aerosol data and tested to be a good agreement. Then direct radiative forcing due to aerosol is also obtained over Hefei site.

2. Instruments and Methods

The instruments used in this study are installed at Anhui Institute of Optics and Fine Mechanics (AIOFM), 15 km west of Hefei city and are listed in Table 1. The PREDE Sky-radiometer is a key instrument of SKYNET network in Aisa and is useful to study aerosol properties. The calibration methodolog, quality control, data reduction precedures and cloud screening for this instrument are presented in [2-4].

The Sky-radiometer is operated continuously everyday except rain and snow , to acquire direct solar and diffuse sky radiances at predefined scattering angles. The data have been analysed by using the SKYRAD.PACK [2] version 4.2 for retrieval of aerosol optical thickness (AOT), SSA, asymmetry factor (ASY), volume size distribution (SD), refractive index (Mr,Mi) and angstrom index (α). Daily mean AOD, SSA, ASY and M at 340, 380, 400, 500, 670, 870, and 1020 nm wavelengths as well as SD and α are calculated after cloud-screening [4]. The sunphotometer is used for comparison with the sky radiometer. And the

Table 1 Instruments and parameters

Instruments	Parameters
Sky radiometer POM-02	AOT,SSA,ASY, Ang.Exp.,
340,380,400,500,675,870,1020 nm	…
Pyranometer CM21 305-2800 nm	diffuse Flux
Pyrheliometer MS-53 305-2800 nm	direct Flux
Microwave Radiometer WVR-1100	Precipitable water path, Liquid water path
Sunphotometer DTF-5	AOD
1050,860,780,670,610,520,400 nm	…

Pyranometer, Pyrheliometer, and Microwave Radiometer are used for detecting diffuse, direct flux and water vapor content, respectively. All of them mentioned above, are operated simultaneously and data collected during Mar., 2007 to Sep., 2010 are used in this paper. In addition, the fluxes at the surface and top of atmosphere are also estimated by a radiative transfer calculation using SBDART model developed by Ricchiazzi et al.[5]. From these calculated fluxes, the radiative forcing due to aerosol can be known. The radiative effect of aerosols on solar radiation can be expressed in two ways, one the difference between the actual atmosphere with aerosols and the atmosphere without aerosols, and the other is the effect of anthropogenic aerosols only, that is the direct radiative forcing due to aerosols [6]. In present study, the former definition is used to get our results.

3. Results and discusion

The AOD values by skyradiometer, which are obtained using both direct and diffuse solar irradiance, are compared with the ones by sunphotometer using direct data. Figure 1 shows the correlation between them in clear days of 2008-2010 and a good agreement is given with the correlation coefficient of 0.973 and sample number of 2993. Note here that the sunphotometer DTF-5 is made in AIOFM and often calibrated on the top of mountain in a very sunshine day. Also, the performance of the sky radiometer was rountinely checked by professional personnel.

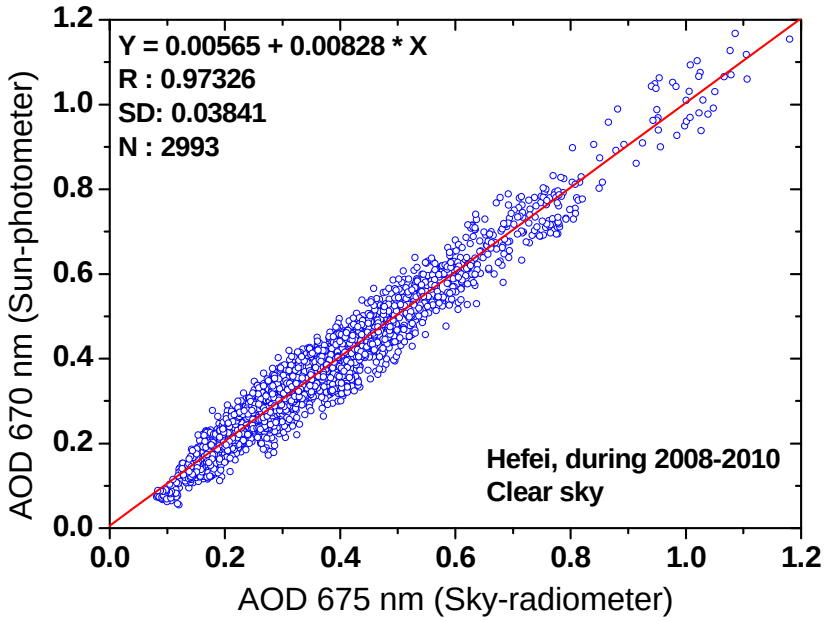

Fig. 1 Scatter diagram of retrieved AOD for the 675 nm channel by sunphotometer and skyradiometer during 2008 to 2010 over Hefei

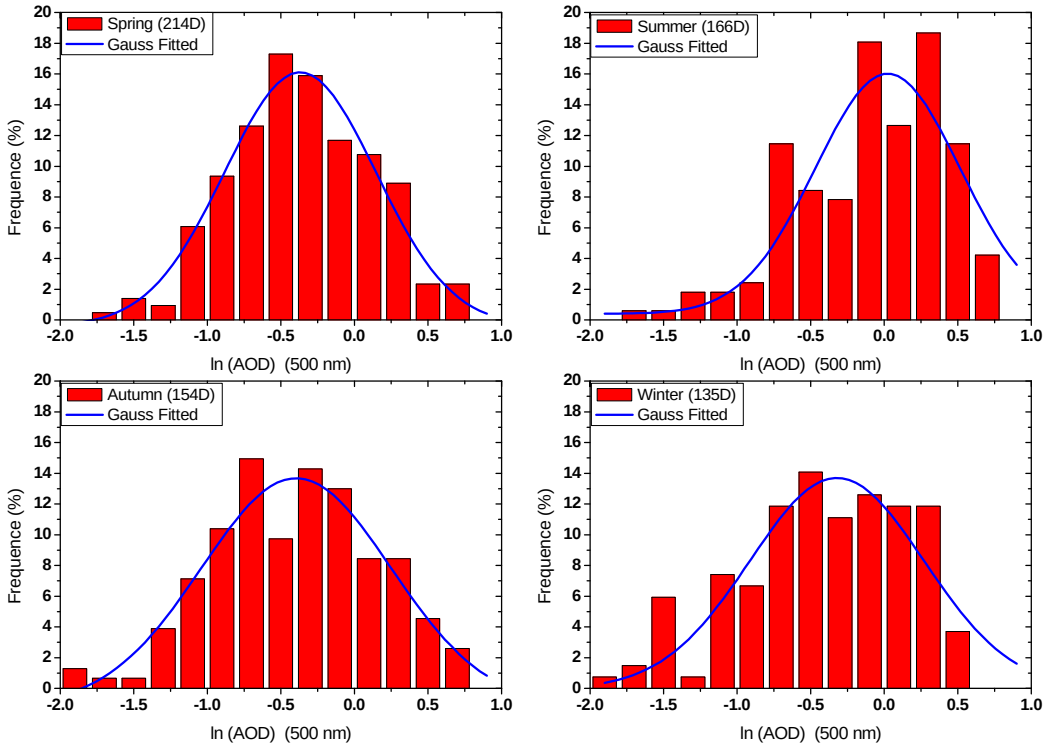

Fig. 2 Frequency distribution of the AOD (500 nm) for the four seasons and the fitted Gaussian model

The AOD is representative of the aerosol loading in the atmosphere column and is important for the identification of aerosol source regions and aerosol evolution. Figure 2 shows the frequency distribution of the AOD (500 nm) for the four seasons. The day number of each season used for analysis is 214 (Spring), 166 (summer), 154 (autumn), and 135 (winter). The data is also transformed to logarithmic scale and fitted with the Gaussian model with a form:

$$y = y_0 + \frac{A}{w\sqrt{\pi/2}} e^{-2\left(\frac{x-x_c}{w}\right)^2}$$

The lognormal probability distribution best represents the frequency distribution of AODs in the spring (R^2=0.962); in autumn, the fit is also good; but in summer and winter the fit is not so strong because of the influence of difference aerosols. So, the the frequency distribution of AODs can be characterized by lognormal probability distribution during the same source of aerosol (e.g., in spring). In spring months, northern and northwestern cold front activities often attack, and the dust particles can be taken to Hefei along the cold air mass. Dust particles often were observed over Hefei in spring [7-10].

Table 2 Seasonal statistics of the AOD based on the fitted Gaussian model

	y_0	A	x_c	w	R^2
Spring	-0.396+0.931	21.283+2.672	-0.368+0.028	1.029+0.094	0.962
Summer	0.392+1.728	19.263+4.933	0.023+0.072	0.983+0.200	0.794
Autumn	-1.138+2.133	23.916+6.904	-0.396+0.045	1.288+0.230	0.910
Winter	-0.027+2.318	20.380+7.178	-0.322+0.068	1.185+0.277	0.818

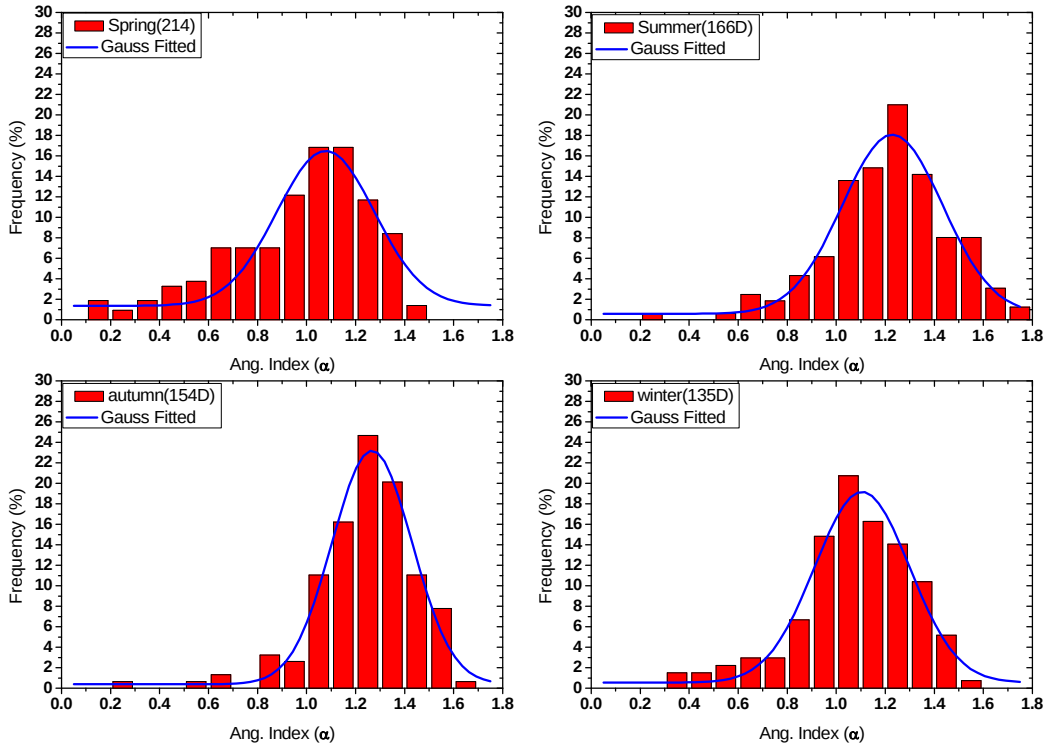

Fig. 3 Frequency distribution of the Angstom index for the four seasons and the fitted Gaussian model

The Angstrom index is determined from the spectral dependence of the AODs, and is a good indicator of the aerosol size. The coefficient is calculated using regression analysis, in which the AOD values for 7 wavelengths (340-1020 nm mentioned above). Figure 3 shows the frequency distribution of α (340-1020 nm) for the four seasons. Also, the gaussian model is used to fit the frequency distribution of α. If the value 0.8 is considered to be the point that can represent different aerosol type, lager dust particles often load in spring and sometimes in winter. In summer and in fall, the aerosols are maily made up of small particles. The wider spread in frequency distribution is seen in the summer than in the fall. The fitted lines in figure 3 illustrate that the frequency distribution of α follow the normal probability function to some great degree; the correlation coefficients are 0.897 (spring), 0.954 (summer), 0.977 (fall), 0.962 (winter). The smallest value in R^2 will be indicator of big dust aerosol and small anthropologic aerosol.

Figure 4 shows the monthly mean AOD (500 nm), α (340-1020 nm), SSA (500 nm) and PWC over Hefei from Mar., 2007 to Sep., 2010 with error bars showing the standard deviation of monthly averaged value. The seasonal variation in AOD is evident with the biggest value in summer and smallest in fall, where a sharp increasing in June and decresing in November. The pattern of the monthly change in α is that smallest value occurs in spring and in December, which indicates that the aerosol particles are large and related to dust events. At the meantime, the in summer and in fall small particles are loaded over Hefei.

And the SSA is another important parameter indicated the aerosol type (absorption or not), which is a key variable in assessing the radiative forcing of aerosols[11]. The main source of error in the derived SSA is due to the calibration of the radiative data, and is about $\pm$0.03. From figure 4, one can see that the SSA in summer is much higher than other seasons and the SSA at end of the fall and at the beginning of the winter is much lower than others. In addition, the water vapor will affect the aerosol loading in summer season as shown in figure 4, and may be correlated to SSA and AOD.

Table 2 Seasonal statistics of the α based on the fitted Gaussian model

alfa	y_0	A	x_c	w	R^2
Spring	1.368+0.736	7.538+1.015	1.078+0.020	0.398+0.048	0.897
Summer	0.576+0.556	8.984+0.779	1.229+0.013	0.410+0.031	0.954
Autumn	0.373+0.430	9.332+0.537	1.267+0.008	0.326+0.018	0.977
Winter	0.878+0.649	8.720+0.800	1.105+0.012	0.380+0.030	0.962

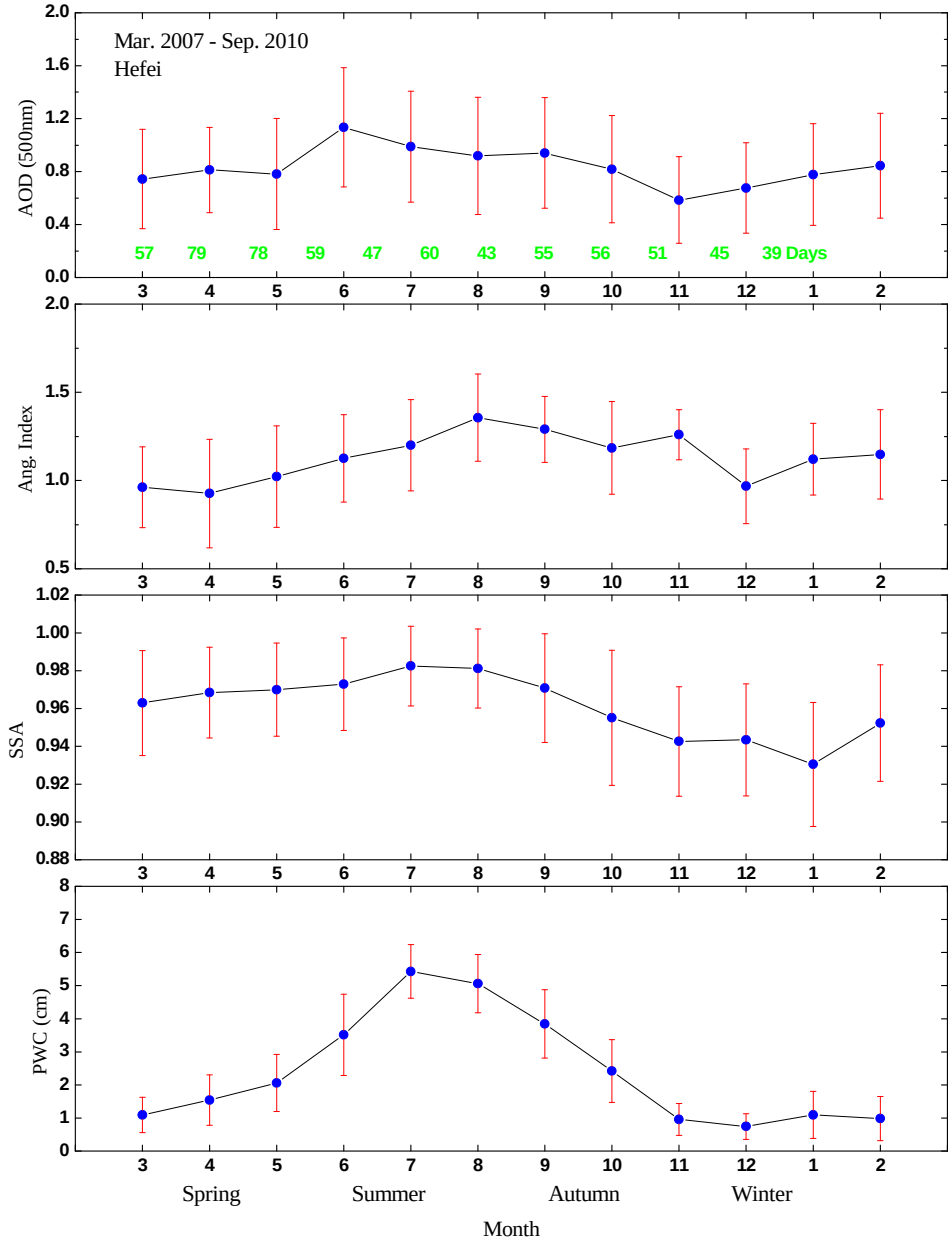

Fig. 4 Monthly averaged AOD (500 nm), α (340-1020 nm), SSA (500 nm) and PWC over Hefei from Mar., 2007 to Sep., 2010 by Sky-radiometer and microwave radiometer

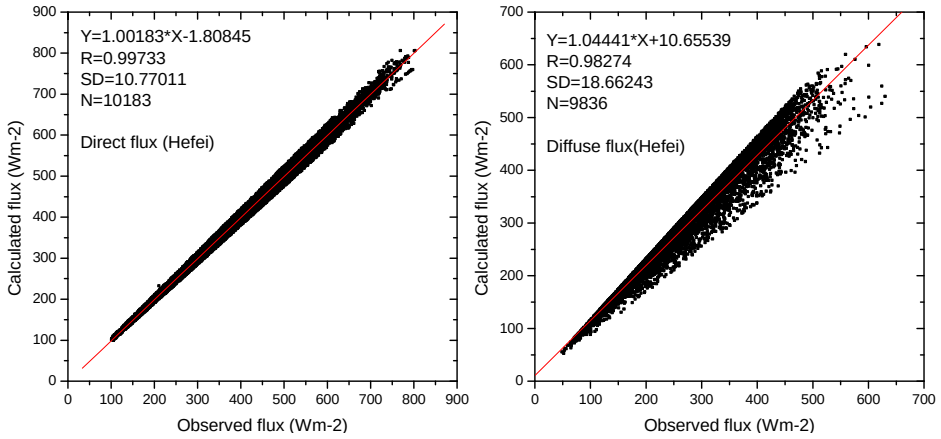

Fig. 5 Scatter plot for the comparison of observed fluxes with the calculated fluxes for the direct and diffuse fluxes

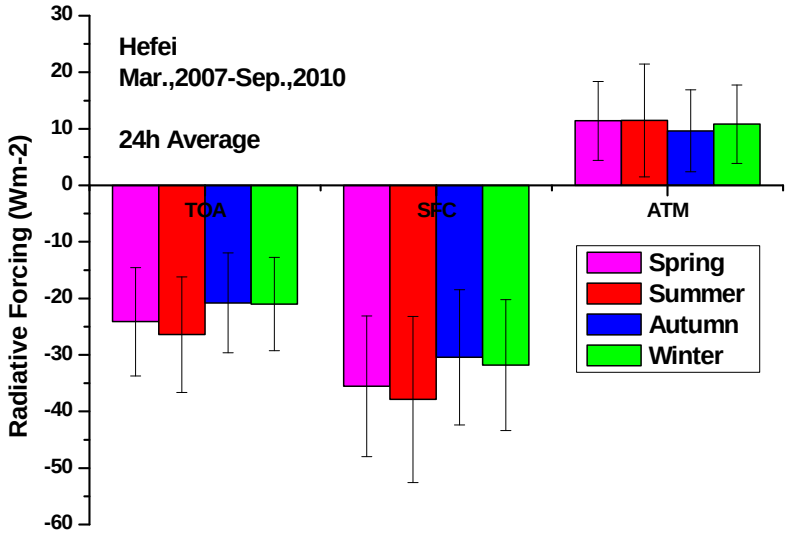

Fig. 6 Seasonal aerosol radiative forcing at the surface, top of the atmosphere, and in the atmosphere during Mar., 2007 to Sep., 2010 over Hefei.

Figure 5 shows the compared results between calculated and measured fluxes with the slope and offset values. The comparison shows a good agreement with the correlation coefficients of 0.997, and 0.983, for direct and diffuse fluxes, respectively. And the SD between calculated and measured surface fluxes ranges from 10 Wm-2 for the direct flux to 19 Wm-2 for the diffuse flux. This discrepency may be caused by errors in the measured or assumed input data as well as errors in the flux observatios, and especially the input parameters related to aerosols.

Figure 6 gives the seasonal aerosol radiative forcing (RF) at the surface (SFC), top of the atmosphere (TOA), and in the atmosphere (ATM). Here, aerosol forcing is integrated over 24 hours to get daily values and used for computing seasonal variations. The result shows that the value in summer is biggest, in fall is smallest. The mean values of RF due to aerosol at SFC, TOA, and in ATM are -33.9, -23.1, and 10.8 Wm-2, respectively. Because of high value in SSA, the relative RF kept in ATM is not so much though the large value of AOD over Hefei.

References

[1] IPCC. 2007. Climate Change 2007: The Physical Science Basic. Contribution of Working Group I Contribution to the Intergovernmental Panel on Climate Change Fourth Assessment Report. Solomon S, Qing D H, Manning M, et al. eds., Cambridge University Press, Cambridge, United Kingdom and New York, N Y, USA

[2] Nakajima, T., G. Tonna, R. Rao, Y. Kaufman, and B. Holben, 1996: Use of sky brightness measurements from ground for remote sensing of particulate polydispersions, Appl. Opt., 35, 2672-2686.

[3] Kim, D., B. Sohn, T. Nakajima, T. Takamura, T. Takemura, B. Choi, and S. Yoon (2004), Aerosol optical properties over east Asia determined from ground-based sky radiation measurements, J. Geophys. Res., 109,D02209, doi:10.1029/2003JD003387.

[4] Khatri, P. and T. Takamura, 2009: J. Meteor. Soc. Japan , 87,189-204.

[5] Ricchiazzi, P., S. Yang, C. Gautier, and D. Sowle, 1998:, Bull. Am. Meteorolo. Soc., 79, 2101-2114.

[6] Remer L A, Kaufman R J. 2006. Aerosol direct radiative effect at the top of the atmosphere over cloud free ocean derived from four years of MODIS data. Atmos. Chem. Phys., 6, 237–253

[7] Zhou, J., G, Yue, C. Jin, F. Qi, W. Yi, T. Li, Y. Chen, L. Xiong, Two-wavelength Mie lidar for monitoring of tropospheric aerosols, ACTA OPTICA SINICA, 20, 1410-1417, 2000.

[8] Zhou, J., G. Yu, C. Jin, F. Qi, D. Liu, H. Hu, Z. Gong, G. Shi, T. Nakajima and T. Takamura, Lidar Observations of Asian Dust over Hefei, China in the Spring of 2000, JGR, 107, D15, AAC51-58, 2002.

[9] Dong Liu, F. Qi，C. Jin, G. Yue and Jun Zhou, Polarization lidar observations of cirrus and Asian dust aerosols over Hefei, Chinese Journal of Atmosphere Sciences, Vol. 27, 1093-1100, 2003.

[10] Jun Zhou, Dong Liu, Guming Yue, Fudi Qi, and Aiyuan Fan (2006), Vertical Distribution and Temporal Variation of Asian Dust Observed over Hefei, China by using a Lidar, Journal of the Korean Physical Society, 49(1), 320-326.

[11] Dubovik, O., B. N. Holben, T. F. Eck, A. Smirnov, Y. J. Kaufman, M. D.King, D. Tanre, and I. Slutsker (2002a), Variability of absorption and optical properties of key aerosol types observed in worldwide locations, J. Atmos. Sci., 59, 590–608.

Aerosol-cloud interactions derived from remote sensing and in-situ aircraft measurements

G. Pandithurai[1], S. Dipu[1] and T. Takamura[2]
[1]*Indian Institute of Tropical Meteorology, Pune, India*
[2]*CEReS, Chiba University, Chiba, Japan*

1. Introduction

The effect of aerosols on cloud microphysical and radiative properties has the greatest uncertainty of all known climate forcing mechanisms. For a constant amount of condensed water, an increase in the number of CCN will generate a cloud that consists of smaller drops and reflects more energy to space, which is commonly referred to as the "albedo effect" [*Twomey, 1977*]. However, because the droplets are smaller they may inhibit collision-coalescence in the cloud, suppressing droplet growth that stops drizzle and extends cloud lifetime [*Albrecht, 1989*]. The indirect effect of aerosols is continuing to be an enormous challenge from both the observational and modeling perspectives, and progress is crucial in order to improve our ability to predict climate change. Current estimates of global average aerosol indirect forcing based on satellite data ranges from -0.6 to -1.7 Wm^{-2}. There is greater realization of the importance of including the indirect effect because direct effect is thought to be insufficient to allow proper simulation of observed temperature changes. Satellite remote sensors have been employed to provide a regional and even global view of aerosol effects on clouds [*Nakajima et al., 2001; Breon et al., 2002*]. More recently, surface-based remote sensing has also been applied to address aerosol effects on cloud microphysics [*Feingold et al., 2006; Pandithurai et al., 2009*], as these surface stations yield high temporal resolution data and because they sample aerosol below, rather than adjacent to clouds and hence they do not suffer from cloud contamination. The main advantage of the surface-based remote sensing is that the effect of aerosol on cloud can be examined in a single column of air at the scale of cloud droplet formation, and at high temporal resolution. Long term observations of aerosol and cloud properties and sensitivity of cloud properties to aerosols over different climatic regions are required for better parameterization of aerosol-cloud interactions. The primary objective of this study is to examine the response of cloud radiative properties to changes in aerosol using surface-based remote sensing systems over Eastern China Sea region that is influenced by the transport of aerosols from the Asian continent. Recent aircraft measurements over India are also used to examine the aerosol indirect effect and the effect of droplet dispersion on indirect effect estimates.

2. Data and Methods

Spring-2008 observational campaign was conducted at Cape Hedo (26.87 N, 128.25 E), Okinawa Island, Japan to study the aerosols and their radiative effects transported from East Asia especially from China. In addition to other observational facilities, this campaign included an operation of Frequency Modulated Continuous Wave (FMCW) Millimeter wave Cloud radar (MMCR) from February 17 to May 04, 2008. The experimental systems used in this study includes a i) Dual frequency microwave radiometer (MWR), ii) Polarization capable dual-wavelength lidar [*Shimizu et al., 2004*], iii) Millimeter wave cloud radar [*Takano et al., 2005*], iv) CCN counter, v) i-skyradiometer (Prede Co., Product Name POM-02), vi) Whole sky imager, vii) Nephelometer and viii) Optical particle counter.

Cloud droplet effective radius (R_{eff}) is retrieved from the reflectivity profiles of FMCW cloud radar operating at 95 GHz and column liquid water path (LWP) derived from MWR. Technical details of the FMCW radar and its comparison with a monostatic 95 GHz cloud radar SPIDER can be found elsewhere [*Takano et al., 2005*]. Liquid water path is an important parameter for studying aerosol-cloud interactions and is not widely measured. The Radiometrics WVR-1100 microwave radiometer is a passive instrument which measures column integrated water vapor and liquid water based on the microwave emissions of atmospheric water vapor and liquid water molecules at 23.8 GHz and 31.4 GHz. Typical retrieval uncertainties in the column integrated liquid water are 25–30 gm^{-2}. The datasets used in this study were obtained from the SKYNET archive (http://atmos.cr.chiba-u.ac.jp), which archives and distributes data collected from most of these instruments.

3. Aerosol effects on cloud droplet size

To investigate the aerosol indirect effect, collocated measurements of different experimental systems were analyzed. As suggested by *Feingold et al. [2006]*, daytime well-mixed boundary layer conditions are considered for aerosol indirect effect analysis to ensure that the surface observations are representative of those that that are

influencing the cloud droplet nucleation properties. Here we used height-averaged cloud droplet effective radius (R_{eff}) and examined changes in R_{eff} as a function of surface aerosol scattering coefficient, CCN number and OPC aerosol size distribution. Aerosol indirect effect estimates are based on relative changes in droplet radius or cloud optical thickness for changes in aerosol loading and is less sensitive to absolute values. As CCN measurements are not available on all the days considered in this analysis, we use βsca as CCN proxy. Analysis shows that about 30% increase in accumulation mode particles led to 15% decrease in droplet effective radius. Wind fields and back trajectory analysis for the experimental days considered in the analysis show the trajectories are of northwesterlies and westerlies, which indicate transport of airmasses from Asian continent towards the Okinawa Island. Data sets of selected days considered in the analysis were sorted for different LWP ranges viz. 50–100, 100–150, 150–200, 200–250 and 250–300 gm^{-2}. The scatter plot between R_{eff} and βsca for different ranges of LWPs shown in Figure 1 and the slope of the linear fit for the above plots give aerosol indirect effect (IE).

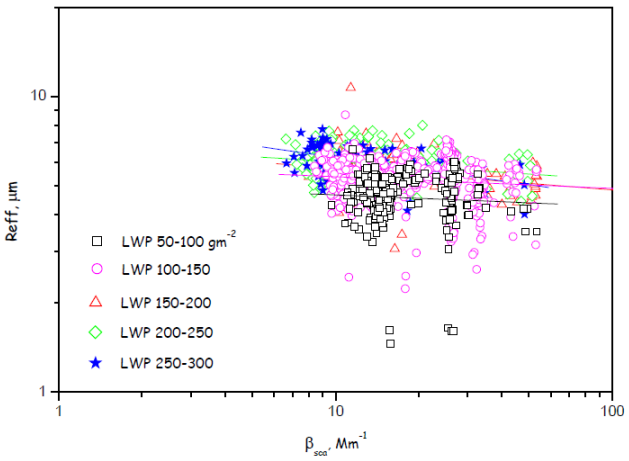

Figure 1. Values of Reff as measured by MMCR versus aerosol scattering coefficient asmeasured by nephelometer.

4. Aerosol indirect effect over India using CAIPEEX Datasets

CAIPEEX (Cloud Aerosol Interaction and Precipitation Enhancement Experiment) phase I is devoted for intensive cloud and aerosol observations using an instrumented aircraft N361JC, over different regions in India, during the period May to September 2009 which includes pre-monsoon, active and break monsoon conditions. Aircraft missions were conducted from different locations in India viz. Pathankot (32.2 N, 75.6 E), Hyderabad (17.5 N, 78.4 E), Bangalore (13N, 77.5E), Bareilly (28.4 N, 79.4 E), Guwahati (26.1 N, 91.6 E) and Pune (18.5 N, 73.8 E). During some of the flights observations were collected over coastal Arabian Sea and Bay of Bengal to study the cloud microphysics of marine clouds and their transformation to continental clouds during the flights. A detailed description of the above CAIPEEX project can be found in the web page: http://www.tropmet.res.in/~caipeex/.

Flight average data sets of warm cloud samples were used in the analysis. The threshold cloud droplet diameter (DL) of modal liquid water content is used as cut-off and cloud samples less than DL values of 24 µm only are considered in this analysis. Measurements of aerosol accumulation mode number concentrations (Nacc) and CCN supersaturation spectrum were obtained from sub-cloud flights before climbing into cloud profiling. First AIE (Twomey effect) is estimated from the ratio of the relative change in cloud droplet number concentration (N_c) with respect to relative change in aerosol number concentration (N_{acc}).

$$N_c = a_a \left(N_{acc}\right)^{b_a} \quad \text{.....(1)}$$

where first AIE or Twomey effect is given as $I_0=1/3b_a$. It is clear that as aerosol concentration increases as cloud droplet number concentration increases. According to equation (1), Twomey effect estimated over Indian region during CAIPEEX campaign is 0.096 which is 1/3 b_a (b_a=0.288).

5. Effect of cloud droplet dispersion on Twomey effect

In most of the studies, aerosol-cloud interaction is explained by considering only changes in the cloud droplet concentration, neglecting changes in the spectral shape of the cloud droplet size distribution. However, it has been shown that the relative dispersion 'ε' has a significant role in determining cloud radiative properties. It is already reported that enhanced ε leads to warming effect, which can offset Twomey effect by 10 to 80% (*Liu and Daum, 2002*). All existing estimates of dispersion effect were based on some empirical β(ε)-N relationship, which has a large uncertainty. In order to reduce the uncertainty or for better estimation of dispersion effect, *Liu et al (2008)* examined the dependence of β on (L/N) (i.e., water per droplet) and described the dependence of β on (L/N) by the following expression,

$$\beta = a_\beta \left(\frac{L}{N}\right)^{-b_\beta} \quad \text{.....(2)}$$

where L is cloud liquid water content, N is cloud droplet number concentration and β is effective radius ratio.

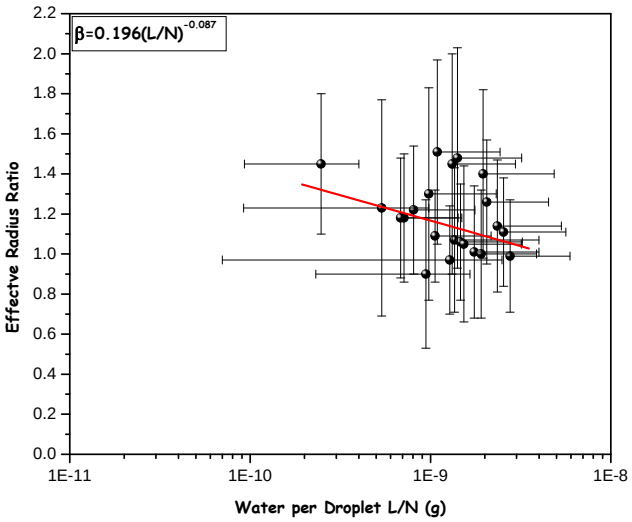

Figure 2. Relation between effective radius ratio and water per droplet obtained fromCAIPEEX flight average data sets

Acknowledgments

We thank SKYNET and CHAMMPS, Cape Hedo for maintaining the experimental facilities at the site. We also thank CAIPEEX team for aircraft measurements and the project was fully funded by Ministry of Earth Sciences, India. Thanks are also due to Global Earth Observation System of Systems (GEOSS), Ministry of Education, Culture, Sports, Science and Technology (MEXT), Japan.

References

Albrecht, B. A. (1989), Aerosols, cloud microphysics, and fractional cloudiness, *Science, 245*, 1227-1230.

Breon, F.-M., D. Tanre, and S. Generoso (2002), Aerosol effect on cloud droplet size monitored from satellite, *Science*, 295, 834-838.

Feingold, G., W. Eberhard, D.E. Lane, and M. Previdi (2003), First measurements of the Twomey effect using ground-based remote sensors, *Geophys. Res. Lett., 30(6), 1287, doi:10.1029/2002GL016633.*

Feingold, G., R. Furrer, P. Pilewskie, L. A. Remer, Q. Min, and H. Jonsson (2006), Aerosol indirect effect studies at Southern Great Plains during the May 2003 Intensive Operations Period, *J. Geophys. Res.*, *111*, D05S14, doi:10.1029/2004JD005648.

Liu, Y. and P. H. Daum (2002), Indirect warming effect from dispersion forcing, *Nature*, 419, 580-581.

Liu, Y., P.H. Daum, H. Guo and Y. Peng (2008), Dispersion bias, dispersion effect and the aerosol-cloud conundrum, *Envrion. Res. Lett.*, doi:10.1088/1748-9326/3/4/045021.

Nakajima, T., A. Higurashi, K. Kawamoto, and J. E. Penner (2001), A possible correlation between satellite-derived cloud and aerosol microphysical parameters, *Geophys. Res. Lett., 28*, 1171–1174.

Pandithurai, G., T. Takamura, J. Yamaguchi, K. Miyagi, T. Takano, Y. Ishizaka, A. Shimizu (2009), Aerosol effect on cloud droplet size as monitored from surface remote sensing over east china sea region, *Geophys. Res. Lett., 36*, L13805, doi:10.1029/2009GL038451.

Shimizu, A., N. Sugimoto, I. Matsui, K. Arao, I. Uno, T. Murayama, N. Kagawa, K. Aoki, A. Uchiyama, and A. Yamazaki (2004), Continuous observations of Asian dust and other aerosols by polarization lidars in China and Japan during ACE-Asia, *J. Geophys. Res., 109*, D19S17, doi: 10.1029/2002JD003253.

Takano, T., K. –I. Akita, H. Kubo, Y. Kawamura, H. Kumagai, T. Takamura, Y. Nakanishi, T. Nakajima (2005), Observations of clouds with the newly developed cloud profiling FM-CW radar at 95 GHz, *Proc. SPIE 5979 art no 597907.*

Twomey, S. (1977), The influence of pollution on the short wave albedo of clouds, *J. Atmos. Sci., 34*, 1149-1152.

Aerosol optical and radiative properties: synergy between sky radiometer and lidar

Sang-Woo Kim

School of Earth and Environmental Sciences, Seoul National University, Seoul, Korea

1. Introduction

Anthropogenic and natural aerosols are important atmospheric constituents that significantly contribute to Earth's radiation budget through a variety of pathways such as direct effects on scattering and absorption of solar radiation, indirect effects on cloud microphysics, and semi-direct effects (Kaufman et al., 2002; Ramanathan et al., 2007; Yoon et al., 2005). In the past 30 ~ 40 years, North East Asia has been experiencing a considerable increase in anthropogenic pollution aerosols. In addition, North East Asia is one of the major source regions of wind-blown mineral dust aerosols. These aerosols significantly influence the solar and terrestrial radiation budgets (Huebert et al., 2003; Kim et al., 2004, 2005, 2008; Nakajima et al., 2007; Ramanathan et al., 2007; Won et al., 2004; Yoon et al., 2005). The aim of this study is (1) to investigate the columnar optical properties and evaluate the resulting aerosol direct radiative forcing and atmospheric heating at Gosan (Korea) for a seven-year period, based on sun/sky radiometer and micro-pulse lidar observations and radiative transfer calculations, (2) to evaluate aerosol lidar ratio (extinction-to-backscatter ratio) using 4-year measurements of elastic-backscatter lidar and sky radiometer at Seoul National University of Seoul, Korea.

2. Aerosol Direct Radiative Forcing (ADRF)

2.1 ADRF calculation

The aerosol direct radiative forcing (ΔF) and forcing efficiency (β, defined as ΔF per unit τ) for the predominantly cloud-free days are calculated using the column radiative model (CRM-2.1.2), which is a stand-alone version of the radiative transfer model implemented in the NCAR Climate Community Model (CCM-3.6). The CRM uses a δ-Eddington approximation with 19 spectral intervals spanning from 0.2 to 5 μm and accounts for several gas absorption spectra; seven spectral bands for O_3 and H_2O and three for CO_2, and the absorption of N_2O, CH_4, CFC-11, CFC-12 are included. The followings are replaced in the original version of the CRM so that it can be used in the present study (Won et al., 2004):

(*a*) The number of computational layers is extended from 18 to 54; from surface to approximately 63 km altitude. The vertical resolution is about 23.7 hPa (i.e., 0.2 km interval near the surface and gradually broadened with increasing altitude, about 2.85 km at top layer).

(*b*) The aerosol module of the CRM is modified to ingest the AERONET measured variables (τ, ω, and g), and subsequently calculate the parameters at the 19 bands from the information obtained at the four AERONET wavelengths. We used a linear regression method in the $\log\lambda$ – $\log\chi$ plane (where λ is the wavelength and χ denotes τ, ω, and g) to determine the aerosol parameters in 19 wavelength-bands.

(*c*) The AOD obtained from AERONET sky radiometer was apportioned with altitude using MPL-derived extinction profiles. The constant values of SSA and g were applied to all altitudes in the calculation of atmospheric heating rate.

In addition, we estimate the effect of aerosols on the radiation budget by considering their vertical distribution (i.e., atmospheric heating rate) on the basis of the aerosol profiles measured by the co-located MPL system.

2.2 ADRF and atmospheric heating rate at Gosan

Figure 1(a) shows the monthly mean temporal variations in the optical properties of aerosols and precipitable water content obtained from AERONET observations. It should be mentioned that almucantar retrievals from AERONET instrument are not sufficient for radiative transfer calculations in November due to routine instrument maintenance and calibration. At the Gosan site, the monthly mean AOD at 675 nm lies between 0.12 and 0.36 (annual mean of 0.29 ± 0.19), with significantly high values (>0.33) observed from April to June, while low-to-moderate monthly mean AODs were apparent during the remaining months. The monthly mean Ångström exponent (Å) range remained fairly low (<1.0) from February to May, indicating the relative dominance of coarse particles to the solar extinction, whereas it was relatively high in the remaining months (>1.2), suggesting the important role played by fine aerosols on radiation. The high AODs observed from March to May can be attributed to the frequent outbreak of Asian dust storms (as indicated by the low Å). Accumulation of locally and regionally emitted fine pollution aerosols (as indicated by the relatively high Å) due to the prevailing stationary anti-cyclonic circulation also leads to an increase in AODs in May and June. Monthly values of SSA are

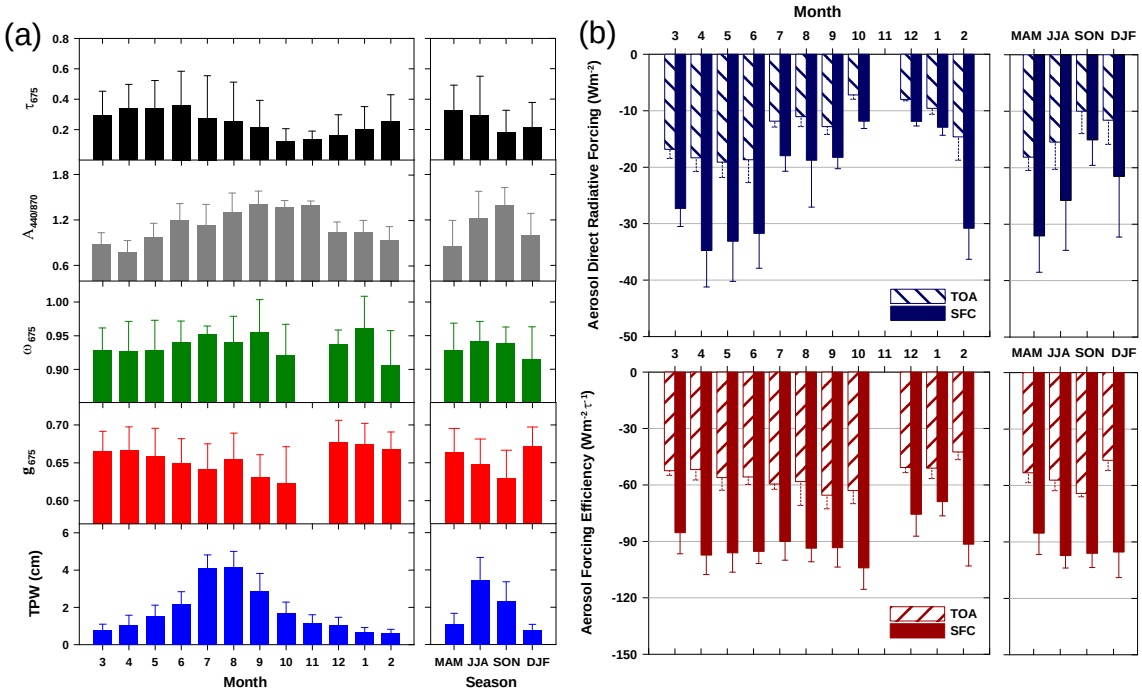

Figure 1. (a) Monthly (left panel) and seasonal (right panel) means of AOD (τ), Ångström exponent (Å), SSA (ω), asymmetric parameter (g), and total amount of precipitable water (TPW) determined by the AERONET Sun/sky radiometer at Gosan from April 2001 to March 2008. **(b)** The monthly (left panel) and seasonal (right panel) variations of aerosol direct radiative forcing (upper panel; W m^{-2}) and forcing efficiency (lower panel; W m^{-2} τ^{-1}) at Gosan.

relatively low from February to May (<0.93) due to the transports of dust as well as fine pollution aerosols (Huebert et al., 2003), whereas high values of SSA (>0.93) are observed during the rest of the period. The annual mean of SSA is 0.93 ± 0.04. The asymmetric parameter (*g*) shows almost constant values (0.65 < *g* < 0.67), except during autumn (~0.63).

Figure 1(b) shows the monthly and seasonal variations in aerosol direct radiative forcing (ΔF; W m^{-2}) and forcing efficiency (β; $\Delta F/\tau$; W m^{-2} τ^{-1}) at Gosan. The monthly mean ΔFs are calculated using the monthly mean aerosol parameters. Similar to the case of AOD variations, strong intra-seasonal and seasonal variations were observed in the aerosol radiative forcings, with quite high values: annual mean of –27.55 ± 9.21 (surface), –15.79 ± 4.44 (TOA), and 11.76 ± 5.82 W m^{-2} (atmosphere). The mean β is evaluated to be –91.85 ± 11.12 W m^{-2} τ^{-1} at the surface and –53.76 ± 6.70 W m^{-2} τ^{-1} at the TOA. From March to June, the surface ΔF (β) was between –27.29 (–85.33) and –34.76 W m^{-2} (–97.19 W m^{-2} τ^{-1}), that at the TOA was between –16.84 (–51.82) and –19.10 W m^{-2} (–56.05 W m^{-2} τ^{-1}), and the atmospheric forcing was between 10.45 and 16.41 W m^{-2}. Significant aerosol forcings from March to May are consistent with high AODs and can be attributed to the wind-blown mineral dust aerosols transported from the Asian continent by the westerlies (Kim et al., 2005, 2007, 2008; Nakajima et al., 2007). Enhanced aerosol direct forcings in May and June are due to an increase in the fine pollution aerosol loads, which is caused by stationary regional meteorological conditions and the associated transport of anthropogenic fine pollution aerosols from China (Kim et al., 2007). The continental air mass becomes weak and the clean marine air mass has not expanded over China/Korea in May and June, thereby mid-latitude westerly zonal flow (i.e., west-to-east flow) is relatively stagnant. The large discrepancy in ΔF between the surface and the TOA, i.e., atmospheric forcing, suggests the presence of light-absorbing aerosols, which is consistent with relatively low SSA. During these periods, atmospheric radiative forcing also increases. These results indicate that aerosols over East Asia can significantly heat the atmosphere. On the other hand, the relatively low monthly mean aerosol direct forcings from July to August and in autumn/winter are directly related to the frequent rainfalls and very high wind speed conditions, respectively.

Monthly and seasonal mean profiles of atmospheric heating rate are shown in Figure 2. The evaluation of ΔF is usually dependent on the total amount of aerosols in the

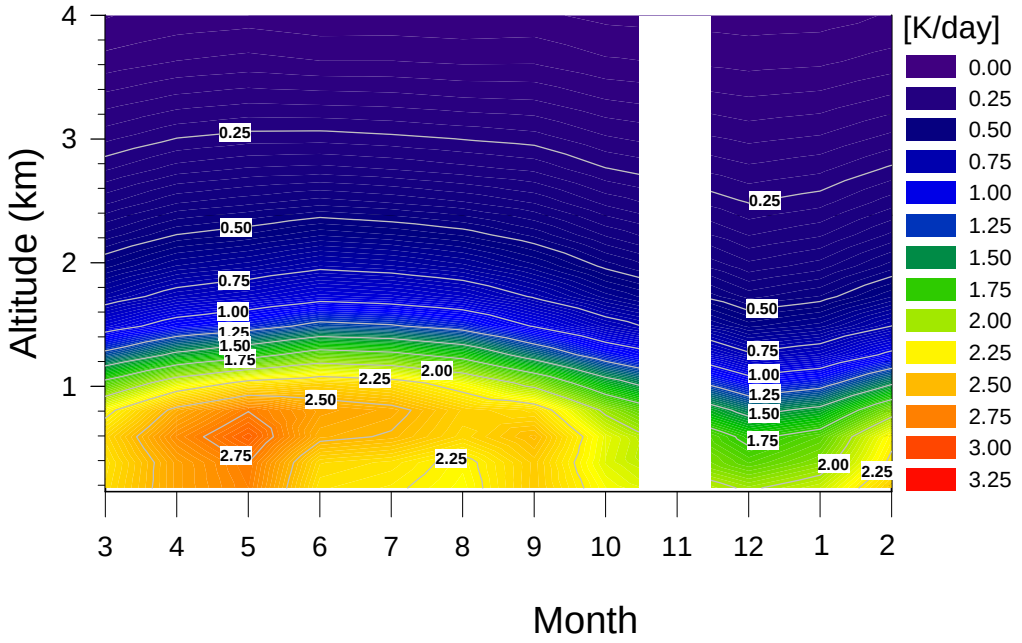

Figure 2. Monthly variations in atmospheric shortwave heating rates (K day^{-1}) at Gosan, Korea.

atmospheric column. However, the radiative heating rate, defined as the rate of temperature change in a layer due to radiative heating and cooling, at a shortwave regime can be influenced by aerosol vertical distributions and the amount of light-absorbing aerosols (i.e., AOD and SSA). The radiative heating of the atmosphere is apparent below an altitude of approximately 1.5 km because most of the aerosols are confined to the planetary boundary layer. The strongest radiative heating occurs in spring and summer due to of the increase in dust aerosols and light-absorbing aerosols (May and June). The monthly mean radiative heating rate in May exceeds 2.7 K day^{-1}, which is almost twice that in autumn and winter. In addition, compared to autumn and winter, the frequent passage of springtime Asian mineral dust aerosols in free troposphere and the seasonal increase of boundary layer mixing height in summer cause significant atmospheric radiative heating above 1 km.

3. Characteristics of the lidar ratio determined from lidar and sky radiometer measurements in Seoul

Figure 3 shows the flow of lidar ratio calculation process by comparing the aerosol optical depth calculated from lidar (τ_{lidar}) and sun/sky radiometer (τ_{sky}) measurements. If the difference between τ_{lidar} and τ_{sky} is less than 0.5%, we finally determine lidar ratio and then extract aerosol extinction profile.

Figure 4 shows seasonal variations of lidar ratio, Ångström exponent, and depolarization ratio from 4-year measurements of elastic-backscatter lidar and sky radiometer at Seoul National University of Seoul, Korea. The mean lidar ratio (with standard deviation) based on 4 years of measurements is found to be 61.69±16.46 sr, and weak seasonal variations are noted with a maximum in JJA (68.06±16.78 sr) and a minimum in DJF (57.18±17.94 sr).

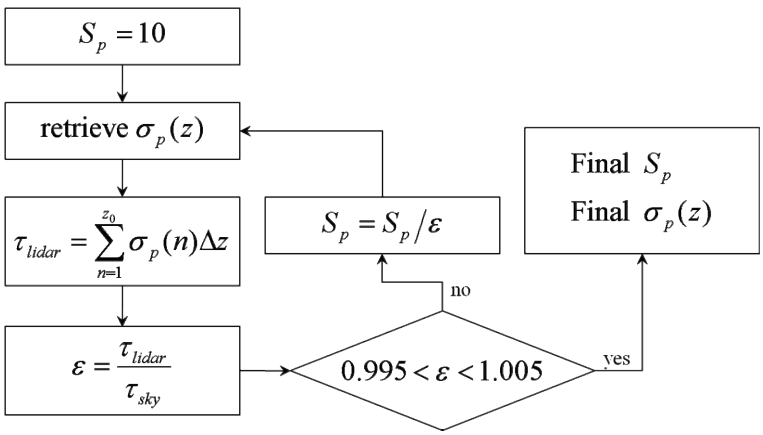

Figure. 3. Flow chart of the algorithm for determination of the lidar ratio and extinction profile.

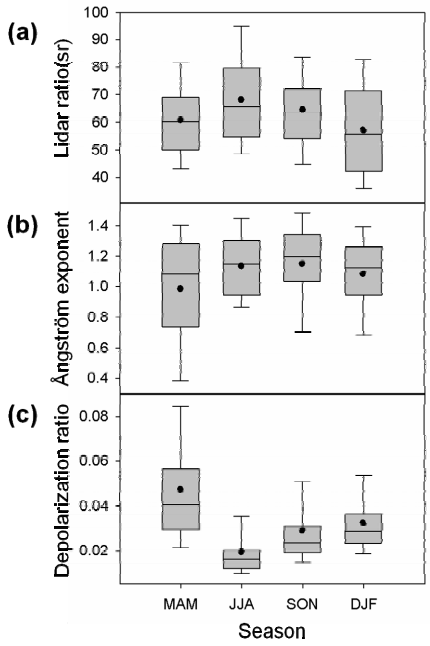

Figure. 4. Seasonal variation of **(a)** lidar ratio, **(b)** Ångström exponent, and **(c)** depolarization ratio at Seoul, Korea. Top and bottom of Boxes and whiskers represent 75th, 25th, 95th and 5th percentile, respectively. Lines in the boxes are median values and dots represent mean values. Lidar ratio and depolarization ratio are at 532 nm, and Ångström exponent is determined from AOT at five wave length (400, 500, 675, 870, 1020 nm).

Table 1. Lidar ratio at 532 nm for different aerosol types.

Aerosol type	Lidar ratio (Sr)	Location	Reference
Clean	32 ± 6	Africa	Voss *et al*., 2001
	35	Europe	Ansmann *et al*., 2001
	45.0 ± 9.5	**Seoul, Korea**	***This Study***
Dust	41 ± 8	Sahara	Voss *et al*., 2001
	42 - 55	Tokyo, Japan	Liu *et al*., 2002
	50.4 ± 9.4	Tokyo, Japan	Murayama *et al*., 2003
	42 ± 4	Except Asia[1)]	Cattrall *et al*., 2005
	45.5 ± 8.6	Anmyeon, Korea	Noh *et al*., 2007
	51.7 ± 13.7	**Seoul, Korea**	***This Study***
Pollution	50 - 70	Portugal	Ansmann *et al*., 2001
	49 - 70	India	Franke *et al*., 2001
	71 ± 10	Urban[1)]	Cattrall *et al*., 2005
	62.2 ± 13.2	**Seoul, Korea**	***This Study***

[1)] Lidar ratios retrieved from 26 AERONET sites across the globe.

Table 1 shows the lidar ratios for for clean, dust, and polluted conditions in Seoul, Korea. The lidar ratios for clean, dust, and polluted conditions in this study are estimated to be 45.01±9.48 sr, 51.68±13.66 sr, and 62.17±13.17 sr, respectively. While the lidar ratio for the polluted condition is appeared to be consistent with previous studies, clean and dust conditions tend to have larger ratios, compared to previous estimates. This discrepancy is thought to be mainly due to the anthropogenic aerosols existing throughout the year around Seoul, which may cause increased lidar ratios even for clean and dust conditions.

4. Summary

We investigate the columnar optical properties of aerosols advected from the Asian continent to Gosan (Korea) and evaluate the resulting direct radiative forcing and atmospheric heating for a seven year period, based on AERONET observations and radiative transfer calculations. We also evaluate aerosol lidar ratio (extinction-to-backscatter ratio) using 4-year measurements of elastic-backscatter lidar and sky radiometer at Seoul National University of Seoul, Korea. The major conclusions of this study are as follows:

1. At the Gosan site, the monthly-mean AOD at 675 nm ranged between 0.12 and 0.36. High AODs were observed from April to June (>0.33), while low-to-moderate monthly mean AODs were apparent during the remaining months. A fairly low Å (<1.0) prevailed from February to May due to Asian dusts.
2. Annual average clear-sky direct forcing (forcing efficiency) at the surface was –27.55 ± 9.21 W m^{-2} (–91.85 ± 11.12 W m^{-2} τ^{-1}) and at TOA was –15.79 ± 4.44 W m^{-2} (–53.76 ± 6.70 W m^{-2} τ^{-1}), thereby leading to an atmospheric absorption of 11.76 ± 5.82 W m^{-2}. From March to June, the surface aerosol radiative forcing (β) ranged between –27.29 (–85.33) and –34.76 W m^{-2} (–97.19 W m^{-2} τ^{-1}), that at TOA was between –16.84 (–51.82) and –19.10 W m^{-2} (–56.05 W m^{-2} τ^{-1}), and the atmospheric forcing was between 10.45 and 16.41 W m^{-2}.
3. The atmospheric absorption translated to an atmospheric heating of 1.5 to 3.0 K day^{-1}. The strongest radiative heating was estimated to occur from April to June (>2.5 K day^{-1}).
4. The mean lidar ratio (with standard deviation) based on 4 years of measurements in Seoul is found to be 61.69±16.46 sr, and weak seasonal variations are noted with a maximum in JJA (68.06±16.78 sr) and a minimum in DJF (57.18±17.94 sr).
5. The lidar ratios for clean, dust, and polluted conditions in Seoul are estimated to be 45.01±9.48 sr, 51.68±13.66 sr, and 62.17±13.17 sr, respectively.

Reference

Anderson, T. L., S. J. Masonis, D. S. Covert, and R. J. Charlson, 2000: In situ measurements of the aerosol extinction-tobackscatter ratio at a polluted continental site. Journal of Geophysical Research, 105, 26907–26915.

Cattrall, C., J. Reagan, K. Thome, and O. Dubovik, 2005: Variability of aerosol and spectral lidar and backscatter and extinction ratios of key aerosol types derived from selected Aerosol Robotic Network locations, Journal of Geophysical Research, 110, D10S11, doi:10.1029/2004JD005124.

Franke, K., A. Ansmann, D. Mu¨ ller, D. Althausen, A. Wagner, and R. Scheele, 2001: One-year observations of particle lidar ratio over the tropical Indian Ocean with Raman lidar. Geophysical Research Letters, 28, 4559–4562.

Huebert, B. J., T. Bates, and co-authors, 2003. An overview of ACE-Asia: Strategies for quantifying the relationships between Asian aerosols and their climatic impacts. J. Geophys. Res., 108(D23), 8633, doi: 10.1029/2003JD003550.

Kaufman, Y. J., D. Tanre, and O. Boucher, 2002. A satellite view of aerosols in the climate system. Nature, 419, 215– 223.

Kim, S.-W., S.-C. Yoon, A. Jefferson, J.-G. Won, E. G. Dutton, J. A Ogren, and T. L. Anderson, 2004. Observation of enhanced water vapor in Asian dust layer and its effect on atmospheric radiative heating rates. Geophys. Res. Lett., 31, L18113, doi: 10.1029/2004GL020024.

Kim, S.-W., S.-C. Yoon, and co-authors, 2005. Aerosol Optical, Chemical and Physical Properties at Gosan, Korea during Asian Dust and Pollution Episodes in 2001. Atmos. Environ., 39(1), 39-50.

Kim, S.-W., S.-C. Yoon, J. Kim, and S.-Y. Kim, 2007. Seasonal and Monthly Variations of Columnar Aerosol Optical Properties Over East Asia Determined from Multi-Year MODIS, LIDAR and AERONET Sun/sky Radiometer Measurements. Atmos. Environ., 41, 1634-1651.

Kim, S.-W., S.-C. Yoon and J. Kim, 2008. Columnar Asian dust particle properties observed by sun/sky radiometer from 2000 to 2006 in Korea. Atmos. Environ., 42, 492–504.

Lee, K.H., J.E. Kim, Y.J. Kim, J. Kim, W. Von Hoyningen-Huene, 2005. Impact of the smoke aerosol from Russian forest fires on the atmospheric environment over Korea during May 2003. Atmos. Environ., 39, 85–99.

Liu, Z., N. Sugimoto, and T. Murayama, 2002: Extinction-to-backscatter ratio of Asian dust observed with high-spectral-resolution lidar and Raman lidar, Applied Optics, 41, 2760-2767.

Murayama, T., S. Masonis, and co-authors, 2003: An intercomparison of lidar-derived aerosol optical properties with airborne measurements near Tokyo during ACE-Asia, Journal of Geophysical Research, 108(D23), 8651, doi:10.1029/2002JD003259.

Nakajima T., S.-C. Yoon, and co-authors, 2007. Overview of the Atmospheric Brown Cloud East Asian Regional Experiment 2005 and a study of the aerosol direct radiative forcing in east Asia. J. Geophys. Res., 112, D24S91, doi:10.1029/2007JD009009.

Noh, Y. M., Y. J. Kim, B. C. Choi, and T. Murayama, 2007: Aerosol lidar ratio characteristics measured by a multi-wavelength Raman lidar system at Anmyeon

Island, Korea. Atmospheric Research, 86, 76-87, doi:10.1016/j.atmosres.2007.03.006.

Ramanathan V., M.V. Ramana, and co-authors, 2007. Warming trends in Asia amplified by brown cloud solar absorption. *Nature*, 448, 575-578 doi: 10.1038/nature06019.

Voss, K. J., E. J. Welton, and co-authors, 2001: Lidar measurements during Aerosols99, Journal of Geophysical Research, 106, 20,821–20,831, doi: 10.1029/2001JD900217.

Won, J.-G., S.-C. Yoon, S.-W. Kim, A. Jefferson, E. G. Dutton and B. Holben, 2004. Estimation of direct radiative forcing of Asian dust aerosols with sun/sky radiometer and lidar measurement at Gosan. Korea. J. of the meteor. Soc. of Japan, 82 (1), 115-130.

Yabe, T., R.Höller, S. Tohno, and M. Kadahara, 2003. An aerosol climatology at Kyoto: Observed local radiative forcing and columnar optical properties. J. Appl. Meteorol., 42, 841–850.

Yoon, S.-C., J.-G. Won, A. H. Omar, S.-W. Kim, B.-J. Sohn, 2005. Estimation of the radiative forcing by key aerosol types in worldwide locations using a column model and the AERONET data. Atmos. Environ., 39(35), 6620-6630.

Lidar Network Observations of Tropospheric Aerosols in East Asia

Nobuo Sugimoto[1], Ichiro Matsui[1], Atsushi Shimizu[1], Tomoaki Nishizawa[1], Boyan Tatarov[1], Soonchang Yoon[2], Dulam Jugder[3], and Tamio Takamura[4]

[1] *National Institute for Environmental Studies, 16-2 Onogawa, Tsukuba, Japan, nsugimot@nies.go.jp*

[2] *Seoul National University, Seoul, Korea*

[3] *Institute of Meteorology and Hydrology, Ulaanbaatar, Mongolia*

[4] *CEReS, Chiba University, Chiba, Japan*

Abstract

Observations of tropospheric aerosols using a ground-based network of two-wavelength (532nm, 1064nm) polarization (532nm) lidars (SKYNET-lidar < NIES Lidar Network < AD-Net < GALION) are reported. Currently, the lidars are continuously operated at 18 locations in East Asia, including 3 stations in Mongolia, Seoul, Korea, and Phimai, Tailand. The data from the lidars in the network are transferred to the National Institute for Environmental Studies (NIES) in real time and processed to derive the attenuated backscattering coefficients at the two wavelengths and the volume depolarization ratio. The extinction coefficient estimates for non-spherical aerosols (dust) and spherical aerosols are also derived automatically with the real-time data processing system. The data from the network are used in various studies on atmospheric environment and climate change. In this paper, we report on the lidar instrument and the network, the data analysis methods for estimating aerosol components, and the results of recent studies on Asian dust, air pollution aerosols, and forest fire smokes. The role of the lidar network in the GAW Aerosol Observation Lidar Network (GALION) and the role of GALION in climate change studies will be also discussed.

Keywords **:** lidar, aerosol, mineral dust, air pollution, SKYNET, data assimilation

1. Introduction

Various kinds of aerosols such as mineral dust, air-pollution aerosols, biomass burning smoke, and forest fire smoke coexist in the East Asian region, and it is important to understand the effects of these aerosols on climate and the environment. We started continuous observation with a compact automatic Mie scattering lidar in 1996 at NIES in Tsukuba in a research project on the effect aerosols in the global warming. In 2001, we constructed lidars in Beijing and Nagasaki and started network observations with the lidars at the three locations. The network has been expanded in the research programs and international cooperation. Some of the lidars were constructed in the Asian-dust monitoring program with the Ministry of the Environment of Japan. Currently, we are operating the lidars at 17 locations in Japan, Korea, Mongolia, and Thailand (the NIES Lidar Network).[1-3)] We also have cooperative stations in Korea and China. Some of the lidars are collocated with the SKYNET radiometers and operated as SKYNET-lidar.[4)] The NIES Lidar Network is a part the Asian dust research network (AD-NET) and the GAW Aerosol Lidar Observation Network (GALION), which is a global lidar network combining existing regional lidar networks.[5-6)]

2. Lidar System and the Network

The lidar used in the network is two wavelength (1064nm, 532nm) Mie-scattering lidar with a depolarization ratio measurement function at 532nm. Figure 1 shows a block diagram of the lidar system. The lidar uses a commercial flashlamp pumped Nd:YAG laser (Quantel Ultra) as a light source. The output power at 1064nm and 532nm is 20mJ and 20mJ. The receiver telescope diameter is 20cm. Polarization components of received light at 532 nm are separated with a polarization prism and detected with two photomultiplier tubes (PMTs) (Hamamatsu). Received light at 1064nm is detected with an avalanche photodiode (APD) (Licel). Signals from the PMTs and APD are digitized with 12-bit analogue-to-digital converters and recorded on a hard disk of the data acquisition PC. The lidars are operated continuously regardless of weather. In the continuous observation, 5-min averaged lidar profiles are measured every 15 minutes. Consequently, 96 sets of profiles are obtained per day. Recently, a detection system for nitrogen Raman scattering (607nm) was added to the lidar at the primary observation sites. Although the Raman scattering signals are useful only in the nighttime, the lidar ratio is obtained for aerosols in the lower troposphere.

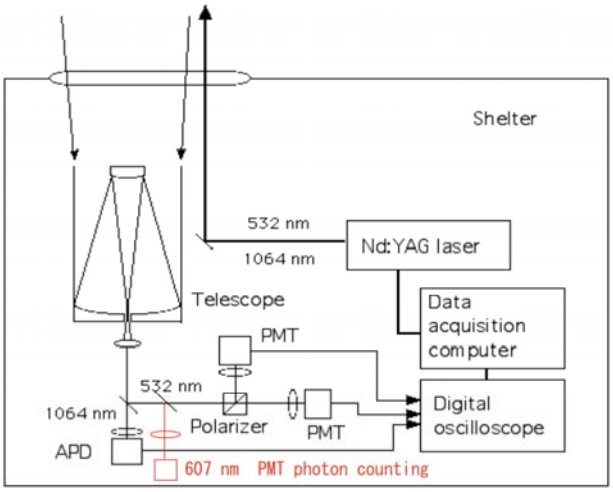

Fig. 1. Block diagram of the lidar system for the network.

The locations of the lidars in the NIES lidar network are listed in Table 1. The lidars in Fukue, Hedo, Chiba, Seoul, Phimai are operated in GEOSS/SKYNET. The lidars in Toyama, Nagasaki, Matsue, Niigata, and Tokyo were constructed by the Ministry of the Environment of Japan in the Asian dust monitoring program. All of the lidars in NIES lidar network, except for cooperative stations, participate in GALION.

A real-time data processing system was developed for the lidar network.[8] It collects data from the lidar stations every hour through the internet and processes the data to derive the attenuated backscattering coefficients at 532nm and 1064nm, the total depolarization ratio at 532nm, and the extinction coefficient estimates for non-spherical dust and spherical aerosols.[9-10] The method used for estimating contributions of dust and spherical aerosols in an aerosol mixture is based on the assumption that the observed aerosols are simple external mixtures of dust and spherical aerosols with different aerosol depolarization ratios. The automatically processed data and quick-look indications are posted on the www page of NIES at http://www-lidar.nies.go.jp/.

A data analysis system was also developed for the Raman signals to derive the extinction coefficient, the backscatter coefficient, and the lidar ratio. Also an algorithm was developed for deriving black carbon concentration as well as dust and spherical aerosols.[11]

Table 1 NIES Lidar Network Stations

Station (S) SKYNET-lidar (C) Cooperative station	Latitude (deg N)	Longitude (deg E)	Altitude (m ASL)	Status O: Operational Since	System B: backscatter D: depolarization R: Raman
Tsukuba	36.05	140.12	30	O 1996	2B+D(+1R)
Nagasaki	32.78	129.86	17	O 2002	2B+D(+1R)
Fukue (S)	32.75	128.68	50	O 2002	2B+D(+1R)
Sapporo	43.06	141.33	30	O 2003	2B+D
Toyama	36.70	137.10	28	O 2004	2B+D
Matsue	35.21	133.01	5	O 2005	2B+D(+1R)
Sendai	38.25	140.90	60	O 2005	2B+D
Cape Hedo (S)	26.87	128.25	60	O 2005	2B+D(+1R)
Niigata	37.84	138.94	1	O 2007	2B+D
Chiba (S)	35.65	140.12	20	O 2007	2B+D
Tokyo	35.69	139.71	42	O 2008	2B+D
Osaka	34.65	135.59	19	O 2008	2B+D
Seoul (S)	37.45	126.95	116	O 2006	2B+D(+1R)
Phimai (S)	15.18	102.57	212	O 2005	2B+D
Ulaanbaatar	47.92	106.90	1320	O 2007	2B+D
Sainshand	44.87	110.12	937	O 2007	2B+D
Zamynuud	43.72	111.90	962	O 2007	2B+D
Beijing (C)	39.97	116.37	70	O 2001	2B+D(+1R)
Daejeon (C)	36.33	127.34	80	2010	2B+D
Hefei (C)	31.90	117.17	30	2002	2B+D
Lanzhou (C)	35.94	104.14	1957	2010	2B+D

3. Studies Using the Lidar Network Data

3-1. Study of Asian dust

Almost all of the Asian dust events since 2001 where dust was transported to Japan were observed with the lidar network. The observed data were compared with the chemical transport model CFORS, and dust emission and transport were studied.

A 4D-Var data assimilation system using the dust extinction coefficient data from the lidar network was developed for Asian dust. It was demonstrated that the assimilation system was able to reproduce the surface PM10, the MODIS aerosol optical depth, and the CALIPSO/CALIOP data.[12-15] 4D-Var data assimilation also proved useful for better estimating the emission of dust in the source region. The change in dust emission with vegetation growth in the Gobi desert in Mongolia was studied with the data assimilation for the dust events in the spring of 2007.[16]

Studies of long-range transport of Asian dust are also being conducted using the lidar network data, CALIPSO/ CALIOP, and global chemical transport models.[17-18]

3-2. Study of forest fire smoke

Smoke plumes from forest fires in Russia and Mongolia are often observed in the spring. In June 2007, dense smoke plumes originating from a forest fire in northern Mongolia were observed in the upper troposphere with the lidars in Nagasaki and Fukue. The smoke from the same origin was also observed with an HSRL in Tsukuba. The optical characteristics of the smoke were studied with the two-wavelength method and the HSRL. The result indicated the lidar ratio and the Angstrom exponent were comparable to those in the previously reported forest fire smoke cases, however the depolarization ratio was two to three times high (0.15). This suggests mixing with solid particles such as ash and/or mineral dust in the strong convection in pyrocumulonimbus. This raised a problem in the lidar data analysis method to derive aerosol components and also in modeling forest fires.[19]

3-3. Climatology of aerosols

Climatological studies are also being done for both dust and spherical aerosols using long-term lidar network data, CALIPSO/CALIOP data, and chemical transport models. The result of a study on the seasonal variation of spherical aerosols in Beijing, Guangzhou, and Cape Hedo showed that the vertical profiles of aerosols exhibited different seasonal variation that can be explained by transport of air pollution with the Asian monsoon system. It was also demonstrated the aerosol profiles derived from the ground-based lidar and CALIPSO agreed well, and the Community Multi-scale Air Quality Modeling System (CMAQ) reasonably reproduced the aerosol distribution and the seasonal variation. The fraction of aerosol components (carbonaceous, sulfate, etc.) at different locations and the contributions of source regions were studied using CMAQ.[20]

3-4. Data assimilation of aerosol climate model

One of the most important subjects in the applications of the lidar network data to climate change studies is data assimilation of aerosol climate models. Currently, studies of data assimilation including lidar data are being conducted at three research groups in Japan. It would be useful to collect all available ground-based lidar profiles (globally, including past data) and provide them for data assimilation studies.

Acknowledgements

We thank Y. Fujiyoshi, T. Hayasaka, T. Takamura, S. Mukai, I. Sano, S-W. Kim, N-H. Kim, C-H. Lee, J. Zhou, C. Xie, Z. Wang, Y. Zhang, D. Batdorj, M. Hashizume, A. Chabangborn, the Ministry of the Environment, Japan, and the Sino-Japan Friendship Center for Environmental Protection in Beijing for cooperation in operating the lidar network. The SKYNET part of this work is supported by the Observational Research Project for Atmospheric Change in Troposphere (GEOSS program) of the Ministry of Education, Culture, Sports, Science and Technology, Japan. The Raman scattering measurements and data analysis study is supported by a Grant-in-Aid for Scientific Research in Innovative Areas under Grant No. 4003 from the Ministry of Education, Culture, Sports, Science and Technology, Japan. The Asian dust study is supported by the Global Environment Research Fund of the Ministry of the Environment, Japan (C-0901).

References

1) Sugimoto, N., Matsui, I., Shimizu, A., Nishizawa, T., Hara, Y., Xie, C., Uno, I., Yumimoto, K., Wang, Z., Yoon, S-C., "Lidar Network Observations of Troposheric Aerosols," Proc. SPIE 7153, doi: 10.1117/12.806540 (2008).

2) Shimizu, A., Sugimoto, N., Matsui, I., Tatarov, B., Xie, C., Nishizawa, T., and Hara, Y., "NIES Lidar Network; Strategies and Applications," 24th International Laser Radar Conference 23-27 June 2008, Boulder (ISBN 978-0-615-21489-4) 707-710 (2008).

3) Sugimoto, N., Shimizu, A., Matsui, I., Itsushi, U., Arao, K., Chen, Y., Zhao, S., Zhou, J. and Lee, C-H., "Study of Dust Transport Using a Network of Continuously Operated Polarization Lidars," Water, Air, and Soil Pollution: Focus, 5, 145-157 (2005).
4) SKYNET www page. http://atmos.cr.chiba-u.ac.jp/
5) Bösenberg, J., et al., "Plan for the implementation of the GAW Aerosol Lidar Observation Network GALION," GAW Report No. 178 (2007).
6) Hoff, R. M., Bösenberg, J., and Pappalardo, G., "The GAW Aerosol Lidar Observation Network (GALION), "the 24th International Laser Radar Conference 23-27 June 2008, Boulder, Colorado (ISBN 978-0-615-21489-4) 719-721 (2008).
8) Shimizu, A., Sugimoto, N., Matsui, I., Detailed Description of Data Processing System for Lidar Network in East Asia, 25th International Laser Radar Conference, 911-913 (2010).
9) Sugimoto, N., Uno, I., Nishikawa, M., Shimizu, A., Matsui, I., Dong, X., Chen, Y. and Quan, H., "Record Heavy Asian Dust in Beijing in 2002: Observations and Model Analysis of Recent Events," Geophys. Res. Lett., 30, 1640, doi:10.1029/2002GL016349 (2003).
10) Shimizu, A., Sugimoto, N., Matsui, I., Arao, K., Uno, I., Murayama, T., Kagawa, N., Aoki, K., Uchiyama, A. and Yamazaki, A., Continuous observations of Asian dust and other aerosols by polarization lidar in China and Japan during ACE-Asia, J. Geophys. Res., 109, D19S17, doi:10.1029/2002JD003253 (2004).
11) Nishizawa, T., Sugimoto, N., Matsui, I., Shimizu, A., Tatarov, B., Okamoto, H., "Algorithm to retrieve aerosol optical properties from high spectral resolution lidar and polarization Mie-scattering lidar measurements," IEEE Trans. Geos. Rem. Sens., 46, 4094-4103 (2008).
12) Yumimoto, K., Uno, I., Sugimoto, N., Shimizu, A., and Satake, S., "Adjoint Inverse Modeling of Dust Emission and Transport over East Asia," 2006GL028551R, Geophys. Res. Lett., 34, L08806, doi:10.1029/2006GL028551 (2007).
13) Yumimoto, Y., Uno, I., Sugimoto, N., Shimizu, A., Liu, Z. and Winker, D. M., "Adjoint inversion modeling of Asian dust emission using lidar observations," Atmos. Chem. Phys. Atmos. Chem. Phys., 8, 2869-2884 (2008).
14) Uno, I., Yumimoto, K., Shimizu, A., Hara, Y., Sugimoto, N., Wang, Z., Liu, Z. and Winker, D. M., "3D Structure of Asian Dust Transport revealed by CALIPSO Lidar and a 4D VAR Dust Model," Geophys. Res. Lett., 35, L06803, doi:10.1029/2007GL032329 (2008).
15) Hara, Y., Yumimoto, K., Uno, I., Shimizu, A., Sugimoto, N., Liu, Z. and Winker, D. M., "Asian dust outflow in the PBL and free atmosphere retrieved by NASA CALIPSO and an assimilated dust transport model," Atmos. Chem. Phys., 9, 1227–1239, (2009).
16) Sugimoto, N., Hara, Y., Yumimoto, K., Uno, I., Nishikawa, M., and Dulam, J., "Dust emission estimated with an assimilated dust transport model using lidar network data and vegetation growth in the Gobi desert in Mongolia, "SOLA, Vol. 6, 125-128, doi:10.2151/sola.2010-032 (2010).
17) Uno, I., Eguchi, K., Yumimoto, K., Takemura, T., Shimizu, A., Uematsu, M, Liu, Z., Wang, Z., Hara Y., and Sugimoto, N., "Asian dust transported one full circuit around the globe," Nature Geoscience, Published Online: 20 July 2009, DOI: 10.1038/NGEO583 (2009).
18) Yumimoto, K., Eguchi, K., Uno, I., Takemura, T., Liu, Z., Shimizu, A., and Sugimoto, N., "An elevated large-scale dust veil from the Taklimakan Desert: Intercontinental transport and three-dimensional structure as captured by CALIPSO and regional and global models," Atmos. Chem. Phys., 9, 8545–8558 (2009).
19) Sugimoto, N., Tatarov, B., Shimizu, A., Matsui, I., and Nishizawa, T., "Optical Characteristics of Forest-Fire Smoke Observed with Two-Wavelength Mie-Scattering Lidars and a High-Spectral-Resolution Lidar over Japan," SOLA, Vol. 6, 093-096, doi:10.2151/sola.2010-024 (2010).
20) Hara, Y., Uno, I., Shimizu, A., Sugimoto, N., Matsui, I., Kurokawa, J., Ohara T., Liu, Z., Zhang, Y., Liu, X., Wang, Z., "An Integrated Analysis of Spherical Aerosol Distribution in Eastern Asia Based on Ground/ Spaced-Based Lidar and a Chemical Transport Model," 25th International Laser Radar Conference, 449-452 (2010).

Shortwave versus longwave aerosol radiative forcing over an urban Environment.

A.S. Panicker[1], G. Pandithurai[2], T.Takamura[3], Dong-In Lee[1]

[1] *Global Research Laboratory, Pukyong National University, 599/1 Daeyeon 3 Dong, Nam Gu, Busan 608737, South Korea.*

[2] *Centre for Climate Change Research, Indian Institute of Tropical Meteorology, Pune, India*

[3] *Centre for Environmental Remote Sensing, Chiba University, Japan*

Abstract

Collocated observations of aerosol optical parameters, radiative fluxes in the longwave (0.4-50μm) and shortwave (0.3-3 μm) spectral regions were used to quantify aerosol radiative forcing in the longwave (LW) and shortwave (SW) spectral regions over an Indian urban site, Pune during October 2004 to May 2005. Aerosol optical parameters derived from a Prede Sun/Sky radiometer such as aerosol optical depth (AOD), single scattering albedo, asymmetry parameter, TOMS column ozone and MODIS water vapor were used in Santa Barbara Discrete ordinate Rdaitive Transfer model (SBDART) to derive short and long wave radiative fluxes. Short wave fluxes were found to be comparing well with the real time observed fluxes from a Short wave Pyranometer. The under estimation of modeled long wave fluxes got improved and found to be comparable with observed fluxes from a Precision infrared radiometer, on the inclusion of six hourly NCEP profiles of temperature and humidity in SBDART model. 'No aerosol' fluxes were also derived using SBDART in both the spectral region. The differences in fluxes with and without aerosol conditions were calculated to derive radiative forcing. The short wave radiative forcing during different seasons viz. Post monsoon (October, November), winter (Dec-Feb) and Pre-monsoon (March- May) respectively found to be -36, -33 and -44 Wm^{-2} at the surface and +0.5,-0.55, +0.4 Wm^{-2} at the Top of the Atmosphere (TOA) . The corresponding long wave enhancement found to be +8.5, +8, +10.5 Wm^{-2} at the surface and, +3.5, +3 and +4.7 Wm^{-2} at TOA. The study suggests that around 23-25% of aerosol cooling in the short wave region is being compensated by long wave enhancement at the surface.

1. Introduction

Aerosols, which are microscopic particles suspended in the atmosphere are key components of the climate system. Apart from their crucial role in air pollution, aerosols influence the climate directly and indirectly through radiative forcing. Direct radiative forcing includes the scattering and absorption of the incoming solar radiation by aerosols, which in turn cools the earth's surface (Badrinath and latha, 2006; Takamura et al., 2007; Panicker et al., 2008). Aerosols influence the climate indirectly by altering cloud microphysical properties and hence increasing albedo and cloud life time (Twomey, 1977). Several studies report aerosol radiative forcing in the shortwave spectral region (Conant, 2000; Jayaraman et al., 1998). But it is shown that aerosol long-wave forcing is of comparable magnitude as that of greenhouse gases in heating the earth's surface and in modifying earth's energy balance (Vogelmann et al. 2003). Direct observations of aerosol IR forcing are rare either at the surface (e.g., Lubin and Simpson, 1994; Spankuch et al. 2000), in the atmosphere (Highwood et al., 2003), or at the top of the atmosphere (Ackerman and Chung, 1992; Hsu et al., 2000). Thus, our understanding of IR aerosol forcing is largely model-based with few direct observations available for validations (Vogelmann et al., 2003). In this scenario, we are trying to estimate aerosol radiative forcing in short and long wave spectral regions, to find the exact modulation of short wave cooling by longwave enhancement at the surface.

2. Instrumentation and Data

The instruments used in this study are (i) Prede sun/sky radiometer; (ii) Pyranometer and (iii) an Infrared radiometer (Pyrgeometer) are installed in the roof of Indian Institute of Tropical Meteorology [IITM], Pune [18°32' N ,73°51' E, 559 m AMSL]. The Prede sky radiometer is an automatic sun tracking instrument, which is capable of measuring direct solar and diffuse sky radiance at five spectral channels. The filters are centered at wavelengths 400, 500, 675, 870 and 1020 nm and a detailed description of calibration methodology and data reduction procedures of this instrument are presented in Nakajima et al. (1996). Once a month, sky radiometer is operated to collect disc sans to estimate solid view angles at different wavelengths as part of the calibration and used in data processing. Absolute calibration is done by PREDE, Japan at the factory and the

last such calibration was done in December 2003. Also, on very clear sky days, absolute calibration constant $V_0(\lambda)$ is estimated using the modified Langley plot technique and found to be consistent with the manufacturer calibration (Pandithurai et al. 2004). A Kipp and Zonen ventilated Pyranometer [Model CM21] and a Pyrgeometer [Eppley Model PIR] are used to measure down-welling short- and long-wave radiative fluxes respectively. Both sensors are ventilated, inspected and cleaned daily to avoid data contamination.

3. Methodology

Aerosol optical parameters derived from a Prede Sun/Sky radiometer such as aerosol optical depth (AOD), single scattering albedo, asymmetry parameter, TOMS column ozone and MODIS water vapor were used in Santa Barbara Discrete ordinate Rdaitive Transfer model (SBDART) to derive short and long wave radiative fluxes. The derived short-long wave fluxes were compared with the observed fluxes from A Pyranometer and Pyrgeometer respectively. 'No aerosol' fluxes were also derived using SBDART in both the spectral region. The differences in fluxes with and without aerosol conditions were calculated to derive radiative forcing.

4. Results and Discussions

4.1. Comparison of Observed and Modeled fluxes

On comparing, modeled Short wave fluxes were found to be matching well with the real time observed fluxes from a Short wave Pyranometer. Longwave fluxes have been estimated for 21 clear sky days during winter 2004-05 at half hourly intervals with SBDART and were compared with Pyrgeometer (PIR) observed fluxes. The fluxes derived with default tropical profile were compared with a mean bias of -4.6 Wm^{-2}. The underestimation of fluxes may be due to fixed tropical model profiles of temperature and humidity used for the entire day. In the longwave, aerosol volume extinction depends more strongly on relative humidity than in most of the shortwave, implying that realistic relative humidity profiles must be taken in to account while modeling the longwave fluxes (Lubin et al., 2002). It is also shown that simultaneous measurements of vertical distribution of aerosols, surface temperature and water vapor are critical to the understanding of LWARF (Zhang and Christopher, 2003). Hence, it is proposed to use temporal variation of realistic vertical profiles of atmospheric temperature and humidity. As such observations on vertical profiles of temperature and humidity were not available over the site, we incorporated six hourly NCEP profiles from surface to 300 mb level in SBDART and diurnal LW fluxes were simulated for all the 21 selected days. The introduction of NCEP profiles reduced the mean bias from -4.6 to -2.2 Wm^{-2}. A scatter plot between observed and modeled LW fluxes with tropical model and realistic six hourly NCEP profiles are shown in figure 1.

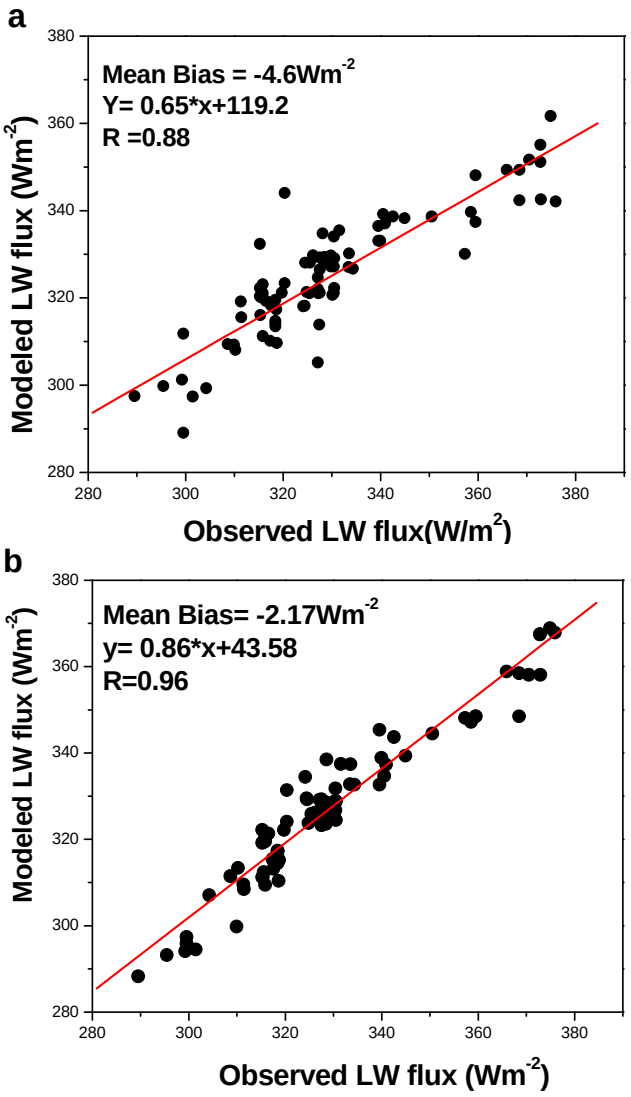

Figure 1: Comparison of Observed fluxes with Modeled LW fluxes (a) with Default model profile (b) with NCEP 6-hr profiles during winter 2004-05.

4.2. Estimation of Aerosol short- Long wave radiative forcing

Aerosol Short- long wave radiative forcing has been estimated as described in section 3.

The short wave radiative forcing during different seasons viz. Post monsoon (October, November), winter (Dec-Feb) and Pre-monsoon (March- May) respectively found to be -36, -33 and -44 Wm^{-2} at the surface and +0.5,-0.55, +0.4

Wm^{-2} at the Top of the Atmosphere (TOA), which are directly correlated with the aerosol loading during respective periods. The positive TOA forcing is attributed to the high absorbing type aerosols present over the experimental station. Aerosol longwave radiative forcing has been estimated using realistic NCEP profiles instead of model profile, along with other inputs specified in section 3. The long wave enhancement found to be +8.5, +8, +10.5 Wm^{-2} at the surface and, +3.5, +3 and +4.7 Wm^{-2} at TOA. The study suggests that around 23-25% of aerosol cooling in the short wave region is being compensated by long wave enhancement at the surface.

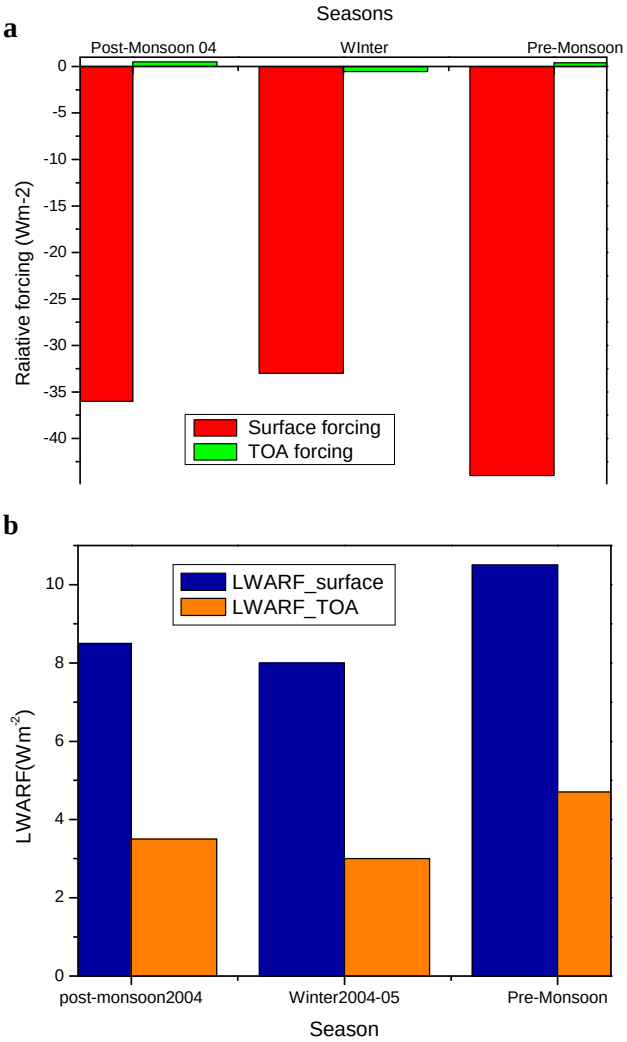

Figure 2: Estimated radiative forcing at surface and TOA (a) for shortwave fluxes, (b) For Longwave fluxes

5. Summary and Conclusions

Collocated observations of aerosol optical parameters, radiative fluxes in the longwave (0.4-50µm) and shortwave (0.3-3 µm) spectral regions were used to quantify aerosol radiative forcing in the longwave (LW) and shortwave (SW) spectral regions over an Indian urban site, Pune during October 2004 to May 2005. The short wave radiative forcing during different seasons viz. Post monsoon (October, November), winter (Dec-Feb) and Pre-monsoon (March-May) respectively found to be -36, -33 and -44 Wm^{-2} at the surface and +0.5,-0.55, +0.4 Wm^{-2} at the Top of the Atmosphere (TOA). The corresponding long wave enhancement found to be +8.5, +8, +10.5 Wm^{-2} at the surface and, +3.5, +3 and +4.7 Wm^{-2} at TOA. The study suggests that around 23-25% of aerosol cooling in the short wave region is being compensated by long wave enhancement at the surface.

Acknowledgements

Authors acknowledge Prof. B.N. Goswami, director IITM, Dr. R. Krishnan and Dr. P.C.S. Devara for their encouragements. A.S.Panicker and Dong-In Lee gratefully acknowledge the Support from National Research Foundation of Korea (NRF) through a grant provided by the Korean Ministry of Education, Science & Technology (MEST) in 2010 (No. K20607010000).

References

1) Ackerman, S. A., and H. Chung (1992), Radiative effects of airborne dust on regional energy budgets at the top of the atmosphere, *J. Appl. Meteorol*., *31*, 223-233.

2) Badrinath, K. V. S., and K. Madhavi Latha (2006), Direct radiative forcing from black carbon aerosols over urban environment, *Advances in Space Research*, 37, 2183-2188.

3) Conant, W. C. (2000), An observational approach for determining aerosol surface radiative forcing: Results from the first phase of INDOEX, *J. Geophys. Res*., *105*, (D12**),** 15347-15360.

4) Highwood, E. J., J. M. Haywood, M. D.Silverstone, S. M. Newman, and J. P. Taylor (2003), Radiative properties and direct effect of Saharan dust measured by theC-130 Aircraft during SHADE.2: Terrestrialspectrum, *J. Geophys. Res.*, *108*, (D18), 8578, doi:10.1029/2002JD002552.

5) Hsu, N. C., J. R. Herman, and C. J. Weaver (2000), Determination of radiative forcing of Saharan dust using combined TOMS and ERBE data, *J .Geophys. Res.*, *105*, *20*,649-20,661.

6) Jayaraman, A., D. Lubin, S. Ramachandran, V. Ramanathan, E. Woodbridge, W. D. Collins, and Zalpuri, K. S. (1998), Direct observations of aerosol radiative forcing over the tropical Indian Ocean during the

January-February 1996 pre-INDOEX cruise, *J. Geophys. Res., 103* (D12), 13,827 -13,836.

7) Lubin, D., and A. S. Simpson (1994), The long-wave emission signature of urban pollution: Radiometric FTIR measurement, *Geophys. Res. Lett., 21*, 37-40

8) Lubin, D., S. K. Satheesh, G. McFarquhar, and A. J. Heymsfield (2002), Long–wave radiative forcing of Indian Ocean tropospheric aerosol, *J. Geophys. Res*., *107*(D19), 10.1029/2001JD00 1183.

9) Nakajima, T., G. Tonna, R. Rao, P. Boi, Y. Kaufman, and B. N. Holben (1996), Use of skybrightness measurements from ground for remote sensing of particulate poly dispersions, *Appl. Opt, 35*, 2672-2686.

10) Pandithurai, G., R. T. Pinker, T. Takamura, and P. C. S. Devara (2004), Aerosol radiative forcing over a tropical urban site in India, *Geophy. Res. Lett, 31*, L12107, doi:10.1029/2004GL019702

11) Panicker, A. S., G. Pandithurai, P. D. Safai, and S. Kewat (2008), Observations of enhanced aerosol longwave radiative forcing over an urban environment, *Geophys. Res. Lett*., *35*, L04817, doi: 10.1029/2007GL032879.

12) Spankuch, D., W. Dohler, and J. Guldner (2000), Effect of coarse biogenic aerosol on down-welling infrared flux at the surface, *J. Geophys. Res*., *105*, 17, 341-17, 350.

13) Takamura, T., N. Sugimoto, A.Shimizu, A.Uchiyama, A.Yamazaki, K.Aoki,T. Nakajima, B.J. Sohn and H. Takenaka (2007), Aerosol radiative characteristics at Gosan, Korea, during the Atmospheric Brown Cloud East Asian Regional Experiment 2005, *J. Geophys. Res., 112*, D22S36, doi:10.1029/2007JD008506.

14) Twomey, S. (1977), The influence of pollution on the shortwave albedo of cluds, *J. Atmos. Sci., 34*., 1149-1152.

15) Vogelmann, A, M., P. J. Flatau, M. Szczodrak, K. M. Markowicz, and P. J. Minnett (2003), Observations of large aerosol infrared forcing at the surface, *Geophy. Res .Lett, 30(12)*, 1655, doi: 10.1029/2002GL016829.

16) Zhang, J., and S. A. Christopher (2003), Long wave radiative forcing of Saharan dust aerosols estimated from MODIS, MISR, and CERES observations on Terra, *Geophy. Res. Lett, 30(23)*, 2188, doi: 10.1029/2003GL018479.

Development of correction method for integrating nephelometer and recent trend of aerosol optical properties based on ground-based measurement at Tsukuba

A. Uchiyama, A. Yamazaki, R.Kudo, and T. Sakami

Meteorological Research Institute, Japan Meteorological Agency,
1-1, Naganine, Tsukuba, Ibaraki, JAPAN 305-0052
uchiyama@mri-jma.go.jp

Abstract

Measurements of Integrating nephelometer has error due to the truncation of light detection area. We developed a correction method using multi-wavelength nephelometer and absorption photometer. The accuracy of the method was evaluated using the simulation data. Applying this method to the data measured at Tsukuba, the recent trend of aerosol optical properties was investigated.

Keywords **:** Integrating Nephelometer, PSAP, Scattering Coefficient of Aerosol, Absorption coefficient of Aerosol, Single scattering albedo of aerosol, asymmetry factor of aerosol

1. Introduction

The optical property of aerosol is one of the important parameters for the earth radiation budget and the atmospheric environment. In order to investigate the optical property of aerosol and to monitor the change of atmospheric environment, scattering and absorption coefficients of aerosol are measured at ground-based observation sites. The scattering coefficient is frequently measured using an integrating nephelometer. The integrating nephelometer cannot measure the light scattered to the extreme forward direction (scattering angle is nearly 0 degree.) and the extreme backward direction (scattering angle is nearly 180 degree.). Therefore, even if the distribution of light source in the nephelometer is correct, the scattering coefficient measured by the nephelometer is underestimated. In this study, the method to correct the scattering coefficients measured using the three wavelength nephelometer and three wavelength absorption photometer is developed. The accuracy of the method is evaluated by the simulation using OPAC (Hess et al, 1998) model. The method is a statistical retrieval one and the volume size distribution and the complex refractive index are simultaneously estimated.

Applying this method to the data measured at Tsukuba during the period from 2002 to 2010, the trend of optical properties of aerosol was investigated.

2. Methods

We use statistically optimized estimation method. The optimized estimate of the parameter is considered to be a value that maximized the following likelihood function

$$L(\mathbf{x}^b, \mathbf{f}^o, \mathbf{x}) = P_b(\mathbf{x}^b) P_o(\mathbf{f}^o)$$
$$= \frac{1}{(2\pi)^{(n+m)/2} |\mathbf{B}|^{1/2} |\mathbf{R}|^{1/2}}$$
$$\times \exp\left[-\frac{1}{2}(\mathbf{x}-\mathbf{x}^b)^T \mathbf{B}^{-1}(\mathbf{x}-\mathbf{x}^b) - \frac{1}{2}(\mathbf{f(x)}-\mathbf{f}^o)^T \mathbf{R}^{-1}(\mathbf{f(x)}-\mathbf{f}^o) \right]$$

When the following function J is minimum, the above function is maximized.

$$J(\mathbf{x}) = \frac{1}{2}(\mathbf{x}-\mathbf{x}^b)^T \mathbf{B}^{-1}(\mathbf{x}-\mathbf{x}^b)$$
$$+ \frac{1}{2}(\mathbf{f}(\mathbf{x})-\mathbf{f}^o)^T \mathbf{R}^{-1}(\mathbf{f}(\mathbf{x})-\mathbf{f}^o)$$

, where $\mathbf{x}$ is parameter to be determined, $\mathbf{x}^b$ is the initial estimate, $\mathbf{f}^0$ is measurement, $\mathbf{f}(\mathbf{x})$ is measurement estimated by forward model. $\mathbf{B}$ and $\mathbf{R}$ are covariance matrices.

In this study, scattering and backscattering coefficients measured by TSI model 3563 at the wavelength of 450, 550 700nm and absorption coefficients measured by Particle Soot Absorption Photometer (PSAP) at wavelength of 462, 526, 650nm are considered as measurement values.

Given the measurement values, we estimate the size distribution of aerosol and complex refractive index using the above method. Using the estimated parameters, we calculate the single scattering properties (scattering coefficients, single scattering albedo, and asymmetry factor) based on Mie Theory. These values are regards as the corrected scattering coefficients and single scattering albedo.

3. Simulation of measurement

The accuracy of the method was evaluated using simulation data. The simulated data is calculated based on OPAC (Hess et al, 1998) model. OPAC model consist of 10 aerosol types.

Each aerosol type is external mixture of basic models. The single scattering properties of mineral dust are calculated using the database for spheroid by Dubovik et al. (2006). The single scattering properties of the other aerosol are calculated based on Mie theory. The truncation of integrating nephelometer is taken into consideration. Each aerosol type includes hygroscopic aerosol. Therefore, scattering properties for each aerosol type depend on relative humidity.

4. Parameter setting and initial value

The statistical optimized method needs the error covariance for each data of measurements and the initial estimates of parameters to be retrieved. We assume that the off-diagonal elements of covariance matrices are zero and diagonal elements are non zero. The following standard deviations (σ) are used in our method.

Scattering and back scattering coefficients:
σ=0.5E-06 (1/m)

Absorption coefficient: σ=0.5E-06 (1/m)

Index of refraction (real part):
σ=(log(1.6)-log(1.4))/2～0.029

Index of refraction（imaginary part）:
σ=(log(0.05)-log(0.005))/2～0.5

Volume size distribution : σ=Δlog(dV/dlogR)～2

Smoothing constrain is also treated as a measurement. It is assumed that the second derivative is zero.

Wavelength dependence of index of refraction:
difference between next points is 5%.

Volume size distribution spectrum:
difference between next points is factor 2.

The range of particle radius is R=0.00631 to 25.1 μm and divided into 19 bins with ΔlogR＝0.2 width. The range of wavelength is λ=0.316 to 1.0 μm and divided into 6 wavelength with Δlogλ＝0.1.

The power low distribution is assumed as the initial estimate of number size distribution.

$$\begin{aligned} dN/dr &= C & r < 0.05\mu\text{m} \\ &= Cr^{-(\alpha+3)} & 0.05\mu\text{m} \le r < 8\mu\text{m} \\ &= Cr^{-6} & 8.0\mu\text{m} \le r \end{aligned}$$

, where α is Ångström exponent.

It is assumed that the initial real part of index of refraction is 1.5. The imaginary part is determined as the estimated single scattering albedo (SSA) at each wavelength is equal to measurement SSA. When we minimize $J(\mathbf{x})$, Gauss-Newton method is used and the initial estimate is replaced by the solution of the previous step.

5. Test results

In Fig. 1, the comparison among truth, measurement and corrected SSA at the wavelength of 550nm is shown. In every case, corrected values are closer to the truth one than measurements. In Desert model (5), the truth is calculated by non-spherical particle model. Even in this case, the correction by spherical model works well. The RMS difference between truth and measurement values is 0.009 to 0.015. The RMS difference between truth and corrected values is 0.002 to 0.004; relative error is 0.3 to 0.5%.

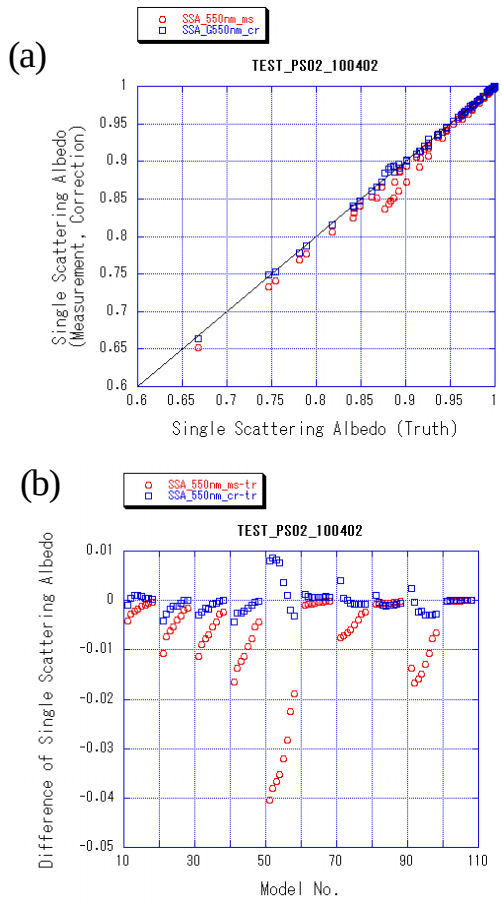

Fig. 1. (a) Comparison among truth, measurement (open circles) and corrected (open squares) single scattering albedo (SSA) at 550nm. (b) difference of SSA between truth and measurement (open circles) and difference of SSA between truth and corrected one (open squares). Model no. = OPAC model no. x10 + humidity ID(1-8). Relative humidity values are 0, 50, 70, 80, 90, 95, 98, 99%.

We also examined accuracy of corrected (estimated) values in the cases that scattering and absorption coefficients have error. In Fig. 2, the comparison among truth, measurement and corrected SSA at 550nm is shown in the case of absorption coefficient with +3% systematic errors. When SSA is small, the error becomes large. But, in most cases, the influence of error was small. We also examined

accuracy in the case of absorption coefficient with +5% errors (Figures are not shown here). Even in this case, the influence of error was small in most cases, because the scattering coefficients are larger than absorption coefficients by several times or one order.

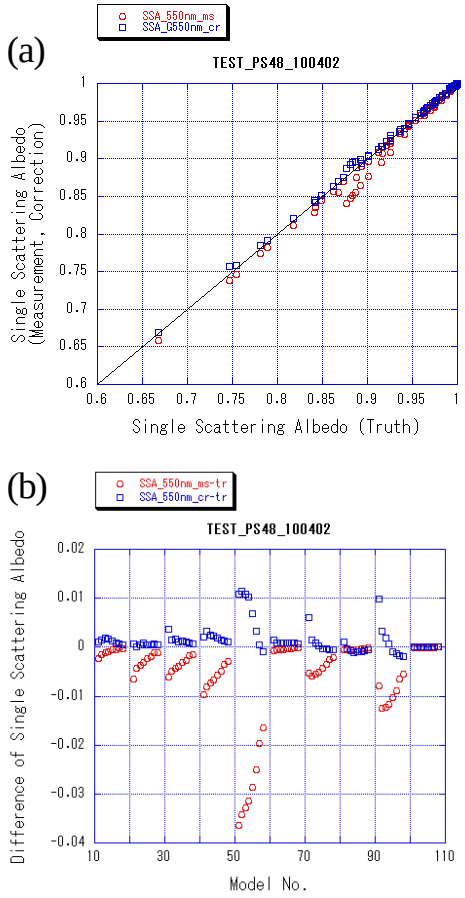

Fig. 2 Same as Fig. 1 except results in the case of absorption coefficient with 3% error.

Though we do not show figures here, the following additional results were obtained.

(1) The measured scattering and absorption coefficients are reconstructed within RMS 3E-07(1/m) and 8E-08(1/m), respectively.

(2) The scattering coefficients are estimated within RMS 1.2E-03 (1/m). When particles are large (for example, relative humidity is high), error is large.

(3) The extinction coefficient shows the same tendency as the scattering coefficients.

(4) The 1% and 3% error of scattering coefficient do not affect to the SSA estimation. In the case of 5% error, the error of the estimated SSA is the same order as the SSA calculated using measurement values.

(5) The RMS error of estimated asymmetry factor is 0.03.

(6) The small structure of size distribution cannot be estimated. In many cases, the mono-modal size distribution is estimated, even if the original size distribution is bi-modal one.

(7) When smoothing constrain of size distribution is strict, there is a tendency that the size distribution in the region of larger particle size becomes large as the particle size increased.

(8) The correlation between the original and estimated effective radiuses is 0.85. But, the estimated effective radius is 1.6 times as large as the original one.

(9) The volume weighted index of refraction is not close to the estimated one. The wavelength dependence is similar to the volume weighted one.

6. Aerosol optical properties at Tsukuba

Applying the above method to the data measured at Tsukuba during the period from 2002 to 2010, the trend of optical properties of aerosol was investigated.

The scattering coefficients are measured using TSI model 3563 at 3 wavelengths 450,550,700nm during the period from January 2002 to present. The absorption coefficient is measured using PSAP at a wavelength 565nm during the same period as TSI nephelometer. The absorption coefficients are measured using PSAP at 3 wavelengths 462, 526, 650nm during the period from March 2006 to present. We only analyzed the data in the dry condition; the relative humidity in nephelometer inlet is less than 50%. When the data of one wavelength PSAP is used, it is assumed that the wavelength dependence of absorption coefficient is $\lambda^{-1.1}$. 1.1 is the mean value from 2006 to 2010.

In Fig. 3, scattering and absorption coefficients are shown. After 2006, both scattering and absorption coefficients are decreasing. The change of absorption coefficients (Cabs) shows seasonal variation. In the winter season, Cabs is large and in the summer season, Cabs is small.

In Fig. 4, SSA at the wavelength of 550nm is shown. The large part of SSA (550nm) is between 0.8 and 0.9 and almost constant. After 2007, SSA(550nm) is slightly increasing. The change of SSA shows seasonal variation. In the winter season, SSA is small, and in the summer season, SSA is large. This seasonal variation is consistent with the change of absorption coefficient.

In Fig. 5, asymmetry factor (g) at the wavelength of 550nm is shown. g(550nm) is between 0.5 and 0.7. After 2007, g(550nm) is slightly decreasing. The change of asymmetry factor also shows seasonal variation. In the winter season, g(550nm) is small, and in the summer season, g(550nm) is large.

Though figures are not shown here, the changes of

Ångström exponent and effective radius (Reff) show seasonal variation. In the winter season, Ångström exponent is high and in the summer season, Ångström exponent is low. In winter season, Reff is small, and in the summer season, Reff is large. After 2008, Ångström exponent is slightly increasing and Reff is slightly decreasing. The trend of g(550nm) is consistent with those of Ångström exponent and Reff.

7. Summary

We examined accuracy of the method developed using that simulation data based on OPAC model. The measured scattering and absorption coefficients can be reconstructed within RMS =2.4 to 3.1E-07(1/m), 0.4 to 0.8E-07(1/m). SSA can be estimated with RMS =0.002～0.004 (relative error 0.3～0.5%). In all cases, the estimated SSA is closer to the truth than the non-corrected measurement one. The RMS error of corrected scattering coefficients was 1.2E-05(1/m), and when the aerosol consists of the larger size particles (for example, relative humidity is high case), the accuracy of estimated scattering coefficient is not good. The RMS error of asymmetry factor is 0.03.

In our method, volume size distribution and index of refraction are retrievel. The small structure of size distribution cannot be estimated. The correlation between the original and estimated effective radiuses is 0.85. But, the estimated effective radius is 1.6 times as large as the original one. We compared between the estimated index of refraction and the volume weighted one, but it is not found the quantitative coincidence between both indexes of refraction. The wavelength dependence was qualitatively coincident.

Applying this method to the data measured during 2002 to 2010 at Tsukuba, the trend of aerosol optical properties is investigated. After 2006, the scattering and absorption coefficients are gradually decreasing. SSA is almost constant, but after 2007, SSA is slightly increasing. The asymmetry factor and Ångström exponent of extinction coefficient also has similar trend. After 2007, the asymmetry factor and Ångström exponent are slightly decreasing and increasing, respectively.

References

1) Hess M., P. Koepke, and I. Schult, 1998: Optical Properties of aerosols and clouds: The software package OPAC, *Bull. Amer. Meteor. Soc.*, **79**, 831-844.

2)Dubovik, O., A. Sinyuk, T. Lapyonok, B. N. Holben, M. Mishchenko, P. Yang, T. F. Eck, H. Volten, O. Muñoz, B. Veihelmann, W. J. van der Zande, J. F. Leon, M. Sorokin, and I. Slutsker, 2006: Application of spheroid models to account for aerosol particle nonsphericity in remote sensing of desert dust, *J. Geophys. Res.*, **111,** D11208, doi:10.1029/2005JD006619.

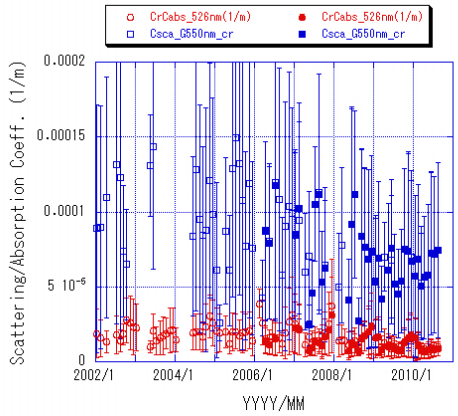

Fig. 3 monthly mean values and standard deviation of scattering coefficients at 550nm and absorption coefficient at 526nm. Open symbols mean that the correction was made using 3wavelngth (3λ) nephelometer and 1wavelength (1λ) PSAP. Closed symbols mean that the correction was made using 3λ nephelometer and 3λ PSAP.

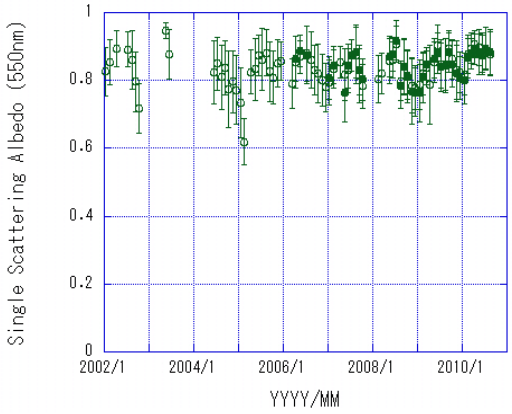

Fig. 4 Same as Fig. 3 except SSA.

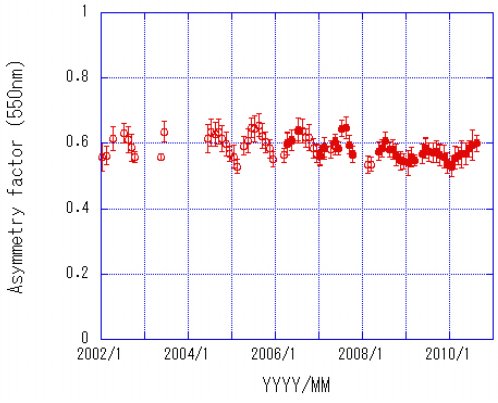

Fig.5 Same as Fig. 3 except asymmetry factor.

Use of spectral irradiances measured at surface to retrieve aerosol optical parameters

Pradeep Khatri[1], Tamio Takamura[1], Akihiro Yamazakai[2], and Yutaka Kondo[3]

[1] *Center for Environmental Remote Sensing , Chiba University,Chiba, Japan*

[2]*Meteorological Research Institute, Tsukuba, Japan*

[3]*Research Center for Advanced Science and Technology, The University of Tokyo*

Abstract

This study presents a method to retrieve key aerosol optical parameters such as aerosol optical thickness and single scattering albedo using spectral direct and diffuse irradiances measured at surface by taking into account the cosine error correction factors in detail. The proposed method is applied to observed spectral irradiance data at Hedo observation site of SKYNET network. We found very good agreement for aerosol optical thickness and reasonable agreement for single scattering albedo with results from sky radiometer.

Keywords: Aerosol optical thickness, single scattering albedo, cosine error correction factor

1. Introduction

Aerosols are known to play important roles on atmospheric heat budget and climate change through their direct and indirect effects. Due to the importance of aerosols on climate change study, they have received considerable interests in the recent years. As a result, aerosols are being monitored by several space- and ground- based remote sensing approaches. Aerosol optical parameters obtained from ground-based remote sensing methods are widely used to validate results from several satellites as well as numerical model simulations. Among several ground-based remote sensing networks in the world, SKYNET network has monitoring sites in different parts of the Asia. Sky radiometer, which measures aerosol optical and physical characteristics, is the key instrument of this network. In order to validate aerosol optical parameters obtained from sky radiometer, a new radiometer that can measure spectral diffuse, direct, and global irradiances is installed at some key SKYNET sites. This study is dedicated to develop algorithm for such newly developed radiometer.

2. Data

We used irradiances measured by spectral radiometer (MS-700) with automated shadow band (Manufacturer: EKO Co., Ltd., Japan). The measurement sequence starts with a measurement made at nadir, i.e., total horizontal irradiances. The band is then rotated so that three measurements are made in seqence; the middle one blocks the sun and other two block strips of sky 9^0 either side. Such side measurements are used to correct diffuse irradiance by taking into account the excess sky blocked by the band when the sun-blocking measurements are made. Direct irradiances can be obtained from measured direct and diffuse irradiances. The spectral range of this instrument is from 301.1 nm to 1147.7 nm with resolution of 3.3nm.Along with such measured spectral irradiances, we used other data such as ozone concentration from TOMS, spectral surface reflectance from MODIS, precipitable water content (PWC) from microwave radiometer in our algorithm. Aerosol optical parameters obtained from sky radiometer were used to compare our retrieved results.

3. Description of an algorithm

Fig. 1 shows a simple flow chart for the retrieval of aerosol optical thickness and single scattering albedo using spectral irradiances measured by MS-700. For our retrieval, we carefully selected the wavelengths at which absorptions by atmospheric constituents such as ozone, water vapor etc. are negligible. The selected wavelengths are 400nm, 500nm, 675nm, 870nm, and1020nm.The cosine error correction factors for direct irradiances at certain zenith and azimuth angles, which were provided by the company, were extrapolated/interpolated to zenith angle ranging from 0 to 90^0 and azimuth angle ranging from 0 to 360^0 at the step of 0.5^0. One can calculate the solar position from given latitude, longitude, and observation time, and apply such interpolated/extrapolated data to correct spectral direct irradiances measured by MS-700. After correcting MS-700 measured direct irradiances, Beer-Lambert law was used to calculate total optical thickness. By subtracting Rayleigh optical thickness and ozone optical thickness from the total optical thickness, aerosol optical thickness (AOT) was calculated.

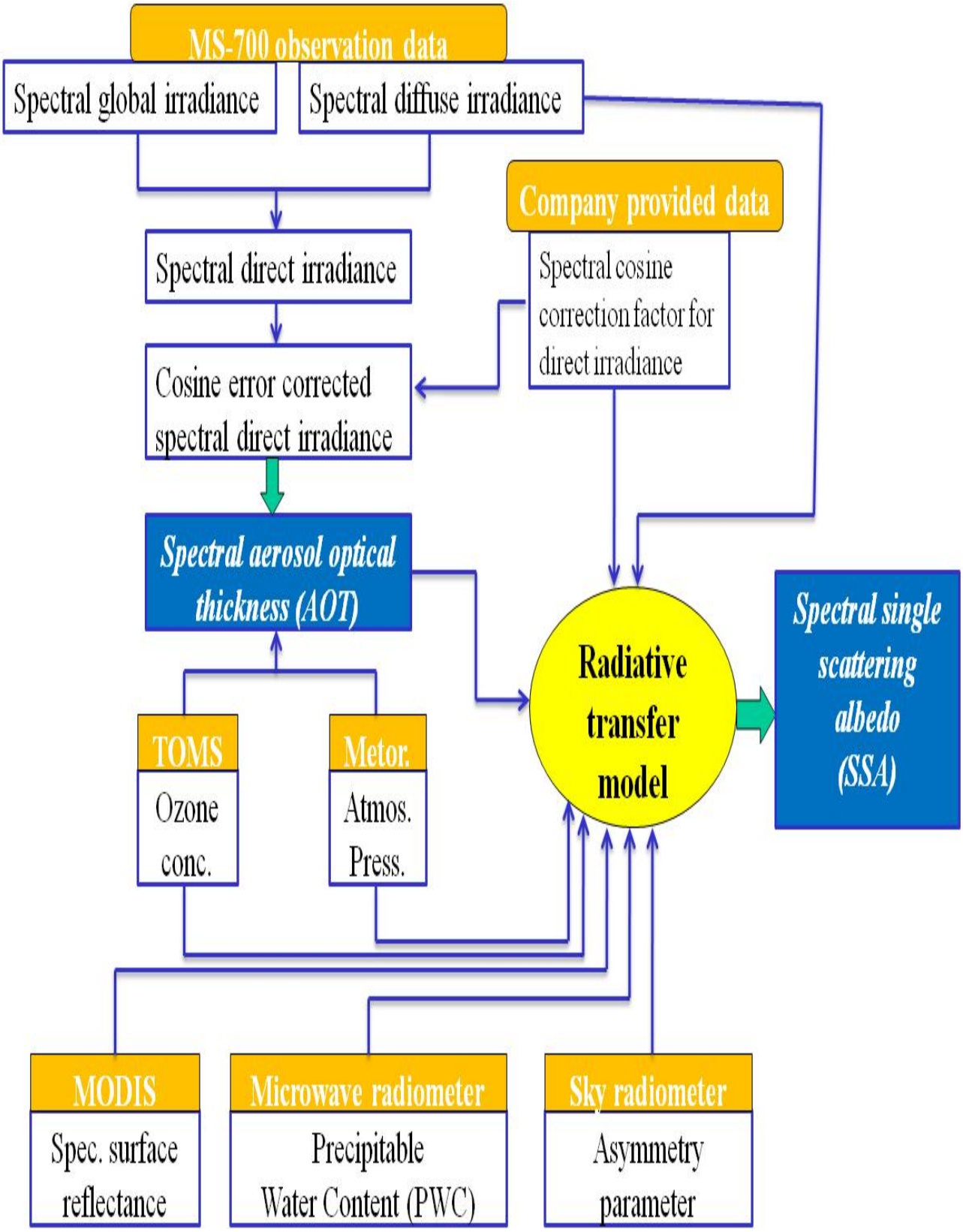

Fig. 1. A simple flow chart showing the retrieval method of aerosol optical thickness and single scattering albedo using spectral irradiances measured by MS-700.

Single scattering albedo(SSA) is the key optical parameter of aerosol. We used radiative transfer (RT) model to estimate SSA. In our method, at first AOT from MS-700, asymmetry parameter from sky radiometer, PWC from microwave radiometer, ozone concentration from TOMS, spectral surface reflectances from MODIS and 31 SSA values ranging from 0.7 to 1.0 at an interval of 0.01 were inputted in RT model to estimate radiances at different directions (zenith angle: 0 to 90^0 and azimuth angle: 0 to 360^0). Therefore, we calculated 31 sets of radiance data at different directions. Such modeled radiances were converted to MS-700 equivalent radiances by applying fine gridded cosine error correction factors for direct irradiances as described above. MS-700 equivalent radiances are defined as such radiances whose integration over the full zenith and azimuth angles should give diffuse irradance equivalent to that measured by MS-700. By integrating MS-700 equivalent radiances at different directions for each value of SSA, we obtained 31 values of MS-700 equivalent diffuse irradiances. One can directly compare such 31 values of MS-700 equivalent diffuse irradiances with directly measured MS-700 diffuse irradiance
to find the most plausible value of SSA. This method can give correct SSA if measured diffuse irradiance by MS-700 is highly qualitative. On the other hand, one may estimate 31 values of MS-700 equivalent diffuse/global ratio or diffuse/direct ratio and compare with respective measured component to find the most plausible value of SSA. The latter method is more suitable if the calibration constant of the instrument is not very accurate.

4. Results and discussion

We applied the above-mentioned algorithm to data measured by MS-700 at Hedo observatory of SKYNET network. We used data observed in the spring season (March, April, and May) of 2009. As an example of retrieved AOTs from MS-700 instrument, we show comparison of MS-700 result with that of sky radiometer at 500nm in Fig. 2. For comparison, we selected Level 2.0 data of sky radiometer, which were analyzed using SKYRAD.pack software[1] and cloud screening algorithm [2]. As shown in Fig. 2, the values of AOTs retrieved from MS-700 agreed quite well with sky radiometer at 500nm by falling data around 1:1 line. The RMSE for data shown in Fig. 2 is 0.024. Though the results for other wavelengths are not shown here, the values of RMSE for the wavelengths of 400nm, 675nm, 870nm, and 1020nm were 0.055, 0.021, 0.020 and 0.026, respectively. Those retrieved results with will be further improved by performing sensitivity studies with different solar spectrum data and technique of picking out solar spectrum data at the wavelengths of our interest.

We retrieved SSA values by applying the first method described in section 3 i.e. we compared measured diffuse irradiance with 31 values of modeled MS-700 equivalent diffuse irradiances.

This is because we verified the calibration constant of MS-700 provided by company by performing closure experiment with standard grating sun photometer (GER-2600). Fig. 3 shows the Comparison of MS-700 measured diffuse irradiance and MS-700 equivalent modeled diffuse irradiance at the wavelength of 500nm.

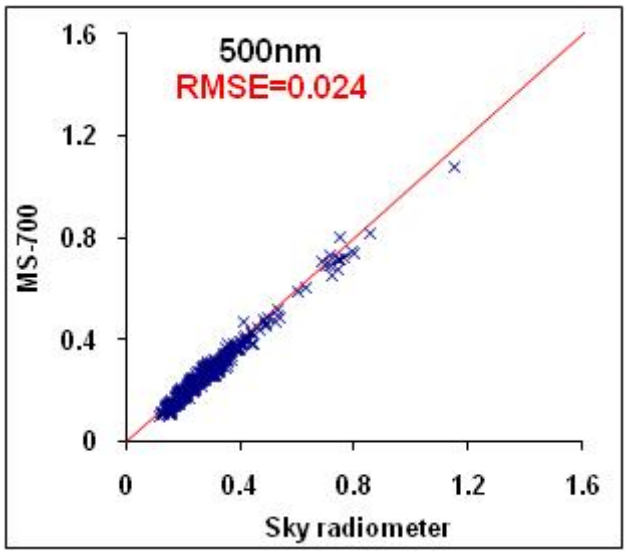

Fig. 2. Comparison of aerosol optical thickness (AOT) at 500nm obtained from MS-700 and sky radiometer.

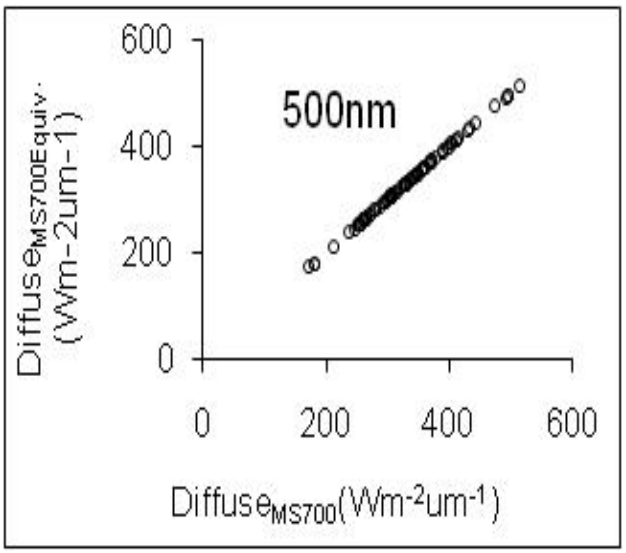

Fig. 3. Comparison of MS-700 measured diffuse irradiance and MS-700 equivalent modeled diffuse irradiance at the wavelength of 500nm.

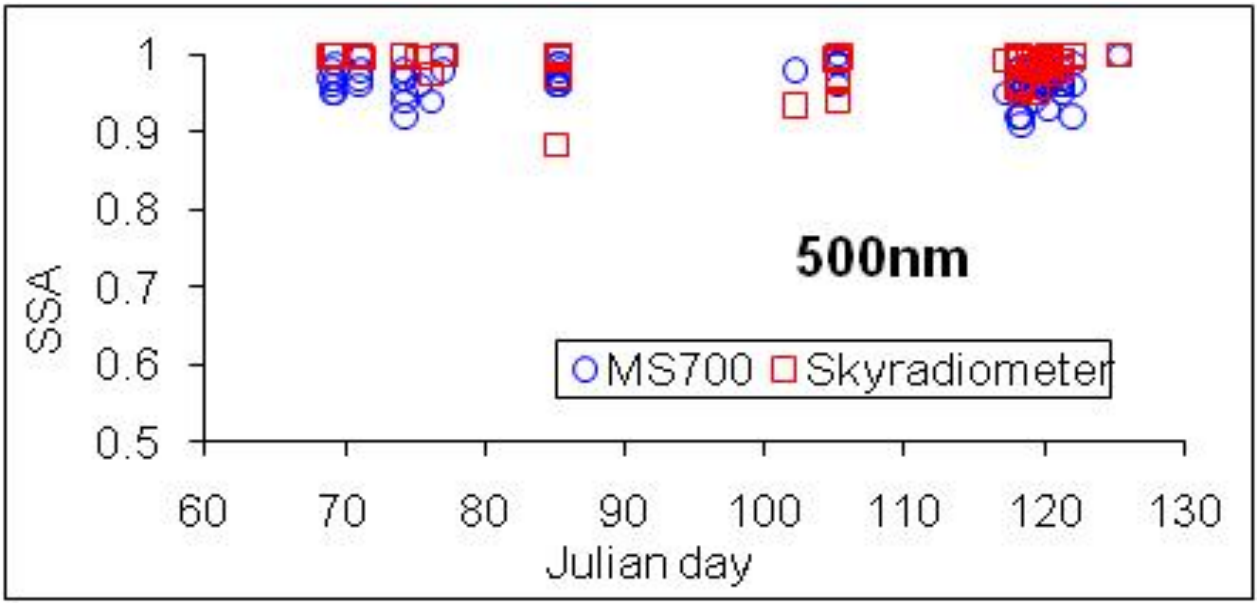

Fig. 4. Time series of SSA values at 500nm retrieved from MS-700 and sky radiometer

Fig. 4 shows the time series of SSA values at 500nm retrieved from MS-700 and sky radiometer. As shown in Fig. 4, the values of SSA at 500nm agreed reasonably. For other wavelengths (not shown here), SSA also agreed reasonably. However, there were some large distinct differences at some observation point at those wavelengths. Based on our sensitivity study, it was observed that retrieved SSA values from data of both MS-700 as well as sky radiometer depend on a number of input parameters. As a part of validating retrieved SSAs from both MS-700 and sky radiometer, spectral SSAs from each instrument as well as other necessary parameters were inputted in a radiative transfer model to estimate broad band diffuse fluxes(0.315-2.8μm), which were then compared with directly measured data. For MS-700 data, the relationship was *Modeled flux=1.05*Measured flux* with R^2=0.983. For sky radiometer data , For sky radiometer data, the relationship was *Modeled flux=1.08*Measured flux* with R^2=0.924. Similarly, the values of RMSE between modeled and measured fluxes for MS-700 and sky radiometer data were 8.15Wm^{-2} and 14.47Wm^{-2}, respectively.

Acknowledgements

This research is performed as a part of the SKYNET activities by the Observational Research Project for Atmospheric Change in the Troposphere (GEOSS program) of the Ministry of Education, Culture, Sports, Science and Technology, Japan. This research is also partially supported by the Global Environmental Research Fund (B-083) of the Ministry of the Environment, Japan.

References

1) Nakajima et al.: Use of sky brightness measurements from ground for remote sensing of particulate polydispersions. *Appl. Opt.*, **35**, 2672-2686, 1996.
2) Khatri, P., and T. Takamura: An algorithm to screen cloud-affected data for sky radiometer data analysis, *J. Meteor. Soc. Japan*, **87**, 189-204.

CEReS

Center for Environmental Remote Sensing,
Chiba University